University of Southampton Research Repository

Thesis: Liam Michael Furness (2020) "Development of Analytical Techniques for Lithium-Sulfur Batteries", University of Southampton, Faculty of Engineering and Physical Sciences, PhD Thesis, 197.

Data: Liam Michael Furness (2020) Dataset for Development of Analytical Techniques for Lithium-Sulfur Batteries. Dataset DOI: https://doi.org/10.5258/SOTON/D1640.

University of Southampton

Faculty of Engineering and Physical Sciences

Chemistry

Development of Analytical Techniques for Lithium-Sulfur Batteries

by

Liam Michael Furness

ORCID ID – 0000-0003-3538-2929

Supervisors – Dr. Nuria Garcia-Araez & Prof. John R. Owen

Thesis for the degree of Doctor of Philosophy

June 2020

University of Southampton

Abstract

Faculty of Engineering and Physical Sciences
Chemistry
Thesis for the degree of Doctor of Philosophy
Development of Analytical Techniques for Lithium-Sulfur Batteries
by
Liam Michael Furness

The aim of this study is to develop analytical techniques that can be used to better understand the lithium-sulfur (Li-S) battery system.

The first technique involves the determination of the total atomic sulfur content and the average polysulfide chain length of a polysulfide solution. These experiments elucidated the 2-phase boundaries and eutonic point, giving an accurate representation of the ternary (lithium sulfide-sulfur-electrolyte) phase diagram. The 2-phase boundary describes the maximum solubility of a polysulfide solution in contact with either solid lithium sulfide or solid sulfur. On the other hand, the eutonic point describes the maximum solubility of a polysulfide solution in contact with both solid lithium sulfide and solid sulfur, thus the concentration of polysulfide species at the eutonic point is the maximum that can be achieved. The saturation concentration of polysulfide species will depend on the nature of the solvent and the lithium salt, and these variables can be tuned to improve the Li-S battery performance. This was observed when increasing the electrolyte salt concentration which limited the polysulfide solubility and in turn improved the cyclability of the Li-S battery. Therefore, the composition of the ternary phase diagram can be implemented to explain changes in Li-S battery galvanostatic cycling performance.

The second technique, electrochemical impedance spectroscopy, will give further insight to the Li-S battery system. This technique, initially developed from Lasia et al. to determine the electroactive surface area of catalysts, has been applied to the cathode formulations for Li-S batteries in this study.[1] Starting with the impedance of the basic components in a Li-S battery to understand features on the Nyquist plot. The complexity of cell setup was increased until the impedance of a full Li-S battery was achieved. This

method allows determination of the specific surface area of different Li-S battery cathode formulations whilst also studying how the specific surface area of an electrode changes during galvanostatic cycling.

Table of Contents

Table of Contents i

Research Thesis: Declaration of Authorship v

Acknowledgements vii

Abbreviations and Units ix

Chapter 1 Introduction 1

1.1 Lithium-Sulfur Battery 1
1.2 Lithium-Sulfur Battery Components 8
1.3 Ternary Phase Diagram for the Lithium Sulfide Battery 14
1.4 Specific Surface Area Determination of the Lithium Sulfide Battery Cathode Materials 18

Chapter 2 Experimental Details 21

2.1 General Preparation of Experimental Equipment and Chemicals 21
2.2 Preparation of Electrolyte for Phase Diagram, GCPL and Impedance Experiments 21
2.3 Preparation of Lithium Polysulfide Solutions 22
2.4 Density of Polysulfide Solutions 22
2.5 Barium Sulphate Gravimetric Analysis 23
2.6 X-ray Diffraction of Barium Sulphate Samples 24
2.7 Determining the Molar Extinction Coefficient of Ferrocenium Tetrafluoroborate in 1,3-Dioxolane 24
2.8 UV-visible Absorption Spectroscopy Redox Titration 24
2.9 Microscope 26
2.10 MEDAC Elemental Analysis 27
2.11 Preparation of Swagelok Cells for GCPL 27
2.12 Electrolyte Concentration Effect on Battery Performance for GCPL 27
2.13 Preparation of Lab Scale Electrodes 28
2.14 Industrial Scale Electrodes 29
2.15 Preparation of Swagelok Cells for Impedance 29
2.16 Potentio Electrochemical Impedance Spectroscopy 32
2.17 Brunauer–Emmett–Teller (BET) Technique 32
2.18 GCPL/Impedance of Industrial Scale Electrodes 33

2.19 Grazing Incidence X-ray Diffraction 34

Chapter 3 Ternary Phase Diagram 35

3.1 Improvements to the Method of Analysing the Polysulfide Solutions 35
3.2 Preparation of Low Concentration Polysulfide Solutions 37
3.3 Gravimetric Determination of the Total Atomic Sulfur Content 40
3.4 UV-visible Absorbance Spectroscopy Redox Titration 44
3.5 Preparation of High Concentration Polysulfide Blends 51
3.6 Eutonic Point for the Ternary Phase Diagram 59
3.7 Preparation of 2-Phase Boundary Polysulfide Solutions 64
3.8 2-Phase Boundaries for the Ternary Phase Diagram 70
3.9 Electrolyte Concentration Effect Phase Diagram 80
3.10 Electrolyte Concentration Effect on Battery Performance 92
3.11 Conclusions 99

Chapter 4 Specific Surface Area Determination of Sulfur Cathodes by Electrochemical Impedance Spectroscopy 101

4.1 Specific Surface Area Determination of Carbon Electrodes 101
4.2 Specific Surface Area Determination of Carbon/Sulfur Electrodes 115
4.3 Specific Surface Area Determination of Carbon/Sulfur Electrodes at Different States of Charge 132
4.4 Conclusions 145

Chapter 5 Conclusions 148
Chapter 6 Appendix 150

6.1 Preparation of Electrolyte 150
6.2 Preparation of Polysulfide Solutions 150
6.3 Density of the Polysulfide Solution 151
6.4 Gravimetric Analysis 152
6.5 UV-visible Absorbance Spectroscopy Redox Titration 152
6.6 Molar Extinction Coefficient of Ferrocenium Tetrafluoroborate in DOL 154
6.7 Molar Fraction Calculations 157
6.8 MEDAC Calculations 161
6.9 Determination of SSA from Fitted Impedance Results 165

6.10 Determination of the Warburg Resistance 168

Chapter 7 References 173

Research Thesis: Declaration of Authorship

Print name:	Liam Michael Furness
Title of thesis:	Development of Analytical Techniques for Lithium-Sulfur Batteries

I declare that this thesis and the work presented in it are my own and has been generated by me as the result of my own original research.

I confirm that:

1. This work was done wholly or mainly while in candidature for a research degree at this University;
2. Where any part of this thesis has previously been submitted for a degree or any other qualification at this University or any other institution, this has been clearly stated;
3. Where I have consulted the published work of others, this is always clearly attributed;
4. Where I have quoted from the work of others, the source is always given. With the exception of such quotations, this thesis is entirely my own work;
5. I have acknowledged all main sources of help;
6. Where the thesis is based on work done by myself jointly with others, I have made clear exactly what was done by others and what I have contributed myself;
7. None of this work has been published before submission.

Signature: Date:

Acknowledgements

I would like to show my gratitude to my academic supervisors Dr. Nuria Garcia-Araez and Prof. John Owen for their continued support throughout my PhD. I feel privileged to be able to work in their prestigious research group where I have learnt many lessons, which will help me in my future academic and non-academic life.

I would like to thank the past and present members of Dr. Nuria Garcia-Araez and Prof. John Owen research group for their help in the lab, scientific discussions, joking around in the office, crosswords in the tea room, cricket, group meals, poker and drinks at The Stag's. In Particular, I would like to thank Dr. James Frith, Dr. James Dibden, Dr. William Richardson, Dr. Thomas Homewood, Dr. Nina Meddings, Dr. Daniel Wright, Dr. Rinaldo Raccichini, Dr. Vivek Padmanabhan, Dr. John Lampkin, Dr. Henry Li, Dr. Niamh Ryall, Dr. Sara Perez-Rodriguez, Dr. Josh Whittam, Dr. Alex Keeler, Sam Fitch, Nikolay Zhelev, Ben Rowden, Max Jenkins, and Liam Lu.

I would like to acknowledge the University of Southampton, the Engineering and Physical Sciences Research Council (EPSRC) (Award Reference – 1792800) and OXIS Energy Limited for funding my PhD.

Finally, I owe a massive thank you to my parents Mike and Sue, my sister Steph, my extended family and my friends who have all supported me through my PhD.

Abbreviations and Units

General Abbreviations

Al-S	aluminium-sulfur battery
aq.	aqueous
$Ba(NO_3)_2$	barium nitrate
$BaSO_4$	barium sulfate
BET	Brunauer-Emmett-Teller
C	carbon/PTFE electrode
C/S	carbon/sulfur/PTFE electrode
C	capacitor
CPE	constant phase element
C	capacitance
C_A	areal capacitance
C_{dl}	double layer capacitance
Cu	copper
DME	1,2-dimethoxyethane
DOL	1,3-dioxolane
e^-	electron
e.g.	for example
et al.	and others
f*	transition frequency
Fc	ferrocene
Fc^+	ferrocenium cation
$FcBF_4$	ferrocenium tetrafluoroborate
GCPL	galvanostatic cycling with potential limitation
GIXRD	grazing incidence X-ray diffraction
i.e.	that is
l	liquid
Li^+	lithium cation
Li-ion	lithium-ion battery
Li_2S_n	lithium polysulfide species

Li_2S	lithium sulfide
Li-S	lithium-sulfur battery
$LiBF_4$	lithium tetrafluoroborate
LiTFSI	lithium bis(trifluoromethanesulfonyl)imide
n	polysulfide chain length
No.	number
ppte.	precipitate
PS	polysulfide
PTFE	polytetrafluoroethylene
R	resistor
R_{CT}	charge transfer resistance
R_S	solution resistance
R_W	Warburg resistance
R-CPE	resistor in series with a CPE
R_1-(CPE/R_2)	resistor in series with, a CPE in parallel with a resistor
R-W_o	resistor in series with an open Warburg element
RBF	round bottom flask
sat.	saturated
s	solid
SEI	solid electrolyte interphase
SA	surface area
SSA	specific surface area
S^{2-}	sulfide
S	sulfur
S_8	cyclic octasulfur
UV/vis	ultraviolet visible
UAV	unmanned aerial vehicle
vs.	versus
vol.%	volume percentage
wt.%	weight percentage
W_o	open Warburg element
XRPD	X-ray powder diffraction
z	number of electrons

Mathematical Abbreviations

A	Absorbance
AR	atomic ratio
a, b, c	unit cell lengths
α, β, γ	unit cell angles
α	transfer coefficient
C/x rate	discharge/charge battery in x hours
c_0^*	concentration of oxidised form initially in the solution
c_x	concentration of x
Δ	change in
D_O	diffusion coefficient of the oxidised species
D_R	diffusion coefficient of the reduced species
ε	molar extinction coefficient
E	formal potential
$E_{1/2}$	half-wave potential
E_{WE}	working electrode potential
F	Faraday's constant (96485 C mol^{-1})
$F_x^{\%}$	found % of x
i	imaginary number ($i = \sqrt{-1}$)
I	current
k_0	standard rate constant
l	cell path length
$[Li^+]_x$	lithium cation concentration in x
$[Li_2S]$	lithium sulfide concentration
m_x	mass of x
M_x	relative molar mass of x
$moles_x$	number of moles of x
MF_x	molar fraction of x
n_x	number of moles of x
n	number of electrons
Ø	diameter
OCV	open circuit voltage

ρ_x	density of x
P_{CPE}	constant phase of the CPE
P_{Wo}	constant phase of the open Warburg element
$Q_{Theoretical}$	theoretical specific capacity
R	ideal gas constant (8.3145 J mol^{-1} K^{-1})
R_{Wo}	resistance of the open Warburg element
R^2	coefficient of determination
RMM_x	relative molar mass of x
Rp	residual of least squares refinement
$[S]_x$	sulfur concentration in x
$[S_n^{2-}]$	polysulfide concentration
$[S]_T^{Sol.}$	total atomic sulfur concentration
T	temperature
T_{CPE}	capacitance of the CPE ($F\ s^{1-P_{CPE}}$)
T_{Wo}	capacitance of the open Warburg element
V_x	volume of x
ω	frequency
wRp	weighted residual
x	extent of titration reaction ($0 \leq x \leq 1$)
χ^2	chi-squared
Z_x	impedance of x
$Z_x(\omega)$	impedance of x at a specific frequency ω
Z'_{Real}	real impedance
$-Z''_{Im}$	imaginary impedance

Units

Prefixes to units: M = mega (10^6), k = kilo (10^3), d = deci (10^{-1}), c = centi (10^{-2}), m = milli (10^{-3}), μ = micro (10^{-6}) and n = nano (10^{-9}).

Å	angstrom
A	ampere
bar	bar
C	coulomb
°C	celsius
cps	counts per second

F	farad
g	gram
Hz	hertz
h	hour
in.	inch
J	joule
K	kelvin
L	litre
m	metre
M	molar
mesh	number of openings per inch
mins	minute
mol	mole
Ω	ohm
rpm	revolutions per minute
s	second
S	siemens
t	tonne
V	volt
W	watt
$	dollars
°	degrees
%	percentage

Chapter 1 Introduction

1.1 Lithium-Sulfur Battery

There is a large amount of practical applications for the lithium sulfur (Li-S) battery including but not limited to electric/hybrid vehicles, large scale energy storage e.g. national grid, and load levelling for renewable energy sources.[2,3] The applications mentioned will also help with lowering carbon dioxide emissions and improving energy efficiency.[4] The development of the secondary batteries are becoming increasingly important when you consider motions are being put forward in the House of Commons to end the sale of new petrol and diesel vehicles by 2040, therefore alternative energy sources will be required.[5]

State of the art Li-ion batteries have some impressive performance statistics such as high cycle efficiency (> 80 %) and long cycle life (500 – 1000 cycles) but the maximum specific energy of ~250 W h kg^{-1} is limiting their use for long range electric vehicles or for grid storage.[6] The main advantage Li-S batteries has over Li-ion batteries is a high theoretical specific energy (gravimetric energy density) of 2567 W h kg^{-1}.[7] Another performance value that is important to Li-S batteries is the energy density (volumetric energy density) which has been summarised in a Ragone plot (Figure 1.1.1).[8]

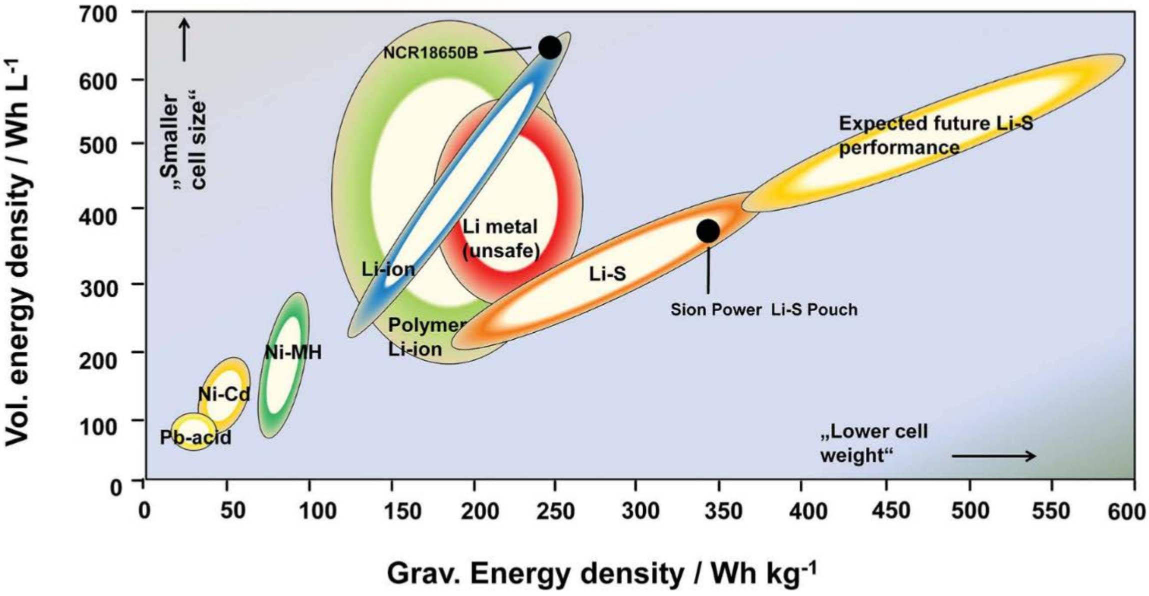

Figure 1.1.1 – Ragone plot of various secondary batteries. Reproduced from Hagen et al..[8]

The current energy density limits the practical applications of the Li-S battery where size is important such as portable devices. However, there are many applications where a smaller weight is key e.g. military and UAVs.[9] The projected Li-S battery performances show similar energy densities but with over double the specific energy. Alongside the better battery performance, Hagen et al. also state the Li-S cells have potential cell costs in \$ kW h^{-1} which are cheaper than the state of the art Li-ion batteries.[8] Therefore this makes the Li-S battery more financially lucrative for electric vehicles.

A techno-economic model from Gallagher et al. establishes the parameter values required to achieve the energy density, specific energy and cost targets for a Li-S transportation battery.[7] The parameter values required for the energy density are areal capacities of > 8 mA h cm^{-2} with electric vehicle life targets of 1000 cycles. The parameter values required for the specific energy and cost targets are; stable operation at high current densities (~ 7 mA cm^{-2}), a limited excess of lithium (~ 50 – 100 %), high capacity retention at high sulfur loadings (~ 7 mg$_S$ cm^{-2}, where the unit of mass g$_S$ refers to the mass of sulfur because sulfur is the active material in Li-S batteries and will be used throughout the thesis) and an electrolyte starved cathode (60 – 70 vol%). Gallagher et al. also suggest the key to achieving these targets are new electrolyte approaches alongside better understanding of reaction mechanism with limited amounts of electrolyte.[7]

One important limitation of Li-S and Li-ion batteries is the cost and global availability of lithium metal. This consideration is not an immediate issue but during this century as electric vehicles will become more prevalent, our demand for lithium will increase. The lithium demand for 2010 to 2100 has been modelled with a maximum required lithium to be 20 Mt from an estimated 39 Mt of available lithium if a 50 % recovery rate for brines, pegmatites and sedimentary rocks is applied.[10] Whereas a report from the U.S. Geological Survey estimates that only 14 Mt of lithium is available.[11] Therefore, it is important to consider lithium as a finite resource that is eventually going to replace fossil fuels, another finite resource. With this in mind, high cycle efficiency and lithium battery recycling are two important aspects to have long-term lithium supply.[12]

However, Li-S batteries do contain sulfur that is the fifth most abundant element of Earth and is a by-product during the processing of crude oil and natural gas, meaning it is cheap and readily available.[13] This makes the cost of high sulfur loaded Li-S batteries competitive with lithium ion cells.[14]

A possible alternative to using lithium is to use aluminium in aluminium sulfur (Al-S) batteries. Aluminium is the third most abundant element and is the most abundant metal in the Earth's crust making it very cheap with respect to lithium and cobalt.[15] The Al-S battery does have a very high theoretical specific energy of 1200 W h kg^{-1} but faces challenges such as poor reversibility and slow electrochemical kinetics limiting the performance of the battery.[16]

Li-S batteries have the potential to be implemented in the next generation of secondary batteries with properties such as the high theoretical specific energy as mentioned previously. In this theoretical ideal scenario, all of the sulfur in the cathode undergoes complete reduction to lithium sulfide (Equation 1.1.1).

$$S_8 + 16\,Li^+ + 16\,e^- \rightarrow 8\,Li_2S$$

Equation 1.1.1 – Complete reduction of elemental sulfur to lithium sulfide.

Therefore, each sulfur atom has a two electron reduction process to create the sulfide species (Equation 1.1.2).

$$S + 2\,e^- \rightarrow S^{2-}$$

Equation 1.1.2 – Complete reduction of atomic sulfur to sulfide.

From this the theoretical specific capacity of atomic sulfur can be determined by;

$$Q_{Theoretical} = \frac{zF}{M_S} = \frac{2 \times 96485\ C\ mol^{-1} \times \left(\frac{1\ h}{3600\ s}\right)}{32.06\ g_S\ mol^{-1}} = 1672\ mA\ h\ g_S^{-1}$$

Equation 1.1.3 – Theoretical specific capacity of atomic sulfur.

where $Q_{Theoretical}$ is the theoretical specific capacity (mA h g^{-1}), z is the number of electrons, F is Faraday's constant (96485 C mol^{-1}) and M_S is relative molar mass of sulfur. The theoretical specific capacity is very high with respect other state of the art rechargeable batteries, however the practical specific capacity is approximately 1200 mA h g_S^{-1}.

In reality, the complete reduction of sulfur to lithium sulfide is a complex process that has multiple redox reactions with several intermediate species.

$$S_8 \xrightarrow{Li^+ + e^-} Li_2S_n \xrightarrow{Li^+ + e^-} Li_2S$$

Equation 1.1.4 – During the reduction of sulfur to lithium sulfide, lithium polysulfide intermediates are produced.

These intermediate species are lithium polysulfide species. The chain length (n) of the polysulfide species will depend on the extent of discharge.

Species	Chain Length	Sulfur Oxidation State
Li_2S_8	8	$-\frac{1}{4}$
Li_2S_7	7	$-\frac{2}{7}$
Li_2S_6	6	$-\frac{1}{3}$
Li_2S_5	5	$-\frac{2}{5}$
Li_2S_4	4	$-\frac{1}{2}$
Li_2S_3	3	$-\frac{2}{3}$
Li_2S_2	2	-1
Li_2S	1	-2

Table 1.1.1 – Summarising the effect of the polysulfide chain length on the average sulfur oxidation state.

Therefore, with a practical specific discharge capacity of 1200 mA h g^{-1} the average sulfur oxidation state will be negative 1.4 (1672 mA h g_S^{-1}/ 1200 mA h g_S^{-1} $\approx$ 1.4) meaning the electrode has not completely discharged. One of the causes of this loss in discharge capacity is a phenomenon known as the polysulfide shuttle effect where the sulfur active material is lost in an irreversible oxidation mechanism at the lithium anode surface.[17] The lithium polysulfide species formed in the electrolyte are very soluble. These intermediate species initially formed in the cathode can diffuse to the lithium metal anode and undergo a parasitic reaction at the electrode surface (Figure 1.1.2).

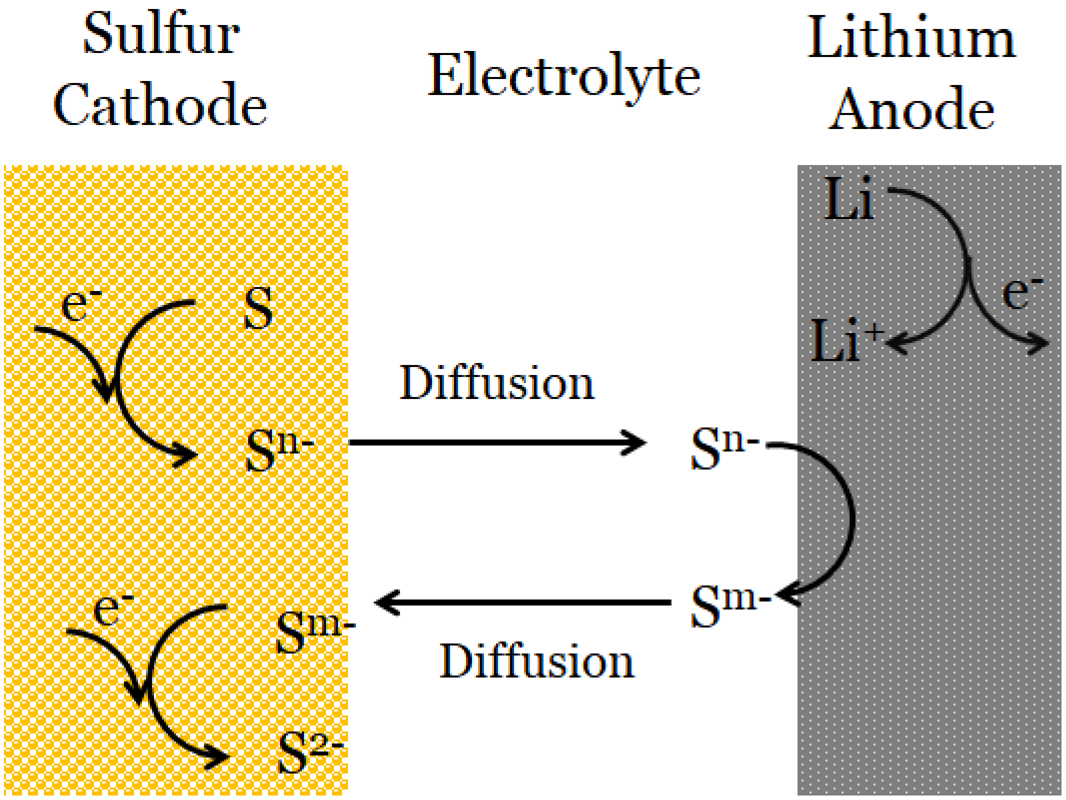

Figure 1.1.2 – Illustration of the polysulfide shuttle effect during discharge, where m > n.[17]

In this parasitic reaction, the polysulfide species undergoes a chemical reduction with the lithium anode surface forming a shorter polysulfide species chain length.

Another cause of discharge capacity loss for Li-S batteries is incomplete sulfur utilization. The intermediate polysulfide species produced during discharge remain unreacted at the end of discharge. The slow mass transport of polysulfide species inside the separator limits further reduction. Offer et al. have proven this by lowering the applied current at the end of discharge to lower the cycle rate and produces extra capacity.[18] Another paper from Gaberscek et al. achieved a similar outcome by adding fresh catholyte (polysulfide solution) to the battery at the end of discharge.[19] Both techniques gain extra capacity by increasing the effective polysulfide concentration at the electrode surface.

The end of discharge has kinetic limitations as shown in a paper from Gasteiger et al. where they performed a rotating-ring disk electrode study to look at the kinetics of the reaction pathways to reduce a sulfur catholyte to lithium sulfide.[20] The initial formation of long chain polysulfide species is fast but the formation of the shorter chain polysulfides and lithium sulfide is slow because they require mediation from polysulfide chemical reactions in this RRDE cell configuration. However for commercial cells the mass transport is the rate limiting step instead of the charge transfer kinetics.[18, 21]

The polysulfide shuttle also affects the charging capacity of the Li-S battery. During charge, the lithium sulfide is oxidised to form sulfur.

$$S^{2-} \rightarrow S + 2e^{-}$$

Equation 1.1.5 – Complete oxidation of the sulfide to atomic sulfur.

Whereas the polysulfide shuttle effectively performs the reverse reaction reducing the polysulfide intermediates into shorter chain length polysulfide species. These two processes in action creates an infinite charging loop (Figure 1.1.3).

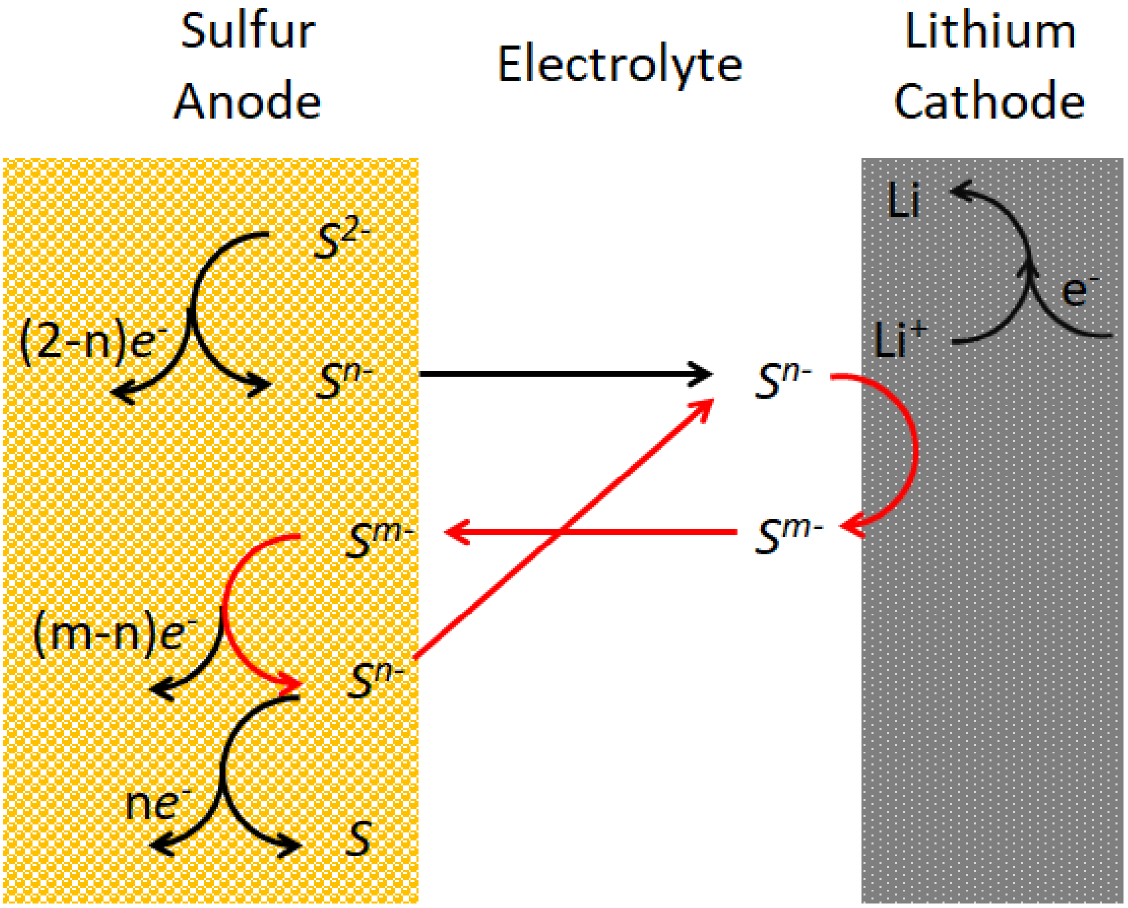

Figure 1.1.1 – Illustration of the polysulfide shuttle effect during charge, where m > n and the red arrows represent the infinite charging loop.

The Li-S battery has other rechargeability issues such as during charging lithium plating forms high surface area dendritic lithium which consumes electrolyte in the formation of a new solid electrolyte interphase (SEI) layer and the polarization of the sulfur electrode at high potentials induces electrolyte degradation. The compounds formed from the electrolyte degradation have a detrimental effect on battery performance. The dissolution of sulfur and lithium sulfide during charge and discharge can cause volume changes. This leads to the structural breakdown of the electrode with each cycle resulting in the capacity to fade.

The charging of the Li-S battery has kinetic limitations as well because the oxidation of lithium sulfide to sulfur in the absence of polysulfides requires very high overpotentials. As mentioned previously, the polysulfide species mediate the redox reaction for the Li-S battery. Therefore if the concentration of polysulfides in the electrolyte is low, due to consumption at the lithium electrode in the polysulfide shuttle, higher overpotentials will be required for charging. Wang et al. show the use of a dual phase electrolyte containing polysulfides, lowering the overpotential applied when charging.[22] However for this dual phase electrolyte they required a ceramic lithium super ionic conductor (LATP) layer to isolate the lithium electrode. This is similar to another paper from Berger et al. where they used a lithiated Nafion (Li^+-Nafion) membrane.[23] Both of these materials only allow the transport of lithium cations meaning the lithium electrode is not prone to the polysulfide shuttle effect. Therefore, the polysulfide intermediates formed that diffuse away from the sulfur electrode cannot be consumed at the lithium electrode surface. This was shown by the lower overpotential for the Li^+-Nafion interlayer since the concentration of polysulfides would be higher.[23]

1.2 Lithium-Sulfur Battery Components

The Li-S battery has four key components; lithium anode, electrolyte, separator and sulfur cathode. The main focus of the literature is on improving performance by optimising the sulfur cathode.[24] Although, the lithium anode is as important in terms of limiting the battery performance.[25] It is common to see Li-S batteries built in coin cell or Swagelok cell configurations where there is an excess of electrolyte and lithium relative to the sulfur. In a pouch cell, which is more representative compared to a commercial cell, the cell will fail earlier than expected due to electrolyte consumption and lithium dendrite growth.[26] The electrolyte is depleted by reacting with the lithium anode surface forming an SEI layer. Common electrolyte solvent 1,3-dioxolane (DOL) forms a stable SEI on the lithium anode whereas 1,2-dimethoxyethane (DME) is more reactive.[27]

Therefore when the cell is being charged and discharged the lithium ion has to diffuse through these two layers. The rate of discharge/charge can affect the nucleation and growth of lithium dendrites.[28] With each plating and stripping cycle fresh lithium metal surface is created which reacts with the electrolyte forming an SEI layer. This process will consume more of the electrolyte and create dead lithium.[29] Lithium dendrites have serious safety concerns because they can cause an internal short circuit in the battery resulting in thermal runaway.[27]

Electrolyte additives, such as lithium nitrate, have also shown improved performance via the catalysis of the oxidation of polysulfide species to sulfur which mitigates the polysulfide shuttle effect.[30] Although, the electrolyte additive still faces the issue of consumption like the electrolyte. Electrochemical pre-treatment and surface coating of the lithium anode interface have both shown improved stability and capacity retention by preventing contact of the polysulfide species.[31-32]

The electrolytes used for Li-S batteries are similar to the electrolytes used for Li-ion batteries.[33] The lithium salt has a medium size anion that is dissolved into a solvent based on small organic molecules with a concentration around 1 M. The most common example of an electrolyte used in the literature for Li-S batteries is 1 M LiTFSI in a 1:1 mixture of DOL and dimethoxyethane (DME).[34] The LiTFSI salt has a high thermal stability, high conductivity and is compatible with ether based solvents such as DOL and DME.[35]

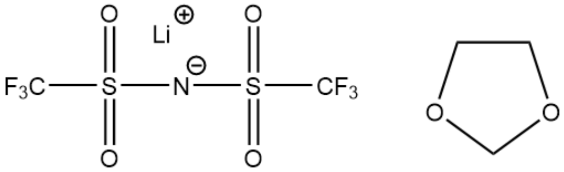

Figure 1.2.1 – The LiTFSI (left) and DOL (right) used to make the standard electrolyte for this study.

LiTFSI has a relatively low lattice energy, which is due to the inductive effect from the CF_3 groups withdrawing electron density from the nitrogen atom, and the negative charge at the nitrogen atom can be delocalised onto the sulfonyl groups (Figure 1.2.2).[36] This means the TFSI anion has a high dissociation ability.

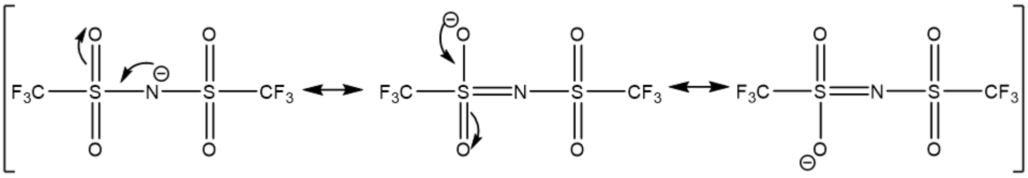

Figure 1.2.2 – Delocalisation of the negative charge on the nitrogen atom onto the sulfonyl groups.[36]

The linear DME offers a higher polysulfide solubility, faster reaction kinetics but is less compatible with the lithium metal anode. Whereas the cyclic DOL creates a more stable SEI at the lithium metal anode interface with low polysulfide solubility and slower reaction kinetics. The mix of the two solvents lead to synergistic effect which improve Li-S battery performance compared to each solvent separately.[37]

One of the key properties for a good electrolyte is low viscosity. The low viscosity electrolytes will allow faster mass transfer and increased polysulfide solubility. This improves the sulfur utilization because the redox reactions take place in solution.[38] Unfortunately this feature also facilitates the polysulfide shuttle.

There have been many reported methods of combating the polysulfide solubility by altering the electrolyte composition. For example, work by Armand et al. using a very concentrated electrolyte solution, which they call “solvent-in-salt” that will lower the polysulfide intermediate solubility.[39] The higher concentration electrolytes have high viscosities meaning there will be low utilization of sulfur and lower initial discharge/charge capacities. However the suppression of the polysulfide shuttle leads to a slower capacity fade.

An alternative to liquid organic electrolytes are the RTIL electrolytes. An example of a binary RTIL electrolyte is lithium bis(trifluoromethanesulfonyl)amide/*N*,*N*-diethyl-N-methyl-*N*-(2-methoxyethyl)ammonium bis(trifluoromethanesulfonyl)amide (Li[TFSA]/[DEME][TFSA]) which is safer than the flammable liquid organic electrolytes and has a high viscosity that limits the polysulfide species mobility which in turn suppresses the polysulfide shuttle.[40] This is further propagated by the weak Lewis acidic/basic nature of RTIL electrolytes, which will have weak interactions with ions corresponding to a low polysulfide species solubility.[41] This also causes the mass transport of the Li-S battery to be slow and experimentally it is found that the sulfur utilization is low.[41] Byon et. al. produced a RTIL/liquid organic electrolyte hybrid that contained *N*-methyl-*N*-propylpiperidinium bis(trifluoromethanesulfonyl)imide (PP13-TFSI) and DME.[42] This found the balance between mobility and solubility of the polysulfide species resulting in improved electrochemical performance of the Li-S battery.

Polymer (solid-state) electrolytes are a good substitute for liquid electrolytes because of their high safety aspects like non-flammability, mechanical stability, and significantly reduced lithium dendrite formation.[43] The polymer electrolyte acts like a separator between the two electrodes retaining the polysulfide species at the sulfur cathode.[43] However this also causes low sulfur utilization. Similar to RTIL/liquid organic electrolyte, a hybrid solid-state/RTIL electrolyte has been developed leading to improved battery performance.[44]

The separator for the Li-S battery is important to maintain the physical integrity of the cell. Some of the key factors for a good battery separator are being an electronic insulator, having minimal electrolyte resistance, having good mechanical stability, having high chemical resistance and being readily wetted by the electrolyte.[45] The two most common separators used for Li-S batteries are glass fibre based separators and polyolefin (i.e. Celgard) based separators. An impedance study from Raccichini et al. characterising the transport properties of electrolytes contained within porous separators showed the differences between the glass fibre based separators and polyolefin based separators.[46] The glass fibre based separators had a higher porosity and a lower tortuosity than the polyolefin based separators meaning there will be good wettability of the separator, high electrolyte conductivity but this will also facilitate the polysulfide shuttle.

The separator can also act as a physical barrier to the polysulfide shuttle. This can be achieved by functionalising the separator/electrode interface. For example in a paper from Kiai et al., their double side coated functionalised separator displayed better cycle stability compared to non-functionalised separators.[47] The potassium in the coatings cause the reutilization of the polysulfide intermediates that have diffused out of the sulfur cathode by enhancing the electrochemical kinetics for conversion of lithium polysulfides to potassium polysulfides.

The cathode material commonly used for Li-S batteries is composed of sulfur, carbon and a binder. The carbon is required for two reasons. Firstly, sulfur is electronically insulating with a very low conductivity $5 \times 10^{-30}\ \mathrm{S\ cm^{-1}}$.[48] Therefore mixing the sulfur with carbon increases the conductivity of the composite $> 10^{-4}\ \mathrm{S\ cm^{-1}}$, making it comparable to conductivities of electrodes used for Li-ion batteries.[48] Secondly, the carbon acts as conductive matrix that supports the sulfur whilst acting as the current collector. Finally the binder is required to hold the electrode species together.

To maintain the advantage of the high energy density of sulfur, the cathode material should have high sulfur loadings of $\sim$ 7 $\mathrm{mg_S\ cm^{-2}}$ with areal capacities of > 8 mA h $\mathrm{cm^{-2}}$.[7] The composite material can be prepared by mechanical mixing (i.e. pestle and mortar or ball milling) or by a melt method. In the melt method, the sulfur is heated to 160 ^{o}C in an autoclave which produces molten sulfur which can better impregnate into the pores of the carbon than mechanical mixing due to the low viscosity.[49] This better traps the sulfur within the porous carbon matrix. This means during battery cycling, the polysulfide intermediates are contained within the cathode area, slowing down the polysulfide shuttle by increasing the path length.

Typically mesoporous carbons (i.e. acetylene black) are used in most recent research because they both entraps the sulfur and its reduced species whilst also providing reasonable pore volumes allowing higher sulfur loadings and better rate capability due to better ion transport.[50] Microporous carbon will immobilize the bulky polysulfide intermediates produced due to the small pore sizes not allowing diffusion meaning the cell will have a long cycle life.[51] However, the low sulfur loadings are required and the slow ion transport means there will be poor sulfur utilization leading to lower discharge capacities. Macroporous carbon allows very fast ionic transport kinetics and a large volumetric space for high sulfur loadings.[52] However due to the fast ion transport, the polysulfide shuttle rate also increases meaning the capacity fade will increase and the cycle life will decrease. The macroporous carbon in my opinion has the highest potential for commercial application allowing high sulfur loadings and high rate capability. Therefore research into stopping the polysulfide shuttle is key to getting slow capacity fade and high coulombic efficiency. This could be achieved by protecting the lithium anode from the polysulfide shuttle such as forming an artificial SEI film on the lithium anode surface.[53]

Another method of slowing down the rate of the polysulfide shuttle is sulfur encapsulation where the intermediate polysulfide species produced are trapped within the cathode. This has been achieved by encapsulating the sulfur within highly ordered mesoporous carbon CMK-3, within multiwalled carbon nanotubes and metal oxides all showing better capacity retention.[54–56]

A paper from Lacey et al. has shown the influence of different cathode binders on the porosity of the composite electrode. In this work they compared poly(vinylidene difluoride) (PVdF), a common binder used for Li-ion and Li-S batteries, to other less commonly used binders in the literature.[57] It was shown that PVdF had low swellability in DOL:DME based electrolytes meaning the choice of binder can have an effect on the accessibility of the electrolyte to the carbon surface, pore volume and the capacity of the cell.

Overall there are many components to the Li-S battery that require optimisation to improve cell performance. However, a review from Cleaver et al. has shown the research community has mainly focused their work on the cathode.[58] They suggest a more balanced approach to the development of the Li-S battery and focusing future work on neglected areas such as cell operation, modelling, electrolyte, anode and cell production.

Alongside the improvements with material research, an increased understanding of mechanism occurring in discharge and charge from analytical techniques is required.[59] With this more complex models for the mechanisms of operation can be developed, which can inform material research and accelerate technology development.

Modelling has been used to develop a degradation aware model that indicates the irreversible and reversible loss of capacity which can be a useful tool to determine the operational parameters for increase cell lifetime with respect to other battery features such as maximum energy or power per cell.[60] Another degradation aware technique called differential thermal voltammetry (DTV) is able to track and quantify the polysulfide shuttle effect of a Li-S battery during charge.[61] The polysulfide shuttle was monitored via changes in cell temperature. The extent of shuttling was dependent on the ambient temperature and the charging current. This work could be used for real-time detection of the polysulfide shuttle to create an adaptive cut-off criterion to minimise degradation and increase coulombic efficiency. Therefore developing analytical techniques to study novel aspects of Li-S battery system is essential in informing further developments in the battery components.

1.3 Ternary Phase Diagram for the Lithium Sulfide Battery

Significant advances in performance have been achieved in recent years, and it has been shown that the electrochemical behavior critically depends on the choice of electrolyte, which has been ascribed to differences in polysulfide solubilities.[33, 39, 62] This work was based upon a previous PhD thesis project from James Dibden, where he developed an analytical method to determine the solubility of polysulfide solutions as well as their speciation (i.e. the average oxidation state of sulfur in the polysulfide solutions, which is related to the average polysulfide chain length).[63] In addition, by using the Nernst equation, the equilibrium discharge profile of lithium sulfur cells was predicted to change with the electrolyte content within the cell. For example, a cell containing a minimum amount of electrolyte, the discharge reactions will produce polysulfide solutions at a concentration beyond the solubility limit, which would then precipitate in the form of solid sulfur and solid lithium sulfide:

$$Li_2S_n \rightarrow Li_2S + (n-1)\,S$$

Equation 1.3.1 – Disproportionation reaction of excess lithium polysulfide species in solution producing solid lithium sulfide and sulfur.

Under these conditions, the composition of the polysulfide solution would remain constant and equal to the solubility limit. This is akin to the production of the saturated polysulfide solutions for the phase diagram where the solutions are also at their solubility limit. Therefore, the discharge reaction would effectively be the reduction of solid sulfur into solid lithium sulfide:

$$S_8 + 16\,e^- + 16\,Li^+ \rightarrow 8\,Li_2S$$

Equation 1.3.2 – Simplified discharge reaction mechanism at the saturation point of the electrolyte in a Li-S cell.

In this region where three phases coexist (solid sulfur, solid lithium sulfide and polysulfide solution), the cell voltage would be constant, and a single long discharge plateau is expected instead of the usual two plateau discharge profile.[63]

This work focuses on the characterization of saturated polysulfide solutions that exist in equilibrium with solid sulfur and solid lithium sulfide, producing a complete phase diagram for an electrolyte (Figure 1.3.1). With these techniques developed in this fundamental study, a phase diagram can be produced which can predict the following characteristics of the Li-S battery system;

- The total atomic sulfur concentration
- The average chain length of the polysulfide species
- The eutonic point which describes the polysulfide saturation point of in the electrolyte
- The 2-phase boundaries which describe the dissolution and precipitation of solid lithium sulfide and sulfur
- Why the eutonic point changes with the variation in electrolyte salt concentration
- Correlating the lower polysulfide solubility in concentrated electrolytes to improvements in the galvanostatic cycling data

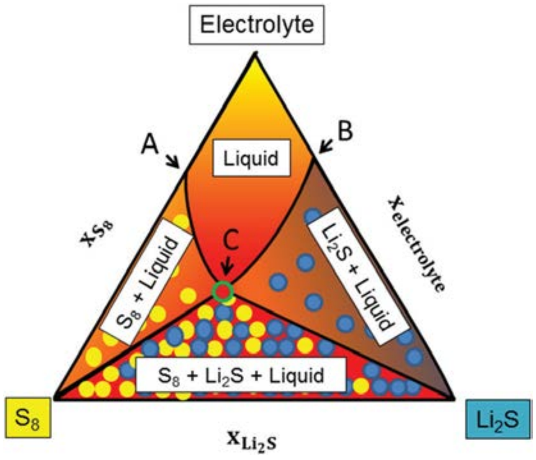

Figure 1.3.1 – Sketch of ternary phase diagram of a sulfur-lithium sulfide-electrolyte system. Reproduced from Dibden et. al..[63]

The sketch of the phase diagram is split into four sections. The top section is the 1-phase region that represents a liquid electrolyte with both the lithium sulphide and sulfur dissolved into the electrolyte forming a polysulfide solution. The left and right sections are the 2-phase regions that represent an electrolyte blend with an excess of sulfur or lithium sulphide present as a solid in the solution. Mixtures of excess solid and polysulfide solution will be referred to as blends. The bottom section is the 3-phase region that represents an electrolyte blend with excess of sulfur and lithium sulphide. Point C is the eutonic point where all the sections intersect and it describes a solution at the maximum saturation of both sulfur and lithium sulphide and therefore the maximum concentration of polysulfide species for a particular electrolyte. The position of the eutonic point on the phase relates to two factors, the maximum polysulfide solubility within the electrolyte and the speciation (i.e. polysulfide chain length) of the saturated species. This means the position of the eutonic point on the phase diagram could be affected by the choice of the salt, the choice of solvent or the concentration of the electrolyte salt. For example, an electrolyte with a high electrolyte salt concentration will have a low polysulfide solubility. The lower polysulfide solubility reduces the polysulfide shuttle in a Li-S battery. The position of the eutonic point on the phase diagram will be higher since the molar fraction coming from the electrolyte will be greater. Therefore the higher the position of the eutonic point on the phase diagram, the better the Li-S battery performance with respect to capacity fade.[39]

These saturated solutions or eutonic point solutions are prepared by mixing an excess of solid sulfur and solid lithium sulfide in a solvent typical of lithium-sulfur batteries (1 M LiTFSI in 1,3-dioxolane). We demonstrate that after filtration of excess solid, the same composition of the saturated solution is obtained when mixing sulfur and lithium sulfide in different ratios, mimicking the discharge behavior of a lithium-sulfur cell with a minimum amount of electrolyte, which would involve the conversion of sulfur to lithium sulfide at a constant polysulfide concentration, as explained above. However the 2-phase boundaries on the phase diagram, between the 1-phase and the 2-phase regions, were prepared by only being in excess of either lithium sulfide or sulfur.

By altering the electrolyte salt concentration, the polysulfide solubility will be affected. A solvent will have a specific saturation point and therefore a solution with an already high lithium salt concentration will limit the solubility of other solutes (lithium sulfide and sulfur). This will be observed on the phase diagram by a change in the position of the eutonic point, were the higher the eutonic point position is on the phase diagram the lower the polysulfide concentration. Then by using the same electrolyte salt concentrations, the correlation between the polysulfide solubility and electrochemical performance can be quantitatively demonstrated.

High magnification optical images of the polysulfide solutions, show the absence of solid particles after filtration of the excess of solid sulfur and solid lithium sulfide. The accuracy of the composition of the saturated polysulfide solutions was confirmed by elemental analysis.

Some previous studies addressed the determination of polysulfide solubilities,[41, 64-69] but the reliability of the present method is superior. The present approach takes into account the composition of polysulfide solution instead of relying on the initial ratio of sulfur and lithium sulfide that is used to prepare the solutions, since some solid might remain unreacted.

The issue with the current procedure of synthesizing the polysulfide solutions is they assume the initial ratio of lithium sulfide and sulfur mixed together in the electrolyte will be the same as the composition polysulfide species in the electrolyte. [41, 64-69] However in this study we show that when you are producing a saturated polysulfide solution, the starting composition of the blend ($[S]_T^{Sol.}$ = 10 M Li_2S_8) is different to the composition of the filtered saturated solution ($[S]_T^{Sol.}$ = 5.6 M $Li_2S_{5.4}$). Their method of determining the total atomic sulfur concentration of the polysulfide solutions is to measure the absorbance of sulfur with UV-vis spectroscopy.[41] However this is limited to low sulfur concentrations because of the limited solubility in ionic liquid solvents.[41] These studies are also missing a method of determining the polysulfide chain length.

There is also a common assumption that because there is a precipitate formed by the solution that this means it is saturated. However in this study we have shown that this is a sign of supersaturation. We proved that our solutions were saturated by increasing the heating time and the amount of excess lithium sulfide and sulfur. The reported methods of producing a saturated polysulfide solution is for ionic liquid solvents which as mentioned previously have a poor polysulfide solubility meaning short heating times are required. [41, 64-69] However this study shows much longer heating times are required for common Li-S battery solvents. Overall, a reliable method of preparing the saturated polysulfide solution in organic solvents where the total atomic sulfur concentration and polysulfide chain length were determined has not been reported.

1.4 Specific Surface Area Determination of the Lithium Sulfide Battery Cathode Materials

Current lithium-sulfur batteries are still far away from the expected theoretical performance, due to a number of fundamental issues such as electrode passivation.[70] During the operation of lithium-sulfur batteries, sulfur gets reduced to lithium sulfide via formation of a number of polysulfide intermediate species. Sulfur or lithium sulfide on their own have a very low solubility in the electrolyte, and hence they are present as solids during most of the battery operation.[41] Batteries are prepared by mixing sulfur (or lithium sulfide) with carbon conductive additive. Due to the insulating nature of sulfur and lithium sulfide, electrochemical reactions do not take place at the surface of these materials.[54]

Instead the discharge reaction is initiated by the dissolution of sulfur in the electrolyte, followed by the diffusion of soluble sulfur to the surface of the carbon material, where it can undergo electron transfer reactions forming polysulfide species.[20] The redox reactions are sped up by the polysulfide species because they act as redox mediators.[20] Only part of the total sulfur reduction capacity comes from direct electrochemical steps, the rest of the capacity comes from chain growth and disproportionation reactions to produce reducible species.[20] Since polysulfide species can undergo multiple subsequent electrochemical and chemical reactions, they can effectively shuttle electrons from carbon to solid sulfur. During this process an electron transfer reaction at the carbon surface reduces the polysulfide species. The reduced polysulfide species diffuses to the sulfur surface, where it will react chemically forming other polysulfide species.[19] Similar reactions can be proposed for the mediation of the oxidation of lithium sulfide by polysulfide species. Indeed, several studies have pointed out the beneficial effect of polysulfide for facilitating the reactions, assisting in the full reduction of all the sulfur during discharge and full re-oxidation of all the lithium sulfide during charge, and helping to overcome the problem of lack of contact of sulfur and/or lithium sulfide particles with the current collector.[20]

Despite the beneficial effect of polysulfides, it is difficult to achieve the high theoretical capacity associated to the full conversion of all sulfur to lithium sulfide and vice versa. As the reactions proceed, part of the carbon particle surface gets blocked by deposition of those insulating materials (sulfur and lithium sulfide), which hamper further electron transfer reactions.[71-73] Different electrode preparation procedures have been explored to mitigate the problem of cathode passivation, such as the method of inserting the sulfur into the carbon material or the selection of carbon material with different specific surface areas.[74] It is important to avoid deposition of the insulating products on the opening of the pores and consequent pore clogging, since that leads to important loss of active area.[71-72] Pore clogging will also lead to slower mass transport, which can also result in the early end of discharge of the cell.[18, 72]

In conclusion, the loss of electrochemically active surface area of Li-S battery cathode is a key process determining the practical capacity achievable in the lithium-sulfur cell.[70] In this work, impedance spectroscopy was used to determine in situ the electrochemically active surface area of Li-S battery cathode. Firstly, the impedance of symmetrical cells with carbon and sulfur-carbon electrodes is presented. This shows the voltage perturbation associated to the impedance measurements is not high enough to induce the electrochemical reduction of sulfur to polysulfides. Therefore, the impedance results are dominated by the capacitor behavior (double-layer charging) of the supporting material at lower frequencies, while at higher frequencies the migration of ions through the porous structure produces the characteristic Warburg impedance behavior (i.e. a 45 line on the Nyquist plot). As shown in a previous study, the impedance in the whole frequency range can be modelled with an open-Warburg element where the effect of the composite electrode composition and structure on the rate of ion transport was analyzed.[46] The effective porosity and tortuosity of different separators and electrodes were determined using impedance with respect to a range of electrolyte concentrations. Therefore this study was able to identify the optimal cell setup with respect to the ion transport expected to improve Li-S battery performance. Considering the porosity of an electrode has a significant effect on the specific capacity.[57] This specific surface area study has the similar aim of developing a toolset to determine the SSA of the electrode. This toolset could be used to identify new materials for Li-S batteries, since the SSA has a significant effect on the active material utilization.[72]

In this work, the electrochemically active surface area was determined for a range of different electrode formulations. Finally, it will be shown that this approach can be used to monitor the electrochemically active surface area of the composite electrode in-situ in lithium-sulfur cells as a function of the state of charge. A number of studies used impedance spectroscopy to characterize the complex reaction mechanism of lithium-sulfur cells such as probing microstructure evolution, confinement of sulfur in microporous carbon to improve battery performance and monitoring the charge transfer resistance with respect to the cycle number to analyse the capacity fade.[75-79] However, to the best of my knowledge, this is the first study that uses impedance to evaluate the electrochemical surface area of sulfur-carbon electrodes. The advantage of using impedance to measure the specific surface area is that an in-situ realistic value is obtained. In contrast, BET analysis uses the physical adsorption of gas molecules to measure the specific surface area. The relatively small nitrogen gas molecules used can reach smaller pores than the electrolyte molecules used in the impedance measurement. The specific surface area is a key property in determining the extent of sulfur utilization i.e. the practical capacity of the battery.[72] Therefore, being able to identify new Li-S cathode materials with a high specific surface area with this impedance toolset will aid in achieving higher practical capacities.[80] Overall the research queries under assessment in the impedance study are the following;

- Specific surface area determination of carbon electrodes
- Optimization in symmetrical impedance cell configuration
- Specific surface area determination of sulfur electrodes with low (24 wt.% S) and high (70 wt.% S) sulfur contents
- Specific surface area determination of industrial scale cathodes (70 wt.% S)
- Quantitative analysis of the transport properties of different electrode formulations
- Development of the Li-S impedance cell to allow for reproducible impedance measurements
- Comparing specific surface determination from impedance and BET analysis
- Specific surface area determination of industrial scale cathodes during galvanostatic cycling

Chapter 2 Experimental Details

2.1 General Preparation of Experimental Equipment and Chemicals

All experimental equipment, before being used, was washed with deionised water then an appropriate organic solvent (e.g. ethanol, acetone or isopropanol). Then the equipment was dried in an oven at 80 ^{o}C. If the equipment was going to be used in the glovebox, then it was dried overnight.

Bis(trifluoromethane)sulfonimide lithium salt (LiTFSI, dried, 99.95%, Sigma Aldrich) was dried under vacuum at 120 ^{o}C for three days. Lithium sulfide (dried, 99.98 %, Sigma Aldrich) and sulfur (dried, powder, 100 mesh, sublimed, Sigma Aldrich) was dried under vacuum at 40 ^{o}C for three days to avoid sublimation.

1,3-dioxolane (DOL, anhydrous, Sigma Aldrich) was dried using molecular sieves (4 Å, beads, 8-12 mesh). The amount of molecular sieve used was equal to a third of the volume of solvent that required drying. The molecular sieve was dried under vacuum at 200 ^{o}C for three days. The molecular sieve was transferred into the glovebox and allowed to cool down to room temperature before adding to the solvent. The molecular sieve was left in the solvent for 3 days. The dried solvent was filtered with a PTFE syringe filter tip (0.2 μm).

2.2 Preparation of Electrolyte for Phase Diagram, GCPL and Impedance Experiments

In an argon-filled glove box, bis(trifluoromethane)sulfonimide lithium salt (LiTFSI, dried, 99.95%, Sigma Aldrich) was dissolved into dried 1,3-dioxolane (DOL, anhydrous, Sigma Aldrich). The concentration of the electrolyte was determined via molarity (where the volume of the solvent added is measured). The LiTFSI was added to a volumetric flask and DOL was added to the volumetric flask until the bottom of the meniscus reached the graduation mark. The volumetric flask was inverted multiple times to dissolve the LiTFSI then additional DOL was added to the volumetric flask to reach the graduation mark again.

The LiTFSI in DOL electrolyte prepared was used in the preparation of the lithium polysulfide solutions and used as an electrolyte for GCPL and impedance cells.

2.3 Preparation of Lithium Polysulfide Solutions

In an argon-filled glove box, lithium sulfide (dried, 99.98 %, Sigma Aldrich) and sulfur (dried, powder, 100 mesh, sublimed, Sigma Aldrich) were added to a vial in ratios to give the chosen polysulfide species (Equation 2.3.1). The concentration of the polysulfide solutions is referred to in terms of its total atomic sulfur concentration (i.e. $[S]_T^{Sol.}$ = 1 M is the same as $[S_5^{2-}]$ = 0.2 M since 0.2 M x 5 = 1 M).

$$(n-1)\,S + Li_2S \rightarrow Li_2S_n$$

Equation 2.3.1 – Reaction of chosen ratios of lithium sulfide and sulfur to produce a lithium polysulfide species with a specific chain length and concentration.

This was dissolved in the LiTFSI in DOL electrolyte. For the low concentration solutions ($[S]_T^{Sol.} \leq 2$ M), they were heated to 60°C and stirred for a week, left to cool to room temperature for 2 days and filtered using a syringe filter tip. The week heating time was a sufficient amount of time for the lithium sulfide and sulfur to completely dissolve into the electrolyte for the low concentration solutions. For the high concentration blends ($[S]_T^{Sol.} >$ 2 M), they were heated to 60°C and stirred for a month. The high concentration solutions require a longer heating time to reach saturation. It was considered that one month heating time was sufficient to reach full dissolution, since some experiments with two months of heating time produced consistent results. After this the blends were cooled to room temperature, decanted into a centrifuge tube and filtered using centrifugation (7500 rpm, 15 mins) three times followed by a PTFE syringe filter tip (0.2 µm). The solution was monitored for 2 days to check if it was supersaturated. If a precipitate formed in the vial the solution was filtered by a PTFE syringe filter tip (0.2 µm) again.

2.4 Density of Polysulfide Solutions

In an argon-filled glove box, the filtered polysulfide solution was added to a pre-weighed volumetric flask and filled to the graduation mark. The filled volumetric flask mass was recorded to determine the mass of polysulfide solution. Since the volume of the polysulfide solution is known, the density can be determined.

$$\rho_{PS} = \frac{m_{PS}}{V_{Volumetric}} \qquad \text{Equation 2.4.1}$$

The errors from the equipment to determine the density were from the resolution of the four decimal point balance, the manufacturers error on the volumetric flask and the fill error when filling the volumetric flask. The error in the mass measurements is half the resolution of the balance (0.0001 g / 2 = 0.00005 g). The total error in the volume measurement is the sum of the manufacturers error and fill error. The fill error is the product of the internal diameter of the volumetric flask (d) and estimating how far the actual filled level could have been from the fill mark (Δx).

$$Fill\ Error = \pi \left(\frac{d}{2}\right)^2 \Delta x \qquad \text{Equation 2.4.2}$$

The error in the density was determined using the following propagation of uncertainty formula;

$$\sigma_\rho = \overline{\rho} \times \sqrt{\left(\frac{\sigma_m}{\overline{m}}\right)^2 + \left(\frac{\sigma_V}{\overline{V}}\right)^2} \qquad \text{Equation 2.4.3}$$

where σ_ρ is the error in the density (g mL^{-1}), $\overline{\rho}$ is the determined value of the density (g mL^{-1}), σ_m is the error in the mass (g), $\overline{m}$ is the measured value of the mass (g), σ_V is the error in the volume (mL) and $\overline{V}$ is the volume of the volumetric flask (mL).

2.5 Barium Sulphate Gravimetric Analysis

In an argon-filled glove box, the filtered polysulfide solution (1 to 3 mL) was added to a round bottom flask (RBF) and the mass was recorded. The polysulfide solution was diluted with DOL (10 mL) and a stirrer bar was added to the RBF. Then it was sealed with a rubber septum to keep the polysulfide solution under inert conditions when taken out of the glove box. Ammonium hydroxide (35 %, 15 mL, Fisher Scientific) was then added to each RBF slowly via a needle and syringe. Then the rubber septum was removed because the polysulfide species is stable under basic conditions. Hydrogen peroxide (30 %, 10 mL, Sigma Aldrich) was added dropwise whilst stirring. The reaction mixtures were heated in an oil bath to 40 °C for 1 hour, then heated to 60 °C for 20 minutes to remove excess ammonia and hydrogen peroxide. The reaction mixtures were cooled to room temperature and excess barium nitrate (99.999 %, Sigma Aldrich) was added. The reaction mixture was stirred for 1 hour then filtered via a pre-weighed glass crucible (porosity grade 4) under vacuum. The barium sulphate retentate was washed with deionised water (3 x 10 mL) and dried in the vacuum oven (80 °C) for 24 hours. The glass crucibles containing the barium sulphate retentate was weighed to determine the barium sulphate mass.

2.6 X-ray Diffraction of Barium Sulphate Samples

The XRD was performed on a Bruker D2 phase in Bragg Brentano geometry. The settings used were as follows:

- Start $2\theta = 10^{o}$ End $2\theta = 80^{o}$
- Increment = 0.04^{o}
- Dwell time = 1 s
- Saved as a RAW V4 .txt file

2.7 Determining the Molar Extinction Coefficient of Ferrocenium Tetrafluoroborate in 1,3-Dioxolane

In an argon filled glove box, a 3 mM ferrocenium tetrafluoroborate (dried, 95 %, Sigma Aldrich) in dried 1,3-dioxolane (DOL, anhydrous, Sigma Aldrich) solution was prepared in a volumetric flask. This solution was stirred for 1 day to fully dissolve the ferrocenium tetrafluoroborate and then filtered with a PTFE syringe filter tip (0.2 µm) to remove any insoluble impurities in the solid ferrocenium tetrafluoroborate that would scatter light in the UV/vis spectrometer. A serial dilution was performed on the 3 mM ferrocenium tetrafluoroborate to produce solutions with concentrations of 2.5 mM, 2 mM, 1.5 mM, 1 mM, 0.5 mM. The absorbance of these solutions was recorded via an UV/vis spectrometer (Ocean Optics DH-2000-BAL UV-Vis NIR light source) in a sealed quartz cuvette.

2.8 UV-visible Absorption Spectroscopy Redox Titration

In an argon-filled glove box, a 3 mM ferrocenium tetrafluoroborate (dried, 95 %, Sigma Aldrich) in dried 1,3-dioxolane (DOL, anhydrous, Sigma Aldrich) solution was prepared in a volumetric flask. This solution was stirred for 1 hour then filtered with a PTFE syringe filter tip (0.2 µm) to remove any insoluble impurities in the solid ferrocenium tetrafluoroborate that would scatter light in the UV/vis spectrometer. The amount of polysulfide solution required for an extent of the titration reaction was weighed into a glass vial. Then the amount of 3 mM ferrocenium tetrafluoroborate required for an extent of the titration reaction was added to the same vial and weighed. The absorbance of these mixtures was recorded via an UV/vis spectrometer (Ocean Optics DH-2000-BAL UV-Vis NIR light source) in a sealed quartz cuvette.

The stoichiometric ratio of the redox reaction between ferrocenium tetrafluoroborate and the polysulfide blend is 2:1. The extent of the titration reaction can be controlled by the amount of the polysulfide solution added to the ferrocenium tetrafluoroborate solution.

$$2\ FcBF_4 + x\ Li_2S_n \rightarrow 2x\ Fc + 2x\ LiBF_4 + \frac{nx}{8}\ S_8 + (2-2x)\ FcBF_4$$

Equation 2.8.1 – Reaction scheme for the redox reaction which includes the extent of the titration (x).

This shows the progress of the reaction, where x describes the extent of the reaction.

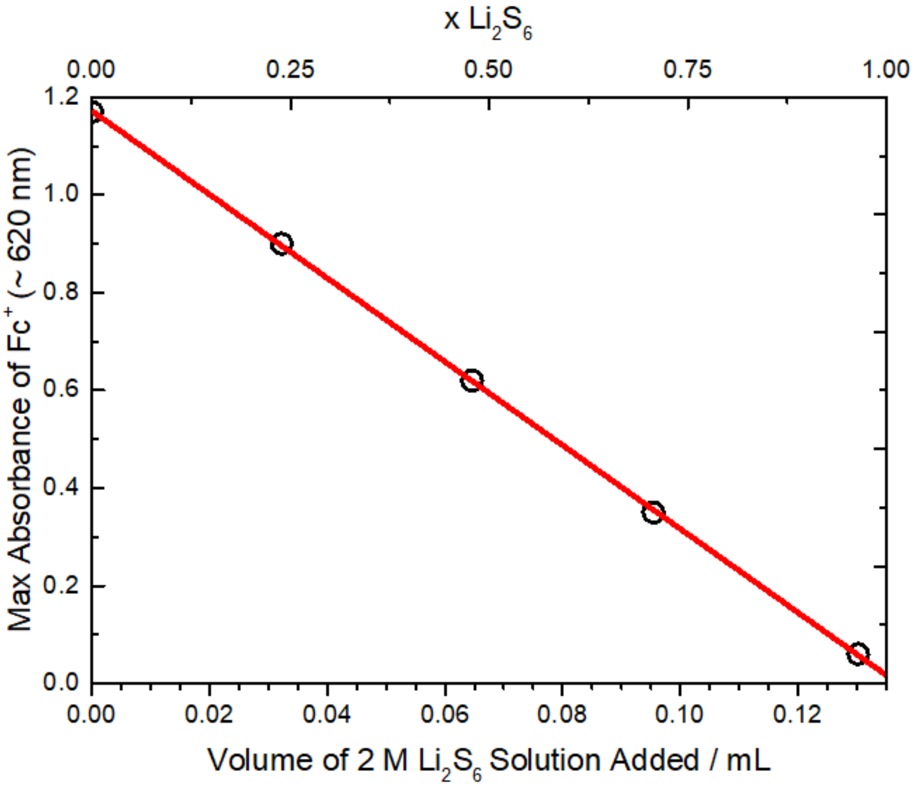

Figure 2.8.1 – Example of UV/visible absorption spectroscopy redox titration experiment max absorbance of ferrocenium tetrafluoroborate solution in DOL (3 mM) at 620 nm plotted against the volume of $[S]_T^{Sol.}$ = 2 M, Li$_2$S$_6$

solution added and plotted against the extent of the titration reaction (0 ≤ x ≤ 1) between ferrocenium tetrafluoroborate solution and the $[S]_T^{Sol.}$ = 2 M, Li_2S_6 solution.

When x = 0 no polysulfide blend has been added and when x = 1 the ferrocenium tetrafluoroborate has been fully reduced to ferrocene. With this x term, the amount of polysulfide solution required for a specific extent of titration reaction can be calculated;

$$V_{PS} = \frac{x \times c_{FcBF_4} \times V_{FcBF_4} \times n}{2 \times c_S} \qquad \text{Equation 2.8.2}$$

where V_{PS} is the volume of the polysulfide solution (L), c_{FcBF_4} is the concentration of the ferrocenium tetrafluoroborate solution, V_{FcBF_4} is the volume of the ferrocenium tetrafluoroborate solution, n is the polysulfide chain length and c_S is the total atomic sulfur concentration.

This method only works when the chain length and the total atomic sulfur concentration values are already known i.e. for the low concentration polysulfide solutions. For high concentration (i.e. 10 – 20 M) polysulfide blends, these values will not be known because the chain length and the total atomic sulfur concentration of the filtered solution will be different to that of the initially prepared blend. The high concentration of the polysulfide solutions was chosen to successfully prepare saturated solutions and is comparable to the concentration range of commercial cell during charge/discharge with a high sulfur loading and a low electrolyte and sulfur ratio. Therefore, for the high concentration saturated polysulfide solutions, small aliquots of the blend were added to the ferrocenium tetrafluroborate solution until the end point was reached.

2.9 Microscope

In an argon-filled glove box, a small droplet of polysulfide solution was transferred into a glass slide well. This was sealed under an inert atmosphere with vacuum grease (Dow Corning high vacuum grease) on another glass slide that was placed on top. The polysulfide droplet was studied using the Olympus BH2 microscope.

2.10 MEDAC Elemental Analysis

In an argon-filled glove box, the polysulfide solution (1 mL) was added to a glass ampoule and was temporarily sealed with a rubber hose with a tap at the end. The ampoule was taken out of the glove box and the polysulfide solution within was frozen using liquid nitrogen. The ampoule was evacuated by attaching a mini diaphragm vacuum pump (VWR, VP 86) whilst sealing the glass using a gas blow torch (iroda, PT-600E & RS, Butane and Propane Gas Torch Refill). This resulted in an inert atmosphere inside the ampoule which would be safe to post to MEDAC Ltd. without degradation of the sample. The analysis techniques performed at MEDAC Ltd. were CHN&S analysis, fluorine analysis and ICP-OES spectroscopic single element analysis of lithium.

2.11 Preparation of Swagelok Cells for GCPL

The metal Swagelok cell components were cleaned in a plastic beaker filled with acetone in a sonicator bath (Cole-Palmer 8891 Ultrasonic Cleaner) and dried in an oven at 80°C for several hours. The first half of the cell was pre-assembled outside of the glove box. The back and front ferrules were placed onto one of the stainless-steel rods and this was placed halfway into the body of the metal Swagelok cell, which had been lined with a sheet of Mylar film (Mylar Electrical & Chemical Insulating Film, RS, thickness 0.125 mm). The end cap of the Swagelok cell was then screwed on to secure the rod in place. The resistance was measured across the half-built cell to make sure the stainless-steel rod was not touching the body of the cell which would cause the cell to short circuit. If built correctly, the measured resistance across the half-built cell should be over limit (i.e. an infinite amount of resistance) as no current will flow through the cell body. This pre-assembled half of the Swagelok cell, along with all other components were then dried again in an oven at 80°C for several hours more. In the argon filled glove box, the rest of the metal Swagelok cell was assembled.

2.12 Electrolyte Concentration Effect on Battery Performance for GCPL

The assembled cells were transferred into a constant climate chamber (Memmert HPP 110, temperature accuracy = 0.1° C) in order to maintain a fixed temperature of 25°C.

All electrochemical measurements were recorded using a Biologic multichannel potentiostat (VMP2) using EC-Lab software.

The 1 inch Swagelok cell setup;

- Lab-scale produced sulfur-containing cathodes (24 wt.% sulfur, Ø = 15 mm)
- Glass-fibre separator (Whatman®, glass microfiber filter, grade GF/F, Ø = 25 mm)
- LiTFSI in DOL electrolyte (0.5, 1 or 2 M, 0.5 mL)
- Lithium metal anode (Ø = 25 mm)

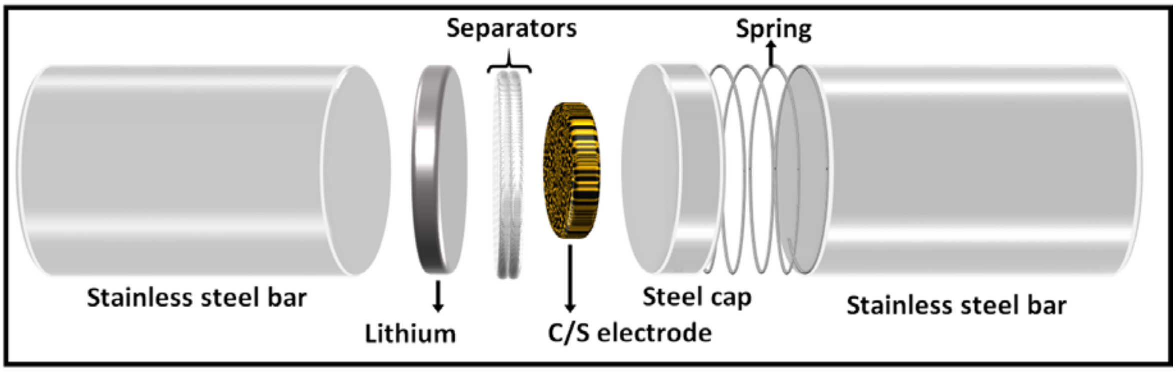

Figure 2.12.1 – Schematic of the 1-inch Swagelok cell setup for GCPL.

The open circuit voltage of the cell was measured for 30 minutes. The cycling potential limits were 1.5 – 2.6 V and the battery was cycled at a C/5 rate (i.e. I = 330 mA g_S^{-1}).

2.13 Preparation of Lab Scale Electrodes

The carbon/ PTFE (C) electrodes were prepared by dry mixing acetylene black (50 % compressed, Chevron Phillip) and Polytetrafluoroethylene (PTFE, fine powder, type 6C-N, Du Pont) in a ground glass mortar for 30 minutes. The weight ratio of conductive carbon (acetylene black) and binder (PTFE) was 66:34. The dry mixture was rolled to a sheet (approximately 125 µm) using a rolling mill (Durston DRM 130) and cut into pellets. The electrodes were dried at 120°C in a glass vacuum oven (Buchi®, pressure < 1 mbar) for at least 24 hours

The carbon/sulfur/PTFE (C/S) electrodes were prepared by dry mixing sulfur (sublimed, 100 mesh, Sigma Aldrich), acetylene black (50 % compressed, Chevron Phillip) and polytetrafluoroethylene (PTFE) in a ground glass mortar for 30 minutes. The weight ratio of active material (sulfur), conductive carbon (acetylene black) and binder (PTFE) was 24:66:10 for the low sulfur content electrodes (average sulfur mass loading ≈ 4 mg cm^{-2}). The ratio for the higher sulfur content electrodes was 70:20:10 (average sulfur mass loading ≈ 14 mg cm^{-2}). The dry mixture was rolled to a sheet (approximately 125 µm) using a rolling mill (Durston DRM 130) and cut into pellets using a handheld precision punch (Nogami). The sulfur containing electrodes were dried at 40°C (lower temperature to avoid sublimation of sulfur) in a glass vacuum oven (Buchi®, pressure < 1 mbar) for at least 24 hours.

2.14 Industrial Scale Electrodes

The industrial-scale electrodes (sulfur content ≈ 70 wt. %; average sulfur mass loading of single-side coated electrode ≈ 1.6 mg cm^{-2}) were supplied by OXIS Energy Ltd. in forms of large sheets. The sulfur content of the industrial scale electrodes was the same as the high sulfur content of the lab scale electrodes. The sulfur loading of the industrial scale electrodes is lower compared to that of the lab scale electrodes because the industrial scale electrode thickness is 47 µm compared to the lab scale electrode thickness of 125 µm. This was cut into pellets and dried at 40°C in a glass vacuum oven (Buchi®, pressure < 1 mbar) for at least 24 hours.

2.15 Preparation of Swagelok Cells for Impedance

Five different Swagelok cell setups were used for the impedance experiments (Figure 2.15.1).

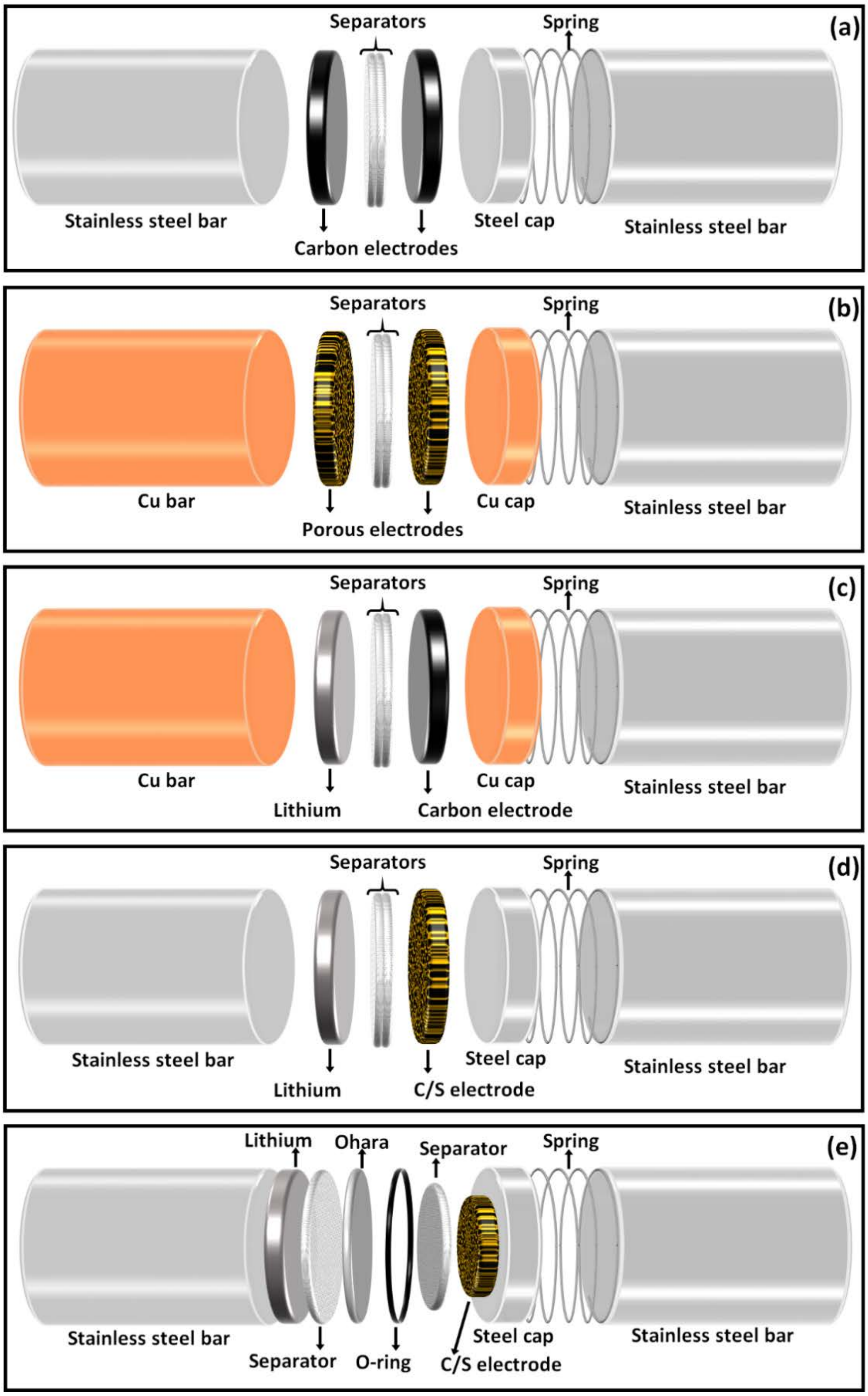

Figure 2.15.1 – Schematics of five different Swagelok cell setups.

The stainless-steel Swagelok cell components were cleaned in a plastic beaker filled with acetone in a sonicator bath (Cole-Palmer 8891 Ultrasonic Cleaner) and dried in an oven at 80°C for several hours. For the cell with copper current collectors, the surface was polished with 1200 grit sandpaper wetted with ethanol followed by polishing with several grades of alumina (25 µm, 3 µm, 0.3 µm and 0.05 µm) wetted with ethanol. The copper current collector components were cleaned in a plastic beaker filled with acetone in a sonicator bath (Cole-Palmer 8891 Ultrasonic Cleaner) and dried under vacuum in the glove box antechamber for only one hour to avoid the formation of oxide layer on the copper surface.

The first half of the cell was pre-assembled outside of the glove box using the same procedure mentioned previously (Section 2.11). However, if the half-built cell contained copper components, then it was dried under vacuum in the glove box antechamber for only one hour to avoid the formation of oxide layer on the copper surface.

For the Swagelok cell setup that uses Ohara glass (e), the O-ring is inserted into the groove in the stainless-steel end cap and vacuum grease (Dow Corning high vacuum grease) is applied so that a seal can be formed during assembly. The Ohara glass was cleaned in plastic beaker filled with IPA in a sonicator bath (Cole-Palmer 8891 Ultrasonic Cleaner) and dried in an oven at 80°C for several hours.

In the argon filled glove box, the rest of the metal Swagelok cells was assembled.

Swagelok cell setup (a) – ½ inch Swagelok cell, with stainless steel current collectors, C electrode (Ø = 11 mm), 2 x glass-fibre separator (Whatman®, glass microfiber filter, grade GF/F, Ø = 12 mm), 1 M LiTFSI in DOL electrolyte (125 µL) and C electrode (Ø = 11 mm).

Swagelok cell setup (b) – ½ inch Swagelok cell, with copper current collectors, OXIS cathode, C/S or C electrode (Ø = 11 mm), 2 x glass-fibre separator (Whatman®, glass microfiber filter, grade GF/F, Ø = 12 mm), 1 M LiTFSI in DOL electrolyte (125 µL) and OXIS cathode, C/S or C electrode (Ø = 11 mm).

Swagelok cell setup (c) – ½ inch Swagelok cell, with copper current collectors, carbon electrode (Ø = 11 mm), 2 x glass-fibre separator (Whatman®, glass microfiber filter, grade GF/F, Ø = 12 mm), 1 M LiTFSI in DOL electrolyte (125 µL) and a lithium metal negative electrode (Ø = 12 mm).

Swagelok cell setup (d) – ½ inch Swagelok cell, with stainless steel current collectors, C/S electrode (Ø = 11 mm), 2 x glass-fibre separator (Whatman®, glass microfiber filter, grade GF/F, Ø = 12 mm), 1 M LiTFSI in DOL electrolyte (125 µL) and a lithium metal negative electrode (Ø = 12 mm). Stainless steel current collectors are required for conventional Li-S cell setup because polysulfide species can react with copper.

Swagelok cell setup (e) – 1 inch Swagelok cell, all stainless steel components, C/S electrode (Ø = 15 mm), 2 x glass-fibre separator (Whatman®, glass microfiber filter, grade GF/F, Ø = 18 mm), 1 M LiTFSI in DOL electrolyte (250 µL), lithium ion conducting glass ceramic (LICGC^{TM}, Ohara Corporation, Ø = 25 mm), 1 x glass-fibre separator (Whatman®, glass microfiber filter, grade GF/F, Ø = 25 mm), 1 M LiTFSI in DOL electrolyte (250 µL) and a lithium metal negative electrode (Ø = 25 mm).

2.16 Potentio Electrochemical Impedance Spectroscopy

The assembled cells were transferred into a constant climate chamber (Memmert HPP 110, temperature accuracy = 0.1° C) in order to maintain a fixed temperature of 25°C. The cell was connected to a VMP2 multi-channel potentiostat (Biologic®) and potentiostatic electrochemical impedance spectroscopy (PEIS) technique was performed. The impedance spectrum was acquired applying a perturbation signal of ± 10 mV using a frequency range of 200 kHz to 10 mHz for cell setups (a) to (d). For the Ohara glass cell setup (e), a perturbation signal of ± 20 mV and a frequency range of 1 MHz to 1 mHz was used. Between each PEIS measurement, an open circuit voltage (OCV) rest of 30 minutes was applied to ensure the system was at equilibrium. Zview® software was used to analyse the impedance data.

2.17 Brunauer–Emmett–Teller (BET) Technique

The electrode mixture was added (< 0.5 g) to a clean, dry, pre-weighed 3/8-inch sample tube and weighed. For the C electrodes, the electrode mixture was heated to 120 ^{o}C and dried under vacuum (micromeritics, VacPrep 061 Sample Degas System). For the C/S electrodes, the electrode mixture was only dried under vacuum (micromeritics, VacPrep 061 Sample Degas System). The mass of the sample vial and electrode mixture was measured at 30-minute intervals during the drying process until the mass remained constant. The sample vial containing the electrode material was connected to the micromeritics TriStar II Surface Area and Porosity to determine the specific surface area of the electrode material.

2.18 GCPL/Impedance of Industrial Scale Electrodes

The Ohara glass cell setup (Figure 2.14.1.e) was used for the GCPL then impedance coupled technique. Swagelok cell setup – 1 inch Swagelok cell, all stainless steel components, OXIS cathode (Ø = 11 mm), 2 x glass-fibre separator (Whatman®, glass microfiber filter, grade GF/F, Ø = 18 mm), 1 M LiTFSI in DOL electrolyte (250 µL), lithium ion conducting glass ceramic (LICGC^{TM}, Ohara Corporation, Ø = 25 mm), 1 x glass-fibre separator (Whatman®, glass microfiber filter, grade GF/F, Ø = 25 mm), 1 M LiTFSI in DOL electrolyte (250 µL) and a lithium metal negative electrode (Ø = 25 mm).

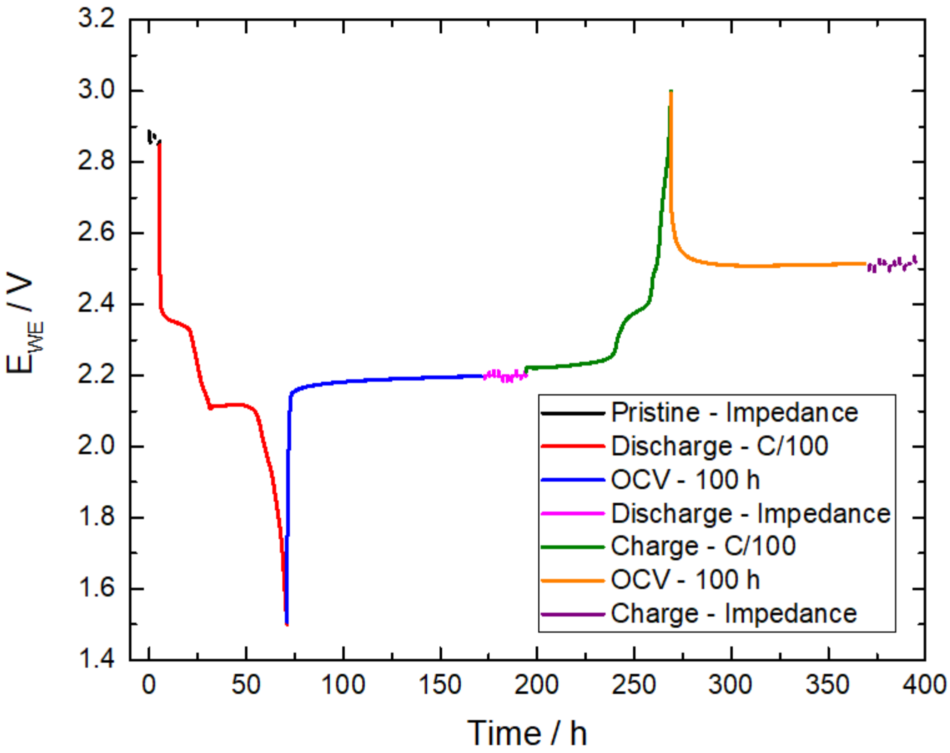

Figure 2.18.1 – Potential profile of the GCPL/impedance technique for the lithium vs. OXIS cathode cell with 1 M LiTFSI in DOL, Ohara glass and stainless steel current collectors in a 1 inch Swagelok cell. The lithium vs. OXIS cathode cell was cycled at C/100 rate between 1.5 V to 3 V. The impedance was measured for the pristine, discharged and charged OXIS cathode (gaps are when the impedance was measured).

The experimental settings for the GCPL then impedance coupled technique are listed below;

1. Pristine Impedance – measured twice with 30-minute OCV rests – perturbation signal of 20 mV and a frequency range of 1 MHz to 1 mHz.

2. Discharge – to 1.5 V at C/100.
3. OCV – 100-hour rest.
4. Discharged Impedance – measured ten times with 30-minute OCV rests – perturbation signal of 20 mV and a frequency range of 1 MHz to 1 mHz.
5. Charge – to 3 V at C/100.
6. OCV – 100-hour rest.
7. Charged Impedance – measured ten times with 30-minute OCV rests – perturbation signal of 20 mV and a frequency range of 1 MHz to 1 mHz.

2.19 Grazing Incidence X-ray Diffraction

The Li-S cells used for the GCPL/impedance analysis were disassembled inside the glovebox. The cathode was then placed in an airtight specimen holder (Bruker, A100B33) onto a carbon stub to keep the film flat and then sealed under an argon atmosphere. The GIXRD was performed on the Rigaku SmartLab. The settings used were as follows:

- Start $2\theta = 5^{o}$ End $2\theta = 85^{o}$
- Increment = 0.02^{o}
- Dwell time = 2 s
- Saved as a RAW V4 .txt file

Chapter 3 Ternary Phase Diagram

3.1 Improvements to the Method of Analysing the Polysulfide Solutions

The polysulfide solutions prepared in this study are akin to the electrolyte in a Li-S battery system. When the cell is charged/discharged polysulfide species form in the electrolyte. Therefore, developing a technique to identify the concentration and speciation (i.e. chain length) of the polysulfide species present in the electrolyte is imperative to improve our understanding of the Li-S battery system.

As mentioned previously, this work was based upon a previous PhD thesis project from James Dibden, where he developed an analytical method to determine the solubility of polysulfide solutions as well as their speciation.[63] James's method needed improving because the variation in the concentration and chain length of the saturated polysulfide solutions lead to an imprecise eutonic point on the phase diagram with low reliability as only four saturated polysulfide solutions were prepared. In this study I have also reported slightly higher concentration polysulfide solutions (James's eutonic point $[S]_T^{Sol.}$ = 5.4 ± 1.5 M, my eutonic point $[S]_T^{Sol.}$= 5.55 ± 0.50 M) suggesting the month compared to three days heating time has optimized the preparation of the saturated solutions, achieving a true eutonic point solution.

In this chapter I will demonstrate the improvements I have made to the method of analyzing the polysulfide solutions.

First, I determined the density of the polysulfide solutions since the accuracy of the autopipette to dispense a set volume of polysulfide solutions was poor. The high viscosity of the polysulfide solutions caused it to stick inside the pipette tip and therefore dispense a volume less than the volume set on the autopipette. By determining the density of the polysulfide solution, the mass of polysulfide solution used for the gravimetric analysis and UV/vis redox titration can be more reliably measured. The alternative is to trust the volume dispensed by the autopipette is the same as the volume set, which is unlikely when dealing with viscous solutions with densities higher than water. Knowing the exact amounts of polysulfide solution used for the analysis is key for determining precise values for the total atomic sulfur concentration, the polysulfide speciation and smaller representative experimental errors from the analysis.

Secondly, for the gravimetric analysis I altered the method to include the dilution of the polysulfide solution with 1,3-dioxolane inside the round bottom flask before it was sealed with a rubber septum. This dilution helped, especially with the high concentration polysulfide solutions, to avoid side reactions when the basic piranha solution (ammonium hydroxide 35 %:hydrogen peroxide 30 %, 3:2) was added. The cause of the side reaction is not known, however I would hypothesise that it was related to the water that is inside basic piranha solution components since polysulfide species will react with water. However under basic conditions (i.e. basic piranha solution), the polysulfide species should be stable in the presence of water. These side reactions cause the loss of sulfur and will lower the effective total atomic sulfur concentration compared to the actual value.

Thirdly, I scaled up the UV/vis redox titration experiments to minimise the associated error from the volume of the PS solutions added. Especially for the high concentration polysulfide solutions, very small volumes of the polysulfide solutions are required leading to large respective errors. For example using a volume of 1 µL of the saturated polysulfide solution will result in a percentage volume error of approximately 7 % compared to using a volume 100 µL with a percentage volume error of approximately 4 %. Therefore, by scaling up the volume of ferrocenium tetrafluoroborate stock solution, larger polysulfide solution sample volumes can be used. This means larger volumes of the polysulfide solution can be used reducing its associated error. It is also important to minimise the volume errors because these variables are used to determine the polysulfide concentration and chain length.

Finally, there has been a high number of repeat experiments that has been performed to determine the eutonic points and the 2-phase boundaries to explicitly show the reliability of these measurements.

Overall the main focus for this work was to improve the reliability of these analytical techniques by removing systematic errors, reducing the experimental error contributions and multiple repeat experiments so that points on the ternary phase diagram could be accurately determined.

3.2 Preparation of Low Concentration Polysulfide Solutions

This work was inspired by the improved battery performance of a Li-S battery reported by Armand being related to the effect of electrolyte concentration.[39] They studied a new class of "solvent-in-salt" electrolyte with very high salt concentration which improves the coulombic efficiency and reduces the capacity fade of the Li-S battery. The cause of the improved battery performance was due to the high electrolyte salt concentration limiting the solubility of the lithium polysulfide species. Therefore with a lower intermediate concentration of polysulfide species during charge and discharge, the polysulfide shuttle has a smaller detrimental effect on the Li-S battery.

The aim for this research was to show the inverse relationship between electrolyte salt concentration and lithium polysulfide concentration (i.e. a solvent with a higher electrolyte salt concentration will have a lower polysulfide solubility). Furthermore, we wanted to correlate this low polysulfide solubility, that restricts the polysulfide shuttle, to improved Li-S battery performance. Therefore we have developed a ternary phase diagram to study the polysulfide saturation point of a common Li-S battery electrolyte.

To test the accuracy and reliability of the analytical experiments used to determine the concentration and speciation of the polysulfide species in solution for the phase diagram, low concentration polysulfide solutions were prepared. Low concentration polysulfide solutions were chosen because they were known from preliminary experiments to dissolve all of the lithium sulfide and sulfur solid. Therefore, the analytical experiments were calibrated against the polysulfide solutions $[S]_T^{Sol.}$ = 0.2 M, Li_2S_5 and $[S]_T^{Sol.}$ = 2 M, Li_2S_6. The concentration of the polysulfide solutions is referred to in terms of its total atomic sulfur concentration i.e. $[S]_T^{Sol.}$ = 1 M is the same as $[S_5^{2-}]$ = 0.2 M since 0.2 M x 5 = 1 M.

The lithium polysulfide solutions were prepared in an argon filled glove box by using varying ratios of lithium sulfide and sulfur as described in Equation 3.2.1.

$$(n-1)\,S + Li_2S \xrightarrow{1\,M\,LiTFSI\,in\,DOL} Li_2S_n$$

Equation 3.2.1 – Preparation of the lithium polysulfide solution where n is the chain length.[64]

The 1 M LiTFSI in DOL electrolyte was prepared using a volumetric flask. The volumetric flask was inverted multiple times to dissolve LiTFSI before the flask was filled to the graduated mark. Equations below (Equation 3.2.2 & Equation 3.2.3) were used to determine the masses of lithium sulfide and sulfur required to synthesise the specified polysulfide solution.

$$Li_2S\ Mass = \frac{[S]_T^{Sol.} \times V_{Li_2S_n\,sol.} \times RMM_{Li_2S}}{Chain\ Length} \qquad \text{Equation 3.2.2}$$

$$S\ Mass = [S]_T^{Sol.} \times V_{Li_2S_n\,sol.} \times RMM_S \times \left(\frac{Chain\ Length - 1}{Chain\ Length}\right) \qquad \text{Equation 3.2.3}$$

Where $[S]_T^{Sol.}$ is the total atomic sulfur concentration (M), $V_{Li_2S_n\,sol.}$ is the polysulfide solution volume (L), RMM_X is the relative molecular mass of species x (g mol^{-1}) and chain length is the number of sulfur atoms in the polysulfide species.

The polysulfide solutions were also prepared in volumetric flasks. Since it takes a significantly long time to dissolve lithium sulfide and sulfur into the electrolyte, an assumption was made that the small amounts of lithium sulfide and sulfur added to the volumetric flask have no effect on the final volume of the solution. This means the change in the height of the meniscus in the volumetric flask during the dissolution of sulfur and lithium sulfide was negligible as it was within the difference in the height of the meniscus from the graduated mark (Δx) when considering fill error volume error.

The polysulfide solutions prepared were $[S]_T^{Sol.}$ = 0.2 M, Li_2S_5 (Table 3.2.1) and $[S]_T^{Sol.}$ = 2 M, Li_2S_6 (Table 3.2.2). The polysulfide solutions were heated at 60 °C and stirred for at least 1 week to dissolve the lithium sulfide and sulfur in the electrolyte. Then the solution was left to cool to room temperature for at least 3 days.

The masses of lithium sulfide and sulfur used to make the polysulfide solutions are all within 2 % of the calculated ideal masses required to make the specified polysulfide solutions (Table 3.2.1 & Table 3.2.2). This means the prepared polysulfide solutions should effectively be $[S]_T^{Sol.}$ = 0.2 M, Li_2S_5 and $[S]_T^{Sol.}$ = 2 M, Li_2S_6, where deviations in the experimentally determined sulfur concentration and polysulfide chain length relate to experimental errors. Therefore, if the deviations are small then this methodology is accurate and reliable meaning it can be applied to analyse the high concentration polysulfide solutions. These high concentration polysulfide solutions are prepared from blends meaning the sulfur concentration and polysulfide chain length are not known.

$[S]_T^{Sol.}$ = 0.2 M, Li_2S_5 Solution No.	Theoretical Li_2S Mass / g	Experimental Li_2S Mass / g	Theoretical Sulfur Mass / g	Experimental Sulfur Mass / g	Theoretical Electrolyte* Mass / g	Experimental Electrolyte* Mass / g
1	0.0092	0.0092	0.0257	0.0259	6.0853	5.9578
2	0.0092	0.0094	0.0257	0.0262	5.9778	6.0258
3	0.0184	0.0188	0.0513	0.0511	11.9237	11.8998

Table 3.2.1 – Preparation of the $[S]_T^{Sol.}$ = 0.2 M, Li_2S_5 polysulfide solution. (* – 1 M LiTFSI in DOL)

$[S]_T^{Sol.}$ = 2 M, Li_2S_6 Solution No.	Theoretical Li_2S Mass / g	Experimental Li_2S Mass / g	Theoretical Sulfur Mass / g	Experimental Sulfur Mass / g	Theoretical Electrolyte* Mass / g	Experimental Electrolyte* Mass / g
1	0.0766	0.0773	0.2672	0.2701	6.0853	5.6845
2	0.0766	0.0767	0.2672	0.2671	5.9778	5.7841
3	0.0766	0.0769	0.2672	0.2672	5.9778	5.7262
4	0.1532	0.1530	0.5344	0.5354	11.9237	11.5342

Table 3.2.2 – Preparation of the $[S]_T^{Sol.}$ = 2 M, Li_2S_6 polysulfide solution. (* – 1 M LiTFSI in DOL)

3.3 Gravimetric Determination of the Total Atomic Sulfur Content

The atomic total sulfur concentration is one of the two parameters required for the ternary phase diagram and it was determined using gravimetric analysis. In an argon filled glove box the polysulfide solutions were placed into a round bottom flask and sealed. The flask was taken out of the glove box and ammonium hydroxide and hydrogen peroxide was added to oxidise the polysulfide to a sulphate species. Excess barium nitrate was added to the solution forming a barium sulfate precipitate via ion exchange (Equation 3.3.1).[63] Barium nitrate was chosen because it has a high solubility water (10.5 g per 100 mL at 25 °C) whereas barium sulfate has a poor solubility in water (0.000245 g per 100 mL at 20 °C). Therefore the barium sulfate can be separated from the excess barium nitrate via vacuum filtration and washing with water.

$$S_n^{2-} \xrightarrow{[O]} n\, SO_4^{2-} \xrightarrow{n\, Ba(NO_3)_2} n\, BaSO_4 + 2n\, NO_3^-$$

Equation 3.3.1 – Reaction scheme for the BaSO$_4$ gravimetric analysis experiment.

The stoichiometric ratio between the initial polysulfide species and the barium sulfate product is 1:1;

$$n_{BaSO_4} = n_S \qquad \text{Equation 3.3.2}$$

where n_{BaSO_4} is the number of moles of barium sulfate (mol) and n_S is the number of moles of sulfur (mol). Equation 3.3.2 can be rewritten as;

$$\frac{m_{BaSO_4}}{M_{BaSO_4}} = [S]_T^{Sol.} \times V_{PS} \qquad \text{Equation 3.3.3}$$

where m_{BaSO_4} is the mass of barium sulphate from the gravimetric analysis experiment (g), M_{BaSO_4} is the relative molar mass of barium sulphate (g mol^{-1}), $[S]_T^{Sol.}$ is the total atomic sulfur concentration (M) and V_{PS} is the volume of the polysulfide solution. Therefore, equation 3.3.3 can be rearranged in terms of the total atomic sulfur concentration.

$$[S]_T^{Sol.} = \frac{m_{BaSO_4}}{M_{BaSO_4} \times V_{PS}} \qquad \text{Equation 3.3.4}$$

The insoluble barium sulfate was filtered in a pre-weighed glass crucible and washed with deionised water. The barium sulfate was dried and weighed to determine the total sulfur concentration of the polysulfide solution (Table 3.3.1 & Table 3.3.2).

$[S]_T^{Sol.}$ = 0.2 M, Li_2S_5 Solution No.	$[S]_T^{Sol.}$ / M
1	0.214 ± 0.015
2	0.222 ± 0.017
3	0.205 ± 0.016
Average	0.214 ± 0.021

Table 3.3.1 – Acquired and averaged total atomic sulfur concentration for $[S]_T^{Sol.}$ = 0.2 M, Li_2S_5 polysulfide solution. Error for average corresponds to a confidence interval at a 95 % confidence level from the three repeat experiments.

$[S]_T^{Sol.}$ = 2 M, Li_2S_6 Solution No.	$[S]_T^{Sol.}$ / M
1	2.311 ± 0.064
2	2.085 ± 0.067
3	2.112 ± 0.065
4	2.192 ± 0.066
Average	2.175 ± 0.162

Table 3.3.2 – Acquired and averaged total atomic sulfur concentration for $[S]_T^{Sol.}$ = 2 M, Li_2S_6 polysulfide solutions. Error for average corresponds to a confidence interval at a 95 % confidence level from three repeat experiments.

The total atomic sulfur concentration was slightly higher than expected for both polysulfide solutions. Initially there was concern that there might be by-products present from the oxidation reaction or excess barium nitrate present that was not removed during the washing stage of the procedure. Therefore, a powder diffraction pattern of each sample was taken (Figure 3.3.1).

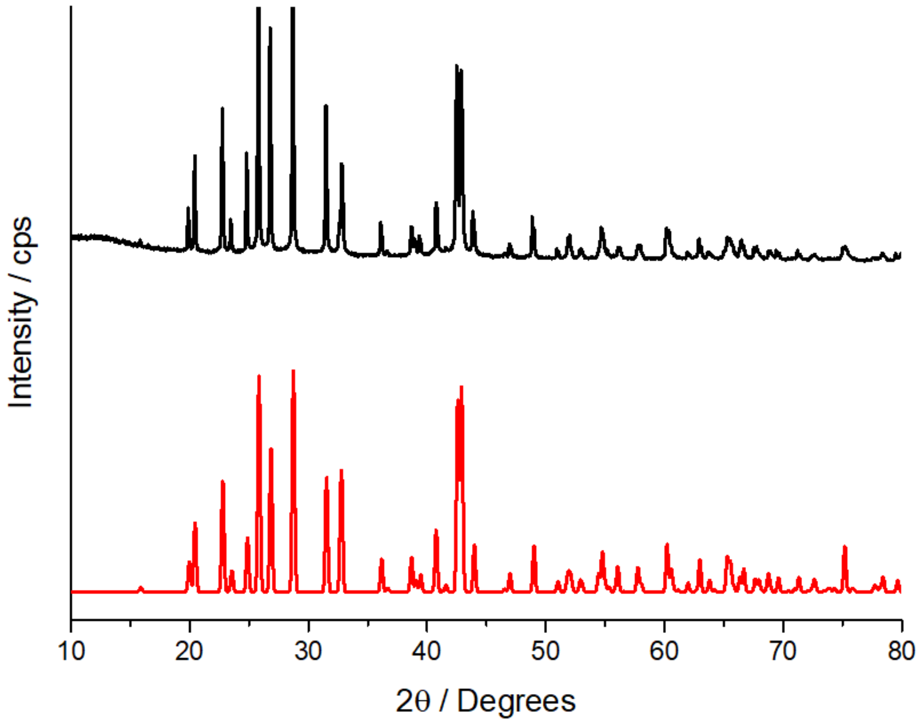

Figure 3.3.1 – XRPD diffraction pattern of barium sulfate from $[S]_T^{Sol.}$ = 0.2 M, Li_2S_5 polysulfide solution (black) and barite standard (red)[81]

All of the powder diffraction patterns only had one phase match that was barite,[81] with a very close match between the theoretical line and the observed data as shown by the relatively flat residual plot (Figure 3.3.2).

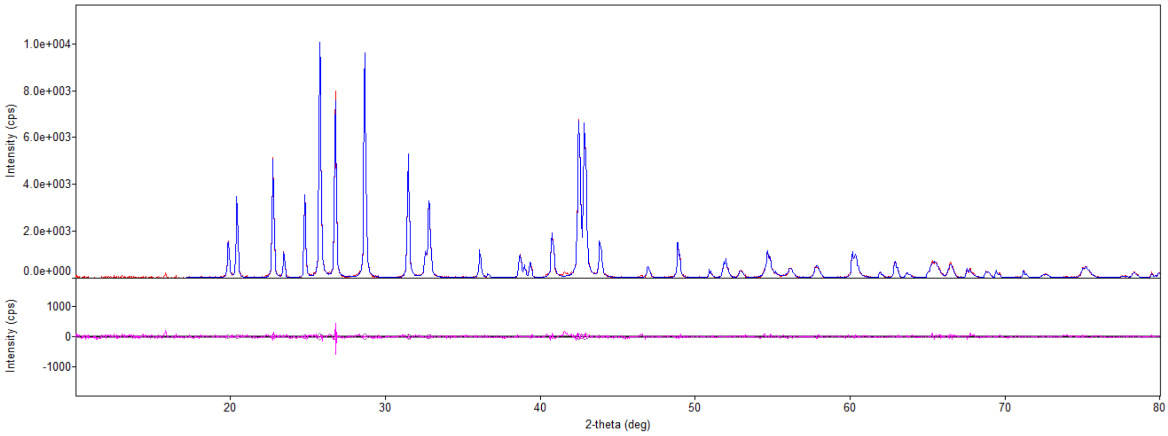

Figure 3.3.2 – XRPD diffraction pattern of barium sulfate from $[S]_T^{Sol.}$ = 0.2 M, Li_2S_5 polysulfide solution (blue) and residual plot (purple).

wRp / %	Rp / %	χ^2	Space Group	a / Å	b / Å	c / Å	α, β + γ / °
6.51	4.86	3.1041	P n m a	8.919(2)	5.458(6)	7.173(6)	90

Table 3.3.3 – XRPD summary of fit and unit cell parameters.

Since there is only one phase present for all the barium sulfate samples, this elucidates that there are no crystalline impurities present in the sample.

The LiTFSI does not affect the barium sulfate mass either because the concentration of LiTFSI in the polysulfide blend is relatively large enough, so that if the LiTFSI was involved in the oxidation reaction, the barium sulfate mass would be drastically affected. This was also checked experimentally by performing the gravimetric analysis experiment on a 1 M LiTFSI in DOL solution containing no polysulfide species. In this control experiment, no barium sulphate was produced.

The average total atomic sulfur concentration of the $[S]_T^{Sol.}$ = 0.2 M, Li_2S_5 polysulfide solution was determined to be 0.214 ± 0.021 M and the average total atomic sulfur concentration of the $[S]_T^{Sol.}$ = 2 M, Li_2S_6 polysulfide solution was determined to be 2.175 ± 0.162 M. Both values of average concentration show the accuracy of this procedure since they are within 10 % of the initially dictated values during the preparation of the solutions. The uncertainties of the average total atomic sulfur concentrations are both within 10 % showing precision of the gravimetric analysis.

Overall, these results show this procedure is well developed, reliable and can be used to determine the total atomic sulfur concentration of the high concentration polysulfide solutions.

3.4 UV-visible Absorbance Spectroscopy Redox Titration

The polysulfide species concentration parameter is also required for the ternary phase diagram and it was determined via UV-visible absorbance spectroscopy redox titration. Using ferrocenium tetrafluoroborate, the polysulfide species can be oxidised to sulfur and ferrocene (Equation 3.4.1).

$$2\ \mathrm{FcBF_4} + \ \mathrm{Li_2S_n} \rightarrow 2\ \mathrm{Fc} + 2\ \mathrm{LiBF_4} + \mathrm{n\ S}$$

Equation 3.4.1 – Complete oxidation of the lithium polysulfide solution using ferrocenium tetrafluoroborate.

The ferrocenium tetrafluoroborate concentration can be probed using UV-visible absorbance spectroscopy since it has an absorbance peak at 620 nm that has no overlap with the absorption spectra from other species in solution (Figure 3.4.1). Therefore the progress of the titration experiment can be tracked. Small-calculated aliquots of the polysulfide solution were added to the ferrocenium solution (Equation 3.4.2).

$$2\ FcBF_4 + x\ Li_2S_n \rightarrow 2x\ Fc + 2x\ LiBF_4 + nx\ S + (2 - 2x)\ FcBF_4$$

Equation 3.4.2 – Variable oxidation of the lithium polysulfide solution using ferrocenium tetrafluoroborate where x is the extent of the titration reaction (0 ≤ x ≤ 1).

The value of x describes the extent of the titration reaction where if x = 0 then no redox reaction has taken place and if x = 1 then the ferrocenium has been completely reduced to form ferrocene. The stoichiometry of the redox reaction (Equation 3.4.2) shows that for the titration experiment to go to completion there should be 0.5 moles of the polysulfide blend to each mole of ferrocenium tetrafluoroborate;

$$\therefore \quad x = 1 \quad \rightarrow \quad 2\ n_{Li_2S_n} = 1\ n_{FcBF_4} \qquad \text{Equation 3.4.3}$$

where $n_{Li_2S_n}$ is the number of moles of the polysulfide species (mol) and n_{FcBF_4} is the number of moles of ferrocenium tetrafluoroborate. Equation 3.4.3 can be displayed in terms of x.

$$x = \frac{2\ n_{Li_2S_n}}{n_{FcBF_4}} \qquad \text{Equation 3.4.4}$$

The x term describes the ratio of the number of moles of each species and can describe the extent of the titration reaction. Equation 3.4.4 can be rewritten in terms of concentration and volume;

$$x = \frac{2 \times [S_n^{2-}] \times V_{Li_2S_n}}{c_{FcBF_4} \times V_{FcBF_4}} \qquad \text{Equation 3.4.5}$$

where $[S_n^{2-}]$ is the concentration of the polysulfide species (M), $V_{Li_2S_n}$ is the volume of the polysulfide solution (L), c_{FcBF_4} is the concentration of ferrocenium tetrafluoroborate solution (M) and V_{FcBF_4} is the volume of the ferrocenium tetrafluoroborate solution (L). The concentration of the polysulfide species present in the solution can be determined by dividing the total atomic sulfur content, determined via gravimetric analysis, by the polysulfide chain length;

$$[S_n^{2-}] = \frac{[S]_T^{Sol.}}{n} \qquad \text{Equation 3.4.6}$$

where n is the chain length of the polysulfide species. Equation 3.4.6 substituted into equation 3.4.5.

$$x = \frac{2 \times [S]_T^{Sol.} \times V_{Li_2S_n}}{c_{FcBF_4} \times V_{FcBF_4} \times n} \qquad \text{Equation 3.4.7}$$

Equation 3.4.7 can be rearranged in terms of the volume of polysulfide blend added.

$$V_{Li_2S_n} = \frac{x \times c_{FcBF_4} \times V_{FcBF_4} \times n}{2 \times [S]_T^{Sol.}} \qquad \text{Equation 3.4.8}$$

Using equation 3.4.8 the amount of polysulfide blend required for a specific extent of titration reaction can be calculated. This procedure only works when the chain length and the total atomic sulfur concentration values are already known i.e. for the low concentration polysulfide solutions. For high concentration polysulfide solutions, these values will not be known because the composition of the blend saturated with excess Li_2S and S present will be different to the filtered solution. Therefore, when the experiment is performed on the high concentration saturated polysulfide blends small aliquots of the blend will have to be added until the end point is reached (i.e. when all of the ferrocenium has been reduced to ferrocene).

The polysulfide and ferrocenium tetrafluoroborate solutions were filtered before the titration experiment to remove any solid precipitate that would affect the UV-vis absorbance spectrometer. The UV-vis absorbance spectroscopy of the ferrocenium tetrafluoroborate/polysulfide solution mixture was measured (Figure 3.4.1 to Figure 3.4.3).

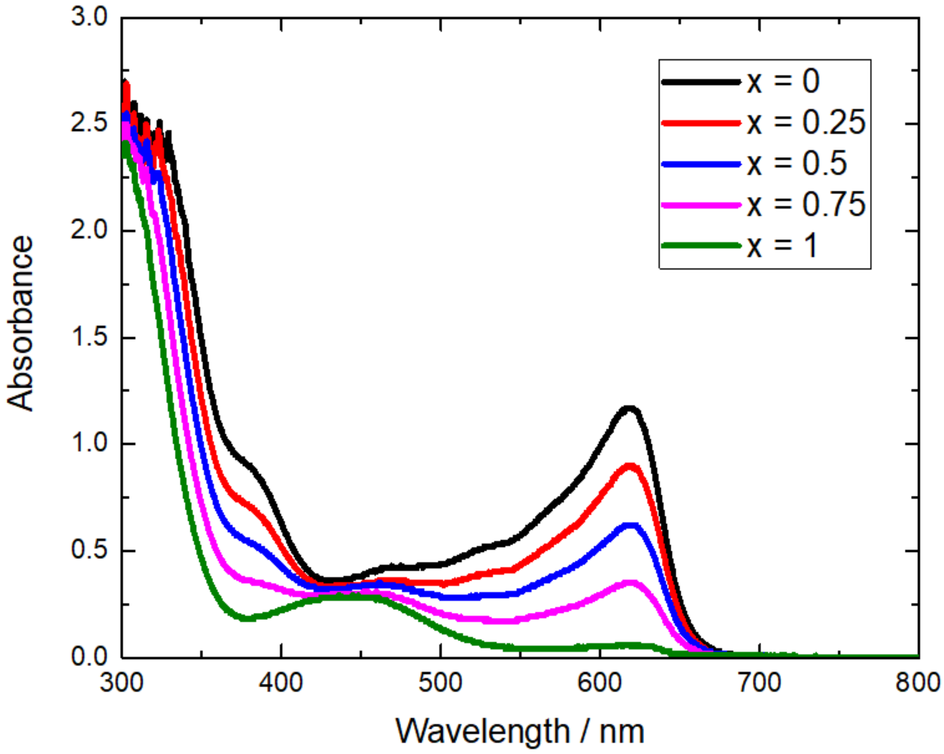

Figure 3.4.1 – UV-Vis spectra with baseline correction obtained for ferrocenium tetrafluoroborate solutions in DOL (3 mM) after addition of known aliquots of polysulfide solutions obtained from the $[S]_T^{Sol.}$ = 2 M, Li_2S_6 solution (0 ≤ x ≤ 1 – extent of the titration reaction).

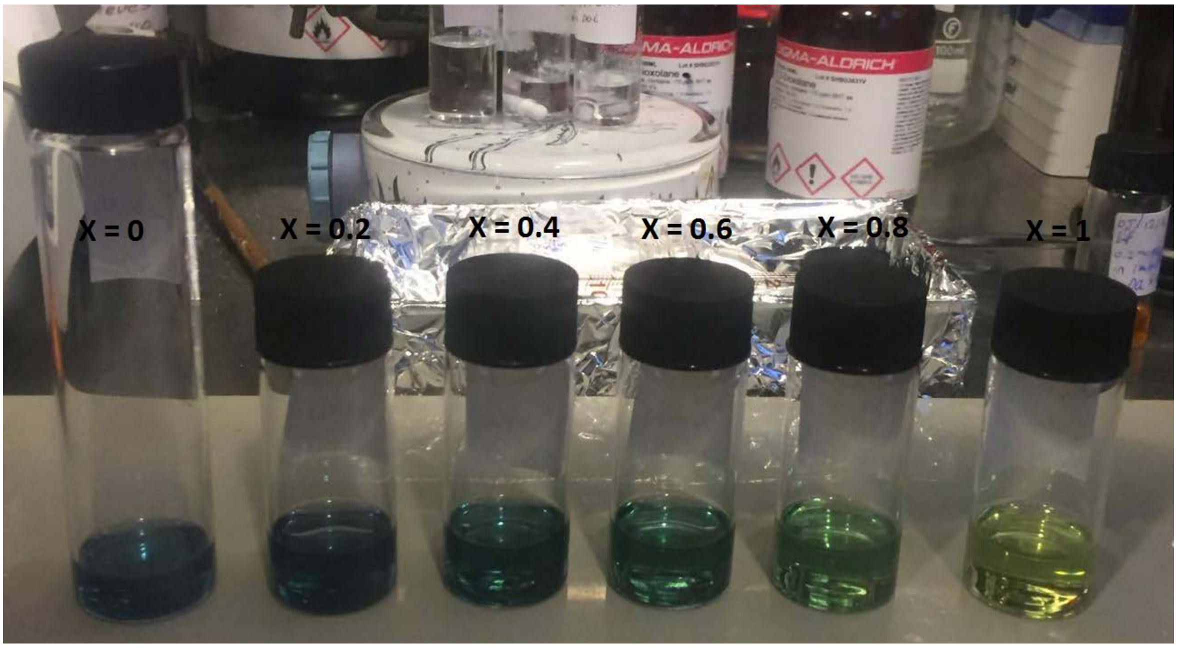

Figure 3.4.2 – Titration of ferrocenium tetrafluoroborate from left to right, where x = 0 is ferrocenium tetrafluoroborate (blue) and x = 1 is completely reduced ferrocene (yellow).

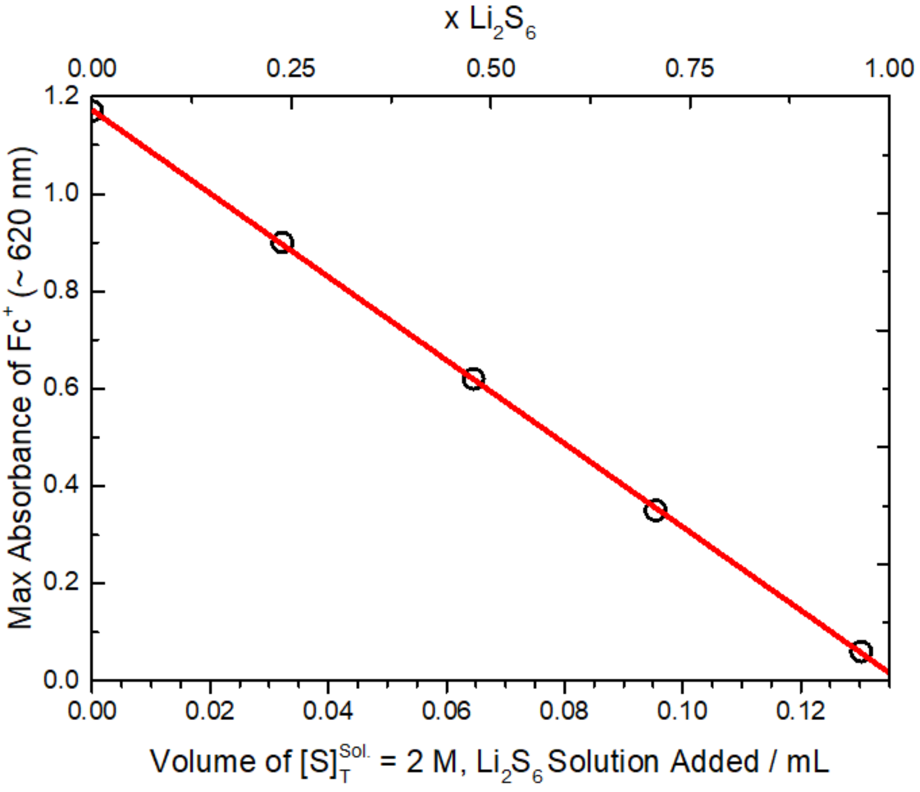

Figure 3.4.3 – Max absorbance of ferrocenium tetrafluoroborate solution in DOL (3 mM) at 620 nm plotted against the volume of $[S]_T^{Sol.}$ = 2 M, Li$_2$S$_6$ solution added and plotted against the extent of the titration reaction (0 ≤ x ≤ 1) between ferrocenium tetrafluoroborate solution and the $[S]_T^{Sol.}$ = 2 M, Li$_2$S$_6$ solution.

The determination of the polysulfide species concentration was initially derived from the Beer-Lambert law;

$$A_{FcBF_4} = \varepsilon_{FcBF_4} \times c_{FcBF_4} \times l \qquad \text{Equation 3.4.9}$$

where A_{FcBF_4} is the absorbance of ferrocenium tetrafluoroborate, ε_{FcBF_4} is the molar extinction coefficient of ferrocenium tetrafluoroborate (M^{-1} cm^{-1}) and l is the path length of the cell (1 cm). Equation 3.4.9 can be rearranged in terms of the concentration of the ferrocenium tetrafluoroborate solution.

$$c_{FcBF_4} = \frac{A_{FcBF_4}}{\varepsilon_{FcBF_4} \times l} = \frac{n_{FcBF_4}}{V_{FcBF_4}} \qquad \text{Equation 3.4.10}$$

Using the stoichiometric ratio between ferrocenium tetrafluoroborate and the polysulfide blend (Equation 3.4.3), the number of moles of ferrocenium tetrafluoroborate consumed (negative sign) is converted into the number of moles of polysulfide blend and is described by its concentration and volume.

$$\Delta n_{FcBF_4} = -2\, n_{Li_2S_n} = -2 \times [S_n^{2-}] \times V_{Li_2S_n} \qquad \text{Equation 3.4.11}$$

Substitute equation 3.4.11 into equation 3.4.10.

$$\frac{-\Delta A_{FcBF_4}}{\varepsilon_{FcBF_4} \times l} = \frac{2 \times [S_n^{2-}] \times V_{Li_2S_n}}{V_{FcBF_4}} \qquad \text{Equation 3.4.12}$$

Equation 3.4.12 can be rearranged in terms of the concentration of the polysulfide species in the solution.

$$[S_n^{2-}] = \left(\frac{-\Delta A_{FcBF_4}}{V_{Li_2S_n}}\right) \times \frac{V_{FcBF_4}}{2 \times \varepsilon_{FcBF_4} \times l} \qquad \text{Equation 3.4.13}$$

The volume of polysulfide blend added to the ferrocenium tetrafluoroborate solution is the variable that is changing and the absorbance is the variable that is being measured. Therefore, in equation 3.4.13 the terms inside the brackets are analogous to the gradient of the plot.

$$[S_n^{2-}] = \frac{-\text{Gradient} \times V_{\text{FcBF}_4}}{2 \times \varepsilon_{FcBF_4} \times l} \qquad \text{Equation 3.4.14}$$

From the concentration of the polysulfide solution, the chain length of the polysulfide species (Equation 3.4.15) and the average sulfur oxidation state (Equation 3.4.16) can be calculated.

$$n = \frac{[S]_{sol.}^{T}}{[S_n^{2-}]} \qquad \text{Equation 3.4.15}$$

$$\text{Average Sulfur Oxidation State} = \frac{2}{n} \qquad \text{Equation 3.4.16}$$

The UV/vis spectroscopic redox titration was performed multiple times for both of the low concentration polysulfide solutions (Table 3.4.1 & Table 3.4.2).

$[S]_T^{Sol.}$ = 0.2 M, Li_2S_5	$[S_n^{2-}]$ / M	Polysulfide Chain Length	Sulfur Oxidation State
1	0.0387 ± 0.0042	5.5 ± 1.1	0.361 ± 0.089
2	0.0380 ± 0.0030	5.83 ± 0.96	0.343 ± 0.068
3	0.0362 ± 0.0059	5.7 ± 1.6	0.35 ± 0.14
Average	0.0376 ± 0.0032	5.68 ± 0.36	0.352 ± 0.022

Table 3.4.1 – Calculated polysulfide blend concentration, chain length, and average sulfur oxidation state for the $[S]_T^{Sol.}$ = 0.2 M, Li_2S_5 polysulfide blend samples. Error for the averaged value corresponds to a confidence interval at a 95 % confidence level from three repeat experiments.

$[S]_T^{Sol.}$ = 2 M, Li_2S_6	$[S_n^{2-}]$ / M	Polysulfide Chain Length	Sulfur Oxidation State
1	0.345 ± 0.025	6.70 ± 0.68	0.299 ± 0.034
2	0.331 ± 0.016	6.31 ± 0.51	0.317 ± 0.028
3	0.335 ± 0.029	6.30 ± 0.78	0.317 ± 0.045
4	0.353 ± 0.042	6.2 ± 1.0	0.322 ± 0.064
Average	0.341 ± 0.016	6.38 ± 0.35	0.314 ± 0.017

Table 3.4.2 – Calculated polysulfide blend concentration, chain length, and average sulfur oxidation state for the $[S]_T^{Sol.}$ = 2 M, Li_2S_6 polysulfide blend samples. Error for averaged value corresponds to a confidence interval at a 95 % confidence level from four repeat experiments.

The average polysulfide chain length of the $[S]_T^{Sol.}$ = 0.2 M, Li_2S_5 polysulfide blend was determined to be 5.68 ± 0.36 and the average polysulfide chain length of the $[S]_T^{Sol.}$ = 2 M, Li_2S_6 polysulfide blend was determined to be 6.38 ± 0.35. The value of the polysulfide chain length for $[S]_T^{Sol.}$ = 0.2 M, Li_2S_5 and $[S]_T^{Sol.}$ = 2 M, Li_2S_6 are within 7 % and 14 % of the initially dictated values during the preparation of the blends with a relatively small error margin (approximately ± 5 % and ± 8 %). Overall, this procedure can reliably determine the polysulfide concentration and polysulfide chain length of low concentration polysulfide solutions as shown by the similarity between the initially set values and the measured variables (e.g. 2 M Li_2S_6 compared to 2.18 ± 0.16 M $Li_2S_{6.38 \pm 0.35}$). Therefore this procedure can be applied to the high concentration polysulfide solutions. This is important because the eutonic point solutions are prepared from a blend where the composition of the saturated solution will be different to the composition of the initial blend. This means we must be able to trust the results from the gravimetric and UV/vis titration experiments for the saturated solution because the composition will effectively be unknown.

3.5 **Preparation of High Concentration Polysulfide Blends**

With the previous results proving that the analytical experiments used to study the low concentration solutions are reliable and accurate, the same experiments were applied to determine the total atomic sulfur concentration and polysulfide species concentration for high concentration polysulfide blends. These high concentration polysulfide blends were prepared so that they would be saturated in both lithium sulfide and sulfur. Therefore, after filtration and experimental derivation of the concentration and speciation of the polysulfide species present, the eutonic point can be plotted on the phase diagram (Figure 3.5.1).[63] This eutonic point solution describes the saturation point of the electrolyte. In a real Li-S cell with high sulfur loading and low electrolyte to sulfur ratio, the electrolyte will become saturated. Therefore this phase diagram can be used as a predicative tool to describe characteristics of the Li-S mechanism.

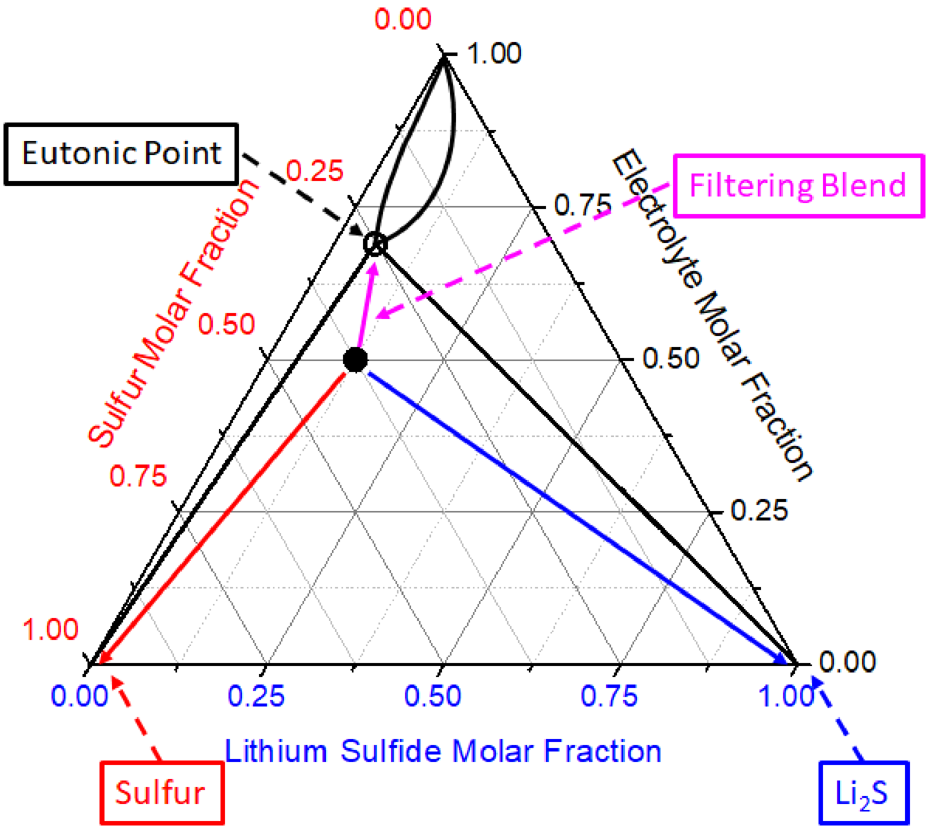

Figure 3.5.1 – Hypothetical phase diagram explanation of a PS blend (black filled circle) being filtered to produce a PS solution (black empty circle).

The hypothetical phase diagram (Figure 3.5.1) describes the preparation of the saturated polysulfide solutions. The black filled circle describes the position of the initially prepared blend on the phase diagram. The blend consists of a mixture of the saturated polysulfide solution, excess lithium sulfide solid and excess sulfur solid. The magenta arrow describes the filtration of the blend (i.e. removing the excess lithium sulfide solid and excess sulfur solid). The black empty circle describes the position of the saturated polysulfide solution or eutonic point of the electrolyte in the phase diagram.

A paper from Gamsjager et al. looking at “phenomena related to the solubility of solids, liquids and gases with one another”, defined the eutonic point as an “isothermally and isobarically invariant reaction of double saturation”.[82] Therefore in this eutonic reaction, reversible dissolution of three or more components is characterized by the composition of a solution that is simultaneously saturated to all (at least two or more) dissolved solutes. The chemical potential of the solvent ($pSolvent$) decreases along the two solubility curves that intersect at the eutonic point, and thus reaches a minimum value at that point. The lower the chemical potential of a solvent, the more saturated the solvent. The two simultaneous equilibrium processes are, for example;

$$A \cdot pSolvent \leftrightarrow A\ (aq., sat.) + pSolvent\ (l) \qquad \text{Equation 3.5.1}$$

$$B \cdot pSolvent \leftrightarrow B\ (aq., sat.) + pSolvent\ (l) \qquad \text{Equation 3.5.2}$$

In the case of our phase diagram, species A and B will be lithium sulfide and sulfur respectively. However when they are dissolved into solution, they will chemically react with each other to form a lithium polysulfide species.

During the discussion of the high concentration polysulfide blends, the results are displayed in inverted commas (i.e. “$[S]_T^{Sol.}$ = 10 M, Li_2S_6”) because the blend is a saturated solution with excess lithium sulfide and sulfur solid. Therefore the total sulfur concentration and chain length of the saturated solution will differ to the prepared blend.

The high concentration polysulfide blends used to determine the eutonic point on the ternary phase diagram were prepared in an argon-filled glove box. The desired masses of lithium sulfide and sulfur were added to a vial and the 1 M LiTFSI in DOL electrolyte (prepared in a volumetric flask) was added (Table 3.5.1).

Polysulfide Blends	Theoretical Li_2S Mass / g	Experimental Li_2S Mass / g	Theoretical Sulfur Mass / g	Experimental Sulfur Mass / g	Theoretical Electrolyte Mass / g	Experimental Electrolyte Mass / g
“$[S]_T^{Sol.}$ = 10 M, Li_2S_2”	2.2975	2.3049	1.6033	1.6099	11.8798	11.7652
“$[S]_T^{Sol.}$ = 10 M, Li_2S_4”	1.1488	1.1494	2.4049	2.4186	11.8798	11.6286
“$[S]_T^{Sol.}$ = 10 M, Li_2S_6 – 1”	0.7658	0.7714	2.6721	2.6775	11.9012	11.8389
“$[S]_T^{Sol.}$ = 10 M, Li_2S_6 – 2”	0.7658	0.7691	2.6721	2.6810	11.8967	11.8098
“$[S]_T^{Sol.}$ = 10 M, Li_2S_6 – 3”	0.7658	0.7689	2.6721	2.6737	11.8967	11.7660
“$[S]_T^{Sol.}$ = 10 M, Li_2S_8 – 1”	0.5744	0.5750	2.8057	2.8248	11.9012	11.7732
“$[S]_T^{Sol.}$ = 10 M, Li_2S_8 – 2”	0.5744	0.5747	2.8057	2.9021	11.9010	11.8222
“$[S]_T^{Sol.}$ = 20 M, Li_2S_8”	1.1488	1.1490	5.6114	5.6128	11.9305	11.9078

Table 3.5.1 – Theoretical and experimental masses of lithium sulfide, sulfur and electrolyte (1 M LiTFSI in DOL) required to prepare the saturated polysulfide blends.

The blends were heated to 60 °C and stirred for a month. Afterwards the blends were cooled down over a period of a week to ensure they were at equilibrium. It can be observed that the high concentration polysulfide blends being prepared are beyond their saturation point since after two weeks of stirring there is still solid present as shown by the orange opaque blends (Figure 3.5.2). The long heating time was required for these high concentration polysulfide solutions because of their higher viscosity (observed visually) compared to the low concentration polysulfide solutions that will slow down the rate of dissolution.

***Figure 3.5.2** – "$[S]_T^{Sol.}$ = 10 M, Li_2S_6" (left) and "$[S]_T^{Sol.}$ = 10 M, Li_2S_8" (right) polysulfide blends after heating at 60 °C and stirring for 2 weeks.*

After the cooling period, the blends had separated into two layers, which is the saturated polysulfide solution as the upper layer, and excess lithium sulfide and sulfur precipitate as the bottom layer (Figure 3.5.3).

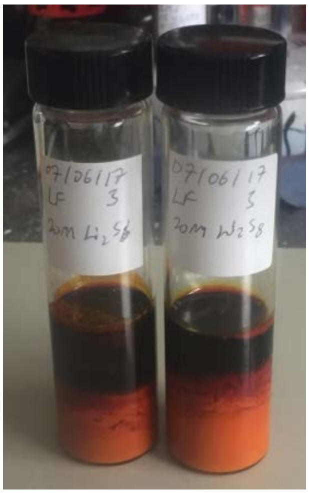

***Figure 3.5.3** – "$[S]_T^{Sol.}$ = 20 M, Li_2S_6" (left) and "$[S]_T^{Sol.}$ = 20 M, Li_2S_8" (right) polysulfide blends after heating at 60 °C and stirring for a month then left to cool down to room temperature for 1 week.*

The upper layer containing the saturated polysulfide solution was decanted into a centrifuge tube and the solution was separated from the blend by means of centrifugation. This process was repeated three times followed by a syringe filtration to ensure all excess solid is removed from the saturated polysulfide solution. The centrifuging and filtering processes removed the excess lithium sulfide and sulfur from the polysulfide blend to produce the saturated polysulfide solution. However, some of the filtered saturated polysulfide solutions were actually supersaturated because when they were agitated, a precipitate formed in the solution (Figure 3.5.4).

Figure 3.5.4 – Pictures of the saturated polysulfide solution (left) and the precipitate from a supersaturated polysulfide solution (right).

This was an interesting observation since the filtered solution was left for a period of a few days where no precipitate formed. Judging from visual observation the viscosity of the supersaturated solutions was far greater than the saturated solutions. Therefore, all the solutions were filtered at least twice using syringe filtration to ensure the solutions were not supersaturated.

To check if the polysulfide solutions were not supersaturated a droplet of the solution was pressed between two glass slides sealed with grease (Figure 3.5.5).

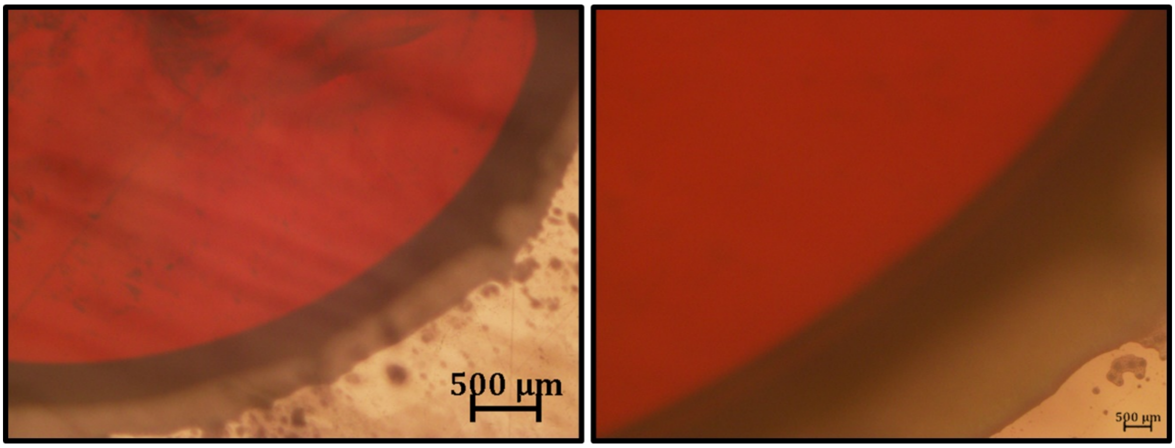

Figure 3.5.5 – Microscope images of a saturated polysulfide solution. Left – 2x magnification of the droplet and right – 5x magnification of the droplet edge.

The observations from the microscope images were a clear solution with no observable seed crystals or precipitates in the droplet. Therefore after the centrifugation and filtration steps, the saturated polysulfide solution has been successfully separated from the undissolved solids.

With the clear saturated polysulfide solutions the densities, total atomic sulfur concentration and polysulfide concentration were determined experimentally (Table 3.5.2).

Polysulfide Blends	Density / g mL^{-1}	$[S]_T^{Sol.}$ / M	$[S_n^{2-}]$ / M	Polysulfide Chain Length	Sulfur Oxidation State
"$[S]_T^{Sol.}$ = 10 M, Li_2S_2"	1.314 ± 0.047	5.84 ± 0.22	1.21 ± 0.12	4.82 ± 0.50	0.414 ± 0.043
"$[S]_T^{Sol.}$ = 10 M, Li_2S_4"	1.327 ± 0.047	6.19 ± 0.24	1.378 ± 0.055	4.49 ± 0.25	0.445 ± 0.025
"$[S]_T^{Sol.}$ = 10 M, Li_2S_6 – 1"	1.26 ± 0.10	5.27 ± 0.61	0.925 ± 0.091	5.70 ± 0.86	0.351 ± 0.053
"$[S]_T^{Sol.}$ = 10 M, Li_2S_6 – 2"	1.323 ± 0.047	5.81 ± 0.22	1.10 ± 0.14	5.26 ± 0.69	0.380 ± 0.050
"$[S]_T^{Sol.}$ = 10 M, Li_2S_6 – 3"	1.351 ± 0.048	6.45 ± 0.25	1.137 ± 0.059	5.67 ± 0.37	0.352 ± 0.023
"$[S]_T^{Sol.}$ = 10 M, Li_2S_8 – 1"	1.27 ± 0.10	4.88 ± 0.50	0.813 ± 0.096	6.00 ± 0.94	0.333 ± 0.052
"$[S]_T^{Sol.}$ = 10 M, Li_2S_8 – 2"	1.302 ± 0.047	4.96 ± 0.20	0.882 ± 0.074	5.63 ± 0.52	0.355 ± 0.033
"$[S]_T^{Sol.}$ = 20 M, Li_2S_8"	1.27 ± 0.10	4.99 ± 0.83	0.881 ± 0.098	5.7 ± 1.1	0.353 ± 0.070
Average	1.302 ± 0.028	5.55 ± 0.50	1.04 ± 0.16	5.41 ± 0.43	0.373 ± 0.032

Table 3.5.2 – Experimentally determined density, total atomic sulfur concentration, polysulfide concentration, polysulfide chain length and average oxidation state of sulfur for the 1 M electrolyte eutonic point polysulfide solutions. Errors for averaged values correspond to a confidence interval at a 95 % confidence level from repeat experiments.

From all of the experiments performed, the average composition of the polysulfide species was $[S]_T^{Sol.}$ = 5.55 ± 0.50 M, $Li_2S_{5.41 \pm 0.43}$. The composition determined by elemental analysis was $[S]_T^{Sol.}$ =6.15 ± 0.65 M, $Li_2S_{5.48 \pm 0.59}$. The polysulfide species compositions determined from these two different methods are very similar proving that the experimental methods of determining the total sulfur concentration and polysulfide concentration are accurate.

The LiTFSI concentration was also determined from elemental analysis to be 0.975 ± 0.0042 M. This is very close to the initially prepared 1 M electrolyte. The slight difference could have been caused by the method of sealing the ampoule that contains the saturated polysulfide solution. During this process, the polysulfide solution was frozen using liquid nitrogen then the ampoule was evacuated with a pump and sealed with a flame. These are quite harsh conditions for the saturated polysulfide solution and could potentially affect the content of the solution.

The initially prepared blend sulfur concentration was $[S]_T^{Sol.}$ = 10 M. However after filtration and analysis the sulfur concentration of the saturated solution was $[S]_T^{Sol.}$ = 5.6 M. This shows that during the preparation of the saturated polysulfide solution, lithium sulfide and sulfur will preferentially precipitate out of supersaturated solution instead of LiTFSI. This means these results will accurately depict the ternary phase diagram for the 1 M electrolyte.

The uncertainty in the measurements for the density, total atomic sulfur concentration and polysulfide species concentration are acceptable (approximately 10 %). The average concentration and composition of the eutonic point solution also seems to be in agreement, if you also consider the error in the measurement. Therefore, these precise values were used to make the ternary phase diagram.

3.6 Eutonic Point for the Ternary Phase Diagram

From the experimentally determined saturated polysulfide solution density, total atomic sulfur concentration, polysulfide concentration and polysulfide chain length values (Table 3.5.2), the molar fractions (MF) of lithium sulphide, sulfur and electrolyte (1 M LiTFSI in DOL) were calculated to for the ternary phase diagram (Table 3.6.1).

Polysulfide Blend	$\mathrm{MF}_{\mathrm{Li_2S}}$	$\mathrm{MF}_{\mathrm{Electrolyte}}$	$\mathrm{MF}_{\mathrm{Sulfur}}$
“$[S]_T^{Sol.}$ = 10 M, Li_2S_2”	0.0667 ± 0.0064	0.678 ± 0.042	0.255 ± 0.014
“$[S]_T^{Sol.}$ = 10 M, Li_2S_4”	0.0746 ± 0.0030	0.665 ± 0.037	0.260 ± 0.013
“$[S]_T^{Sol.}$ = 10 M, Li_2S_6 – 1”	0.0536 ± 0.0053	0.695 ± 0.087	0.252 ± 0.035
“$[S]_T^{Sol.}$ = 10 M, Li_2S_6 – 2”	0.0605 ± 0.0075	0.682 ± 0.045	0.258 ± 0.014
“$[S]_T^{Sol.}$ = 10 M, Li_2S_6 – 3”	0.0600 ± 0.0031	0.660 ± 0.038	0.280 ± 0.014
“$[S]_T^{Sol.}$ = 10 M, Li_2S_8 – 1”	0.0476 ± 0.0056	0.714 ± 0.088	0.238 ± 0.030
“$[S]_T^{Sol.}$ = 10 M, Li_2S_8 – 2”	0.0504 ± 0.0042	0.716 ± 0.041	0.233 ± 0.012
“$[S]_T^{Sol.}$ = 20 M, Li_2S_8”	0.0515 ± 0.0057	0.708 ± 0.089	0.240 ± 0.049
Average	0.0581 ± 0.0077	0.690 ± 0.018	0.252 ± 0.013

Table 3.6.1 – Table of molar fractions of lithium sulfide, sulfur and electrolyte for the 1 M electrolyte eutonic point. Errors for averaged values correspond to a confidence interval at a 95 % confidence level from repeat experiments.

The calculated molar fraction from experimental results for the saturated polysulfide solutions were plotted into a ternary phase diagram to elucidate the position of the eutonic point (Figure 3.6.1).

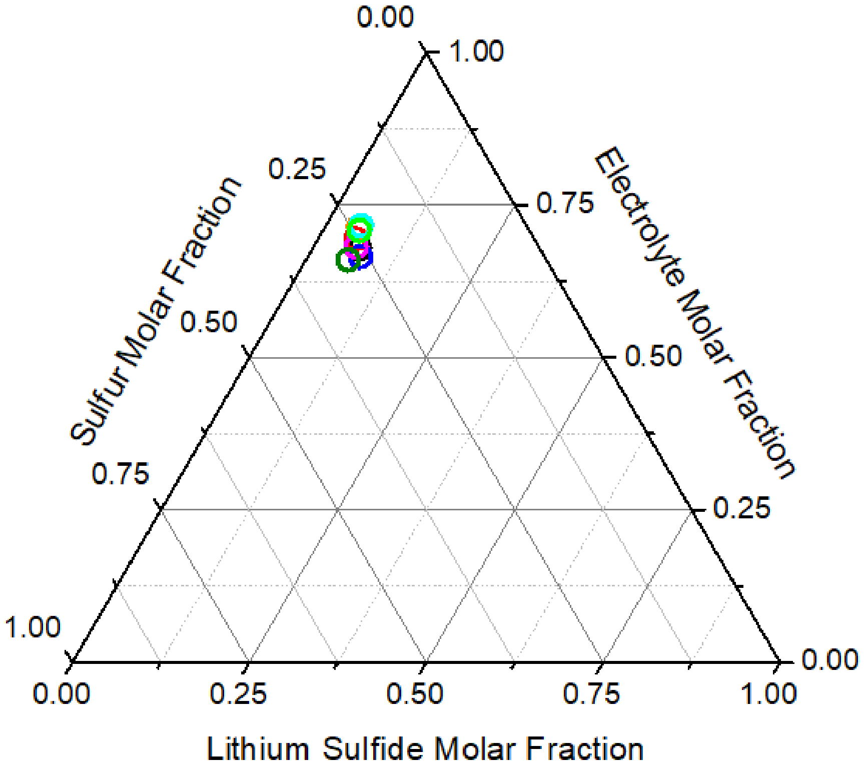

***Figure 3.6.1** – Experimental ternary phase diagram of the eutonic point of a system containing lithium sulfide, sulfur and 1 M LiTFSI in DOL electrolyte. Black Circle – "$[S]_{T}^{Sol.}$ = 10 M, Li_2S_2", blue circle – "$[S]_{T}^{Sol.}$ = 10 M, Li_2S_4", red circle – "$[S]_{T}^{Sol.}$ = 10 M, Li_2S_6 – 1", magenta circle – "$[S]_{T}^{Sol.}$ = 10 M, Li_2S_6 – 2", dark green circle – "$[S]_{T}^{Sol.}$ = 10 M, Li_2S_6 – 3", orange circle – "$[S]_{T}^{Sol.}$ = 10 M, Li_2S_8 – 1", cyan circle – "$[S]_{T}^{Sol.}$ = 10 M, Li_2S_8 – 2" and light green circle – "$[S]_{T}^{Sol.}$ = 20 M, Li_2S_8" (The diameter of circle bears no error information).*

The reliability in the preparation and analysis of the saturated polysulfide solutions is very good. This can be seen when comparing the size of the uncertainties for the molar fractions mostly being within 10 % (Table 3.6.1). The high overlap between the eutonic points from the different saturated polysulfide solutions show the high precision of these measurements (Figure 3.6.1).

Representing errors for the average eutonic point on a ternary phase will result in three error bars that are at an angle of 60^{o} from each other. Assuming the error bars were the same size, this would result in a hexagon of error surrounding the data point. Similar to how errors depicted on a Cartesian plot, there are two error bars at an angle of 90^{o} from each other and assuming the error bars are the same size would result in a square of error surrounding the data point.

However, the error bar for the molar fraction of electrolyte is relatively large when compared to the molar fraction of lithium sulfide and sulfur even though its percentage error is less than 10 % (Table 3.6.1). This does not mean the results are not reliable, it is because the majority of the polysulfide solution is made from the electrolyte. Therefore, the pictorial representation of the average eutonic point with all three error bars results in two smaller error bars and one large error bar (Figure 3.6.2). Therefore, to simplify figure 3.6.2 the excess error bar boundaries were removed (Figure 3.6.3).

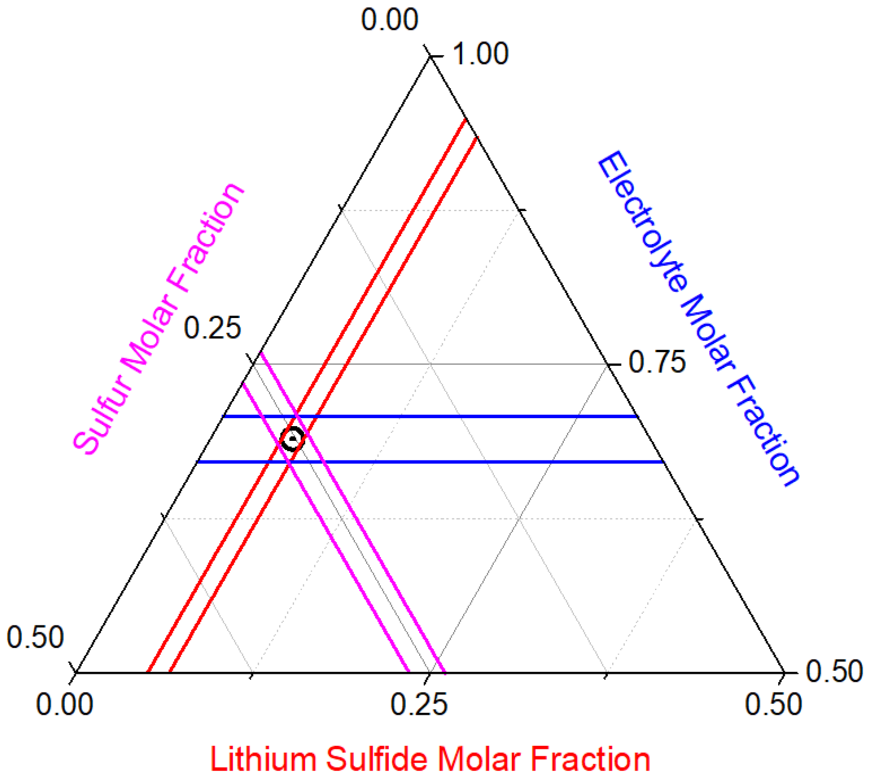

***Figure 3.6.2** – Zoomed in experimental ternary phase diagram of the averaged eutonic point from the 1 M LiTFSI in DOL electrolyte saturated polysulfide solutions (black circle) with the error bar boundaries coloured to match their respective molar fraction axis.*

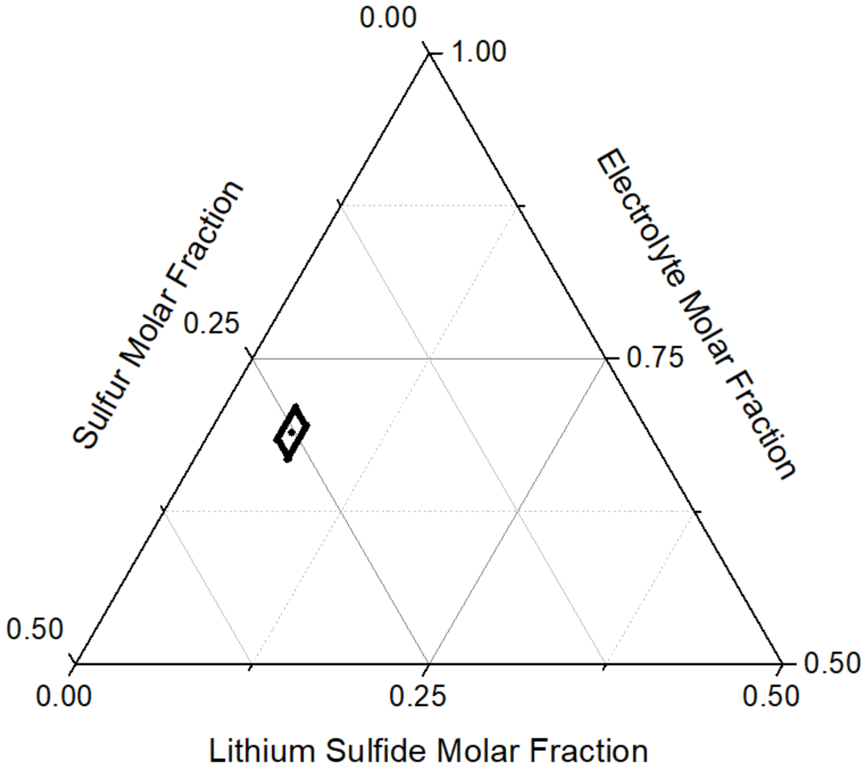

Figure 3.6.3 – Zoomed in experimental ternary phase diagram of averaged eutonic point from the 1 M LiTFSI in DOL electrolyte saturated polysulfide solutions (black point) with the region of error described by the black diamond.

This results in a diamond shape of error surrounding the average eutonic point. The size of the error area is small which shows the precision of the average eutonic point. From this experimentally determined eutonic point a hypothetical ternary phase diagram was formed (Figure 3.6.4).

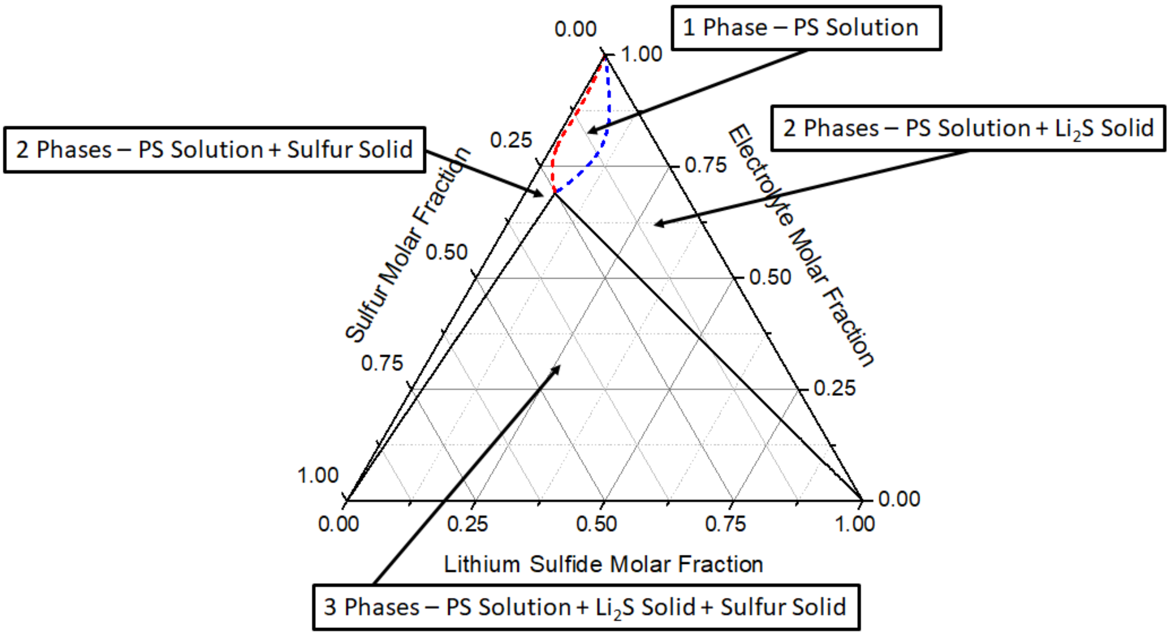

Figure 3.6.4 – Hypothetical ternary phase diagram based on the experimental eutonic point for the 1 M LiTFSI in DOL electrolyte.

From the average eutonic point, the lower 3-phase boundaries can be determined. These boundaries are straight lines from the eutonic point to the bottom left corner of the phase diagram that represents pure sulfur and to the bottom right corner of the phase diagram that represents lithium sulfide. The lower phase boundaries on these two regions are straight lines because the polysulfide solution is at saturation therefore by adding lithium sulfide to a saturated solution with excess sulfur solid present will not aid dissolution of the excess sulfur solid and vice versa.

The region that is still unknown is the 2-phase boundaries. The hypothetical upper 2-phase boundaries are curved because the solubility of sulfur in the polysulfide solution increases when lithium sulfide is added and vice versa.[82]

From the results obtained thus far, an accurate and reliable eutonic point for the ternary phase diagram has been determined with a reasonable uncertainty (< 10 %). Next the upper phase boundaries on the two phase regions will be determined by preparing a polysulfide blend that is saturated in sulfur or lithium sulfide to locate the 2-phase boundaries phase diagram.

3.7 Preparation of 2-Phase Boundary Polysulfide Solutions

To complete the phase diagram, the 2-phase boundaries were experimentally determined. From the phase diagrams results, an average composition of eutonic solution was determined to be $[S]_T^{Sol.}$ = 5.6 M, $Li_2S_{5.4}$. Using the eutonic point, polysulfide blends where chosen in the 2-phase region (Figure 3.7.1). The 2-phase boundary points chosen were at least at a similar height as the eutonic point or lower on the phase diagram. This means the 2-phase boundary initial blends prepared would have a total atomic sulfur concentration similar to or greater than the eutonic point total atomic sulfur concentration ($[S]_T^{Sol.}$ = 5.6 M). However if the points are too low on the phase diagram (i.e. high total atomic sulfur concentration), the isolation of the polysulfide solution from the undissolved solid becomes very difficult. The 2-phase region to the left of the eutonic point has excess sulfur resulting in a chain length longer than eutonic point species ($n > 5.4$) and to the 2 phase region to the right has excess Li_2S resulting in a chain length shorter than eutonic point species ($n < 5.4$). The following points selected on the phase diagram (Figure 3.7.1) were chosen to determine the 2-phase boundaries.

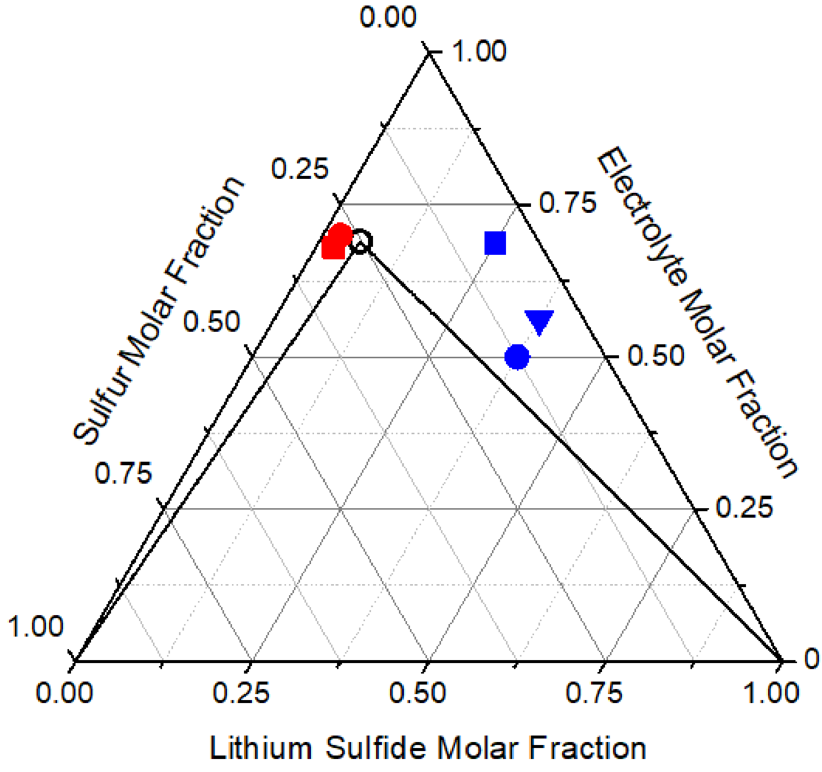

Figure 3.7.1 –Ternary phase diagram that displays the 2 phase boundary blends for the 1 M LiTFSI in DOL electrolyte. Black empty circle – average eutonic point, red filled square – "$[S]_T^{Sol.}$ = 5.7 M, $Li_2S_{12.8}$", red filled circle – "$[S]_T^{Sol.}$ = 5.2 M, Li_2S_{12}", blue filled square – "$[S]_T^{Sol.}$ = 5.25 M, $Li_2S_{1.25}$", blue filled circle – "$[S]_T^{Sol.}$ = 10.25 M, $Li_2S_{1.3}$" and blue filled upside-down triangle – "$[S]_T^{Sol.}$ = 8.2 M, $Li_2S_{1.17}$".

Similar to how eutonic point blends were prepared to be saturated in both Li_2S and sulfur, these blends were chosen because they are only saturated in either lithium sulfide or sulfur. To prove the chosen 2-phase blends are only saturated in either lithium sulfide or sulfur, the amounts of Li_2S and sulfur needed to prepare the eutonic solution was determined (Table 3.7.1).

Composition of the Eutonic Point Polysulfide Solution	$[S]_T^{Sol.}$ / M	$[Li_2S]_{initial}$ / M	$[S]_{initial}$ / M
$Li_2S_{5.4}$	5.6	1.0	4.6

Table 3.7.1 – Concentrations of lithium sulfide and sulfur used to prepare the eutonic solution for the 1 M LiTFSI in DOL electrolyte.

This can be used to estimate the amount of dissolved and undissolved solid in the polysulfide blend when preparing the 2-phase polysulfide solutions by subtracting the relative amounts of lithium sulfide and sulfur from a eutonic point solution (Table 3.7.2).

Composition of Polysulfide Blend	$[S]_T^{Sol.}$ / M	[Li_2S]$_{initial}$ / M	[S]$_{initial}$ / M	[Li_2S]$_{ppte}$ / M	[S]$_{ppte}$ / M
$Li_2S_{12.8}$	5.7	0.45	5.25	0.45 – 1 = **– 0.55**	5.25 – 4.6 = **0.65**
Li_2S_{12}	5.2	0.43	4.77	0.43 – 1 = **– 0.57**	4.77 – 4.6 = **0.17**
$Li_2S_{1.25}$	5.25	4.2	1.05	4.2 – 1 = **3.2**	1.05 – 4.6 = **– 3.55**
$Li_2S_{1.3}$	10.25	7.88	2.37	7.88 – 1 = **6.88**	2.37 – 4.6 = **– 2.23**
$Li_2S_{1.17}$	8.2	7.01	1.19	7.01 – 1 = **6.01**	1.19 – 4.6 = **– 3.41**

Table 3.7.2 – Concentrations of lithium sulfide and sulfur used to prepare the 2-phase region boundary blends where the blend is saturated with sulfur or lithium sulfide for the 1 M LiTFSI in DOL electrolyte.

Using the composition of the eutonic point it can be shown that these polysulfide blends are only saturated in either lithium sulfide or sulfur by the only one of the precipitate values being positive. If the precipitate value is negative then the solution is not saturated with respect to that species (Table 3.7.2). The fact that one of the precipitate values is negative means that there is not enough of that reagent to produce a polysulfide solution with the composition of the eutonic point.

Now with the knowledge of the composition of the eutonic point and its position on the phase diagram polysulfide blends were prepared with the purpose to define the 2 phase boundaries (Table 3.7.3).

Using the previously developed experimental techniques the density, total atomic sulfur concentration and polysulfide concentration were determined for the 2-phase boundary solutions (Table 3.7.4).

Polysulfide Blends	Theoretical Li_2S Mass / g	Experimental Li_2S mass / g	Theoretical Sulfur Mass / g	Experimental Sulfur Mass / g	Theoretical Electrolyte Mass / g	Experimental Electrolyte Mass / g
"$[S]_T^{Sol.}$ = 5.7 M, $Li_2S_{12.8}$"	0.2229	0.2224	1.8355	1.8421	12.0398	11.8635
"$[S]_T^{Sol.}$ = 5.2 M, Li_2S_{12}"	0.2165	0.2175	1.6621	1.6627	12.0398	11.8234
"$[S]_T^{Sol.}$ = 5.25 M, $Li_2S_{1.25}$"	1.9311	1.9387	0.3369	0.3405	11.8997	11.7653
"$[S]_T^{Sol.}$ = 10.25 M, $Li_2S_{1.3}$"	3.5324	3.5397	0.8217	0.8255	11.8997	11.5998
"$[S]_T^{Sol.}$ = 8.2 M, $Li_2S_{1.17}$"	4.0414	4.0401	0.4701	0.4711	12.0706	11.8562

Table 3.7.3 – Theoretical and experimental masses of lithium sulfide, sulfur and electrolyte (1 M LiTFSI in DOL) required to prepare the 2 phase boundary blends.

Polysulfide Blends	Density / g mL^{-1}	$[S]_T^{Sol.}$ / M	$[S_n^{2-}]$ / M	Polysulfide Chain Length	Sulfur Oxidation State
“$[S]_T^{Sol.}$ = 5.7 M $Li_2S_{12.8}$”	1.253 ± 0.033	2.530 ± 0.071	0.411 ± 0.023	6.03 ± 0.38	0.331 ± 0.021
“$[S]_T^{Sol.}$ = 5.2 M Li_2S_{12}”	1.255 ± 0.033	2.477 ± 0.070	0.400 ± 0.037	6.33 ± 0.61	0.316 ± 0.030
“$[S]_T^{Sol.}$ = 5.25 M $Li_2S_{1.25}$”	1.230 ± 0.033	1.416 ± 0.040	0.823 ± 0.057	1.72 ± 0.13	1.163 ± 0.087
“$[S]_T^{Sol.}$ = 10.25 M $Li_2S_{1.3}$”	1.258 ± 0.033	3.334 ± 0.093	1.078 ± 0.093	3.09 ± 0.28	0.647 ± 0.059
“$[S]_T^{Sol.}$ = 8.2 M $Li_2S_{1.17}$”	1.287 ± 0.046	2.228 ± 0.086	0.479 ± 0.019	4.65 ± 0.26	0.430 ± 0.024

Table 3.7.4 – Experimentally determined density, total atomic sulfur concentration, polysulfide concentration, polysulfide chain length and average oxidation state of sulfur of the 2-phase boundary polysulfide solutions for the 1 M LiTFSI in DOL electrolyte.

The results are initially quite promising because for 2-phase boundary solutions to the left of the eutonic point the total sulfur concentration is lower and the polysulfide chain length is longer than the average eutonic point species $[S]_T^{Sol.}$ = 5.6 M, $Li_2S_{5.4}$. Likewise for the 2-phase boundary solutions to the right of the eutonic point the total sulfur concentration is also lower and the polysulfide chain length is shorter than the average eutonic point species $[S]_T^{Sol.}$ = 5.6 M, $Li_2S_{5.4}$.

The lower total sulfur concentration shows that the solution is not saturated in both lithium sulfide and sulfur. The range of polysulfide chain lengths obtained from the 2-phase boundary solutions displays that the developed procedures and analytical measurements can produce and observe polysulfide species of varying chain lengths.

3.8 2-Phase Boundaries for the Ternary Phase Diagram

The results from the barium sulphate gravimetric analysis and the UV/vis spectroscopic redox titration techniques were converted into molar fraction (Table 3.8.1) and plotted into the ternary phase diagram (Figure 3.8.1).

Polysulfide Blend	$\mathrm{MF_{Li_2S}}$	$\mathrm{MF_{Electrolyte}}$	$\mathrm{MF_{Sulfur}}$
“$[S]_T^{Sol.}$ = 5.7 M, $Li_2S_{12.8}$”	0.0266 ± 0.0015	0.836 ± 0.031	0.1371 ± 0.0048
“$[S]_T^{Sol.}$ = 5.2 M, Li_2S_{12}”	0.0259 ± 0.0024	0.840 ± 0.032	0.1345 ± 0.0051
“$[S]_T^{Sol.}$ = 5.25 M, $Li_2S_{1.25}$”	0.0571 ± 0.0040	0.902 ± 0.032	0.0411 ± 0.0048
“$[S]_T^{Sol.}$ = 10.25 M, $Li_2S_{1.3}$”	0.0677 ± 0.0059	0.791 ± 0.032	0.1415 ± 0.0083
“$[S]_T^{Sol.}$ = 8.2 M, $Li_2S_{1.17}$”	0.0306 ± 0.0012	0.857 ± 0.041	0.1119 ± 0.0056

Table 3.8.1 – Table of molar fractions of lithium sulfide, sulfur and electrolyte for the 2-phase boundary for the 1 M LiTFSI in DOL electrolyte.

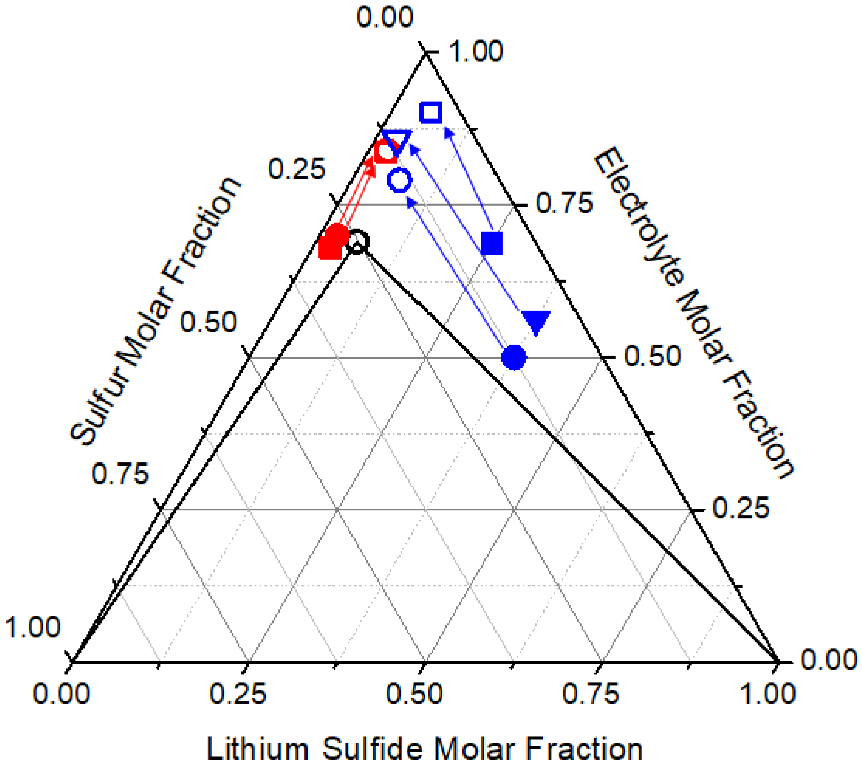

Figure 3.8.1 – Experimental ternary phase diagram of the 2 phase boundaries PS solutions before and after filtering (filled = blend, empty = filtered) for the 1 M LiTFSI in DOL electrolyte. Black circle – average eutonic point, red square – "$[S]_T^{Sol.}$ = 5.7 M, $Li_2S_{12.8}$", red circle – "$[S]_T^{Sol.}$ = 5.2 M, Li_2S_{12}", blue square – "$[S]_T^{Sol.}$ = 5.25 M, $Li_2S_{1.25}$", blue circle – "$[S]_T^{Sol.}$ = 10.25 M, $Li_2S_{1.3}$" and blue upside-down triangle – "$[S]_T^{Sol.}$ = 8.2 M, $Li_2S_{1.17}$".

The 2-phase polysulfide blends prepared (represented by filled shapes) after separation and filtration (represented by arrows) result in solutions (represented by shapes outlines) that map out the 2 phase boundaries on the left and right side of the 1-phase region in the phase diagram.

The method of which these 2-phase boundary solutions map out the 2-phase boundary is described in figure 3.8.2.

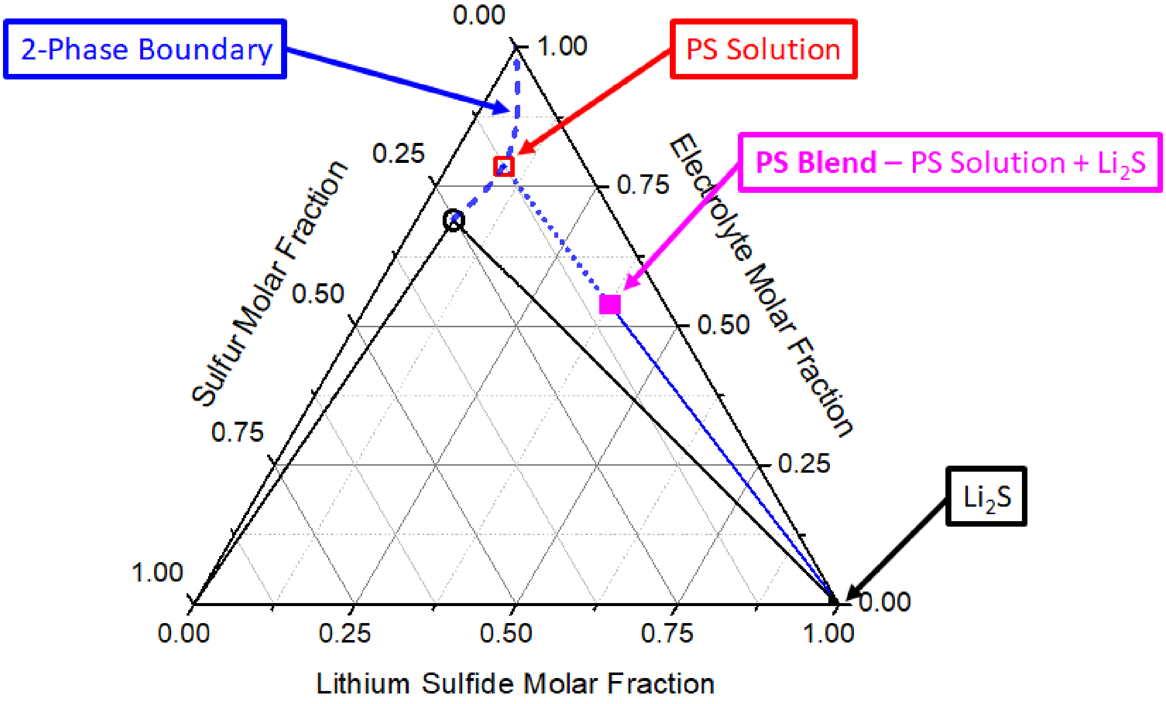

Figure 3.8.2 – Example phase diagram of the 2-phase boundary PS solutions mapping out the 2-phase boundary.

The prepared polysulfide blend will determine the right 2-phase boundary because the blend is saturated in lithium sulfide. A straight line can be made (blue line) between the point that represents the blend (magenta point) and the bottom right corner of the phase diagram that represents pure lithium sulfide. The 2-phase boundary polysulfide solution point (red square outline) that is determined experimentally should be in line with the extrapolated blue dotted line which represents filtration. The 2-phase boundary polysulfide solution point (red square outline) then can be used to map out the right 2-phase boundary.

For the left 2-phase boundary, the 2-phase boundary polysulfide solutions points are in line with the extrapolated line (Figure 3.8.3).

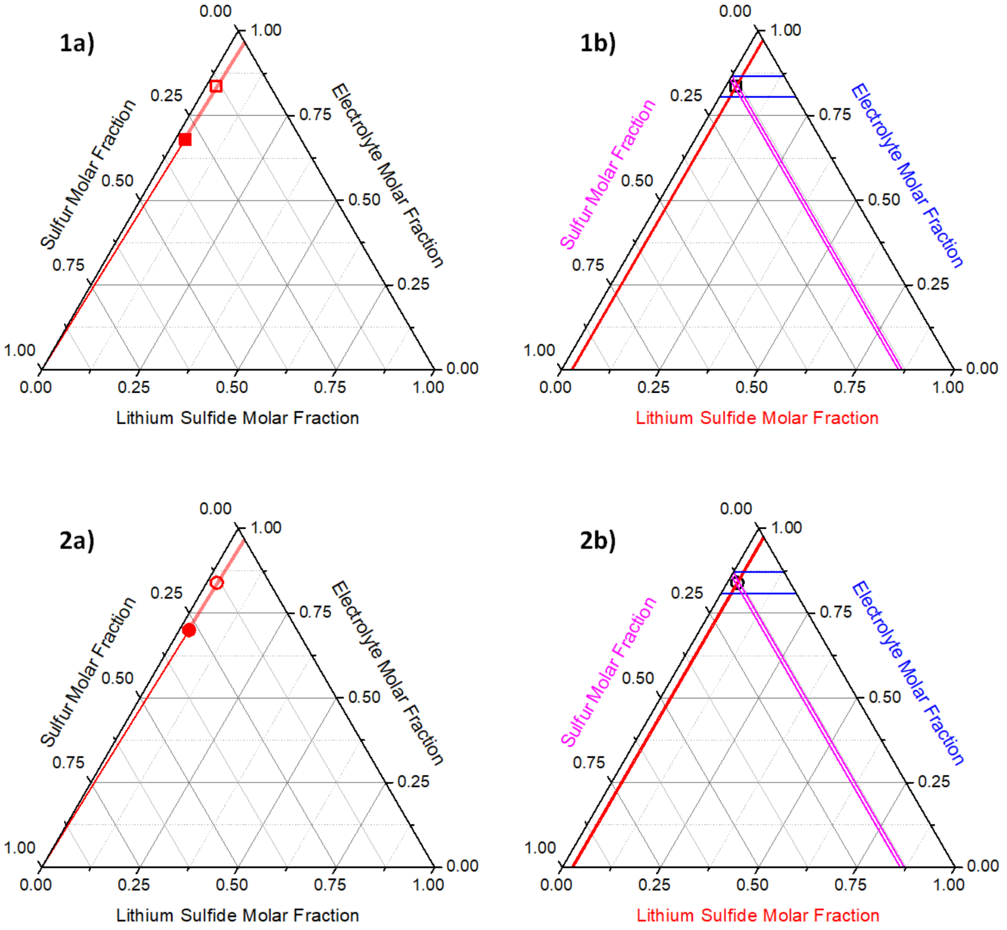

Figure 3.8.3 – Phase diagrams of the left 2-phase boundary PS solutions. 1a) is the “$[S]_T^{Sol.}$ = 5.7 M, $Li_2S_{12.8}$” blend (red square) and filtered solution (red empty square). 1b) is the respective errors for the “$[S]_T^{Sol.}$ = 5.7 M, $Li_2S_{12.8}$” filtered solution. 2a) is the “$[S]_T^{Sol.}$ = 5.2 M, Li_2S_{12}” blend (red circle) and filtered solution (red empty circle). 2b) is the respective errors for the “$[S]_T^{Sol.}$ = 5.2 M, Li_2S_{12}” filtered solution.

The size of the errors for the molar fractions are all relatively small (at most 10 %) showing that these points are reliable. The two slightly different left 2-phase boundary polysulfide solutions appear in close proximity to each other showing the precision in these results.

For the right 2-phase boundary, the 2-phase boundary polysulfide solutions points had slightly diverged from the extrapolated line (Figure 3.8.4).

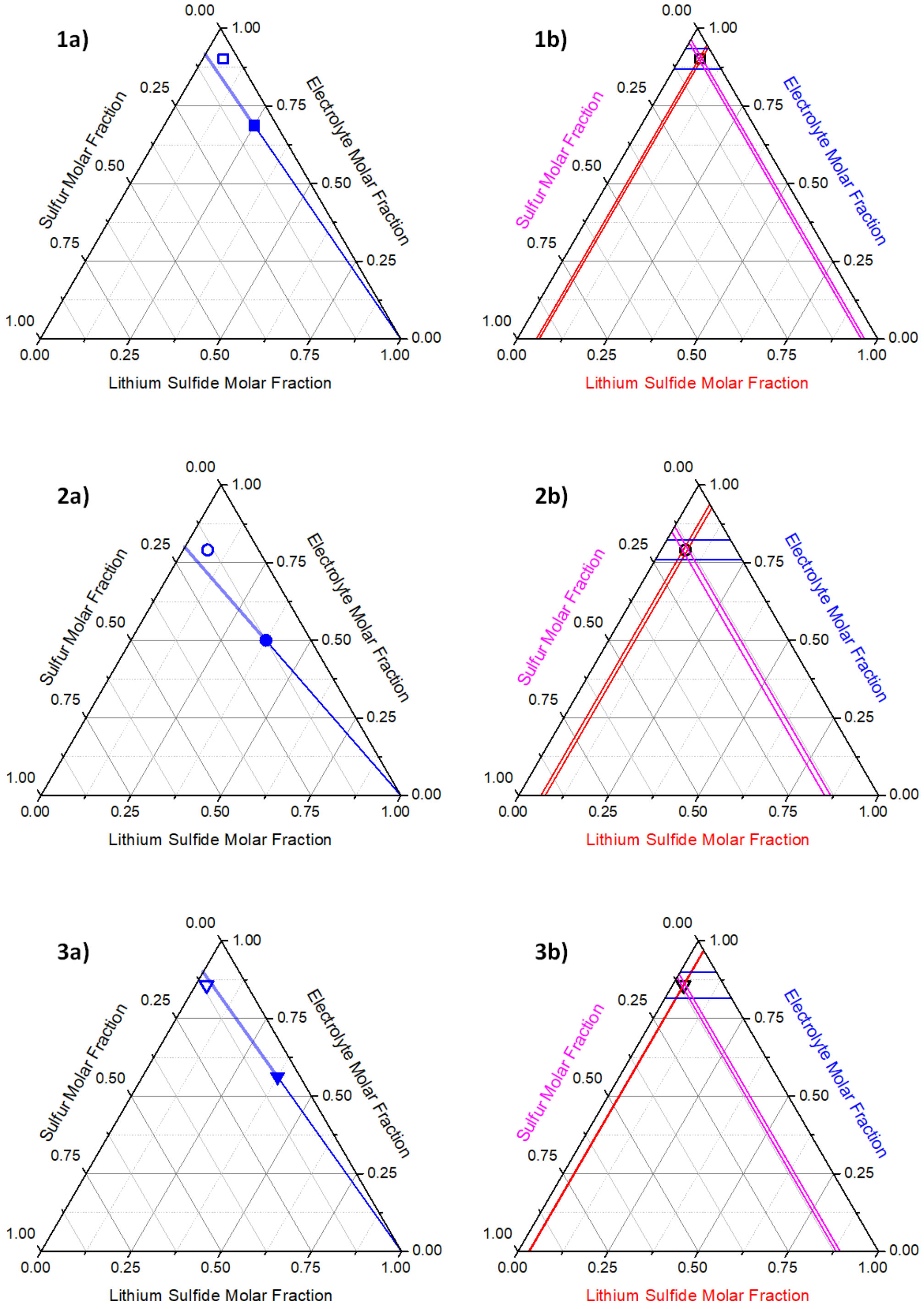

Figure 3.8.4 – Phase diagrams of the right 2-phase boundary PS solutions. 1a) is the "$[S]_T^{Sol.}$ = 5.25 M, $Li_2S_{1.25}$" blend (blue filled square) and filtered solution (blue empty square). 1b) is the respective errors for the "$[S]_T^{Sol.}$ = 5.25 M, $Li_2S_{1.25}$" filtered solution. 2a) is the "$[S]_T^{Sol.}$ = 10.25 M, $Li_2S_{1.3}$" blend (blue filled square) and filtered solution (blue empty square). 2b) is the respective errors for the "$[S]_T^{Sol.}$ = 10.25 M, $Li_2S_{1.3}$" filtered solution. 3a) is the "$[S]_T^{Sol.}$ = 8.2 M, $Li_2S_{1.17}$" blend (blue filled square) and filtered solution (blue empty square). 3b) is the respective errors for the "$[S]_T^{Sol.}$ = 8.2 M, $Li_2S_{1.17}$" filtered solution.

However, when you consider the errors for the molar fractions the right 2-phase boundary polysulfide solutions are in line with the extrapolated line. This difference could also be due to the method of determining the position of the blend on the phase diagram not being accurate, since the density of the blend is not known. Therefore, assumptions have to be made for the polysulfide solution density such as the density of lithium sulfide and sulfur solid is the same as their density when they are dissolved into the electrolyte. What is more concerning is the difference in position of “$[S]_T^{Sol.}$ = 8.2 M, $Li_2S_{1.17}$” compared to “$[S]_T^{Sol.}$ = 5.25 M, $Li_2S_{1.25}$” and “$[S]_T^{Sol.}$ = 10.25 M, $Li_2S_{1.3}$” polysulfide solution data points. This suggests that the right 2-phase boundary is not as reliable as the left 2-phase boundary because of this variance.

To get an idea of where the left 2-phase boundary is located on the phase diagram, cubic spline interpolation was used to fit the polysulfide solution data points. Cubic spline interpolation is a method of constructing new data points within a range of known data points. In the case of the phase diagram this means fitting a curve to the experimentally determined points on the phase diagram.

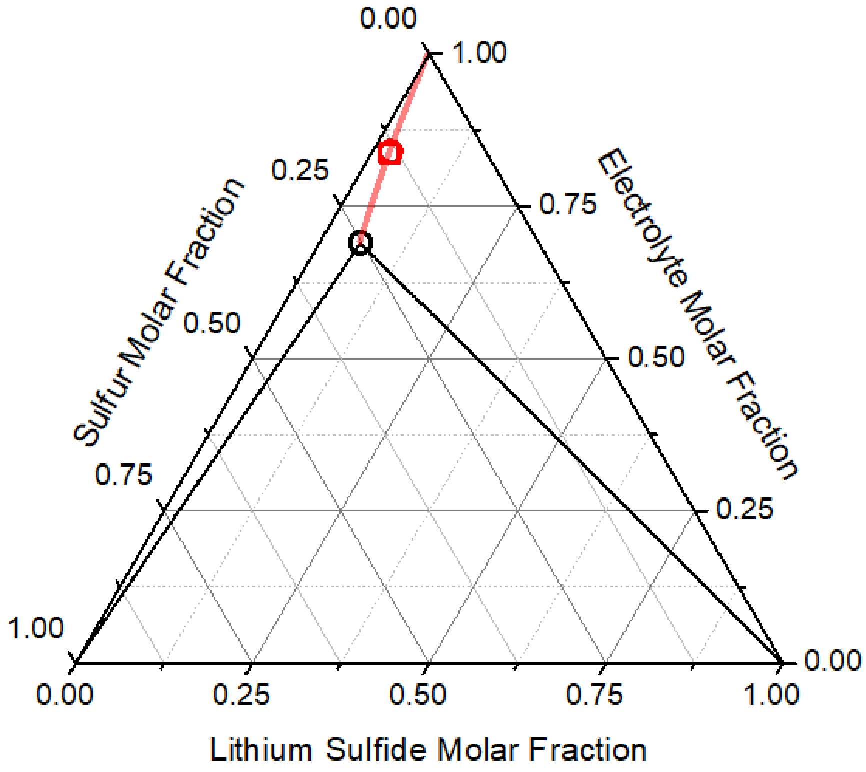

Figure 3.8.5 – Cubic spline interpolation of average eutonic point (black circle), “$[S]_T^{Sol.}$ = 5.7 M, $Li_2S_{12.8}$” (red square), “$[S]_T^{Sol.}$ = 5.2 M, Li_2S_{12}” (red circle) and point (0,1,0) for the 1 M LiTFSI in DOL electrolyte.

A cubic spline interpolation of the average eutonic point, the "$[S]_T^{Sol.}$ = 5.7 M, $Li_2S_{12.8}$" polysulfide solution, the "$[S]_T^{Sol.}$ = 5.2 M, Li_2S_{12}" polysulfide solution and the top of the phase diagram was used to define the left 2-phase boundary (Figure 3.8.5). For the interpolation, it was assumed that the solubility of pure lithium or pure sulfur in electrolyte is zero so that the interpolated curve would end at the top of the phase diagram. This assumption is reasonable because the solubility of pure lithium sulfide and sulfur in electrolyte is very low.[83]

A cubic spline interpolation of the average eutonic point, the "$[S]_T^{Sol.}$ = 8.2 M, $Li_2S_{1.17}$" polysulfide solution and the top of the phase diagram was used to define the right 2-phase boundary (Figure 3.8.6).

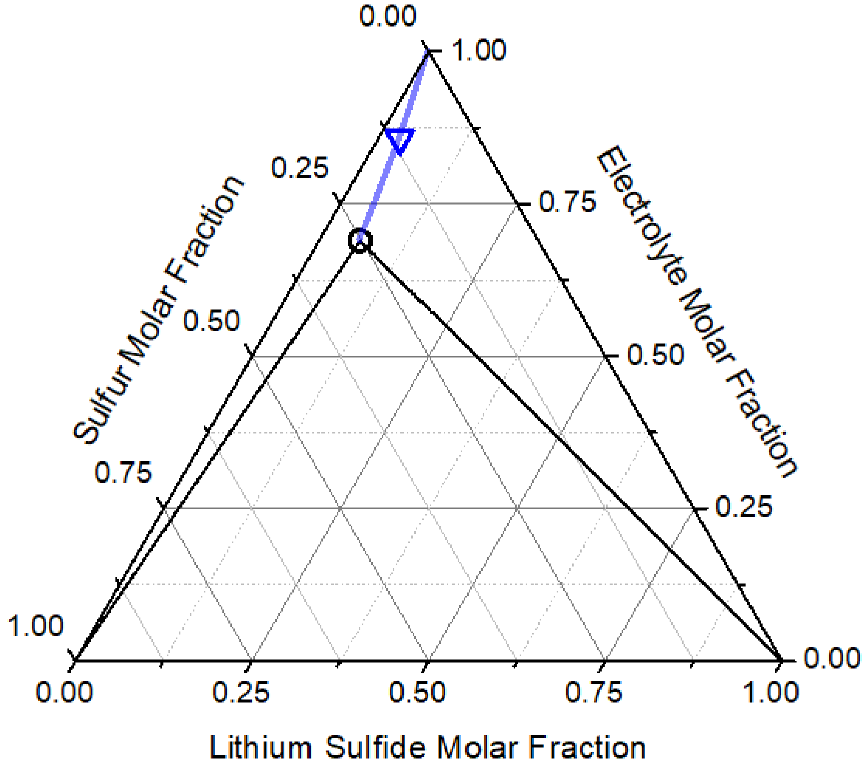

Figure 3.8.6 – Cubic spline interpolation of average eutonic point (black circle), "$[S]_T^{Sol.}$ = 8.2 M, $Li_2S_{1.17}$" (blue upside-down triangle) and point (0,1,0) for the 1 M LiTFSI in DOL electrolyte.

The right 2-phase boundary from the "$[S]_T^{Sol.}$ = 8.2 M, $Li_2S_{1.17}$" polysulfide solution differs from the boundary from the cubic spline interpolation of the average eutonic point, the "$[S]_T^{Sol.}$ = 5.25 M, $Li_2S_{1.25}$" polysulfide solution, the "$[S]_T^{Sol.}$ = 10.25 M, $Li_2S_{1.3}$" polysulfide solution and the top of the phase diagram (Figure 3.8.7).

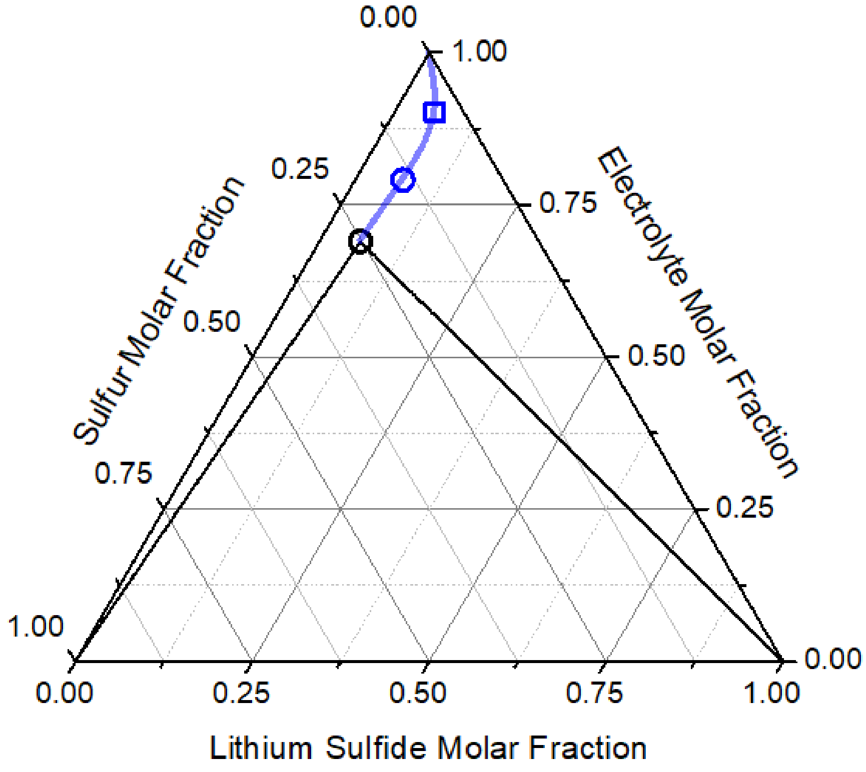

Figure 3.8.7 – Cubic spline interpolation of average eutonic point (black circle), “$[S]_T^{Sol.}$ = 5.25 M, $Li_2S_{1.25}$” (blue square), “$[S]_T^{Sol.}$ = 10.25 M, $Li_2S_{1.3}$” (blue circle) and point (0,1,0) for the 1 M LiTFSI in DOL electrolyte.

This shows that there is significant uncertainty in the right 2-phase boundary which could be due to experimental errors such as the solution composition was not exactly the equilibrium solution composition of the blend. For example, inhomogeneous mixing of the polysulfide blend could produce a solution that is not at equilibrium. This issue can be solved by repeat experiments, producing more 2-phase boundary solutions to map out a more reliable right 2-phase boundary.

The phase diagram (Figure 3.8.7), determines the interpolated curve from two experimental data points instead of one (Figure 3.8.6). Therefore, I will assume that it is the more reliable and accurate depiction of the right 2-phase boundary. Combining the two 2-phase boundary phase diagrams (Figure 3.8.5 & Figure 3.8.7) together results in a complete ternary phase diagram for the 1 M LiTFSI in DOL electrolyte (Figure 3.8.8).

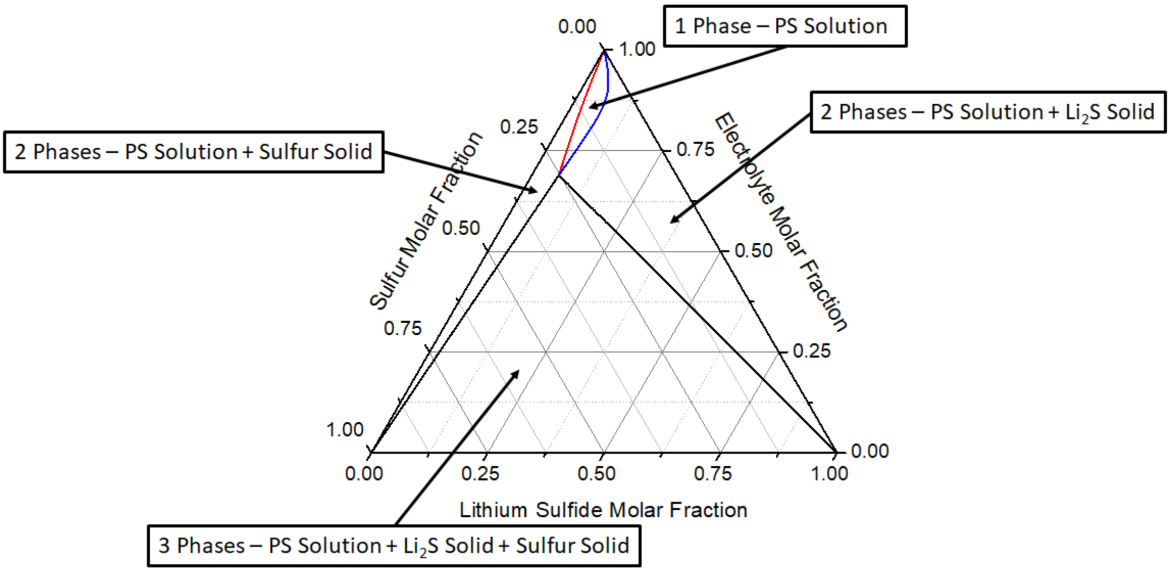

Figure 3.8.8 – Combination of figures 3.8.5 and 3.8.7 producing a complete ternary phase diagram for the 1 M LiTFSI in DOL electrolyte.

From the eutonic point to the saturation point of just lithium sulfide in the electrolyte along the right 2-phase boundary, the total atomic sulfur concentration decreases when the polysulfide chain length decreases from $Li_2S_{5.4}$ to Li_2S_2. Likewise with the left 2-phase boundary, the total atomic sulfur concentration also decreases whilst the polysulfide chain length increases from $Li_2S_{5.4}$ to Li_2S_6 and compositions approaching Li_2S_8. Therefore the average polysulfide chain lengths higher and lower than the composition of the eutonic point (n = 5.4) have a lower polysulfide solubility in the electrolyte. This is caused by the fact these solutions are in the 2-phase region and only saturated in lithium sulfide or sulfur. Therefore adding more sulfur to the electrolyte saturated with just lithium sulifde will increase the solubility of the lithium suflide (and vice versa). This shows the rich variety of polysulfide species that can be formed in the 1-phase region with the caveat of limited concentration and that the highest solubility in the electrolyte was obtained with an average composition equivalent to $Li_2S_{5.4}$.

Further work is required to get more accurate and reliable 2-phase boundaries, especially the 2-phase boundary to the right of the eutonic point because the current 2-phase boundaries are based on a couple of data points. Compare this to the determination of the eutonic point, where there are several experiments corroborating the same result. This can be resolved by repeat experiments, optimising the preparation and filtration of the 2-phase polysulfide blends ensuring the solution is at equilibrium. This could be achieved by producing more solutions in the 2-phase region where they are only saturated in lithium sulfide or sulfur. After filtration and analysis this will provide a higher number of data points for the interpolation curve which describes the 2-phase boundary. This will give accurate depiction of solubility of different polysulfide species at their saturation concentration whilst also describing the amount of lithium sulfide and sulfur precipitation.

3.9 Electrolyte Concentration Effect Phase Diagram

Using the well-developed procedures and analytical techniques used to produce the ternary phase diagram for the 1 M LiTFSI in DOL electrolyte, the same experiments were applied to determine the total atomic sulfur concentration and polysulfide chain length for polysulfide solutions with different electrolyte concentrations. The electrolyte concentrations that were chosen were 0.5 M and 2 M LiTFSI in DOL.

To obtain eutonic points for the two different electrolyte concentrations, polysulfide blends were prepared so that they would be saturated in both lithium sulfide and sulfur.

The desired masses of lithium sulfide and sulfur were added to a vial and the 0.5 M electrolyte (Table 3.9.1) or 2 M electrolyte (Table 3.9.3) was added. The density, total atomic sulfur concentration and polysulfide concentration were determined for the 0.5 M electrolyte (Table 3.9.2) and 2 M electrolyte (Table 3.9.4).

Polysulfide Blend	Theoretical Li_2S Mass / g	Experimental Li_2S Mass / g	Theoretical Sulfur Mass / g	Experimental Sulfur Mass / g	Theoretical Electrolyte Mass / g	Experimental Electrolyte Mass / g
“$[S]_T^{Sol.}$ = 10 M, Li_2S_4”	1.1488	1.1491	2.4049	2.4174	11.3001	11.1694
“$[S]_T^{Sol.}$ = 10 M, Li_2S_6”	0.7658	0.7739	2.6721	2.6898	11.2990	11.2584
“$[S]_T^{Sol.}$ = 10 M, Li_2S_8”	0.5744	0.5783	2.8057	2.8173	11.2990	11.0988

Table 3.9.1 – Theoretical and experimental masses of lithium sulfide, sulfur and electrolyte (0.5 M LiTFSI in DOL) required to prepare the saturated polysulfide blends.

Polysulfide Blend	Density / g mL^{-1}	$[S]_T^{Sol.}$ / M	$[S_n^{2-}]$ / M	Polysulfide Chain Length	Sulfur Oxidation State
“$[S]_T^{Sol.}$ = 10 M, Li_2S_4”	1.32 ± 0.15	9.6 ± 1.5	1.86 ± 0.52	5.2 ± 1.7	0.39 ± 0.12
“$[S]_T^{Sol.}$ = 10 M, Li_2S_6”	1.308 ± 0.047	8.33 ± 0.32	1.20 ± 0.23	6.9 ± 1.3	0.288 ± 0.055
“$[S]_T^{Sol.}$ = 10 M, Li_2S_8”	1.282 ± 0.046	7.92 ± 0.31	1.17 ± 0.19	6.8 ± 1.1	0.296 ± 0.049
Average	1.303 ± 0.045	8.6 ± 2.2	1.41 ± 0.96	6.3 ± 2.4	0.32 ± 0.13

Table 3.9.2 – Experimentally determined density, total atomic sulfur concentration, polysulfide concentration, polysulfide chain length and average oxidation state of sulfur for the 0.5 M LiTFSI in DOL electrolyte eutonic point polysulfide solutions. Errors from averaged values correspond to a confidence interval at a 95 % confidence level from repeat experiments.

Polysulfide Blend	Theoretical Li_2S Mass / g	Experimental Li_2S Mass / g	Theoretical Sulfur Mass / g	Experimental Sulfur Mass / g	Theoretical Electrolyte Mass / g	Experimental Electrolyte Mass / g
“$[S]_T^{Sol.}$ = 10 M, Li_2S_4”	1.1488	1.1520	2.4049	2.4105	13.4155	13.1961
“$[S]_T^{Sol.}$ = 10 M, Li_2S_6 – 1”	0.7658	0.7646	2.6721	2.6697	13.3927	13.0161
“$[S]_T^{Sol.}$ = 10 M, Li_2S_6 – 2”	0.7658	0.7669	2.6721	2.6815	13.4256	13.1332
“$[S]_T^{Sol.}$ = 10 M, Li_2S_8 – 1”	0.5744	0.5759	2.8057	2.8036	13.3927	13.1173
“$[S]_T^{Sol.}$ = 10 M, Li_2S_8 – 2”	0.5744	0.5994	2.8057	2.9135	13.3387	13.1136
“$[S]_T^{Sol.}$ = 10 M, Li_2S_8 – 3”	0.5744	0.6280	2.8057	2.8886	13.3387	13.0291
“$[S]_T^{Sol.}$ = 10 M, Li_2S_8 – 4”	0.5744	0.5758	2.8057	2.8126	13.4256	13.1606

Table 3.9.3 – Theoretical and experimental masses of lithium sulfide, sulfur and electrolyte (2 M LiTFSI in DOL) required to prepare the saturated polysulfide blends.

Polysulfide Blend	Density / g mL^{-1}	$[S]_T^{Sol.}$ / M	$[S_n^{2-}]$ / M	Polysulfide Chain Length	Sulfur Oxidation State
"$[S]_T^{Sol.}$ = 10 M, Li_2S_4"	1.45 ± 0.17	0.90 ± 0.14	0.111 ± 0.027	8.2 ± 2.3	0.245 ± 0.070
"$[S]_T^{Sol.}$ = 10 M, Li_2S_6 – 1"	1.445 ± 0.079	1.077 ± 0.067	0.234 ± 0.024	4.59 ± 0.55	0.436 ± 0.052
"$[S]_T^{Sol.}$ = 10 M, Li_2S_6 – 2"	1.43 ± 0.17	0.93 ± 0.14	0.1824 ± 0.0078	5.09 ± 0.80	0.393 ± 0.062
"$[S]_T^{Sol.}$ = 10 M, Li_2S_8 – 1"	1.420 ± 0.051	1.643 ± 0.064	0.304 ± 0.023	5.40 ± 0.45	0.370 ± 0.031
"$[S]_T^{Sol.}$ = 10 M, Li_2S_8 – 2"	1.404 ± 0.050	0.990 ± 0.038	0.194 ± 0.016	5.11 ± 0.46	0.392 ± 0.035
"$[S]_T^{Sol.}$ = 10 M, Li_2S_8 – 3"	1.402 ± 0.050	1.043 ± 0.040	0.201 ± 0.017	5.19 ± 0.49	0.385 ± 0.036
"$[S]_T^{Sol.}$ = 10 M, Li_2S_8 – 4"	1.40 ± 0.16	1.31 ± 0.20	0.149 ± 0.018	8.8 ± 1.7	0.228 ± 0.044
Average	1.423 ± 0.019	1.13 ± 0.24	0.196 ± 0.057	6.0 ± 1.6	0.350 ± 0.074

Table 3.9.4 – Experimentally determined density, total atomic sulfur concentration, polysulfide concentration, polysulfide chain length and average oxidation state of sulfur for the 2 M LiTFSI in DOL electrolyte eutonic point polysulfide solutions. Errors from averaged values correspond to a confidence interval at a 95 % confidence level from repeat experiments.

For the 0.5 M electrolyte the average species is $[S]_T^{Sol.}$ = 8.6 ± 2.2 M, $Li_2S_{6.3 \pm 2.4}$ compared to the 1 M electrolyte average species $[S]_T^{Sol.}$ = 5.55 ± 0.50 M, $Li_2S_{5.41 \pm 0.43}$. Therefore decreasing the electrolyte concentration from 1 M to 0.5 M, the total sulfur concentration increases. The polysulfide chain length remains relatively similar between the two electrolyte concentrations.

For the 2 M electrolyte the average species is $[S]_T^{Sol.}$ = 1.13 ± 0.24 M, $Li_2S_{6.0 \pm 1.6}$ compared to the 1 M electrolyte average species $[S]_T^{Sol.}$ = 5.55 ± 0.50 M, $Li_2S_{5.41 \pm 0.43}$. Therefore increasing the electrolyte concentration from 1 M to 2 M, the total sulfur concentration decreases. The polysulfide chain length again remain relatively similar between the two electrolyte concentrations.

The results for the 0.5 M and 2 M electrolyte results are not as precise as the 1 M electrolyte as shown by the errors being larger than 10 %. In the case of 0.5 M electrolyte, there were fewer solutions prepared. However the composition determined by elemental analysis was $[S]_T^{Sol.}$ = 8.15 ± 0.60 M, $Li_2S_{6.09 \pm 0.45}$ which is similar to the experimentally determined values showing the reliability of these results. The electrolyte concentration determined from elemental analysis was 0.530 ± 0.086 M that is similar to the initially prepared 0.5 M meaning these results are relevant to the 0.5 M phase diagram.

The 2 M electrolyte saturated polysulfide solution uncertainties are larger than the 1 M electrolyte because of the relatively small amounts of polysulfide solution remaining after filtration. This was due to the ratio of undissolved solid to polysulfide solution in the blend being too high. Meaning, trying to prepare a $[S]_T^{Sol.}$ = 10 M polysulfide blend for the 2 M electrolyte where the maximum sulfur concentration is approximately 1 M, there will be a lot of undissolved solid to separate from the saturated polysulfide solution. Therefore smaller quantities of solution had to be used for the analysis which lead to larger errors. Now with the knowledge of the total sulfur concentration of the 2 M electrolyte, I would prepare a less concentrated blend such as $[S]_T^{Sol.}$ = 5 M so that I can still be confident the position of the blend on the phase diagram is well within the 3-phase region and it should be more successful at obtaining a higher yield of saturated polysulfide solution. The low yield of the 2 M electrolyte saturated polysulfide solutions also meant that elemental analysis could not be performed on the solution. This meant there was no reference to check the accuracy for the values obtained from experimental analysis.

From the experimentally determined saturated polysulfide solution density, total atomic sulfur concentration, polysulfide concentration and polysulfide chain length values for the 0.5 M electrolyte (Table 3.9.2), the molar fractions of lithium sulphide, sulfur and electrolyte were calculated for the ternary phase diagram (Table 3.9.5).

Polysulfide Blends	$\mathrm{MF_{Li_2S}}$	$\mathrm{MF_{Electrolyte}}$	$\mathrm{MF_{Sulfur}}$
"$[S]_T^{Sol.}$ = 10 M, Li_2S_4"	0.086 ± 0.024	0.55 ± 0.13	0.359 ± 0.071
"$[S]_T^{Sol.}$ = 10 M, Li_2S_6"	0.058 ± 0.011	0.600 ± 0.057	0.342 ± 0.019
"$[S]_T^{Sol.}$ = 10 M, Li_2S_8"	0.0578 ± 0.093	0.610 ± 0.051	0.332 ± 0.018
Average	0.067 ± 0.040	0.588 ± 0.073	0.345 ± 0.034

Table 3.9.5 – Table of molar fractions of lithium sulfide, sulfur and electrolyte for the 0.5 M LiTFSI in DOL electrolyte eutonic point. Errors from averaged values correspond to a confidence interval at a 95 % confidence level from repeat experiments.

The averaged molar fractions from experimental results for the 0.5 M electrolyte saturated polysulfide solution was plotted into a ternary phase diagram to elucidate the position of the eutonic point (Figure 3.9.1).

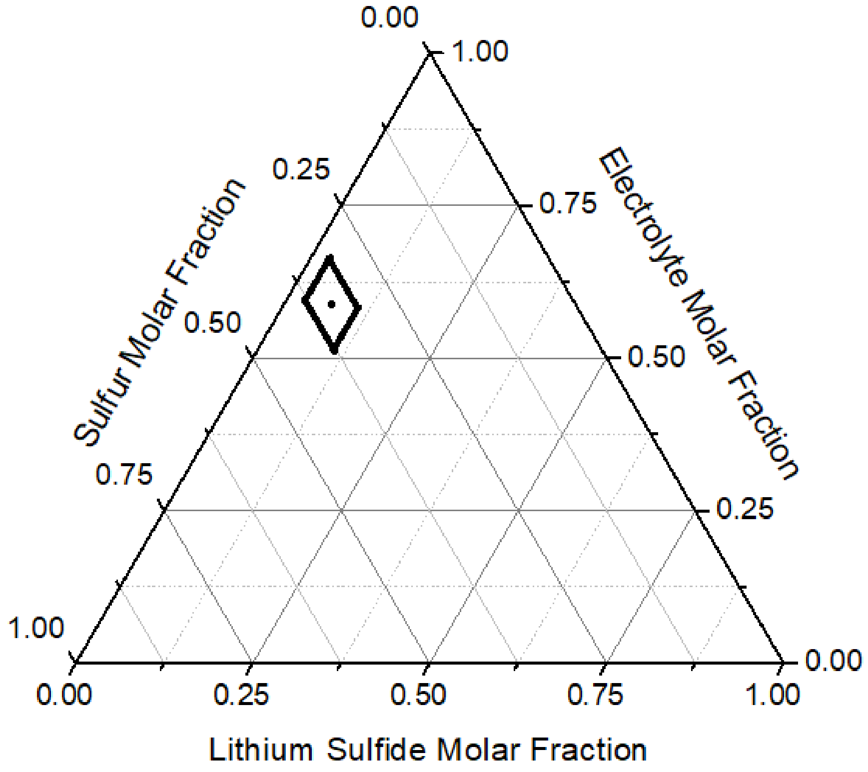

Figure 3.9.1 – Experimental ternary phase diagram of averaged eutonic point from the 0.5 M LiTFSI in DOL electrolyte saturated polysulfide solutions (black point) with the region of error described by the black diamond.

From the experimentally determined saturated polysulfide solution density, total atomic sulfur concentration, polysulfide concentration and polysulfide chain length values for the 2 M electrolyte (Table 3.9.4), the molar fractions of lithium sulphide, sulfur and electrolyte were calculated for the ternary phase diagram (Table 3.9.6).

Polysulfide Blends	$\mathrm{MF}_{\mathrm{Li_2S}}$	$\mathrm{MF}_{\mathrm{Electrolyte}}$	$\mathrm{MF}_{\mathrm{Sulfur}}$
“$[S]_T^{Sol.}$ = 10 M, Li_2S_4”	0.0079 ± 0.0019	0.94 ± 0.18	0.0567 ± 0.0100
“$[S]_T^{Sol.}$ = 10 M, Li_2S_6 – 1”	0.0167 ± 0.0017	0.923 ± 0.084	0.0600 ± 0.0050
“$[S]_T^{Sol.}$ = 10 M, Li_2S_6 – 2”	0.01321 ± 0.00056	0.93 ± 0.18	0.054 ± 0.010
“$[S]_T^{Sol.}$ = 10 M, Li_2S_8 – 1”	0.0214 ± 0.0016	0.884 ± 0.054	0.0944 ± 0.0048
“$[S]_T^{Sol.}$ = 10 M, Li_2S_8 – 2”	0.0143 ± 0.0012	0.927 ± 0.055	0.0585 ± 0.0031
“$[S]_T^{Sol.}$ = 10 M, Li_2S_8 – 3”	0.0148 ± 0.0013	0.923 ± 0.055	0.0619 ± 0.0032
“$[S]_T^{Sol.}$ = 10 M, Li_2S_8 – 4”	0.0108 ± 0.0013	0.91 ± 0.17	0.084 ± 0.014
Average	0.0141 ± 0.0040	0.919 ± 0.017	0.067 ± 0.014

Table 3.9.6 – Table of molar fractions of lithium sulfide, sulfur and electrolyte for the 2 M LiTFSI in DOL electrolyte eutonic point. Errors from averaged values correspond to a confidence interval at a 95 % confidence level from repeat experiments.

The averaged molar fractions from experimental results for the 2 M electrolyte saturated polysulfide solution were plotted into a ternary phase diagram to elucidate the position of the eutonic point (Figure 3.9.2).

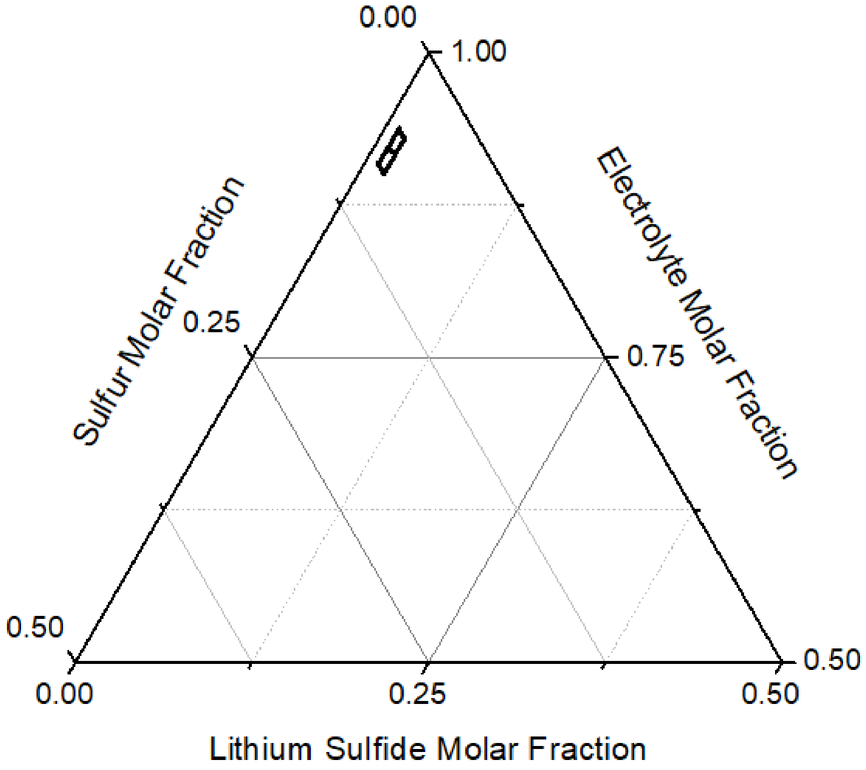

Figure 3.9.2 – Zoomed in experimental ternary phase diagram of averaged eutonic point from the 2 M LiTFSI in DOL electrolyte saturated polysulfide solutions (black point) with the region of error described by the black diamond.

Combining the eutonic point phase diagrams (Figure 3.6.3, Figure 3.9.1 & Figure 3.9.2) the trend of the total sulfur concentration and the polysulfide chain length with respect to the electrolyte concentration can be observed (Figure 3.9.3).

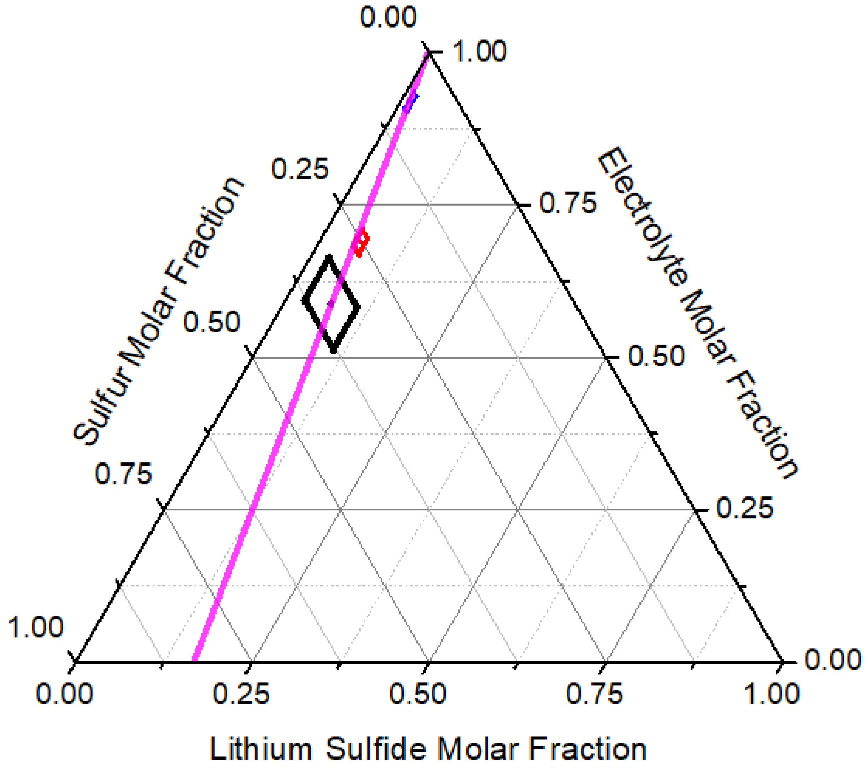

Figure 3.9.3 – Phase diagram showing the relationship between the LiTFSI concentration, the average polysulfide chain length and total sulfur concentration with their respective errors. Black – 0.5 M LiTFSI in DOL, red – 1 M LiTFSI in DOL, blue – 2 M LiTFSI in DOL and magenta line – average chain length.

Firstly, the magenta line in the phase diagram represents the polysulfide species $Li_2S_{5.8}$ at any concentration. The chain length of 5.8 ± 0.6 was determined from the average chain length across the three electrolyte concentrations. This line intersects with all three electrolyte concentration eutonic points. This suggests that the most soluble polysulfide species has an average composition equivalent to Li_2S_6 and is independent of the electrolyte concentration.

Secondly, the position of the eutonic point on the phase diagram appears higher with the higher concentration electrolytes. The y-axis of the ternary phase diagram is the molar fraction of electrolyte, therefore the higher concentration electrolyte eutonic points appear higher on the phase diagram since a larger proportion of the saturated solution will come from the electrolyte salt. There is an inversely proportional relationship between the total sulfur concentration and the electrolyte concentration (Figure 3.9.4).

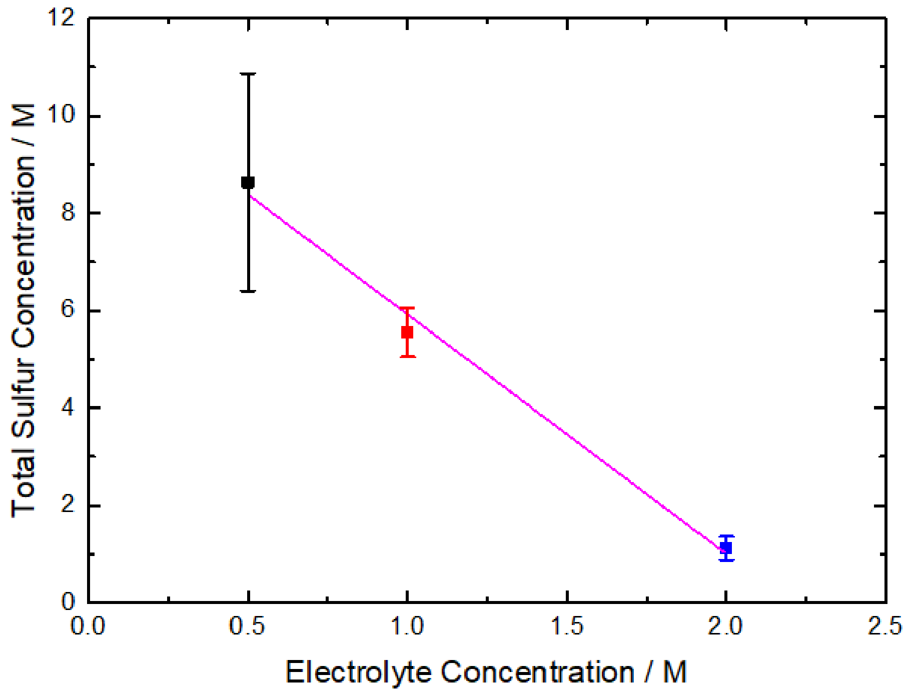

Figure 3.9.4 – The correlation between the electrolyte concentration and the averaged total sulfur concentration (magenta line – line of best fit).

The downwards trend of the total sulfur concentration decreasing with the electrolyte concentration as predicted from the common ion effect was observed. Even with the relatively large errors from the analysis of the 0.5 M and 2 M electrolyte saturated polysulfide solutions there is no overlap between the different eutonic points. To examine this relationship, regression analysis was performed (Table 3.9.7).

Gradient	- 4.77 ± 0.52
Intercept	10.57 ± 0.74 M
R^2	0.9601

Table 3.9.7 – Regression analysis results for figure 3.9.4.

From the regression analysis, the highest theoretical total sulfur concentration in a 0 M electrolyte (i.e. DOL) is $[S]_T^{Sol.}$ = 10.57 ± 0.74 M and the electrolyte salt concentration at which no polysulfide species would be present in the electrolyte is 2.22 ± 0.29 M. The R^2 value is very close to 1 which would normally suggest a linear relationship. However, I think more eutonic points for different electrolyte salt concentrations, such as 1.5 M, have to be determined before I could feel confident on commenting if this is a linear relationship.

Overall the phase diagram (Figure 3.9.3) shows the correlation between electrolyte salt concentration and the polysulfide concentration, the higher the electrolyte salt concentration the lower the polysulfide solubility. Improvements to the preparation of the eutonic point blends need to be made to increase the yield of the eutonic point saturated solutions to reduce the uncertainties in the analysis and to do elemental analysis of the 2 M electrolyte saturated eutonic point solution to check the accuracy. Further work is required to fully understand the type of trend, linear or quadratic, between the electrolyte salt concentration and the total sulfur concentration. Looking at saturated polysulfide solutions with electrolyte salt concentrations below 0.5 M and above 2 M could predict the extent of polysulfide shuttling within a Li-S battery which will be dependent on the electrolyte salt concentration.

3.10 Electrolyte Concentration Effect on Battery Performance

As discussed previously an important problem with Li-S batteries being used for energy storage is the self-discharge due to the polysulfide shuttle. Different charging/discharging regimes, different salts, solvents, etc. can all be optimised which will affect the stability of the battery. Therefore using the same electrolyte compositions used for the phase diagram study of the electrolyte concentration effect, galvanostatic cycling was used to study the effect of the 0.5 M, 1 M and 2 M LiTFSI in DOL electrolytes (Molality – 0.44 mol $kg^{-1}_{solvent}$, 0.84 mol $kg^{-1}_{solvent}$ and 1.5 mol $kg^{-1}_{solvent}$) on the battery performance.

The Swagelok cell setup was chosen as a "principal comparison lab cell" instead of a commercial setup such as a multilayer pouch cell (Figure 3.10.1).[84] There is a lot more to consider to get good battery performance for multilayer pouch cells such as electrode layout, electrode coating procedure, a reduced electrolyte excess required to achieve a relevant specific energy, a lower lithium excess and stack pressure.[84] Even with these differences the trend between the electrolyte concentration and battery performance should be the same. The higher electrolyte concentrations will still have a lower polysulfide solubility. This is an intrinsic property of the electrolyte that will not be affected by the cell configuration. However I would expect the absolute values of the capacity and the rate of capacity fade for a commercial cell to be different to the Swagelok cell.

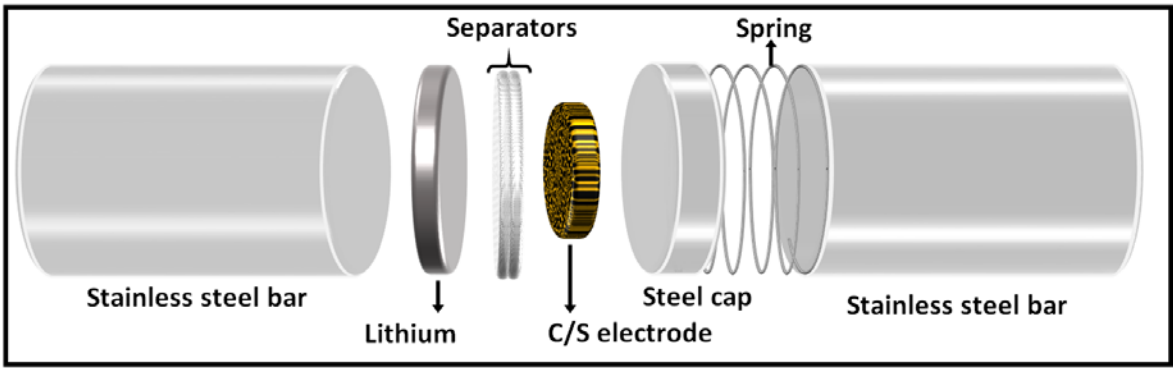

Figure 3.10.1 – Schematic of the 1-inch Swagelok cell setup for GCPL containing lithium anode, two glass fibre separators wetted with electrolyte and C/S electrode with 24 wt.% sulfur.

For each electrolyte salt concentration, three cells were cycled at rate of C/5 for discharge (Figure 3.10.2) and C/5 for charge (Figure 3.10.3).[39] From the discharge capacity graph, the 1 M electrolyte had the highest initial discharge capacity of approximately 1200 mA h g^{-1} followed by the 0.5 M electrolyte and then the 2 M electrolyte. The 2 M electrolyte has the lowest initial discharge capacity due to limited solubility of polysulfides in the electrolyte. These polysulfides can act as redox mediators improving the utilization of sulfur in the cathode and increasing the capacity as seen for the 1 M electrolyte.[20] This order changes very quickly over the first 25 cycles due to the significant rate of capacity fade with the 0.5 M and 1 M electrolytes. The capacity fade rate is slower for the 2 M electrolyte. One interesting observation is the 1 M and 2 M electrolytes have more reproducible results than the 0.5 M electrolyte, suggesting the 0.5 M electrolyte cells are being affected more by the polysulfide shuttle. The 0.5 M electrolyte cells also have the highest rate of capacity fade initially. An interesting observation of the 0.5 M electrolyte cells was the different stages in the discharge profile. Two of the cells capacity fade rate reduced between cycle 10 and 75. However by cycle 100 the discharge capacities of these two cells were the same as the lowest performing cell. The cause of this feature is unknown and therefore further work is required to make sure this phenomena is real and doesn’t come from differences in cell configuration.

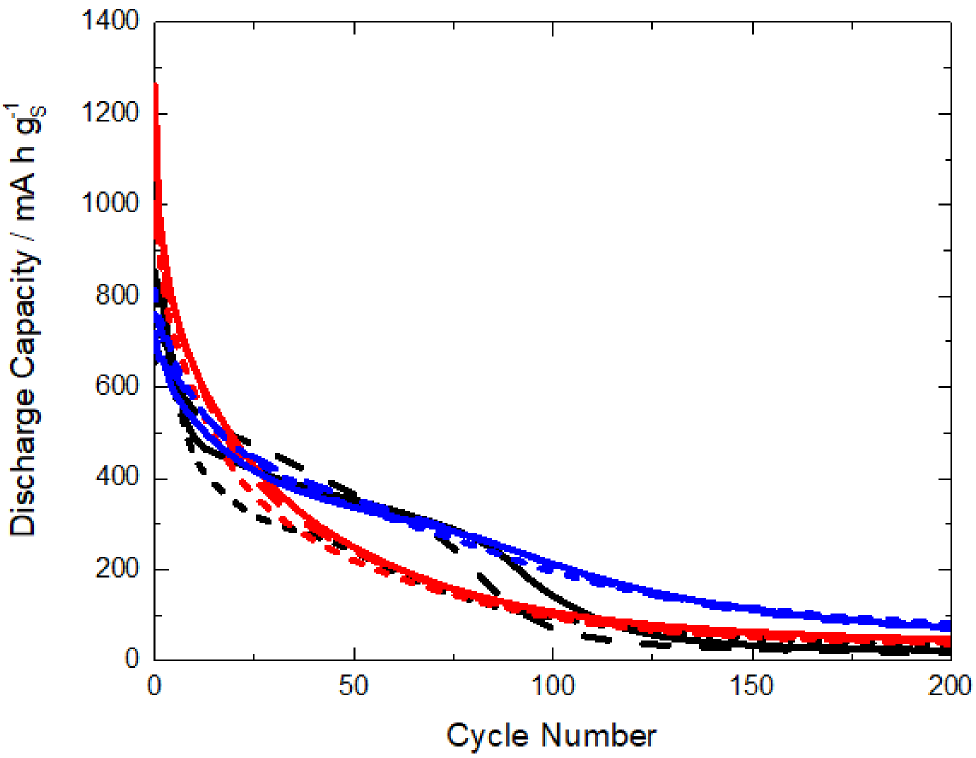

Figure 3.10.2 – Discharge capacities at C/5 rate (i.e. I = 330 mA g^{-1}_S) of Li vs. C/S (24 wt.% sulfur) Swagelok cells, each containing different concentrations of LiTFSI in DOL electrolyte (0.5 M – black, 1 M – red and 2 M – blue) repeated three times. Cycling potential limits of 1.5 to 2.6 V.[39] Capacities are normalised to the mass of sulfur (g_S) in the cathode.

In the first 100 cycles, the discharge capacity decreases by 87 % for 0.5 M, 91 % for 1 M and 73 % for 2 M. Even though the decrease in discharge capacity is greater for the 1 M electrolyte cell compared to the 0.5 M electrolyte cell, the absolute value of the discharge capacity is still higher for the 1 M electrolyte cell. After 100 cycles, the order of the three electrolyte concentrations remain constant. I have only displayed the first 200 cycles but there are no significant changes in the discharge capacity of the cell between 200 to 500 cycles. Overall increasing the electrolyte concentration results in a more consistent and slower capacity fade and a longer cell life. This phenomena would remain the case for commercial cells because the relationship between the electrolyte salt concentration and polysulfide solubility is an intrinsic property of the electrolyte. Therefore even under the stricter conditions required for good performance of a pouch cell such as low electrolyte/sulfur ratios, a higher electrolyte salt concentration will reduce the polysulfide shuttle.

From the charge capacity graph, the 0.5 M and 1 M electrolyte cells have the highest initial capacity of approximately 1200 mA h g^{-1} compared to the 2 M electrolyte cell with an initial capacity of approximately 800 mA h g^{-1} (Figure 3.10.3). As seen in the discharge profile (Figure 3.10.2) of two of the 0.5 M electrolyte cells, there are different stages in the charge profile. They have a slower rate of capacity fade up to cycle 75. However by cycle 100 the charge capacities of these two cells were the same as the lowest performing cell. Further work is required to make sure this phenomena is not caused by the poor reproducibility of the cell. Increasing the electrolyte concentration suppresses the polysulfide shuttling and therefore decreases the charge capacity and improves the coulombic efficiency. This means the lower electrolyte salt concentrations have a superficially high charge capacities because of the polysulfide shuttle effect, which can be observed by their low coulombic efficiencies.

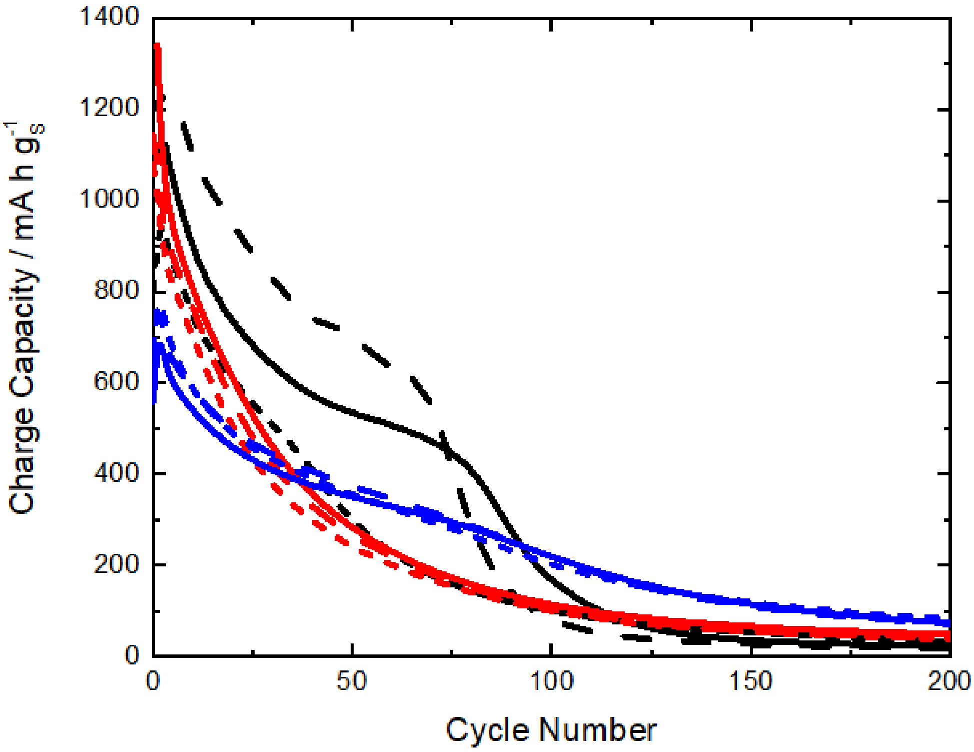

Figure 3.10.3 – Charge capacities at C/5 rate (i.e. I = 330 mA g$^{-1}_S$) of Li vs. C/S (24 wt.% sulfur) Swagelok cells, each containing different concentrations of LiTFSI in DOL electrolyte (0.5 M – black, 1 M – red and 2 M – blue) repeated three times. Cycling potential limits of 1.5 to 2.6 V.[39] Capacities are normalised to the mass of sulfur (g$_S$) in the cathode.

This trend continues for the first 100 cycles for the 0.5 M and 1 M electrolyte concentrations. This is due to the overcharging of the cell where the polysulfide shuttle effect is slowly discharging the cell as the cell is charging. This gives a superficially high value of the charge capacity for the 0.5 M and 1 M electrolyte cells. This feature is more obvious when the comparison is made between the coulombic efficiency and the cycle number (Figure 3.10.4). The fast capacity fade for the 0.5 M and 1 M electrolyte is also due to the polysulfide shuttle.

The coulombic efficiencies for the Li-S batteries containing the different concentration electrolytes were determined as follows;

$$\text{Coulombic Efficiency} = \frac{\text{Discharge Capacity}}{\text{Charge Capacity}} \qquad \text{Equation 3.10.1}$$

The coulombic efficiency for the 0.5 M electrolyte cells over the first 100 cycles is very low with minimum values of approximately 50 % compared to the minimum value of coulombic efficiencies for the 1 M and 2 M electrolyte cells of being approximately 80 % and 95 % respectively. After the first 100 cycles the coulombic efficiencies are above 90 % for all electrolyte concentrations, however this is less impressive when you consider the magnitude of the discharge and charge capacities from the batteries. Overall, the higher the electrolyte salt concentration, the higher the coulombic efficiency.

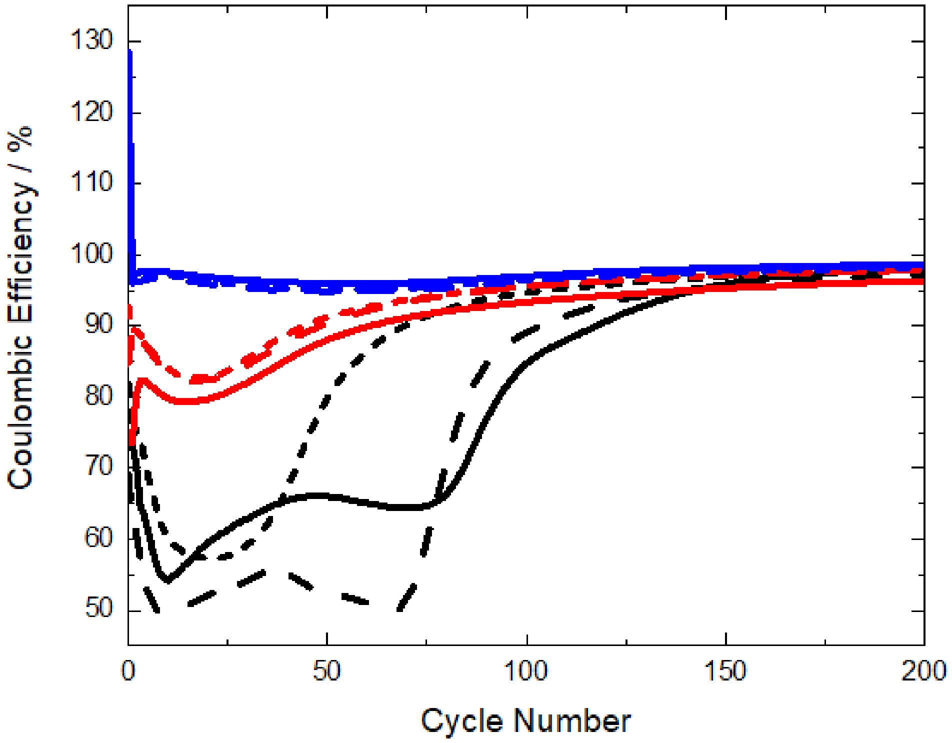

Figure 3.10.4 – Coulombic efficiency of Li vs. C/S (24 wt.% sulfur) Swagelok cells, each containing different concentrations of LiTFSI in DOL electrolyte (0.5 M – black, 1 M – red and 2 M – blue) repeated three times.

These results show the improved performance of the high concentration electrolytes are in agreement with Armand's report on solvent-in-salt electrolytes which they also attribute to the lower solubility of the polysulfide species.[39] This will cause lower concentrations of polysulfide in the electrolyte which reduces the potency of the polysulfide shuttle effect.

The aim was to make a simple system to study the electrolyte that was used for the phase diagram study. These results are successful in showing that a higher electrolyte salt concentration results in better coulombic efficiency and slower capacity fade with cycling due to the suppression of the polysulfide shuttling. This is in full agreement with the results of the analysis of the polysulfide solutions demonstrating a smaller solubility of the polysulfides with increasing the electrolyte salt concentration. However the negative effect of the higher electrolyte salt concentration is they have a poor rate capability due to the lower intermediate polysulfide concentration that can act as redox mediators. To get slower capacity fades similar to published values improvements to the electrode and electrolyte would have been needed.[39] The electrode preparation could be improved by using more advanced techniques such as sulfur impregnation into carbon nanotubes. The electrolyte could be improved by using additives such as lithium nitrate to suppress the polysulfide shuttle. However in the latter case, this would affect the electrolyte composition and it would no longer be representative of the electrolyte solutions used to prepare the phase diagram polysulfide solutions.

To conclude the phase diagram (Figure 3.9.3) which shows the change in the position of the eutonic point with respect to the electrolyte concentration can be quantitatively linked to the performance of the Li-S battery during galvanostatic cycling. The phase diagram (Figure 3.9.3) depicts the maximum solubility of the polysulfide species decreases with increasing electrolyte salt concentration. The lower polysulfide solubility reduces the polysulfide shuttle effect increasing the coulombic efficiency, cyclability and slower capacity fade of Li-S cells with high electrolyte salt concentrations. However, the low polysulfide concentrations limit the active material utilization as shown by the initially low initial charge and discharge capacities since the intermediate polysulfide species act as redox mediators.[20]

3.11 Conclusions

Overall, the procedure has been developed to determine total atomic sulfur concentration of polysulfide species and the average atomic sulfur oxidation state and the average chain length of polysulfide species in polysulfide solutions with repeatable accurate results. Therefore, the $BaSO_4$ gravimetric analysis and the UV-vis titration can be used to determine total atomic sulfur content and the polysulfide chain length for the saturated eutonic point polysulfide solutions and the 2-phase boundary polysulfide solutions.

For the eutonic point of the 1 M LiTFSI in DOL electrolyte, the average concentration and composition was determined to be approximately $[S]_T^{Sol.}$ = 5.6 M, $Li_2S_{5.4}$. This was obtained from a range of several different starting polysulfide blend compositions in the 3-phase region. This shows the reliability of the synthetic procedure to produce a saturated polysulfide solution. The accuracy of these results was also confirmed by elemental analysis.

The molar fractions of lithium sulphide, sulfur and electrolyte were calculated from the total sulfur and lithium polysulfide concentration of the saturated polysulfide solution to plot the eutonic point on the ternary phase diagram.

The preparation and analysis of the 2-phase boundaries polysulfide blends were successful in developing a technique to determine the 2-phase boundaries to the left and right of the eutonic point. With the phase diagram of the 1 M electrolyte eutonic point and the phase diagram of the 2-phase boundaries for the 1 M electrolyte, a complete phase diagram for the 1 M LiTFSI in DOL electrolyte was made. Further work will include the preparation and analysis of more polysulfide blends, especially for the right 2-phase boundary, to map out more of the boundary and to reduce the uncertainty in the position of the boundary.

Another phase diagram was made from the saturated eutonic point polysulfide solutions with 0.5 M and 2 M electrolyte salt concentrations. Further work is needed to reduce the uncertainty in the 0.5 M and 2 M eutonic points by repeat measurements. Preparing lower concentration polysulfide blends (i.e. less excess lithium sulfide solid and sulfur solid) for the 2 M electrolyte will increase the yield of saturated solution because it will be easier to filter the blend with less excess solid. This will allow elemental analysis on the saturated 2 M eutonic point polysulfide solution.

All three phase diagrams suggest that the average composition of the most soluble polysulfide species is Li_2S_6 which is independent of the electrolyte salt concentration and the reduced solubility of polysulfide species is related to electrolyte salt concentration.

Varying the concentration of the electrolyte gave expected results for the electrochemical testing of Li-S cells, where with higher electrolyte salt concentrations, the coulombic efficiency and cycling stability increases. This agrees with the solvent in salt theory that the high concentration of LiTFSI in the electrolyte lowers the solubility of polysulfide which reduces the polysulfide shuttle effect.[39] Therefore, the phase diagram quantitatively links the solubility of the polysulfide species in the electrolyte to the performance of a Li-S battery.

Other variables that would have an impact on the position of the eutonic point would be the temperature of the solution and different electrolyte solvents such as DOL/DME (1:1, volume ratio). I would hypothesise that temperatures above room temperature would promote a higher total atomic sulfur concentration for the eutonic point solution. The electrolyte solvent mixture DOL/DME would also have a higher total atomic sulfur concentration for the eutonic point solution compare to just DOL because DME has a higher polysulfide solubility.[37]

Chapter 4 Specific Surface Area Determination of Sulfur Cathodes by Electrochemical Impedance Spectroscopy

4.1 Specific Surface Area Determination of Carbon Electrodes

Electrochemical impedance spectroscopy is a very useful technique and can be used to study different components (e.g. electrolyte, separator and electrode) of a battery to gain a better understanding of their electrochemical properties to maximise performance. In this study, electrochemical impedance spectroscopy was used to determine the specific surface area of carbon and carbon/sulfur electrodes. With the final aim of being able to do quantitative analysis of the impedance of a Li-S cell during galvanostatic cycling. Being able to observe the active specific surface area of the cathode during cycling could explain the early end of discharge due to pore blocking where the effective active specific surface area would be very low.

Initially the carbon electrode was studied since it is a simple system that can act as a proof of concept for the more complex sulfur electrodes. The composition of the carbon electrode was acetylene black 66 wt.% and PTFE 34 wt.%. The carbon electrodes impedance was measured using ½ inch Swagelok cell in a symmetrical cell setup (Figure 4.1.1).

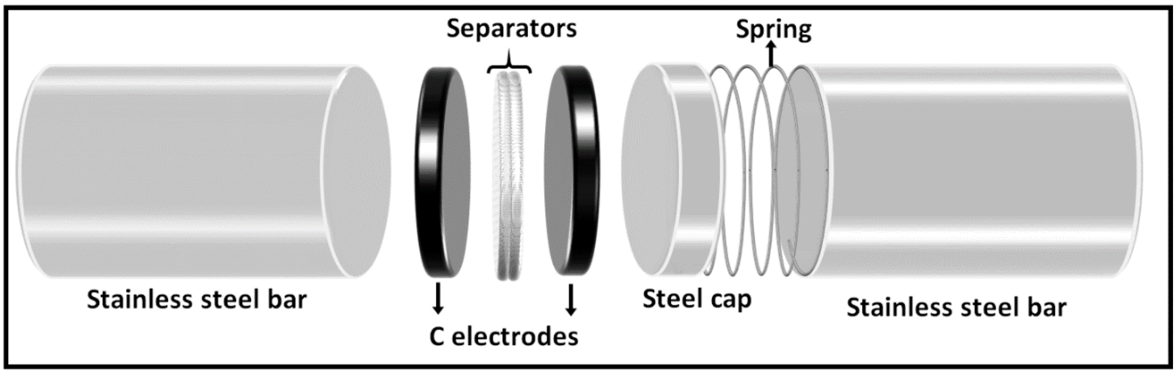

Figure 4.1.1 – Schematic of symmetrical carbon vs. carbon ½ inch Swagelok cell setup with 1 M LiTFSI in DOL and stainless steel current collectors.

The impedance cell setup was initially kept simple, since the various components can be studied by impedance, and therefore it is easier to attribute the features on the Nyquist plot to components in the cell. The battery components in this simple symmetrical cell setup and further cells are the same as the components used in commercial pouch cells. Therefore the features observed on the Nyquist plot for the Swagelok cell will be the same for the pouch cell. However the main difference will be the frequencies were the features appear. The method used to determine the specific surface area of the cathode from a Swagelok cell would be the same for a pouch cell. In the symmetrical cell setup are the aforementioned carbon electrodes separated by two glass fibre separators (GF/F) wetted with 1 M LiTFSI in DOL electrolyte. The impedance of the symmetrical cell setup can be described as:

$$Z_T(\omega) = 2\, Z_+(\omega) + Z_{Sep}(\omega) \qquad \text{Equation 4.1.1}$$

where $Z_T(\omega)$ represents the total impedance at a specific frequency ω (Ω), $Z_+(\omega)$ is the impedance of the porous positive electrode at a specific frequency ω (Ω) and $Z_{Sep}(\omega)$ is the impedance of the separator at a specific frequency ω (Ω).

The impedance of the carbon vs. carbon symmetrical cell setup was measured and plotted into a Nyquist plot (Figure 4.1.2).

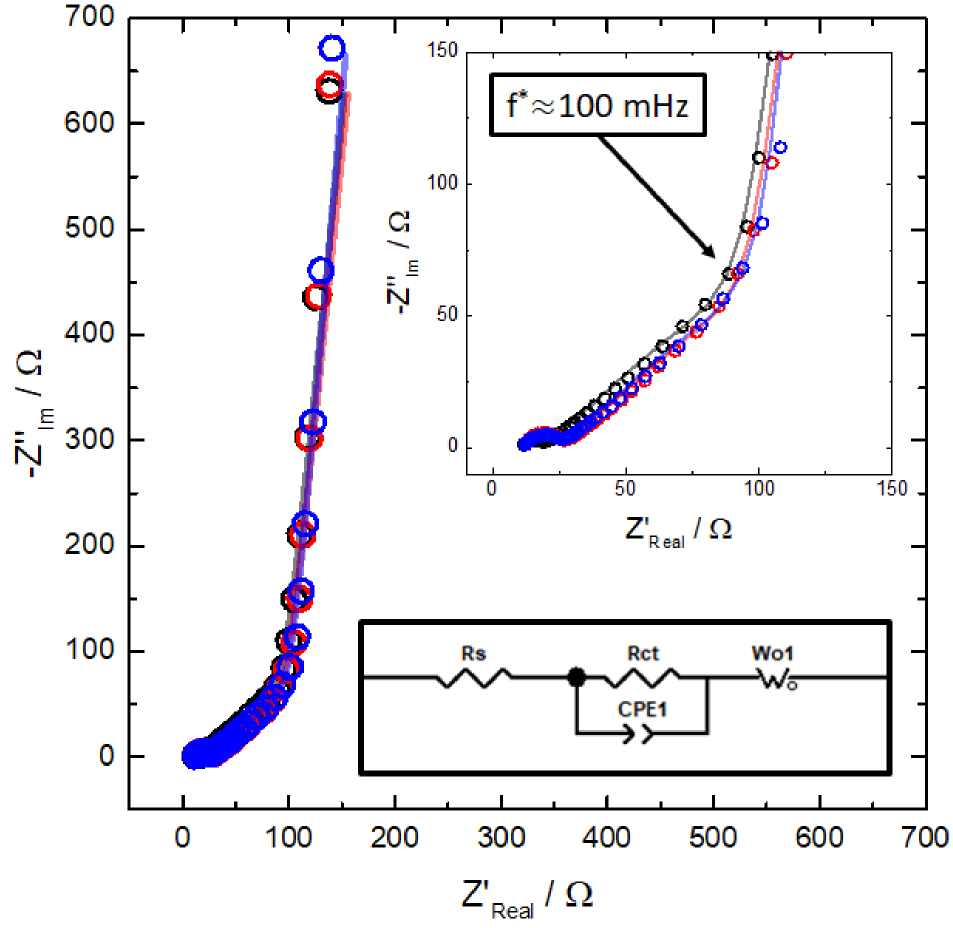

Figure 4.1.2 – Nyquist plot of carbon vs. carbon symmetrical cell with 1 M LiTFSI in DOL and stainless steel current collectors in a ½ inch Swagelok cell repeated three times where f is the transition frequency (data points – raw data, lines – fitted data). Equivalent circuit (black box) used to fit the raw impedance data. Frequency range – 200 kHz to 10 mHz. Voltage perturbation – ± 10 mV.*

The equivalent circuit used to fit the raw impedance data was a resistor in series with a constant phase element (CPE) and resistor in parallel and in series with an open Warburg element (Figure 4.1.3). The phenomena under assessment contributing to the impedance spectra of this symmetrical cell setup are the electrolyte interactions with the porous separator (ion transport) and the porous electrode (ion transport and double layer charging). These features will occur in a commercial pouch cell but in a different frequency domain.

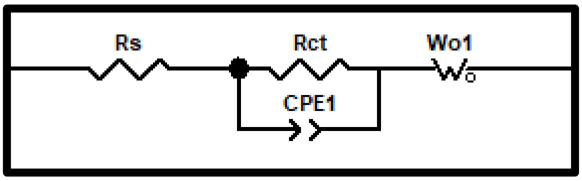

Figure 4.1.3 – Equivalent circuit used to fit the raw carbon vs. carbon symmetrical cell with stainless steel current collectors impedance data.

The impedance response from the porous electrodes across the frequency range described by the equivalent circuit defined as the transmission line model as proposed by Robert De Levie.[85-86] The choice of the equivalent circuit elements were based upon a previous impedance study on the impedance characterisation of transport properties of electrolytes within porous electrodes and separators for Li-S batteries.[46] In the equivalent circuit, the first resistor (Rs) represents the uncompensated resistance from the electrolyte wetted separators as shown by the offset from the origin on the Nyquist plot. The uncompensated resistance is defined as the resistance between the working and reference electrodes relating to the potential drop across the electrolyte wetted separators when measuring the working electrode potential.[87]

The second component is a constant phase element (CPE1) in parallel with a resistor (Rct) has been attributed to the stainless steel current collectors as shown by the depressed semicircle on the Nyquist plot at high frequency. The stainless steel current collectors contain nickel and chromium, which can form an oxide layer and will interfere with the impedance measurements.[46] This oxide layer can be described as a resistor in parallel with a CPE. The CPE represents the capacitive properties of the electronically insulating oxide layer where inhomogeneous accumulation of charge occurs upon the surface of the stainless steel current collectors. The resistor represents the transport of the ionic species into the oxide layer.

The third component is an open Warburg element which represents the migration of ionic species within the electrode as shown by a 45° diagonal line at intermediate frequencies on the Nyquist plot. The 45° line can be explained by de Levie's "transmission line" model (Figure 4.1.4).[85-86]

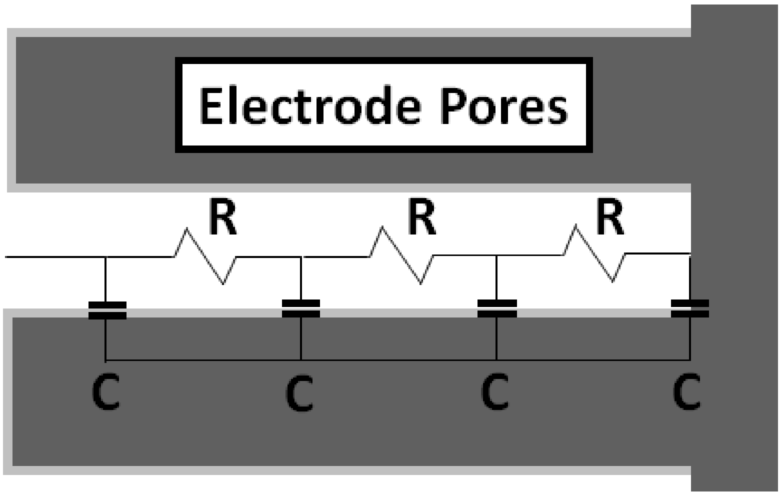

Figure 4.1.4 – Schematic illustration of de Levie's "transmission line" model within the pores of a porous electrode.

The transmission line contains a long chain of resistors in parallel to capacitors, where the resistors models the transport of the ionic species through the porous electrode and the capacitors models the double layer charging that occurs at the interface between the electrolyte and the surface of the porous electrode. The impedance response of a resistor will be in phase with the perturbation. The impedance response of a capacitor will be 90° out of phase with the perturbation. Therefore the equal combination of the two components (0° from the resistor and 90° from the capacitor) results in a 45° line.

At low frequencies, or conversely at long times, the ionic species will reach the end of the pore i.e. the impedance response is dominated by capacitive behaviour. Proof of this capacitive behaviour can be seen on the Nyquist plot as the phase shift of 90° (vertical line) at low frequencies. The frequency at which the transport behaviour changes to the blocking behaviour has been denoted on the Nyquist plot as f* which represents when this transition occurs in the frequency domain. The blocking behaviour is the double layer charging at the whole electrode-solution interface. Therefore, since the interest of this study is the specific surface area (SSA) which can be inferred from the blocking behaviour of the electrode, the equivalent circuit of a resistor in series with a CPE was used to fit the raw impedance data (Figure 4.1.5).

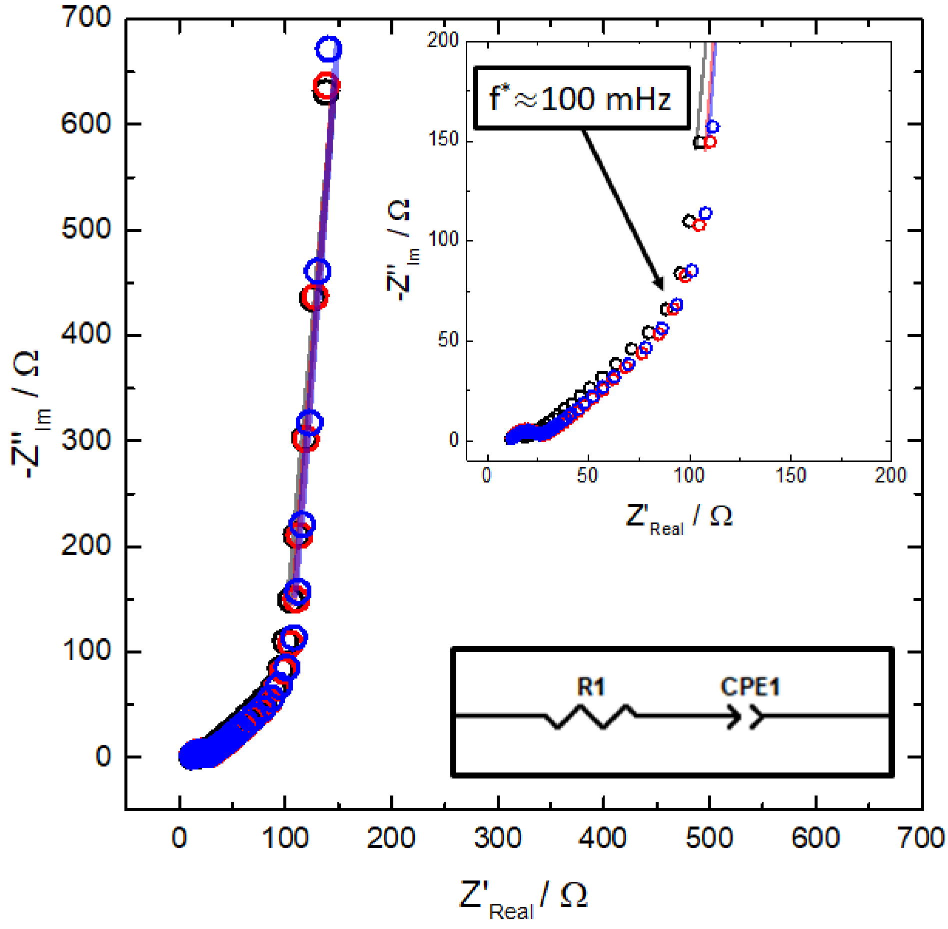

Figure 4.1.5 – Nyquist plot of carbon vs. carbon symmetrical cell with 1 M LiTFSI in DOL and stainless steel current collectors in a ½ inch Swagelok cell repeated three times where f* is the transition frequency (data points – raw data, lines – fitted data). Equivalent circuit (black box) used to fit the low frequency region of the raw impedance data. Frequency range – 200 kHz to 10 mHz. Voltage perturbation – ± 10 mV.

The impedance of the resistor in series with a CPE can be described as:

$$Z_T(\omega) = Z_{R_1}(\omega) + Z_{CPE_1}(\omega) = R_1 + \frac{1}{T_{CPE_1}(i\omega)^{P_{CPE_1}}} \qquad \text{Equation 4.1.2}$$

where $Z_{R_1}(\omega)$ is the impedance of the resistor at a specific frequency ω (Ω), $Z_{CPE_1}(\omega)$ is the impedance of the CPE at a specific frequency ω (Ω), T_{CPE_1} is the capacitance of the CPE ($F\ s^{1-P_{CPE}}$), P_{CPE_1} is the constant phase of the CPE and R_1 is the resistance of the resistor (Ω). The total resistance from the R_1 resistor comes from three different components (Figure 4.1.6).

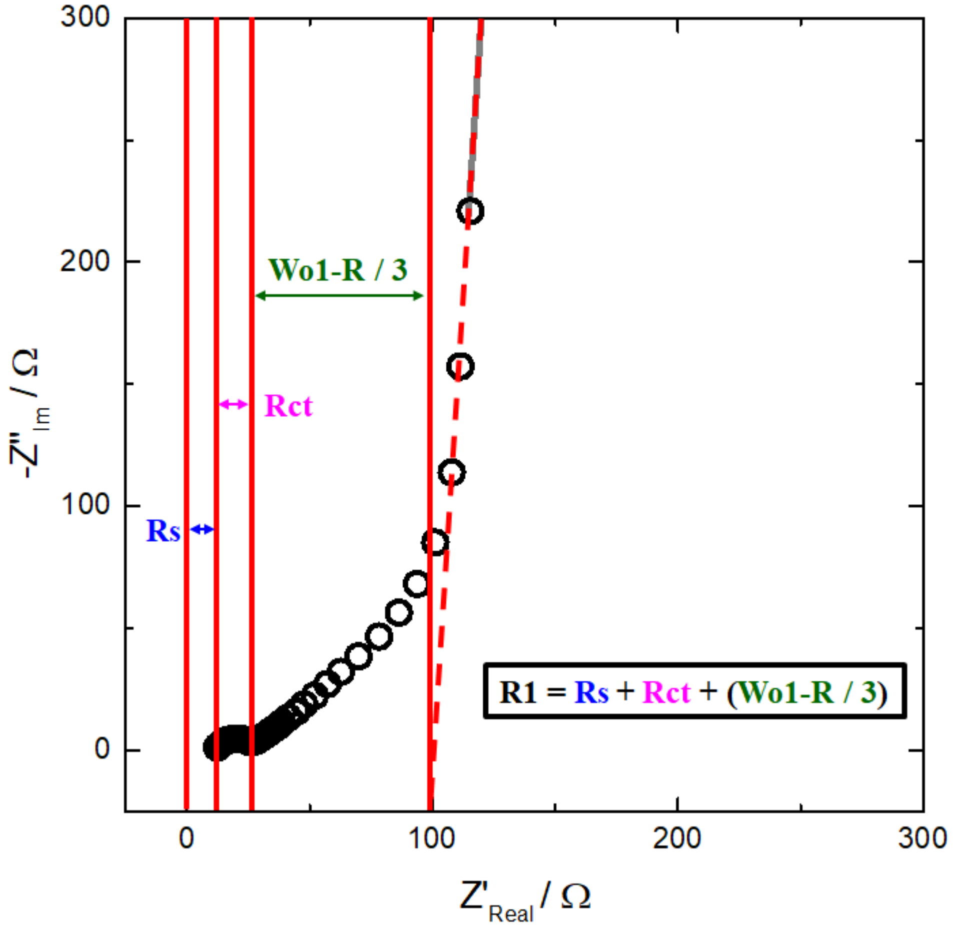

Figure 4.1.6 – Defining the R1 resistor on the Nyquist plot for the carbon vs. carbon symmetrical cell with stainless steel current collectors.

The R1 resistor represents the sum of the resistances from the solution resistance (Rs), the charge transfer resistance (Rct) and the Warburg resistance (Wo1-R). The CPE represents the blocking behaviour of the electrode where non-ideal double layer charging occurs at the electrode interface. The divergence of the blocking behaviour from a purely vertical line can be observed at low frequency. This is why a CPE was chosen to fit the impedance data because the surface on the pores within the electrode act as non-ideal capacitors where the constant phase P is less than 1.

In an attempt to remove the depressed semi-circle, observed at high frequency on the Nyquist plot, polished copper current collectors were used (Figure 4.1.7).

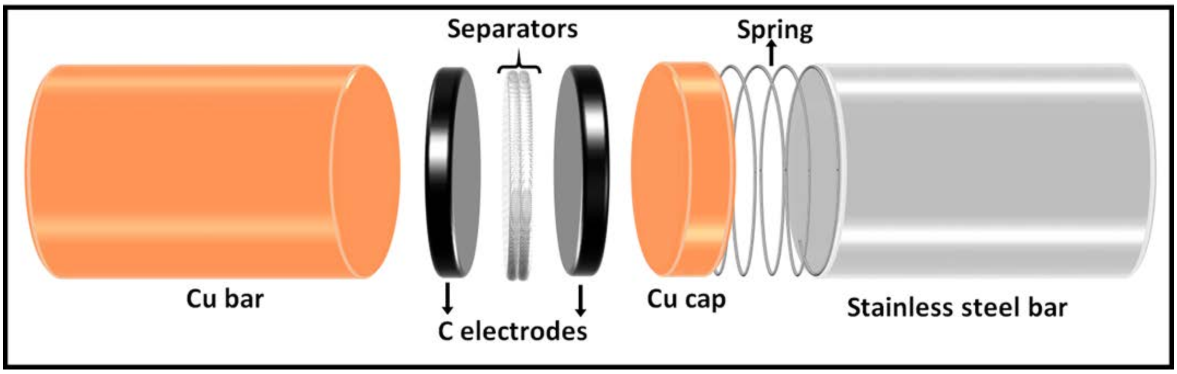

Figure 4.1.7 – Schematic of symmetrical carbon vs. carbon ½ inch Swagelok cell setup with 1 M LiTFSI in DOL and polished copper current collectors.

The process of polishing should remove the oxide layer on the surface of the copper and leave a fresh homogenous copper surface interface. The impedance of the carbon vs. carbon symmetrical cell setup with polished current collectors was measured and plotted into a Nyquist plot (Figure 4.1.8). The raw impedance data was fitted using the R-CPE series equivalent circuit.

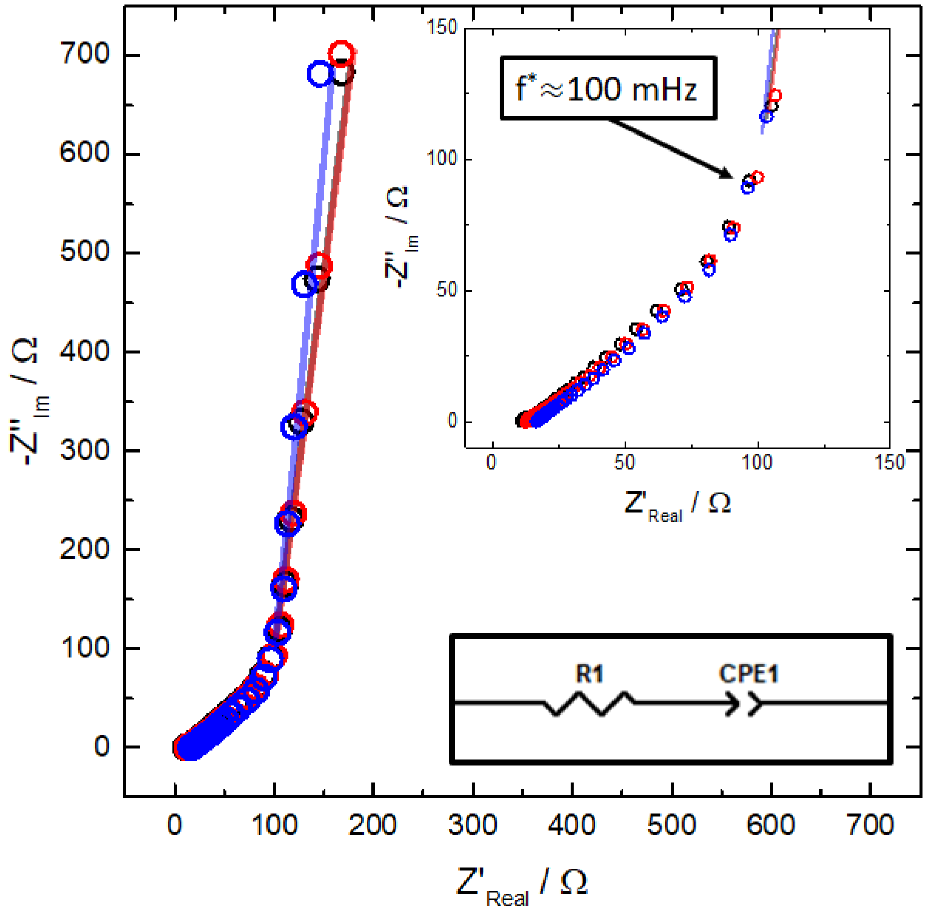

Figure 4.1.8 – Nyquist plot of carbon vs. carbon symmetrical cell with 1 M LiTFSI in DOL and polished copper current collectors in a ½ inch Swagelok cell repeated three times where f is the transition frequency (data points – raw data, lines – fitted data). Equivalent circuit (black box) used to fit the low frequency region of the raw impedance data. Frequency range – 200 kHz to 10 mHz. Voltage perturbation – ± 10 mV.*

Using the polished copper current collectors, the depressed semi-circle at high frequencies has been removed. Therefore using the polished copper current collectors removes the impedance features that arise from the stainless steel current collectors. This results in a clear and concise Nyquist plot which is easier to fit the raw data.

Now with the knowledge of what features on the Nyquist plot represent in terms of the components of the symmetrical cell, this can be applied to lithium vs. carbon cell setup (Figure 4.1.9).

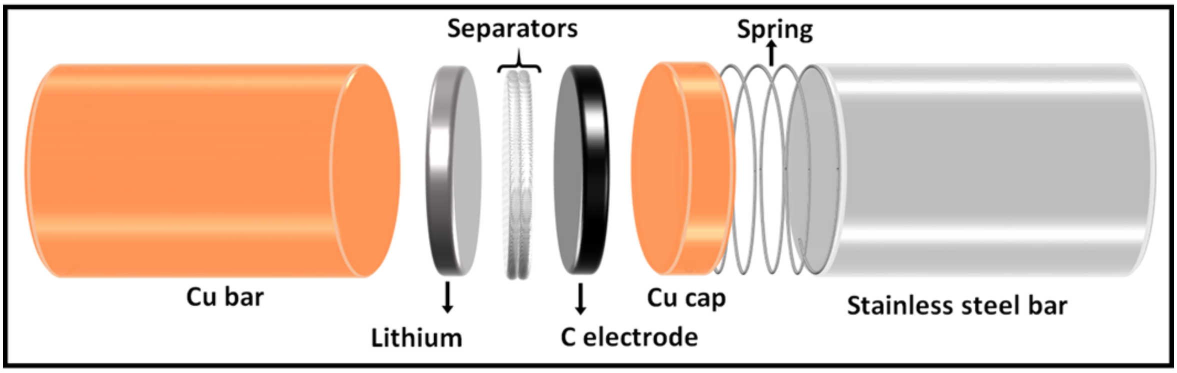

Figure 4.1.9 – Schematic of a lithium vs. carbon ½ inch Swagelok cell setup with 1 M LiTFSI in DOL and polished copper current collectors.

Lithium was used as the counter electrode and the carbon electrode was used as the working electrode. Analysis of the lithium vs. carbon cell setup will result in a mixed profile of the impedance, which can be described as:

$$Z_T(\omega) = Z_+(\omega) + Z_M(\omega) \qquad \text{Equation 4.1.3}$$

where $Z_M(\omega)$ is the impedance of the metal electrode at a specific frequency ω (Ω). However, the impedance of the carbon electrode is already known and therefore any new features on the Nyquist plot can be attributed to lithium impedance (Figure 4.1.10). The low frequency region of the raw impedance data was fitted using the R-CPE series equivalent circuit.

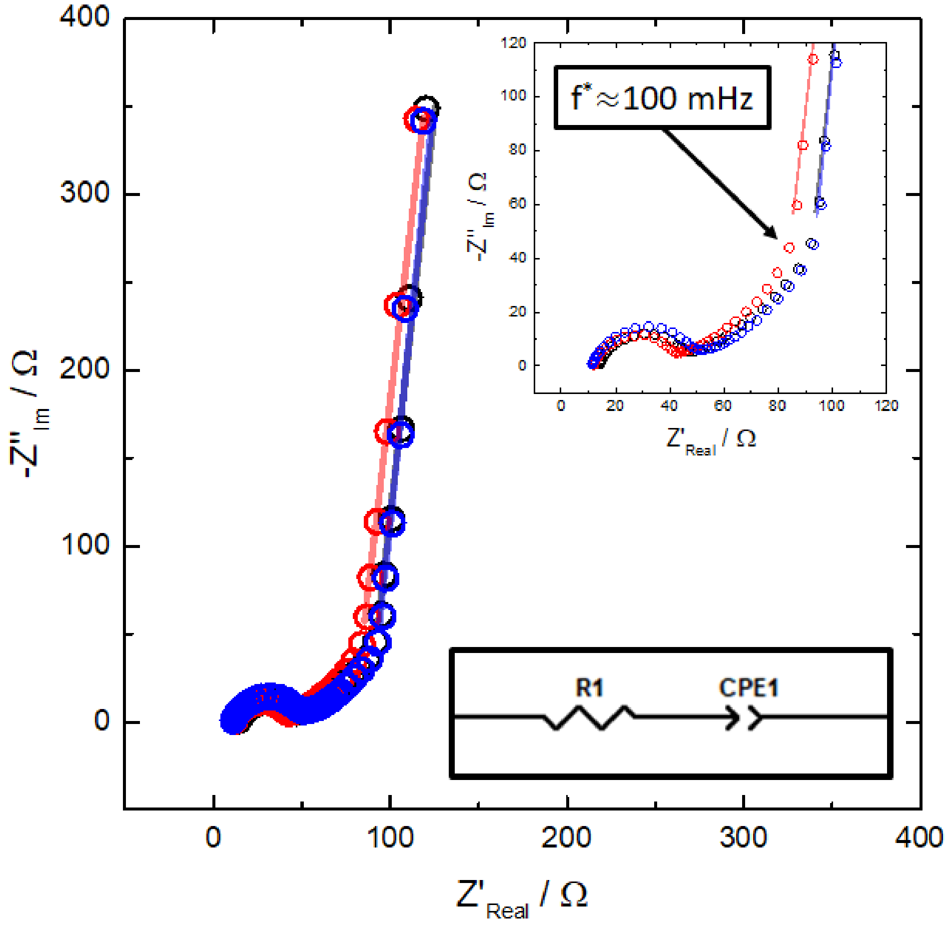

Figure 4.1.10 – Nyquist plot of lithium vs. carbon cell with 1 M LiTFSI in DOL and polished copper current collectors in a ½ inch Swagelok cell repeated three times where f* is the transition frequency (data points – raw data, lines – fitted data). Equivalent circuit (black box) used to fit the low frequency region of the raw impedance data. Frequency range – 200 kHz to 10 mHz. Voltage perturbation – ± 10 mV.

At high frequency on the Nyquist plot, a depressed semicircle can be observed. Comparing this to the Nyquist plot from the symmetrical cell setup that also used polished copper current collectors, it is safe to attribute the depressed semicircle to the presence of the lithium anode.[46] A solid electrolyte interface (SEI) layer forms on the surface of the lithium anode when in contact with electrolyte. The SEI layer will allow ion species to travel through it (charge transfer resistance) and will also accumulate charge at the surface (double layer charging). Therefore it can be modelled as a resistor in parallel with a capacitor.

The numerical values from fitting the carbon electrode impedance data in the three different cell setups using the R-CPE series equivalent circuit were used to determine the

SSA. Equations derived by Lasia,[88] allow the estimation of the double layer capacitance of the CPE in a R-CPE series equivalent circuit;

$$T_{CPE} = C_{dl}^{P_{CPE}} \times R_1^{-(1-P_{CPE})} \qquad \text{Equation 4.1.4}$$

where C_{dl} is the double layer capacitance of the electrode (F). The variables T_{CPE}, P_{CPE} and R_1 come from fitting the low frequency region of the impedance spectra. Equation 3.1.4 can be rearranged in terms of the double layer capacitance.

$$C_{dl} = \left[T_{CPE} \times (R_1)^{(1-P_{CPE})}\right]^{1/P_{CPE}} \qquad \text{Equation 4.1.5}$$

Two different cell setups, conventional and symmetrical, were used for the impedance measurements. For the lithium vs. carbon cell setup, the double layer capacitance is equal to the capacitance of the electrode ($C_{dl} = C_{Electrode}$). For the symmetrical cell setup, the double layer capacitance is equal to half of the capacitance of the electrode because the two electrodes in the cell are like two capacitors in series;

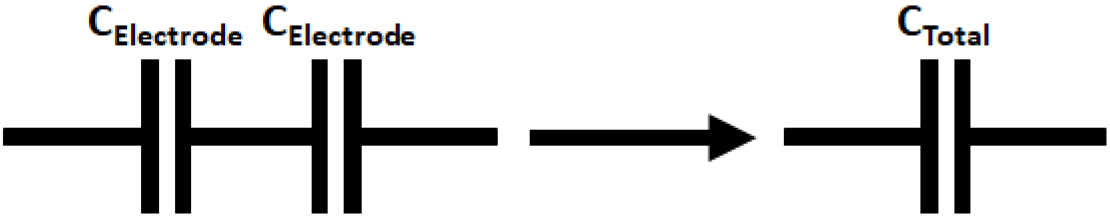

Figure 4.1.11 – Two capacitors in series equivalent to a single capacitor.

$$C_{Total} = \frac{1}{\left(\frac{1}{C_{Electrode}} + \frac{1}{C_{Electrode}}\right)} = \frac{1}{\left(\frac{2}{C_{Electrode}}\right)} = \frac{C_{Electrode}}{2} \qquad \text{Equation 4.1.6}$$

where C_{Total} is the total capacitance measured by impedance (F) and $C_{Electrode}$ is the double layer capacitance of one electrode (F). Therefore, the capacitance of each electrode is twice the total capacitance ($2\,C_{Total} = 2\,C_{dl} = C_{Electrode}$). With the capacitance of the electrode, the area of the can be determined by;

$$SA = \frac{C_{Electrode}}{C_A} \qquad \text{Equation 4.1.7}$$

where SA is the electroactive surface area of the electrode (m^2) and C_A is the areal capacitance of carbon ($F\ m^{-2}$). The areal capacitance of carbon was assumed to be 0.1 $F\ m^{-2}$ based on an article that reports the carbon electrodes have a value of areal capacitance close to 0.1 F m^{-2}.[89] With the electroactive specific area of the electrode, the specific surface area of the electrode can be determined by;

$$SSA = \frac{SA}{m_{Carbon}} \qquad \text{Equation 4.1.8}$$

where SSA is the specific surface area with respect to carbon ($m^2\ g^{-1}$) summarized in table 4.1.1.

Cell Setup	Current Collector	R-CPE Series Fit			SSA / $m^2\ g^{-1}$
		R / Ω	$T_{CPE} / F\ s^{1-P_{CPE}}$	P_{CPE}	
C vs. C	Steel	95.7 ± 9.9	0.0211 ± 0.0013	0.949 ± 0.011	49.6 ± 3.0
C vs. C	Copper	89.9 ± 3.4	0.0185 ± 0.0020	0.924 ± 0.027	44.2 ± 4.5
Li vs. C	Copper	86 ± 13	0.0378 ± 0.0017	0.930 ± 0.011	43.0 ± 1.1

Table 4.1.1 – Summary of the averaged values obtained through fitting the low frequency region of the raw impedance data with the R-CPE series circuit and the averaged SSA of the carbon electrode. Errors correspond to a confidence interval at a 95 % confidence level from repeat experiments.

The P_{CPE} values are all very close to 1 meaning the electrodes exhibit almost ideal capacitive behaviour. The capacitance of the symmetrical cells is half of the lithium vs. carbon cell setup because the two identical electrodes are like two capacitors in series, the capacitance of each electrode is twice the total capacitance as described previously (Figure 4.1.11 & Equation 4.1.6).

The SSA of the carbon electrodes, which is normalized by the mass of carbon, is quite consistent between the three cells setups, especially between the cells that use copper current collectors. To check the accuracy of these measurements Brunauer–Emmett–Teller (BET) analysis was also performed on the electrode material and the two materials that made up the electrode separately (Table 4.1.2).

Material	Technique	SSA / m^2 g^{-1}
Acetylene Black	BET	79.1 ± 5.6
PTFE	BET	9.55 ± 0.83
Carbon Electrode	BET	50.3 ± 6.7
Carbon Electrode	Impedance	44.2 ± 4.5

Table 4.1.2 – SSA from BET and impedance of the carbon electrode and its substituent materials. Errors correspond to a confidence interval at a 95 % confidence level from repeat experiments.

The SSA from BET for the carbon electrode substituent materials shows that the acetylene black has a much higher SSA than PTFE. Since PTFE does not give an electrochemical response, the values of surface area from impedance measurements have been normalised to the mass of carbon.

The value of the SSA of the acetylene black is higher than the SSA of the carbon electrode both from BET. This is caused by the PTFE binder decreasing the surface area by blocking pores.

The value of the SSA of the carbon electrode from BET is higher than from impedance. This is caused by the relatively bulky electrolyte species not being able to access the smaller pores in the carbon electrode compared to the nitrogen molecules used in BET. This difference is important because it shows that the SSA from impedance data are in-situ measurements that portray a realistic value of the SSA inside a battery which can be affected by other sources like electrolyte composition. Overall, these preliminary results for the carbon electrode show that impedance can accurately and reliably determine the SSA of an electrode.

4.2 Specific Surface Area Determination of Carbon/Sulfur Electrodes

The composition of the carbon/sulfur (C/S) electrodes was acetylene black 66 wt.%, sulfur 24 wt.% and PTFE 10 wt.%. Comparing this to carbon electrode, the relative amount carbon in both electrodes is the same. However, some of the PTFE binder has been replaced by sulfur to see the effect on the SSA by adding sulfur to the electrode.

The C/S – 24 wt.% sulfur electrodes impedance was measured using the previously developed symmetrical cell setup with polished copper current collectors (Figure 4.2.1).

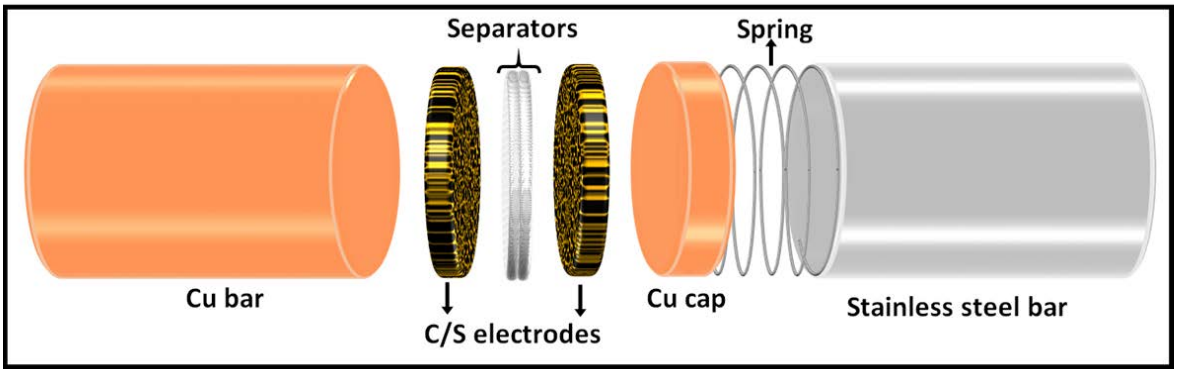

Figure 4.2.1 – Schematic of symmetrical C/S vs. C/S – 24 wt.% sulfur ½ inch Swagelok cell setup with 1 M LiTFSI in DOL and polished copper current collectors.

The impedance of the C/S vs. C/S – 24 wt.% sulfur symmetrical cell setup with polished current collectors was measured and plotted into a Nyquist plot (Figure 4.2.2).

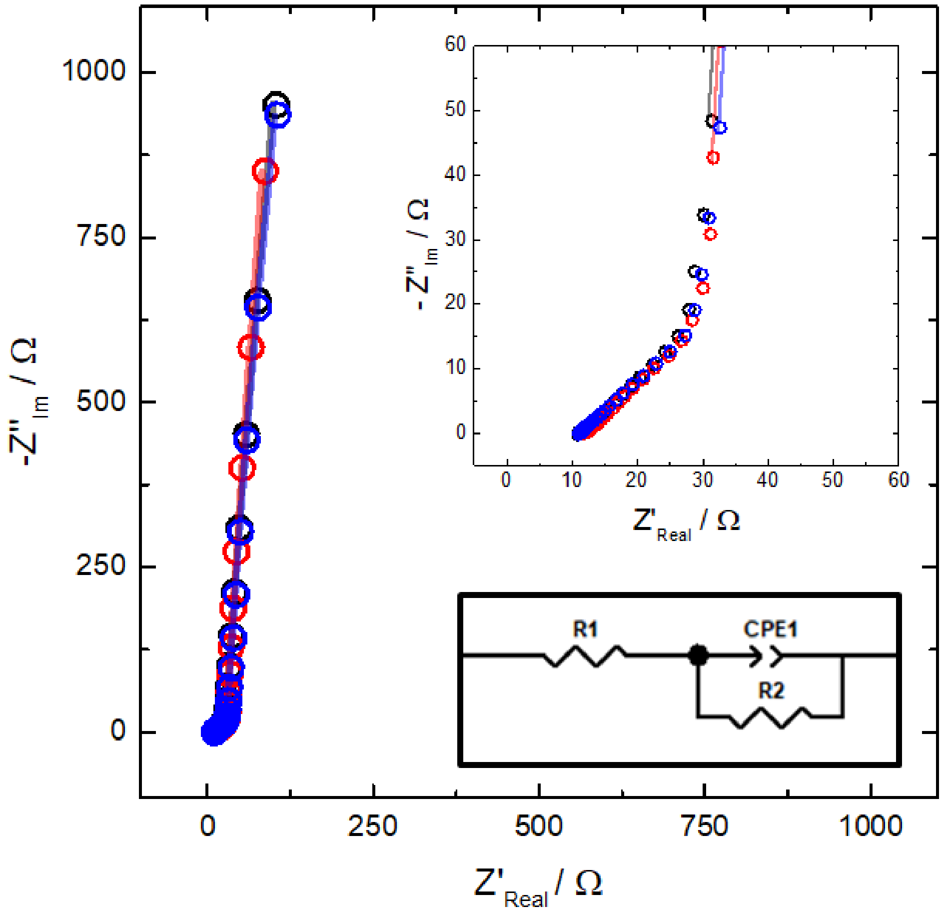

Figure 4.2.2 – Nyquist plot of C/S vs. C/S – 24 wt.% sulfur symmetrical cell with 1 M LiTFSI in DOL and polished copper current collectors in a ½ inch Swagelok cell repeated three times (data points – raw data, lines – fitted data). Equivalent circuit (black box) used to fit the low frequency region of the raw impedance data. Frequency range – 200 kHz to 10 mHz. Voltage perturbation – ± 10 mV.

However the raw impedance data was fitted using a different equivalent circuit to the circuit used for the carbon electrodes. The equivalent circuit still has a resistor in series with a capacitor but now there is a second resistor in parallel with the CPE (Figure 4.2.3). Other equivalent circuits such as a resistor in series with a CPE and a resistor in series with an open Warburg element were also tried to fit the impedance spectra. They both gave similar values for the double layer capacitance which is used to determine the SSA. However the resistor in series with a R/CPE parallel circuit gave a better fit (i.e. fitted to more data points) with the lowest percentage error when fitting the variables.

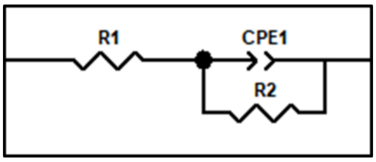

Figure 4.2.3 – Equivalent circuit used to fit the low frequency region of the raw C/S vs. C/S symmetrical cell with polished copper current collectors impedance data.

The impedance of the resistor in series with a R/CPE parallel circuit can be described as:

$$Z_T(\omega) = Z_{R_1}(\omega) + \frac{Z_{CPE_1} Z_{R_2}}{Z_{CPE_1} + Z_{R_2}} = R_1 + \frac{R_2}{R_2 T_{CPE_1} (i\omega)^{P_{CPE_1}} + 1} \qquad \text{Equation 4.2.1}$$

where R_2 is attributed to the charge transfer resistance from sulfur redox reactions because the addition of sulfur to the electrode was the only change made comparing to the carbon vs. carbon symmetrical cell with polished copper current collectors. The effect of the addition resistor can be observed on the Nyquist plot by a slight curve in the blocking behaviour at low frequency.

Now with understanding of the impedance from the C/S vs. C/S – 24 wt.% sulfur symmetrical cell, lithium was used as the counter electrode and the C/S – 24 wt.% sulfur electrode was used as the working electrode (Figure 4.2.4). Stainless steel current collectors had to be used instead because polysulfide species can react with copper.

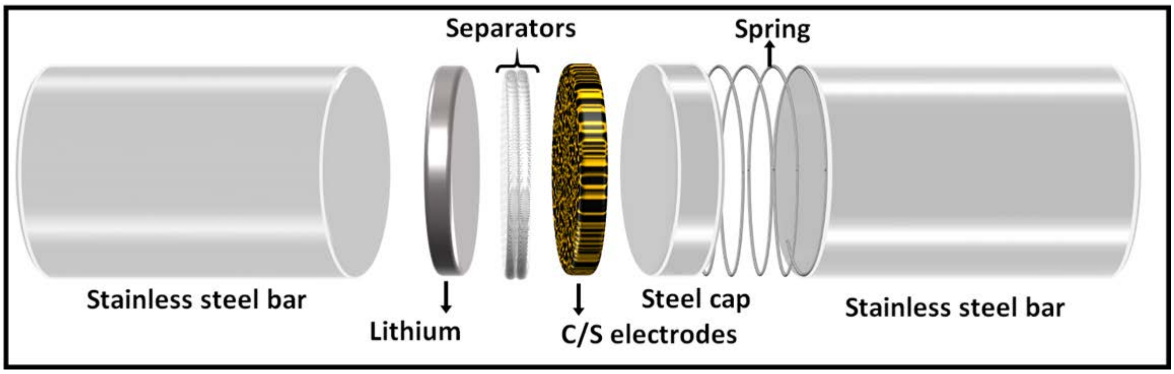

Figure 4.2.4 – Schematic of a lithium vs. C/S – 24 wt.% sulfur ½ inch Swagelok cell setup with 1 M LiTFSI in DOL and stainless steel current collectors.

However there were issues with the impedance measurements of the lithium vs. C/S – 24 wt.% sulfur cell setup which can be observed by the unreproducible Nyquist plots (Figure 4.2.5). At high frequencies, the two semicircles observed have been attributed to lithium anode and the stainless steel current collector. The larger semicircle has a similar value of resistance compared to lithium vs. carbon cell (Figure 4.1.10). In the low frequency region the initial migration of ionic species within the porous electrode can be observed as a 45° line.

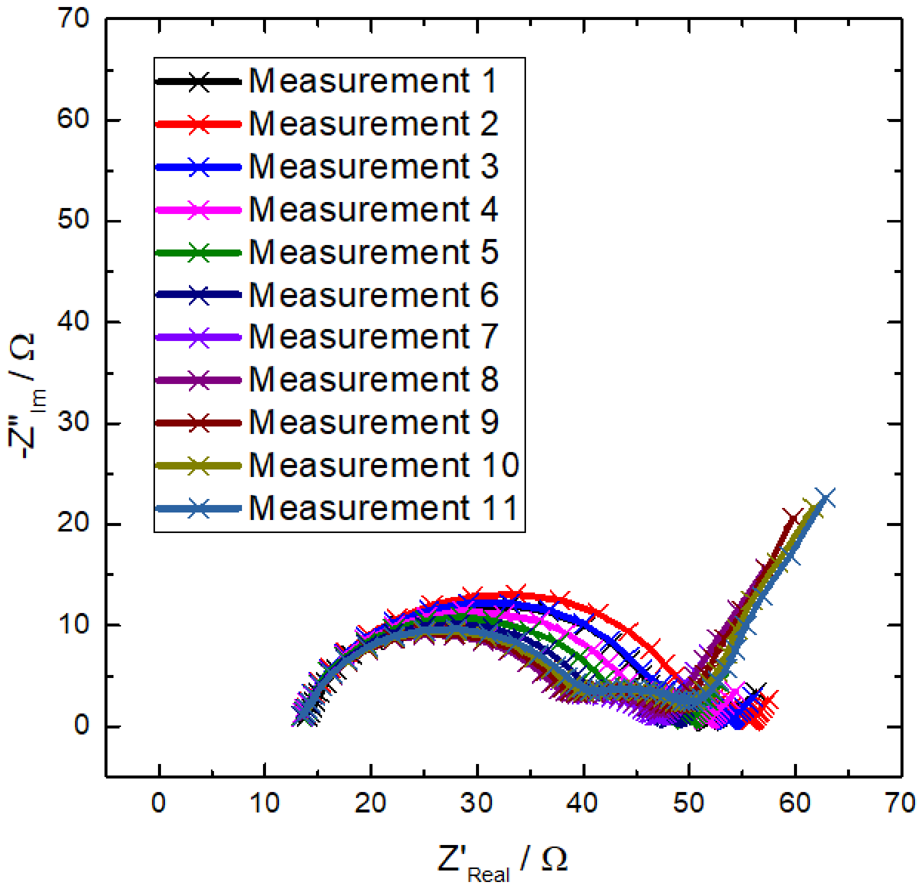

Figure 4.2.5 – Raw impedance data from the lithium vs. C/S – 24 wt.% sulfur ½ inch Swagelok cell setup with 1 M LiTFSI in DOL, glass fibre separator and stainless steel current collectors.

The cause of these different impedance measurements is the polysulfide shuttle effect discharging the battery spontaneously (Figure 4.2.6). The impedance is changing with each measurement due to the dissolution of sulfur into the electrolyte as polysulfide that will affect the solution resistance of the electrolyte.[90] The variation of the impedance with respect to the state of charge has been reported in the literature.[90] In the potential window of 2.35 V to 2.27 V the impedance decreases from measurement 1 to 7 then increases from measurement 7 to 11. This means the decreasing state of charge does not directly correlate to the resistance.[90] This means the system is not in equilibrium which is an essential prerequisite for impedance measurements.

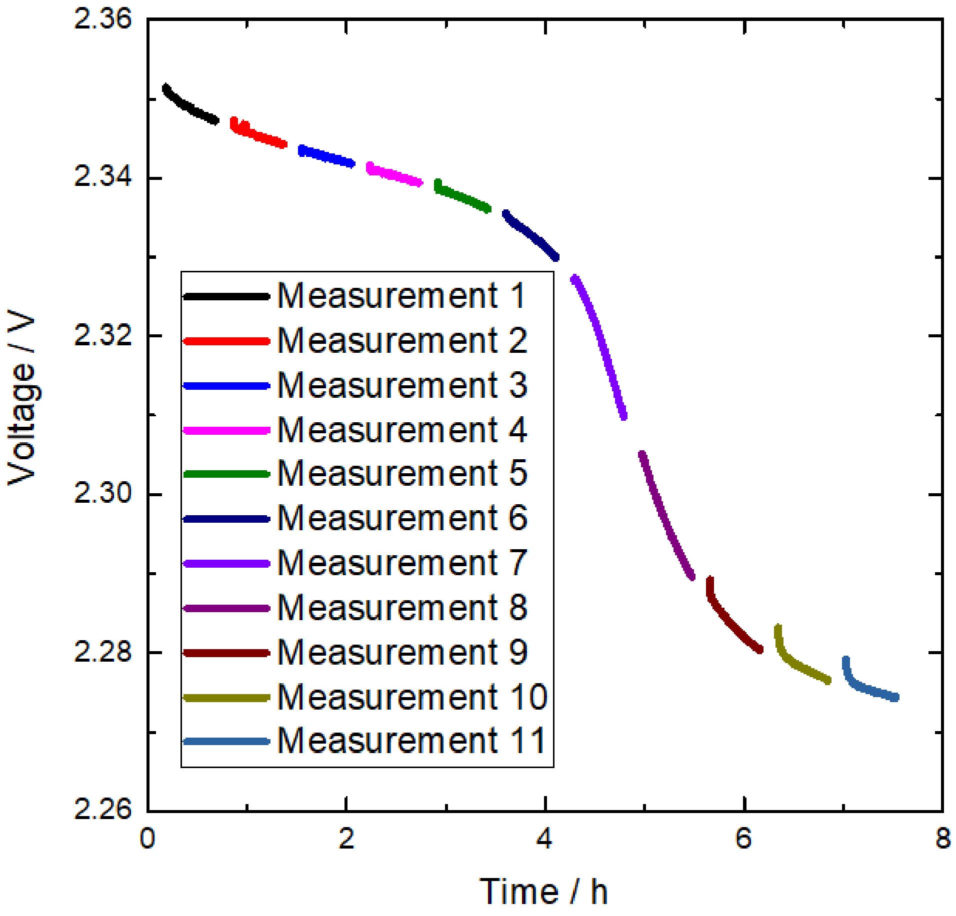

Figure 4.2.6 – Open circuit voltage monitoring during the impedance measurements with the glass fibre separator (gaps are when the impedance was measured).

The approximate open circuit voltage of a standard fully charged Li-S battery is 3 V, therefore the time taken to prepare the cell (30 minutes) it has already discharged to 2.4 V. During the impedance measurements (7 hours) there is a further decrease of the open circuit voltage of 80 mV. This shows the instability of this cell setup.

In an attempt to minimise the effect of the polysulfide shuttle during the impedance measurements of the cell, a polyolefin based separator was used instead of the glass fibre separator (Figure 4.2.7). Even though the polyolefin based separator is significantly thinner than the glass fibre based separator, it has a much higher tortuosity and would effectively slow down the rate of the polysulfide shuttle by increasing the path length.

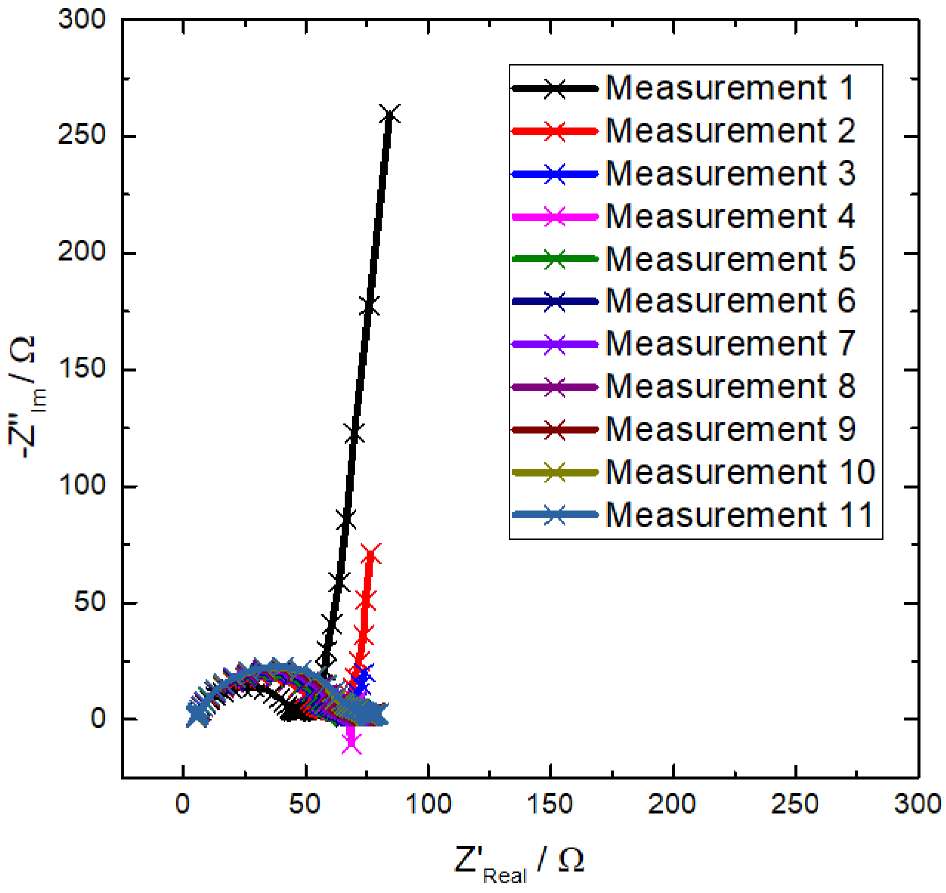

Figure 4.2.7 – Raw impedance data from the lithium vs. C/S – 24 wt.% sulfur ½ inch Swagelok cell setup with 1 M LiTFSI in DOL, polyolefin based separator and stainless steel current collectors.

The polyolefin based separator slowed down the rate of discharge from the polysulfide shuttle effect as shown by the higher initial open circuit voltage of 2.5 V (Figure 4.2.8) compared to the glass fibre cell of 2.4 V and the first impedance measurement looks similar to a small extent to the previous experiments. However this is not enough to stabilise the cell for the long term and the impedance of the cell changes. The impedance response for the polyolefin based separator is increasing with each measurement which differs to the impedance response for the glass fibre based separator cell (Figure 4.2.5). The difference in these impedance responses could be related to the open circuit potential for the polyolefin based separator (2.47 V to 2.34 V) being higher than that of the glass fibre based separator (2.35 V to 2.27 V). As previously discussed, there is not a direct correlation between the impedance and the state of charge because the Li-S battery electrolyte is considerably affected by the initial processes during discharge such as the dissolution of sulfur increasing the viscosity of the electrolyte.[90]

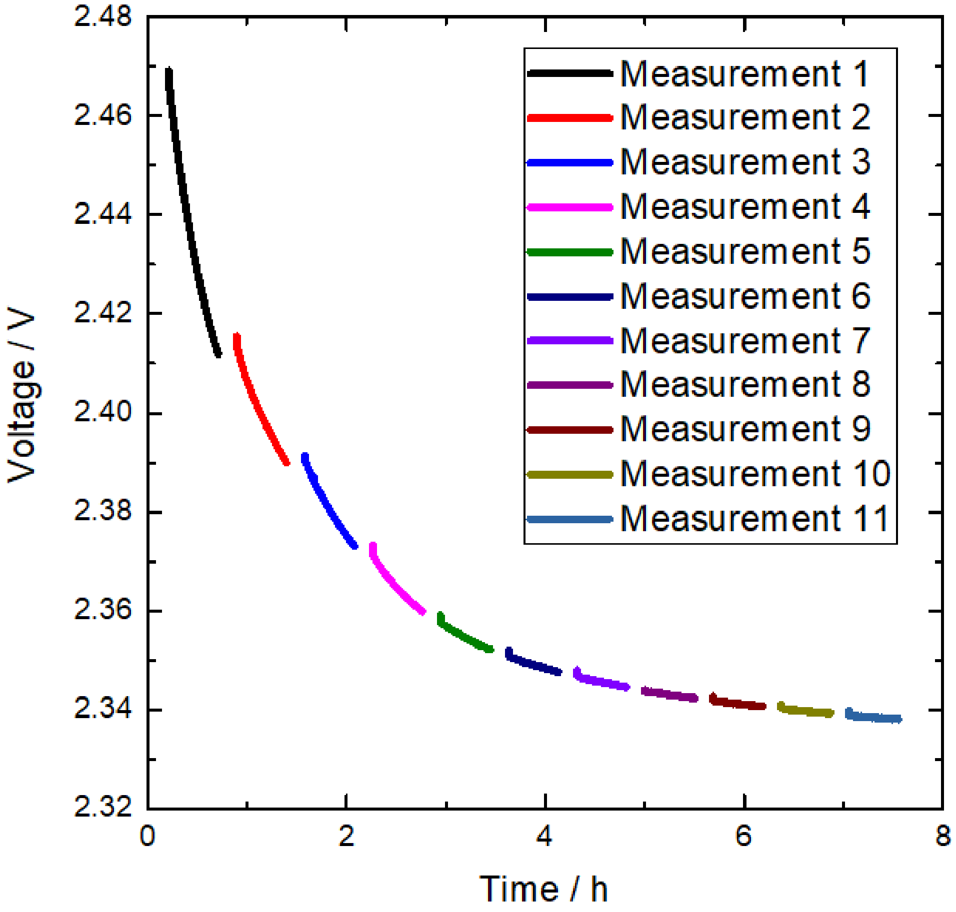

Figure 4.2.8 – Open circuit voltage monitoring during the impedance measurements with the polyolefin based separator (gaps are when the impedance was measured).

In a method to completely remove the polysulfide shuttle effect on the impedance data, lithium ion conducting Ohara glass was used in the cell setup (Figure 4.2.9).

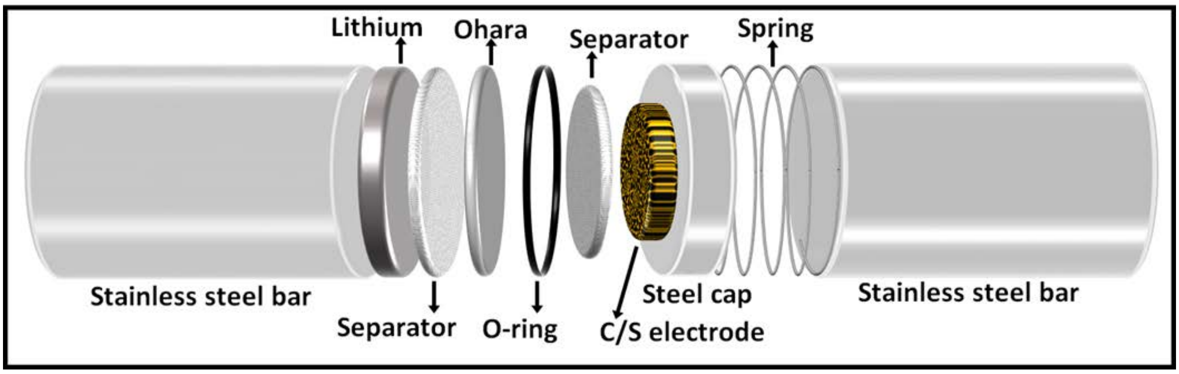

Figure 4.2.9 – Schematic of a lithium vs. C/S 1 inch Swagelok cell setup with 1 M LiTFSI in DOL, Ohara glass and stainless steel current collectors.

The Ohara glass is a solid-state ionic conductor that has very small pores that only let lithium ions through. This keeps the two sides of the cell isolated and stable effectively acting like a membrane. The impedance of the lithium vs. C/S cell setup with Ohara glass was measured and plotted into a Nyquist plot (Figure 4.2.10). The R_1-(CPE/R_2) equivalent circuit (Figure 4.2.3) was used to fit the low frequency region of the raw impedance data.

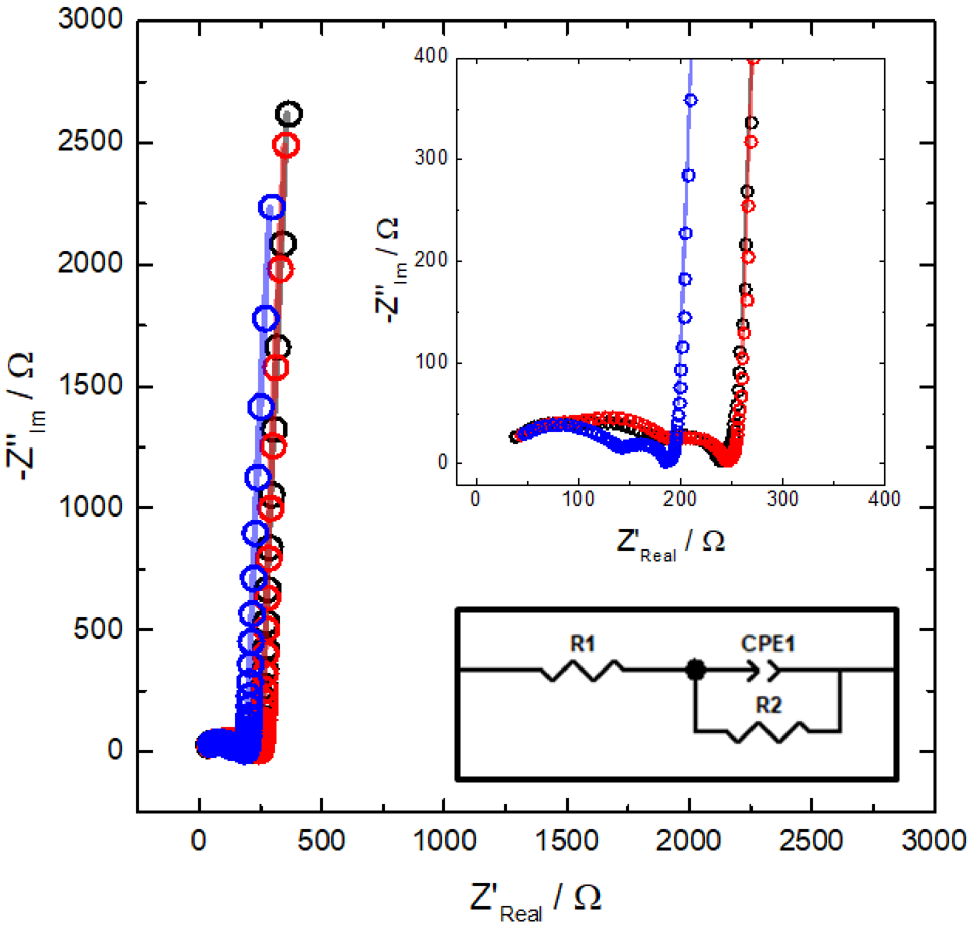

Figure 4.2.10 – Nyquist plot of lithium vs. C/S – 24 wt.% sulfur with 1 M LiTFSI in DOL, Ohara glass and stainless steel current collectors in a 1 inch Swagelok cell repeated three times (data points – raw data, lines – fitted data). Equivalent circuit (black box) used to fit the low frequency region of the raw impedance data. Frequency range – 1 MHz to 1 mHz. Voltage perturbation – ± 20 mV.

At low frequency, the shape of the Nyquist plot for the lithium vs. C/S – 24 wt.% sulfur cell setup with Ohara glass is similar to C/S vs. C/S – 24 wt.% sulfur symmetrical cell. At high to moderate frequencies there are two additional depressed semicircles which I have attributed to the lithium anode interface and the Ohara glass interface. This was based upon the semicircle observed at high frequencies for the Li-S cells with glass fibre and polyolefin based separators which came from the lithium anode. The other semicircle has been attributed to the Ohara glass which is a solid state lithium ion conductor that only allows lithium ion transport and blocks polysulfide transport, and its impedance behaviour can be modelled by a resistor coupled to a capacitor in parallel.

Using the Ohara glass, the consistency of the impedance measurements is far more reliable than using glass fibre or polyolefin based separators. This can be related to the stability of the open circuit voltage (Figure 4.2.11).

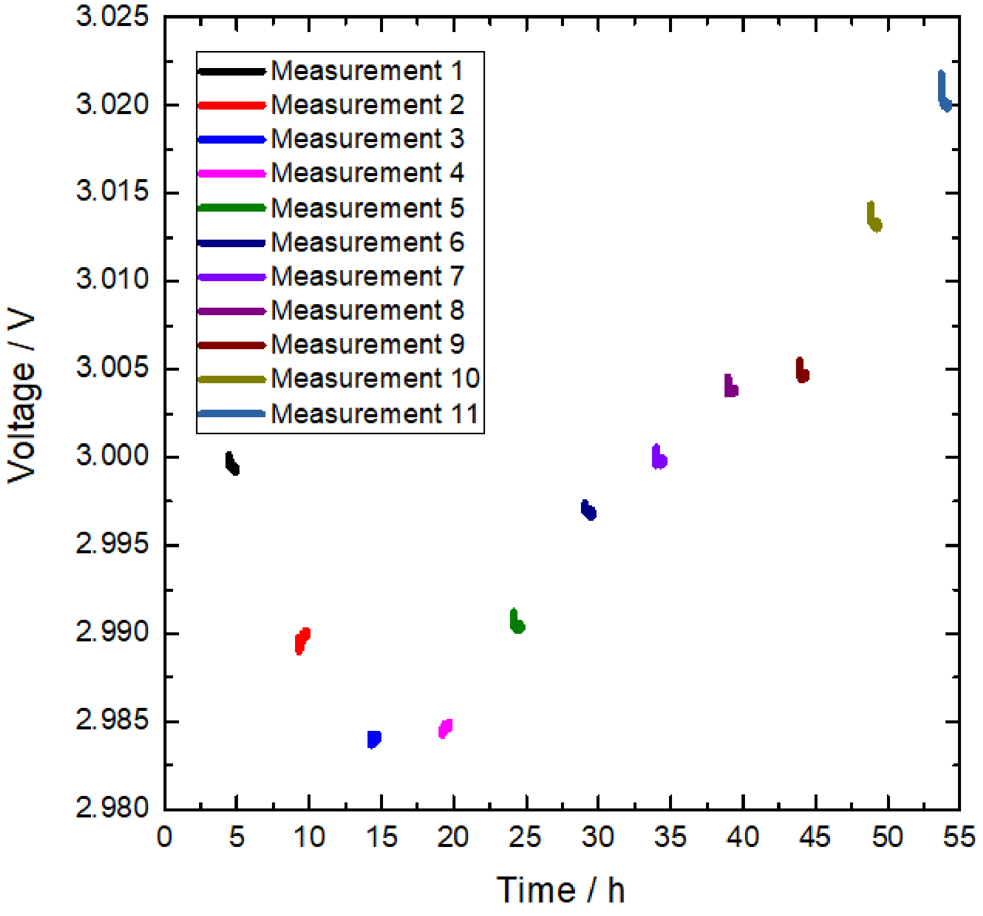

Figure 4.2.11 – Open circuit voltage monitoring during the impedance measurements with Ohara glass (gaps are when the impedance was measured).

The initial open circuit voltage of the lithium vs. C/S cell with Ohara glass is 3 V and over the course of the impedance measurements the potential slowly fluctuates by ± 20 mV about the 3 V initial open circuit voltage. The fluctuations of the open circuit voltage about 3 V relates to the end point of impedance measurement where the potential applied was varied ± 20 mV about the 3 V initial open circuit voltage. Therefore, this proves that Ohara glass stops the polysulfide shuttle effect meaning quantitative data can be extrapolated from the impedance of the C/S electrodes.

Equations derived by Lasia,[88] allow the estimation of the double layer capacitance of the CPE in a R_1-(CPE/R_2) equivalent circuit;

$$T_{CPE} = C_{dl}^{P_{CPE}} \times (R_1^{-1} + R_2^{-1})^{(1-P_{CPE})} \qquad \text{Equation 4.2.2}$$

Equation 3.2.2 can be rearranged in terms of the double layer capacitance.

$$C_{dl} = \left[T_{CPE} \times (R_1^{-1} + R_2^{-1})^{-(1-P_{CPE})}\right]^{1/P_{CPE}} \qquad \text{Equation 4.2.3}$$

From the double layer capacitance the SSA was determined (as discussed previously Equation 4.1.6 to 4.1.8). The values from fitting and the determined SSA of the C/S – 24 wt.% sulfur electrode in the symmetrical cell setup were compared to those obtained with the Li-S Ohara cell setup (Table 4.2.1).

Cell Setup	Current Collector	R_1-(CPE/R_2) Fit				SSA / m^2 g^{-1}
		R_1 / Ω	T_{CPE} / $F\ s^{1-P_{CPE}}$	P_{CPE_1}	R_2 / Ω	
C/S vs. C/S – 24 wt.% sulfur	Copper	28.9 ± 2.3	0.0156 ± 0.0027	0.9605 ± 0.0065	88000 ± 78000	33.2 ± 2.9
Li vs. C/S – 24 wt.% sulfur – Ohara	Steel	237 ± 85	0.059 ± 0.013	0.9783 ± 0.0035	470000 ± 500000	35.8 ± 5.1

Table 4.2.1 – Summary of the averaged values obtained through fitting the low frequency region of the raw impedance data with the R_1-(CPE/R_2) equivalent circuit and the averaged SSA of the C/S – 24 wt.% sulfur electrode. Errors correspond to a confidence interval at a 95 % confidence level from repeat experiments.

The large size of the R_1 error (corresponding to a confidence interval at a 95 % confidence level from repeat experiments) for the lithium vs. C/S – 24 wt.% sulfur Ohara cell is related to variance of charge transfer resistance from different pieces of Ohara. The size of R_2 and its respective uncertainty is very high because the solubility of sulfur in the electrolyte is low and the open circuit voltage is very high, when referring to Li^+/Li scale. Therefore the kinetics of the reaction are slow leading to a high charge transfer resistance as reported by Andrzej Lasia,[91] assuming that there is only the oxidised form initially in the solution;

$$R_{ct} = \frac{RT}{n^2F^2k_0C_0^*}\frac{1+\exp\left[\frac{nF}{RT}\left(E-E_{\frac{1}{2}}\right)\right]}{[(D_O/D_R)^{1/2}]^{\alpha}\exp\left[(1-\alpha)\frac{nF}{RT}\left(E-E_{\frac{1}{2}}\right)\right]} \qquad \text{Equation 4.2.4}$$

where R_{ct} is the charge transfer resistance, R is the ideal gas constant, T is the temperature, n is the number of electrons, F is Faraday's constant, k_0 is the standard rate constant, C_0^* is the concentration if the oxidised form initially in the solution, E is the formal potential, $E_{1/2}$ is the half-wave potential, D_O is the diffusion coefficient of the oxidised species, D_R is the diffusion coefficient of the reduced species and α is the transfer coefficient. Equation 4.2.4 implies Butler-Volmer type kinetics (i.e. slow electron transfer), however this equation was not used to fit the Li-S cell data. The equation is being used to explain the size of the charge transfer resistance. The charge transfer resistance is very high because the Li-S battery was at potentials very different to the half-wave potential (3 V vs. 2.45 V). The half wave potential equals the formal potential if the diffusion coefficients of reduced and oxidised species are the same. Since the solubility of sulfur in a vast majority of solvents is low,[92] trace concentrations could vary a lot due to small differences in experimental parameters such as presence of contaminants in trace quantities. The P_{CPE} values are all very close to 1 meaning the electrodes exhibit almost ideal capacitive behaviour.

The similarity of the SSAs from the two cell setups is impressive since the symmetrical cell setup uses a ½ inch Swagelok cell with copper current collectors and is fairly different to the lithium vs. C/S – 24 wt.% sulfur cell setup uses a 1 inch Swagelok cell with stainless steel current collectors and Ohara glass. The differences in Li-S Ohara glass cell setup compared to the symmetrical cell setup were a larger electrode diameter, a higher electrolyte volume, the lithium anode and the Ohara glass separator. The Ohara glass stabilises the open circuit voltage of the Li-S cell allowing for the accurate measurement of the specific surface area. This shows the reliability of this technique to determine the SSA. The SSA is slightly higher for the lithium vs. C/S – 24 wt.% sulfur cell setup which may be due to some polysulfide formation.

Material	Technique	SSA / $m^2 g^{-1}$
C/S – 24 wt.% sulfur Electrode	BET	28.4 ± 3.7
C/S – 24 wt.% sulfur Electrode	Impedance	33.2 ± 2.9
Carbon Electrode	BET	50.3 ± 6.7
Carbon Electrode	Impedance	44.2 ± 4.5

Table 4.2.2 – SSA from BET and impedance of the C/S – 24 wt.% sulfur and carbon electrodes. Errors correspond to a confidence interval at a 95 % confidence level from repeat experiments.

To check the accuracy of these measurements BET analysis was also performed on the C/S – 24 wt.% sulfur electrode material (Table 4.2.2). The SSA from BET for the C/S – 24 wt.% sulfur electrode material is lower than the SSA from impedance (the opposite relationship is observed for the carbon electrodes). This is caused by sulfur blocking the pores of the electrode which therefore cannot be in contact with the nitrogen molecules but the electrolyte can solubilise a small amount of the sulfur which exposes more of the porous carbon surface.

Comparing the carbon electrode SSA to the C/S – 24 wt.% sulfur electrode SSA, the SSA decreases when sulfur is added to the electrode which is related to sulfur blocking the pores of the porous carbon structure. To study the extent of the pore blocking effect, high sulfur content electrodes were prepared. The composition was acetylene black 20 wt.%, sulfur 70 wt.% and PTFE 10 wt.% (C/S – 70 wt.% sulfur).

The sulfur content of 70 wt.% was chosen so that the lab-scale electrodes could be compared against industrial-scale electrodes supplied by OXIS Energy Limited with an approximate sulfur content of 70 wt.%.

The impedance of the C/S vs. C/S – 70 wt.% sulfur symmetrical cell setup with polished current collectors was measured and plotted into a Nyquist plot (Figure 4.2.12). The R_1-(CPE/R_2) equivalent circuit (Figure 4.2.3) was used to fit the raw impedance data.

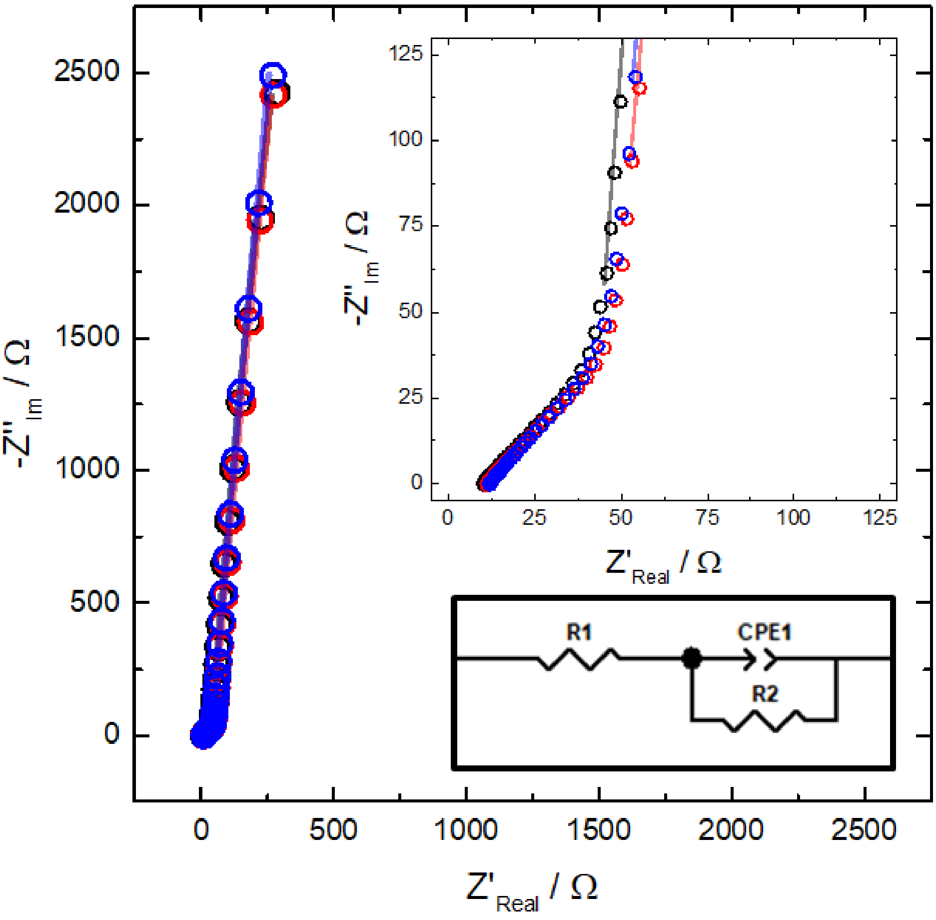

Figure 4.2.12 – Nyquist plot of C/S vs. C/S – 70 wt.% sulfur symmetrical cell with 1 M LiTFSI in DOL and polished copper current collectors in a ½ inch Swagelok cell repeated three times (data points – raw data, lines – fitted data). Equivalent circuit (black box) used to fit the low frequency region of the raw impedance data. Frequency range – 200 kHz to 10 mHz. Voltage perturbation – ± 10 mV.

The Nyquist plot for the high sulfur content electrodes is similar to the low sulfur content electrodes (Figure 4.2.2). Both cell setups have the same uncompensated solution resistance and the curved blocking behaviour at low frequency.

The impedance of the OXIS cathode vs. OXIS cathode symmetrical cell setup with polished current collectors was measured and plotted into a Nyquist plot (Figure 4.2.13). The R_1-(CPE/R_2) equivalent circuit (Figure 4.2.3) was used to fit the low frequency region of the raw impedance data.

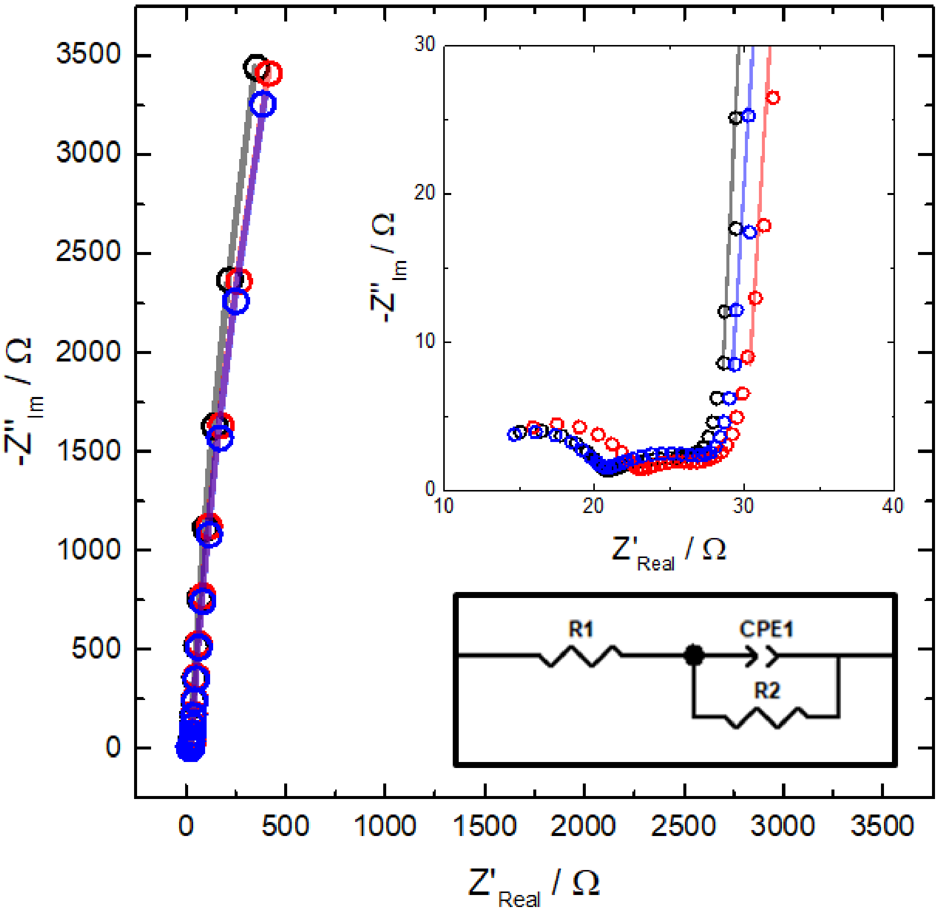

Figure 4.2.13 – Nyquist plot of OXIS cathode vs. OXIS cathode symmetrical cell with 1 M LiTFSI in DOL and polished copper current collectors in a ½ inch Swagelok cell repeated three times (data points – raw data, lines – fitted data). Equivalent circuit (black box) used to fit the low frequency region of the raw impedance data. Frequency range – 200 kHz to 10 mHz. Voltage perturbation – ± 10 mV.

The Nyquist plot for the industrial scale electrodes is similar to the lab scale electrodes with the curved blocking behaviour at low frequency. However at high frequency there are two additional depressed semicircles which have been attributed to the aluminium current collector in the OXIS cathode. Similar to the stainless steel current collectors the aluminium will have an oxide layer on the surface.

The results from fitting the impedance data and determining the SSA for the carbon electrode, C/S – 24 wt.% sulfur electrode, C/S –70 wt.% sulfur electrode and OXIS Cathode have been summarised in table 3.2.3. The SSA of carbon in OXIS cathodes has been calculated assuming that the cathode formulation contains 20% of carbon and 10% of binder. If the binder content was smaller (for example, 5%), then the result of the SSA would be 0.8 times smaller: 142 ± 18 $m^2\ g^{-1}$.

Cell Setup	Current Collector	R_1-(CPE/R_2) Fit				SSA / $m^2\ g^{-1}$
		R_1 / Ω	T_{CPE} / $F\ s^{1-P_{CPE}}$	P_{CPE}	R_2 / Ω	
C vs. C	Copper	89.9 ± 3.4	0.0185 ± 0.0020	0.924 ± 0.027	N/A	44.2 ± 4.5
C/S vs. C/S – 24 wt.% S	Copper	28.9 ± 2.3	0.0156 ± 0.0027	0.9605 ± 0.0065	88000 ± 78000	33.2 ± 2.9
C/S vs. C/S – 70 wt.% S	Copper	43.5 ± 5.0	0.00565 ± 0.00029	0.949 ± 0.011	300000 ± 420000	28.3 ± 1.3
OXIS vs. OXIS	Copper	29.0 ± 2.1	0.00420 ± 0.00019	0.964 ± 0.013	68000 ± 14000	178 ± 22

Table 4.2.3 – Summary of the averaged values obtained through fitting the raw impedance data and the averaged SSA from carbon, C/S – 24 wt.% sulfur, C/S – 70 wt.% sulfur and OXIS electrode symmetrical cell setups. Errors correspond to a confidence interval at a 95 % confidence level from repeat experiments.

Comparing the lab-scale electrodes, as the sulfur content increases the SSA with respect to carbon decreases. The 70 wt.% sulfur electrode has the same amount of sulfur in the electrode as the industrial-scale electrode but the OXIS cathode has a higher SSA. The high SSA will mitigate the low conductivity of sulfur and should improve battery performance.

The SSA for the four different electrode types were also measured using BET (Table 4.2.4). The similarities of the SSA value between the two techniques diverge as more sulfur is added to the electrode. This is due to sulfur blocking the pores of the electrode. Therefore this suggests that the impedance technique best represents the real SSA of an electrode in a battery compared to BET.

Electrode Type	BET SSA / m^2 g^{-1}	Impedance SSA / m^2 g^{-1}
Carbon Electrode	50.3 ± 6.7	44.2 ± 4.5
C/S – 24 wt.% S Electrode	28.4 ± 3.7	33.2 ± 2.9
C/S – 70 wt.% S Electrode	10.0 ± 2.0	28.3 ± 1.3
OXIS Cathode	14.4 ± 2.8	178 ± 22

Table 4.2.4 – Comparing the SSA determined by BET and impedance measurements for the carbon, C/S – 24 wt.% sulfur, C/S – 70 wt.% sulfur and OXIS electrodes. Errors correspond to a confidence interval at a 95 % confidence level from repeat experiments.

The better optimised industrial-scale electrode transport properties can also be observed when comparing the Warburg resistances (Table 4.2.5). These fitting variables were obtained by fitting the impedance data (see fitting in appendix section 6.10) with the equivalent circuit of a resistor in series with an open Warburg element (Figure 4.2.14).

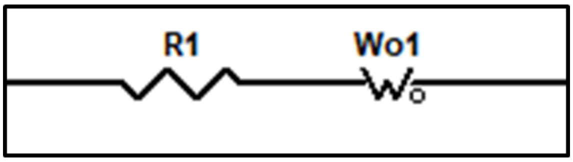

Figure 4.2.14 – Equivalent circuit of a resistor in series with an open Warburg element used to fit the raw impedance data for the carbon, C/S – 24 wt.% sulfur, C/S – 70 wt.% sulfur and OXIS electrode symmetrical cells.

The impedance of the resistor in series with an open Warburg element equivalent circuit can be described as:

$$Z_T = Z_1 + Z_{Wo1} = R_1 + R_{Wo1}\frac{coth([T_{Wo1}i\omega]^{P_{Wo1}})}{(T_{Wo1}i\omega)^{P_{Wo1}}} \qquad \text{Equation 4.2.5}$$

where R_{Wo1} represents the resistance of the electrolyte within the porous electrode, T_{Wo1} represents the characteristic time constant and P_{Wo1} represents the exponent related to non-ideal capacitive behaviour (ideal P_{Wo1} = 0.5).

Electrode Type	Average R_{Wo1} / Ω	Thickness / mm	Normalized Average R_{Wo1} / Ω mm^{-1}
Carbon Electrode	232 ± 15	0.125	1856 ± 120
C/S – 24 wt.% S Electrode	51.9 ± 5.6	0.125	416 ± 45
C/S – 70 wt.% S Electrode	110 ± 14	0.125	880 ± 110
OXIS Cathode	12.6 ± 1.6	0.047	268 ± 34

Table 4.2.5 – Normalized Warburg resistance comparison of the carbon, C/S – 24 wt.% sulfur, C/S – 70 wt.% sulfur and OXIS electrodes. Errors correspond to a confidence interval at a 95 % confidence level from repeat experiments.

The carbon electrode has a very high Warburg resistance because the electrode is very compact (low porosity) and has a PTFE content of 34 wt.%, where PTFE has a high electrical resistance. For the C/S lab-scale electrodes, increasing the sulfur content increases the Warburg resistance because the presence of sulfur appears to make the electrode even more compact causing pore blocking leading to slower ion transport. The insulating properties of sulfur will also lower the conductivity of the electrolyte within the electrode. Just in case the difference in the Warburg resistances was due to electrode thicknesses since the OXIS cathode is thinner than the lab scale electrodes, the Warburg resistances were normalized with respect to the electrode thickness. The industrial-scale electrode has a much lower normalized Warburg resistance coupled with the highest SSA show that this electrode is best optimised for battery performance. A low Warburg resistance means the electrode will exhibit fast ion transport which is essential for the mediation of the redox reactions improving sulfur utilization and specific capacity.[19-20] The better transport properties of the OXIS cathode could be from their electrode formulation procedure or the type of carbon used. Overall the developed symmetrical cell with polished copper current collectors impedance technique can be used alongside traditional electrode material testing techniques, such as galvanostatic cycling, to identify new electrode materials for Li-S batteries with the aim of improving battery performance. This technique provides a quick and accurate determination of the specific surface area and therefore new electrode materials can be developed with better transport properties improving active material utilization.

4.3 Specific Surface Area Determination of Carbon/Sulfur Electrodes at Different States of Charge

The Ohara glass cell setup (Figure 4.2.9) was successful at stopping the polysulfide shuttle effect, keeping the Li-S battery at equilibrium, meaning the impedance could be measured correctly. The SSA determined from the impedance results was related to an effectively “pristine” electrode. In this study, experiments were conducted to observe the effect of galvanostatic cycling on the SSA of the electrode. For example during discharge, sulfur undergoes reducing redox reactions creating polysulfide intermediates in the electrolyte which can diffuse away from the cathode and react with the lithium anode. However, the Ohara glass should stop this from happening. When the polysulfide intermediates are fully reduced lithium sulfide is produced. This could have an effect on the SSA because of the localisation of the redox reaction, i.e. at the electrode surface or within the electrode, and the lithium sulfide could block the pores of the carbon matrix. During the redox reaction, the electrode is also exposed to volumetric expansion of sulfur which could affect the structure of the porous carbon matrix.

Therefore a procedure was developed using a GCPL/impedance coupled technique to study the SSA at the end of discharge and the end of charge, before comparing the results against the pristine starting electrode (Figure 4.3.1). This procedure has been summarised in the potential vs. time plot (Figure 4.3.2).

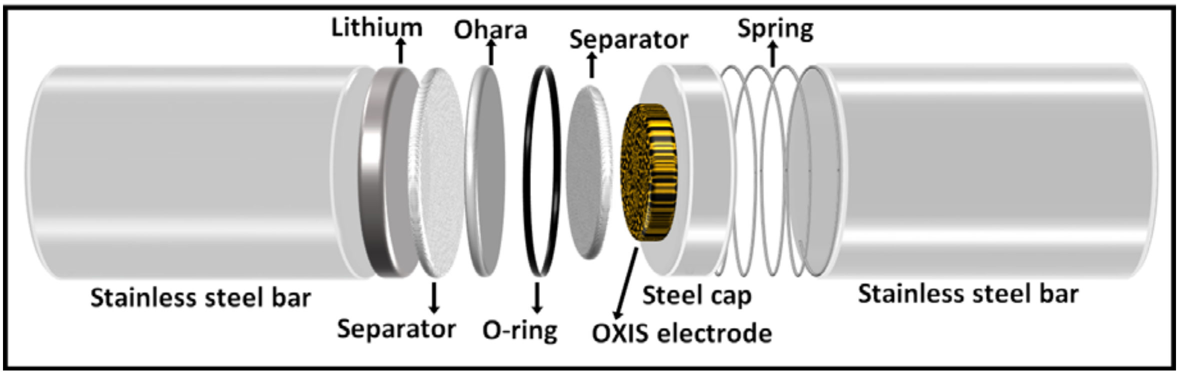

Figure 4.3.1 – Schematic of the lithium vs. OXIS cathode 1 inch Swagelok cell setup with 1 M LiTFSI in DOL, Ohara glass and stainless steel current collectors used for the GCPL/impedance technique.

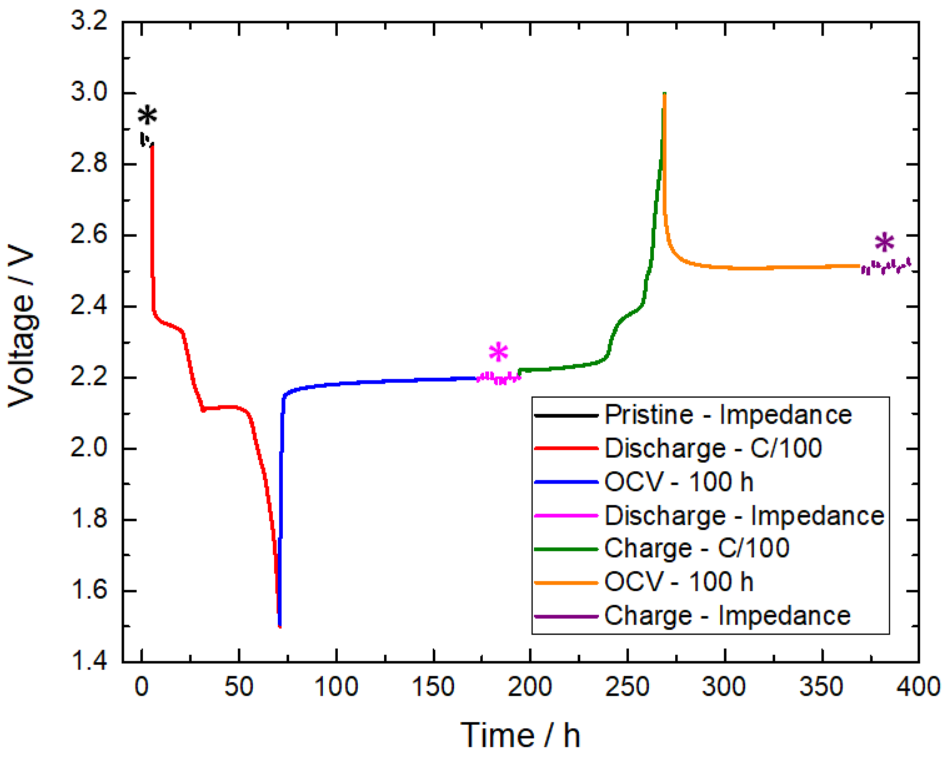

Figure 4.3.2 – Potential profile of the GCPL/impedance technique for the lithium vs. OXIS cathode cell 2 with 1 M LiTFSI in DOL, Ohara glass and stainless steel current collectors in a 1 inch Swagelok cell. The lithium vs. OXIS cathode cell was cycled at C/100 rate between 1.5 V to 3 V. The impedance was measured (*) for the pristine, discharged and charged OXIS cathode (gaps are when the impedance was measured).

Initially the impedance of the pristine electrode was measured. Next the cell was discharged at a slow rate (C/100 to 1.5 V vs. Li^+/Li) to ensure that all of the sulfur within the electrode had reduced into lithium sulfide. After this the open circuit voltage was measured. During this step the potential quickly increased from the final discharge potential 1.5 V and then plateaued at 2.2 V. This was also observed by Gaberšček et. al, when they were trying to probe the rate limiting processes by impedance spectroscopy at the end of discharge and they noticed very fast rise in voltage during relaxation in direction of quasi-equilibrium.[19]

There are two theories to this observation. The first explanation is that the solid lithium sulfide in the cathode is reacting with polysulfide species in solution to form longer chain polysulfide species.[93] The second explanation is related to the mass transfer of the polysulfide intermediates near the end of discharge.[18] The concentration of the polysulfide species at the surface will decrease over time until it reaches zero at the end of discharge, even though there are polysulfide intermediates that have not been fully reduced in the bulk. At this time, the rate of discharge, which is determined by the current applied, is too fast relative to the mass transfer of the polysulfide intermediate. The concentration of the polysulfide intermediate at the electrode surface during cycling decreases to zero with respect to time. Therefore, the application of the open circuit voltage step allows the concentration gradient to reach an equilibrium where the polysulfide concentration at the surface will increase causing the open circuit voltage to increase.

The open circuit voltage step was 100 hours long to allow the potential to stabilise before measuring the impedance of the discharged electrodes. Next the cell was charged at a slow rate (C/100 to 3 V vs. Li^+/Li) and allowed to rest for 100 hours. During this rest step, the potential decreased from the final charge potential 3 V due to the similar processes that caused the potential increase for the discharged cell. Finally the impedance of the charged electrode was measured.

The capacities from the discharge and charge steps from the GCPL/impedance cell have been summarised in table 4.3.1.

Cell No.	$OCV_{Pristine}$ / V	Discharge Capacity / mA h g^{-1}	$OCV_{Discharged}$ / V	Charge Capacity / mA h g^{-1}	Coulombic Efficiency
1	3.06	1406	2.22	613	44
2	2.89	1242	2.20	1180	95
3	2.89	1219	2.21	1018	84
4	2.96	1208	2.25	597	49
5	2.90	1261	2.21	1097	87

Table 4.3.1 – Discharge capacities with their initial potential, charge capacities with their initial potential and coulombic efficiency for the lithium vs. OXIS cathode cell with 1 M LiTFSI in DOL electrolyte, Ohara glass and stainless steel current collectors in a 1 inch Swagelok cell.

The discharge capacity is quite high with respect to the theoretical capacity (1672 mA h g^{-1}). This was due to the low current being applied allowing for better sulfur utilization and the Ohara glass stopping any capacity losses due the polysulfide shuttle effect. The charge capacities are smaller than the discharge capacities. Since Ohara glass is being used, this will stop the overcharging of the cell. The charge capacities could be lower because of the difficulty to fully oxidise lithium sulfide to sulfur (sluggish reaction kinetics). However, the charge capacities for cells 1 and 4 are significantly lower, showing that there is a significant cell to cell variability and that further improvements in the cell set-up are required to improve the reproducibility. This also affects the potential profile for the resting step after charge (Figure 4.3.3).

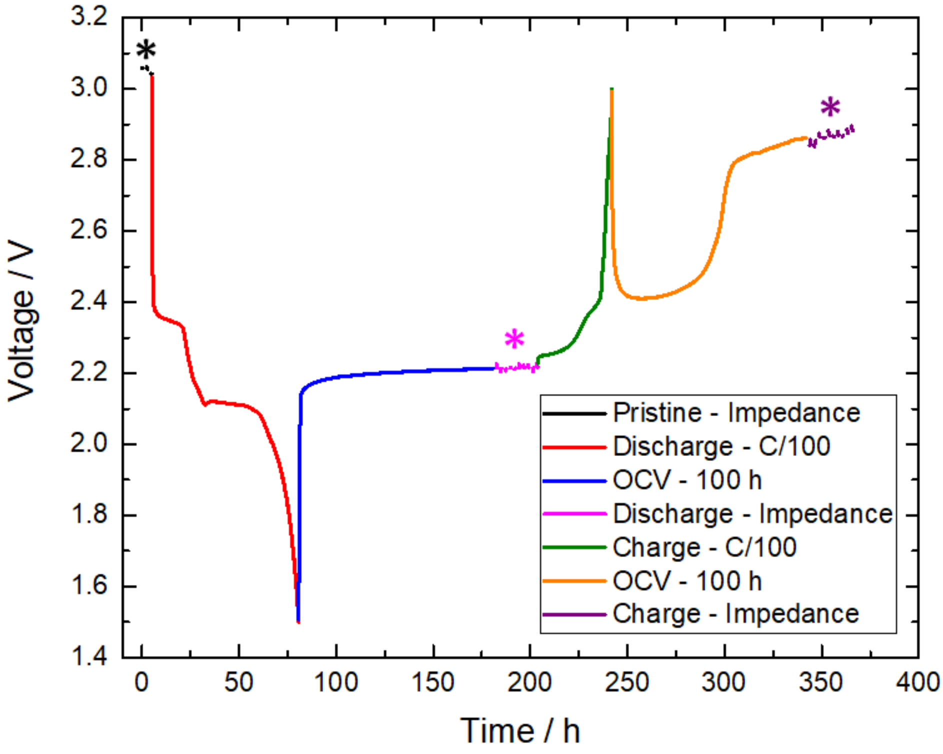

Figure 4.3.3 – Potential profile of the GCPL/impedance technique for the lithium vs. OXIS cathode cell 1 with 1 M LiTFSI in DOL, Ohara glass and stainless steel current collectors in a 1 inch Swagelok cell. The lithium vs. OXIS cathode cell was cycled at C/100 rate between 1.5 V to 3 V. The impedance was measured (*) for the pristine, discharged and charged OXIS cathode (gaps are when the impedance was measured).

Comparing the potential profile obtained from cell 2 (Figure 4.3.2) with cell 1 (Figure 4.3.3) after charging, the potential plateaued at 2.5 V and 2.9 V respectively. Therefore, for the impedance measurements after the charge step, the cells were split into two groups related to their open circuit voltage.

The impedance of the pristine lithium vs. OXIS cathode cell setup with Ohara glass was measured and plotted into a Nyquist plot (Figure 4.3.4). The impedance was measured twice for each cell to check the reliability of the measurement. The R_1-(CPE/R_2) equivalent circuit (Figure 4.2.3) was used to fit the low frequency region of the raw impedance data.

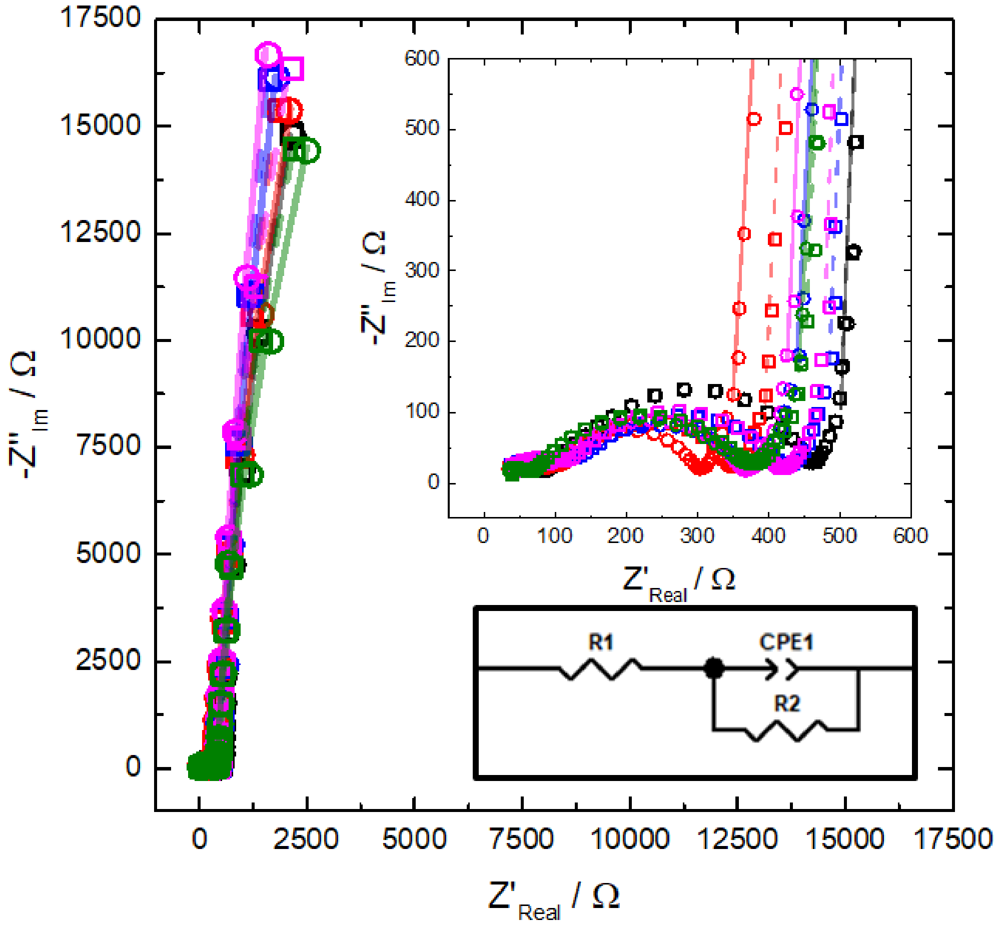

Figure 4.3.4 – Nyquist plot of the lithium vs. pristine OXIS cathode cell with Ohara glass and stainless steel current collectors in a 1 inch Swagelok cell repeated five times (data points – raw data, lines – fitted data, circle & solid line – 1st impedance measurement, square & dashed line – 2nd impedance measurement, cell 1 – black, cell 2 – red, cell 3 – blue, cell 4 – magenta and cell 5 – green). Equivalent circuit (black box) used to fit the low frequency region of the raw impedance data. Frequency range – 1 MHz to 1 mHz. Voltage perturbation – ± 20 mV.

At low frequency, the shape of the Nyquist plot for the pristine lithium vs. OXIS cathode cell setup with Ohara glass is similar to OXIS cathode vs. OXIS cathode symmetrical cell (Figure 4.2.13). At high to moderate frequencies there are two additional depressed semicircles. The larger semicircle could also be the amalgamation of multiple semicircles. These semicircles have been attributed to the lithium anode interface, the Ohara glass interface and aluminium current collector. However this frequency region was not fitted and generalised as a resistor.

The numerical values from fitting the pristine lithium vs. OXIS cathode cell setup with Ohara glass impedance data in the symmetrical cell using the R_1-(CPE/R_2) equivalent circuit and the SSA determined from these values are summarized in table 4.3.2.

Cell Setup	OCV / V	R_1-(CPE/R_2) Fit				SSA / m^2 g^{-1}
		R_1 / Ω	T_{CPE} / $F\ s^{1-P_{CPE}}$	P_{CPE}	R_2 / Ω	
OXIS vs. OXIS	0.021 ± 0.035	29.0 ± 2.1	0.00420 ± 0.00019	0.964 ± 0.013	68000 ± 14000	178 ± 22
$OXIS_{Pristine}$ vs. Li	2.925 ± 0.064	443 ± 35	0.00890 ± 0.00034	0.9734 ± 0.0034	320000 ± 120000	194 ± 10

Table 4.3.2 – Summary of the averaged values obtained through fitting the raw impedance data with the R_1-(CPE/R_2) equivalent circuit and the averaged SSA of the OXIS cathode vs. OXIS cathode symmetrical cell setup and the lithium vs. pristine OXIS cathode cell setup with Ohara glass. Errors correspond to a confidence interval at a 95 % confidence level from repeat experiments.

The averaged P_{CPE_1} value is close to 1 showing the pristine OXIS cathodes exhibit almost ideal capacitive behaviour. The size of the uncertainties for the fitted variables, except R_2, have small errors showing the reliability of the impedance measurements. The average SSA of the pristine OXIS cathodes is similar to the SSA determined from the OXIS cathode vs. OXIS cathode symmetrical cell setup value 178 ± 22 m^2 g^{-1} with the error considered. The SSA determined from the lithium vs. OXIS cathode cell setup being slightly higher than the symmetrical cell setup trend was also observed for C/S electrode. The open circuit voltage being slightly lower than the 3 V starting potential could be the cause of this variance because in this discharge a small amount of polysulfide is formed from sulfur that would reveal free surface on the porous carbon matrix.

After the impedance measurements of the pristine OXIS cathode, the cell was discharged and left to rest for 100 hours. Then the impedance of the discharged lithium vs. OXIS cathode cell setup with Ohara glass was measured and plotted into a Nyquist plot (Figure 4.3.5). The impedance was measured ten times for each cell to check the reliability of the measurement but on the Nyquist plot I have only shown the first and last measurements. The R_1-(CPE/R_2) equivalent circuit (Figure 4.2.3) was used to fit the low frequency region of the raw impedance data.

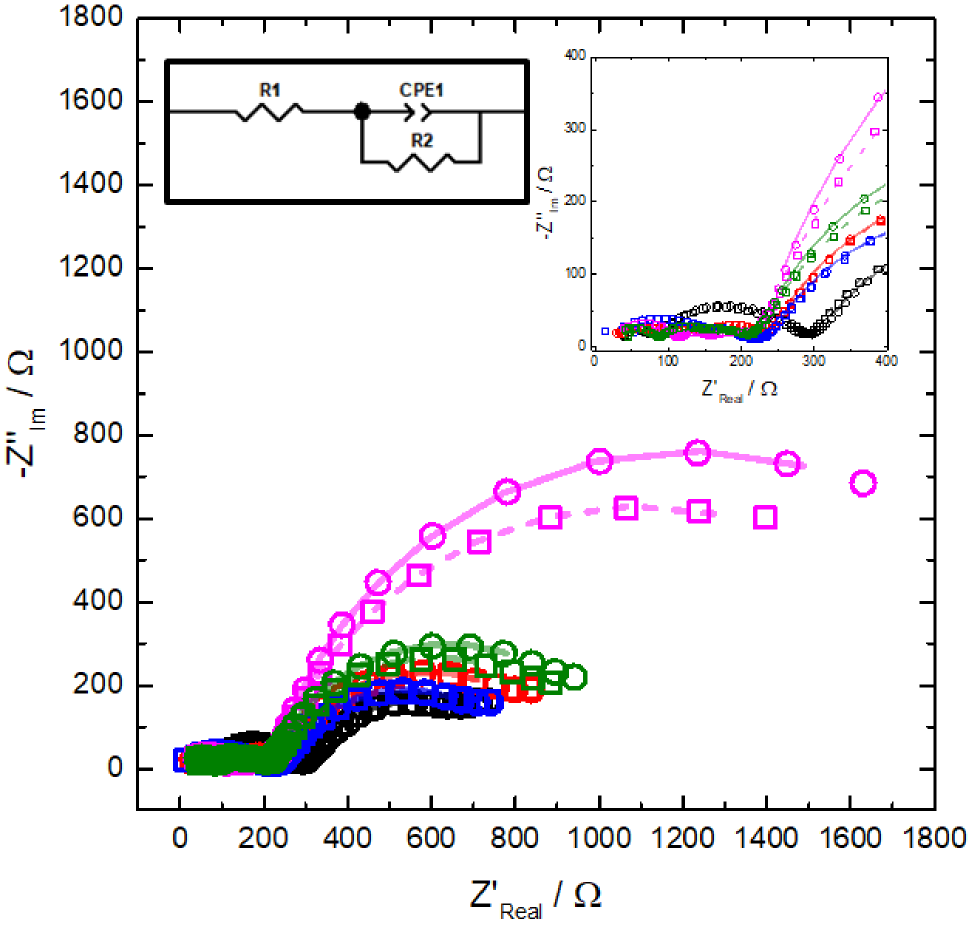

Figure 4.3.5 – Nyquist plot of the lithium vs. discharged OXIS cathode cell with Ohara and stainless steel current collectors in a 1 inch Swagelok cell repeated five times (data points – raw data, lines – fitted data, circle & solid line – 1st impedance measurement, square & dashed line – 10th impedance measurement, cell 1 – black, cell 2 – red, cell 3 – blue, cell 4 – magenta and cell 5 – green). Equivalent circuit (black box) used to fit the low frequency region of the raw impedance data. Frequency range – 1 MHz to 1 mHz. Voltage perturbation – ± 20 mV.

At low frequency, the shape of the Nyquist plot for the discharged lithium vs. OXIS cathode cell setup is very different to pristine cell setup. Instead of seeing the initial arc of the semicircle for the pristine electrode, the majority of the semicircle can be seen for the discharged electrode. At high to moderate frequencies there are additional depressed semicircles, however this frequency region was not fitted and generalised as a resistor.

The numerical values from fitting the discharged lithium vs. OXIS cathode cell setup with Ohara glass impedance data in the symmetrical cell using the R_1-(CPE/R_2) equivalent circuit and the SSA determined from these values are summarized in table 4.3.3.

Cell Setup	OCV / V	R_1-(CPE/R_2) Fit				SSA / m^2 g^{-1}
		R_1 / Ω	T_{CPE} / $F\ s^{1-P_{CPE}}$	P_{CPE}	R_2 / Ω	
OXIS vs. OXIS	0.021 ± 0.035	29.0 ± 2.1	0.00420 ± 0.00019	0.964 ± 0.013	68000 ± 14000	178 ± 22
$\text{OXIS}_{\text{Pristine}}$ vs. Li	2.925 ± 0.064	443 ± 35	0.00890 ± 0.00034	0.9734 ± 0.0034	320000 ± 120000	194 ± 10
$\text{OXIS}_{\text{Discharged}}$ vs. Li	2.214 ± 0.012	241 ± 21	0.01567 ± 0.00091	0.736 ± 0.034	910 ± 370	481 ± 61

Table 4.3.3 – Summary of the averaged values obtained through fitting the raw impedance data with the R_1-(CPE/R_2) equivalent circuit and the averaged SSA of the OXIS cathode vs. OXIS cathode symmetrical cell setup, the lithium vs. pristine OXIS cathode cell setup with Ohara glass and the lithium vs. discharged OXIS cathode cell setup with Ohara glass. Errors correspond to a confidence interval at a 95 % confidence level from repeat experiments.

The averaged P_{CPE_1} value is not close to 1 showing the discharged OXIS cathodes exhibit non-ideal capacitive behaviour which could be due to the formation of lithium sulfide at the end of discharge and could create an inhomogeneous surface on the cathode. The size of the uncertainties for the fitted variables, except R_2, have small errors showing the reliability of the impedance measurements. The relatively large error for the R_2 resistance from five repeat experiments is not due to a systematic error but due to low probability of replicating how the electrode discharges. Small differences in cell preparation or experimental conditions could alter the electrochemical behaviour. However the size of the R_2 resistance is much smaller than the resistance from the pristine electrode. This suggests a much higher concentration of polysulfide intermediates are present in the electrolyte. The increase in the open circuit voltage from the final discharge potential of 1.5 V to 2.2 V also suggests that polysulfide intermediates are present in the electrolyte. Therefore, to say the OXIS cathodes are fully discharged would be an incorrect statement. These partly discharged electrodes exhibit a higher SSA than the pristine electrode which suggests the lithium sulfide is not equally spread over the porous carbon matrix surface as sulfur is in the pristine electrode. However, this trend may change when the cell is fully discharged and all of the polysulfide intermediate is reduced into lithium sulfide. The size of the SSA error relates to the inconsistencies that occur when discharging a sulfur electrode that undergoes multiple redox reactions

After the impedance measurements of the discharged OXIS cathode, the cell was charged and left to rest for 100 hours. Then the impedance of the charged lithium vs. OXIS cathode cell setup with Ohara glass was measured and plotted into a Nyquist plot (Figure 4.3.6). The impedance was measured ten times for each cell to check the reliability of the measurement but on the Nyquist plot I have only show the first and last measurement. The R_1-(CPE/R_2) equivalent circuit (Figure 4.2.3) was used to fit the low frequency region of the raw impedance data.

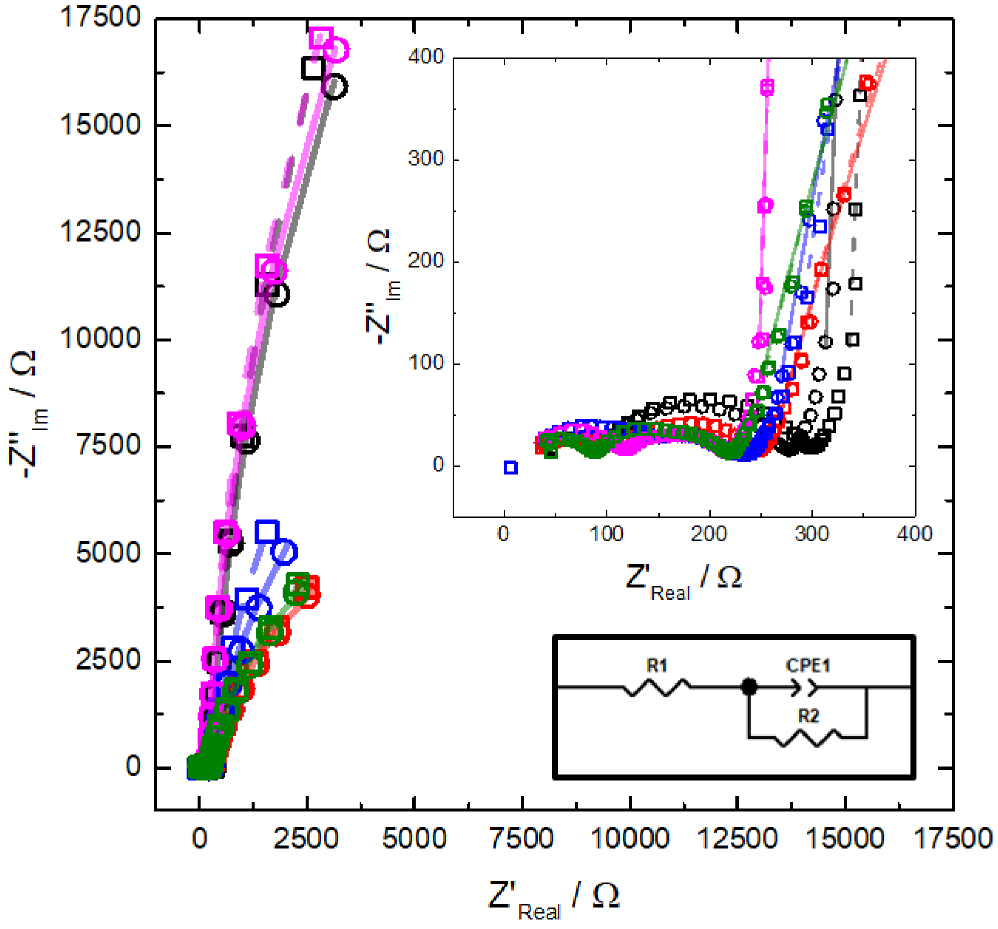

Figure 4.3.6 – Nyquist plot of the lithium vs. charged OXIS cathode cell with Ohara glass and stainless steel current collectors in a 1 inch Swagelok cell repeated five times (data points – raw data, lines – fitted data, circle & solid line – 1st impedance measurement, square & dashed line – 10th impedance measurement, cell 1 – black, cell 2 – red, cell 3 – blue, cell 4 – magenta and cell 5 – green). Equivalent circuit (black box) used to fit the low frequency region of the raw impedance data. Frequency range – 1 MHz to 1 mHz. Voltage perturbation – ± 20 mV.

Looking at the Nyquist plot, two different impedance responses can be observed. Cells 1 and 4 (black and magenta) look more similar to the Nyquist plot for the pristine OXIS cathode compared to cells 2, 3 and 5 (red, blue and green). This would suggest that cells 1 and 4 have returned to the pristine electrode conditions whereas cells 2, 3 and 5 still have intermediate polysulfide species present in the electrolyte as shown by the more pronounce curve in the low frequency region. At high to moderate frequencies there are additional depressed semicircles, however this frequency region was not fitted and generalised as a resistor.

The numerical values from fitting the discharged lithium vs. OXIS cathode cell setup with Ohara glass impedance data in the symmetrical cell using the R_1-(CPE/R_2) equivalent circuit and the SSA determined from these values are summarized in table 4.3.4.

Cell Type	OCV / V	R_1-(CPE/R_2) Fit				SSA / m^2 g^{-1}
		R_1 / Ω	T_{CPE} / $F\ s^{1-P_{CPE}}$	P_{CPE}	R_2 / Ω	
OXIS vs. OXIS	0.021 ± 0.035	29.0 ± 2.1	0.00420 ± 0.00019	0.964 ± 0.013	68000 ± 14000	178 ± 22
$\text{OXIS}_{\text{Pristine}}$ vs. Li	2.925 ± 0.064	443 ± 35	0.00890 ± 0.00034	0.9734 ± 0.0034	320000 ± 120000	194 ± 10
$\text{OXIS}_{\text{Discharged}}$ vs. Li	2.214 ± 0.012	241 ± 21	0.01567 ± 0.00091	0.736 ± 0.034	910 ± 370	481 ± 61
$\text{OXIS}_{\text{Charged}}$ vs. Li – Cells 1 + 4	2.856 ± 0.025	284 ± 71	0.00844 ± 0.00016	0.9796 ± 0.0047	134000 ± 31000	189.8 ± 5.3
$\text{OXIS}_{\text{Charged}}$ vs. Li – Cells 2, 3 + 4	2.502 ± 0.015	251 ± 16	0.0148 ± 0.0020	0.866 ± 0.033	27000 ± 17000	362 ± 28

Table 4.3.4 – Summary of the averaged values obtained through fitting the raw impedance data with the R_1-(CPE/R_2) equivalent circuit and the averaged SSA of the OXIS cathode vs. OXIS cathode symmetrical cell setup, the lithium vs. pristine OXIS cathode cell setup with Ohara glass, the lithium vs. discharged OXIS cathode cell setup with Ohara glass and the lithium vs. charged OXIS cathode cell setup with Ohara glass. Errors correspond to a confidence interval at a 95 % confidence level from repeat experiments.

The averaged P_{CPE_1} value is for cells 1 and 4 are very close to 1 showing the charged OXIS cathodes exhibit almost ideal capacitive behaviour. Cells 1 and 4 also have a SSA similar to the SSA obtained from the pristine OXIS cathode 194 ± 10 m^2 g^{-1} because the impedance was measured at similar potentials of 2.9 V. The step up in potential for cells 1 and 4 occurred during the resting step (Figure 4.3.3). Whereas for cells 2, 3 and 5 the average P_{CPE_1} value is not close to 1 and the SSA is higher than the SSA obtained from the pristine OXIS cathode because of the lower potential of the cell during the impedance measurement. The potential of 2.5 V suggests the cell has not been fully charged and there are intermediate polysulfide species present in the electrolyte. The R_2 resistance is low also suggesting that there is a higher concentration of intermediate polysulfide species.

Comparing the charged OXIS cells 2, 3 and 5 to the impedance results from the discharged OXIS cathode, the SSA is lower because the potential is higher suggesting more of the intermediate polysulfide species have been oxidised to form sulfur. This is also supported by the higher R_2 resistance for cells 2, 3 and 5 which means there is a lower concentration of intermediate polysulfide species.

Overall, the main concept for the GCPL/impedance coupled technique observed is that small differences in the cell preparation or other experimental conditions such as electrolyte volume, electrode alignment or the condition of the Ohara glass can produce different electrochemical behaviour, which is reflected in the different OCV and SSA values (Table 4.3.5).

Cell Type	OCV / V	Average SSA
OXIS vs. OXIS	0	178 ± 22
$OXIS_{Pristine}$ vs. Li	2.925 ± 0.064	194 ± 10
$OXIS_{Discharged}$ vs. Li	2.214 ± 0.012	481 ± 61
$OXIS_{Charged}$ vs. Li – Cells 1 + 4	2.856 ± 0.025	189.8 ± 5.3
$OXIS_{Charged}$ vs. Li – Cells 2, 3 + 4	2.502 ± 0.015	362 ± 28

Table 4.3.5 – Summary of the SSA for the OXIS cathode at different states of charge. Errors correspond to a confidence interval at a 95 % confidence level from repeat experiments.

Starting with the pristine electrodes with the lowest SSA at 2.9 V, the SSA increases for partly charged cells 2, 3 and 5 at 2.5 V and the partly discharged electrodes have the highest SSA at 2.2 V. Therefore, this shows that during the discharge of the Li-S battery the SSA increases between 3 V to 2.2 V. The trend between 2.2 V to 1.5 V is unknown. Future work would involve developing the GCPL/impedance technique so that the impedance was measured at 3 V and 1.5 V. This could be achieved by doing a potential hold whilst measuring the impedance.

The charged cells 1 and 4 SSA is similar to the SSA obtained for the pristine OXIS cathode, considering the error. However this comparison is being made for an electrode that has undergone one discharge/charge cycle. This technique could be tested over many cycles to study the degradation (i.e. the effect on the SSA) of a Li-S battery cathode during galvanostatic cycling.

To study the species present in the OXIS cathode using grazing incidence X-ray diffraction (GIXRD), additional cells were built to be disassembled at different states of charge i.e. pristine, discharged and charged (Figure 4.3.7). GIXRD uses a small incident angle for the incoming X-ray beam meaning the technique is surface sensitive.[94] The electrode material layer that is supported on the aluminium current collector is very thin. GIXRD therefore will only penetrate the surface of electrode material meaning the phases observed will only be coming from the electrode material and not the current collector. The disadvantage of GIXRD is the limited in-plane spatial resolution (i.e. beam footprint).

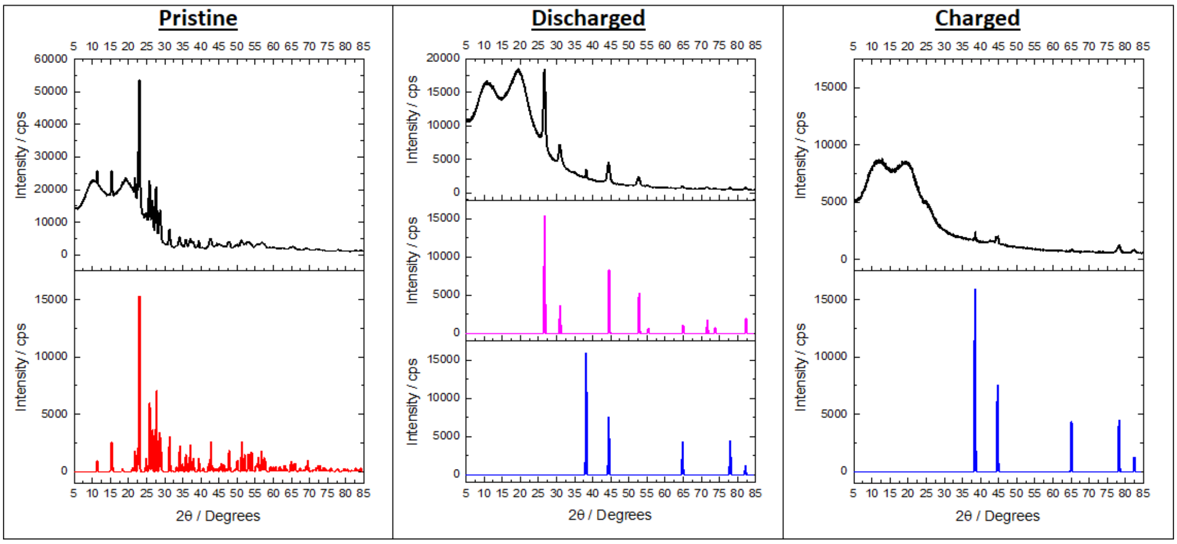

Figure 4.3.7 – GIXRD (black) of the pristine (left), discharged (middle) and charged (right) OXIS cathodes with the sulfur[95] (red), lithium sulfide[96] (magenta) and aluminium[97] (blue) diffraction pattern references.

For all three states of charge, two broad peaks can be observed at 10° and 20° is from the carbon in the electrode. For the pristine OXIS cathode, the other diffraction pattern observed is from sulfur. For the discharged OXIS cathode, one of the observed diffraction patterns is from lithium sulfide. This shows that all of the sulfur in the electrode has reacted, producing either lithium sulphide or polysulfides. For the charged OXIS cathode, the diffraction pattern for sulfur is not observable. This could be due to the production of amorphous sulfur after charging making it difficult to observe the diffraction pattern.[98] The presence of the aluminium diffraction pattern for the discharged and charged OXIS cathode suggests breakdown of the electrode structure during cycling caused by the volumetric expansion of sulfur or lithium sulfide to polysulfide species.

4.4 Conclusions

Through the analysis of the carbon electrodes and carbon/sulfur electrodes, the impedance response on the Nyquist plot had high reproducibility. This is shown by the reasonable error (< 10 %) of the specific surface area from repeat experiments of separate cells using the symmetrical cell setup that uses copper current collectors (C/S vs. C/S – 24 wt.% Sulfur SSA = 33.2 ± 2.9 $m^2\ g^{-1}$). This cell design gives the simple and predictable Nyquist plot to fit which is ideal for quantitative comparisons between different electrode formulations.

The Li-S battery setup developed using Ohara glass stopped the self-discharge during impedance measurements by blocking the polysulfide shuttle. The comparison between the lithium vs. C/S cell setup against the symmetrical cell setup shows the determined SSA for the C/S electrodes were similar (C/S vs. C/S SSA = 33.2 ± 2.9 $m^2\ g^{-1}$ & Li vs. C/S SSA = 35.8 ± 5.1 $m^2\ g^{-1}$) showing the accuracy of the impedance measurements. There were many differences in the cell design such as the symmetrical cell setup uses a ½ inch Swagelok cell with copper current collectors. The lithium vs. C/S cell setup uses a 1 inch Swagelok cell with stainless steel current collectors and Ohara glass. The differences in Li-S Ohara glass cell setup compared to the symmetrical cell setup were a larger electrode diameter, a higher electrolyte volume, the lithium anode and the Ohara glass separator. The Ohara glass stabilises the open circuit voltage of the Li-S cell allowing for the accurate measurement of the specific surface area. This shows the technique of determining the specific surface area from the impedance data is consistent and independent of the cell configuration. This means the specific surface area of the sulfur cathode determined from the symmetrical cell setup is a fair assessment of the specific surface area of a sulfur cathode in Li-S cell and could potentially be applied to other cell configurations such as coin cells and pouch cells. The other advantage of the symmetrical cell setup is that it avoids the polysulfide shuttle discharging the cell.

BET analysis was initially useful as a proof of concept for the SSA for the carbon electrodes. However, when BET was used to determine the SSA of the carbon/sulfur electrodes the value was much lower than the value obtained from impedance analysis. This was due to sulfur blocking the pores of the carbon matrix and therefore the nitrogen gas could not reach areas of the electrode. Whereas in the impedance cell, the electrolyte solubilises a small amount of the sulfur allowing access to these areas. Therefore the SSA values determined by BET analysis are not suitable for Li-S battery cathodes. The impedance technique developed in this study should be used instead because the SSA determined from impedance is an in-situ representative measurement of the SSA that considers how different electrolytes would interact within the porous electrode structure.

To verify this theory, carbon/sulfur electrodes were prepared with different amounts of sulfur in the electrode. These were compared to an industrial scale electrode from OXIS Energy Ltd. with similar amounts of sulfur to the lab scale electrodes. From the analysis of the lab scale electrodes, an increase in sulfur content reduced the SSA and increased the Warburg resistance which relates to the conductivity of the electrolyte within the electrode. For the industrial scale electrode, even though it had a very high sulfur content it still had the highest SSA and lowest Warburg resistance. This shows that the impedance technique developed in this study can be used to quantitatively compare the transport properties of different Li-S battery cathode formulations.

The final objective was to measure the impedance at different states of charge. However, the poor stability of the open circuit voltage after the discharge/charge steps due to polysulfide species still present in the electrolyte gave different impedance responses. Grazing incidence X-ray diffraction was used to study the species in the electrode and it proved that the cell had fully discharge/charged. The GIXRD for the pristine and discharged electrodes showed the conversion of sulfur to lithium sulfide in the electrode but X-ray diffraction was unable to detect the polysulfide intermediates. Even though the Li-S cells were not strictly at the fully discharged and charged states, the impedance measurements still showed the effect of the electrochemical history on the SSA. By allowing the system to reach a steady-state over the 100 hour rest, reproducible impedance measurements could be performed. Impedance measurements directly after charge or discharge were affected by the non-stationary distortion (NSD) because the system was not given enough time to reach equilibrium. The main concept for the GCPL/impedance coupled technique observed is that small differences in the cell preparation or other experimental conditions such as electrolyte volume, electrode alignment or the condition of the Ohara glass can produce different electrochemical behaviour, which is reflected in the different OCV and SSA values. Future work for the GCPL/impedance coupled technique will involve the development of the experiment parameters so that the impedance is measured at the end of discharge/charge. This could be achieved by using constant current then constant voltage (CC-CV) protocol to ensure stable open circuit potential by converting the trace polysulfide intermediates into sulfur when charging or lithium sulfide when discharging. Another possible solution to the voltage drift could be by applying a potential hold during the impedance measurement. The GCPL/impedance coupled technique could be used to monitor the impedance during the whole cycle life of the battery, instead of just one cycle. The measured SSA of the electrode could be studied against the cycle number to observe electrode degradation and pore blocking.

Chapter 5 Conclusions

The Li-S battery has the potential to be the next generation of secondary batteries due to the high theoretical specific energy of 2567 W h kg^{-1}.[7] This is much higher than the specific energy of the state of the art Li-ion batteries, meaning it could extend the driving range of an electric vehicle.[6] However Li-S batteries face serious challenges such as the polysulfide shuttle effect, low sulfur utilization, low cyclability and poor coulombic efficiency. This limits the working specific energy of the Li-S battery, restricting the commercial viability. Therefore, a deeper understanding of the complex redox mechanism and the variables that improve performance is required. Here we have shown the development of two analytical techniques that can be used to study the Li-S system, a ternary phase diagram and electrochemical impedance spectroscopy determination of the SSA. The phase diagram is a fundamental study of a common electrolyte for the Li-S battery system determining the polysulfide saturation point of the electrolyte and the relative solubility of different polysulfide species. This toolset can be applied to novel electrolytes to discover their properties. The impedance technique could identify new Li-S cathode materials with a high specific surface area and aid in achieving higher practical capacities.

A ternary phase diagram for the 1 M LiTFSI in DOL electrolyte system was constructed from the experimentally determined eutonic point which was confirmed by elemental analysis and 2-phase boundaries. The complete ternary phase diagram can be used as a predictive tool for determining the polysulfide solubility, the formation of solid products (lithium sulfide and sulfur) and the electrochemical response (Nernst equation) from the discharge profile. The experimentally determined eutonic points for the 0.5 M and 2 M LiTFSI in DOL electrolytes along with the eutonic point for the 1 M LiTFSI in DOL electrolyte showed the inversely proportional relationship between the electrolyte salt concentration and the polysulfide solubility within the electrolyte. This was also confirmed by galvanostatic cycling data, whereby the higher electrolyte salt concentrations showed a more efficient and longer lasting cell due to limited polysulfide solubility restricting the detrimental polysulfide shuttle effect. We also observed lower initial capacities for the higher electrolyte concentrations because the intermediate polysulfide species act as redox mediators improving the active material utilization.[20]

The preparation and analysis of more polysulfide blends would improve the accuracy of the 2-phase boundaries and reduce the uncertainty in their position for the 1 M LiTFSI in DOL electrolyte system. Further work will include studying different variables that would have an impact on the position of the eutonic point in the phase diagram such as the temperature of the solution, different electrolyte solvents (e.g. DOL/DME (1:1, volume ratio) or diglyme) and different electrolyte salts (e.g. LiTf or $LiNO_3$).

The electrochemical impedance spectroscopy analysis was first applied to a simple system of a carbon vs. carbon symmetrical cell setup. This means that any changes to the simple cell setup, such as replacing the carbon electrode with lithium, would result in new features on the Nyquist plot could be attributed to the lithium. The symmetrical cell setup with polished copper current collectors produced highly reproducible impedance responses with simple Nyquist plots making it easy to fit the raw impedance data. The SSA of the carbon electrode from impedance analysis was confirmed by BET analysis showing it was an accurate and reliable method. This technique was then applied to sulfur cathodes prepared in-house and supplied by OXIS Energy Ltd. We showed the effect of increasing the sulfur content of the electrode reduces the SSA and directly compared lab-scale 70 wt.% sulfur electrode and the OXIS cathode. The industrial-scale electrode had better transport properties compared to the lab-scale electrode such as the higher SSA and lower Warburg resistance meaning it will be optimized for battery performance.[19] Finally this method was applied to a Li-S cell at different states of charge to study the effect of galvanostatic cycling on the SSA of the electrode. GIXRD of the pristine and discharged sulfur cathodes confirmed the conversion of sulfur to lithium sulfide. Overall, this impedance analysis methodology could be used as a quantitative tool to study the SSA of prospective electrode preparations or materials for Li-S batteries.

Future work for the GCPL/impedance coupled technique will involve the development of the experiment parameters to ensure the impedance is measured at the end of discharge/charge. Then the GCPL/impedance coupled technique could be used to monitor the impedance during the whole cycle life of the battery. The measured SSA of the electrode could be studied against the cycle number to observe electrode degradation and pore blocking.

Chapter 6 Appendix

6.1 Preparation of Electrolyte

The electrolyte was prepared in terms of molarity i.e. 1 mole of solute per 1 litre of solvent. The mass of LiTFSI required was determined by;

$$m_{LiTFSI} = c_{Electrolyte} \times V_{Electrolyte} \times M_{LiTFSI} \qquad \text{Equation 6.1.1}$$

where m_{LiTFSI} is the mass of LiTFSI (g), $c_{Electrolyte}$ is the concentration of the electrolyte (mol L^{-1}), $V_{Electrolyte}$ is the volume of the electrolyte (L) and M_{LiTFSI} is the relative molar mass of LiTFSI (g mol^{-1}). Worked example, preparation of 10 ml solution of 1 M LiTFSI in DOL.

$$m_{LiTFSI} = 1\, mol\, L^{-1} \times 0.01\, L \times 287.09\, g\, mol^{-1} = 2.8709\, g \qquad \text{Equation 6.1.2}$$

6.2 Preparation of Polysulfide Solutions

The speciation of the target polysulfide species in solution will dictate the relative amounts of lithium sulfide and sulfur are required to synthesise it.

$$(n-1)\, S + Li_2S \xrightarrow{1\, M\, LiTFSI\, in\, DOL} Li_2S_n$$

Equation 6.2.1 – Preparation of the lithium polysulfide solution where n is the chain length.

For example, 1 mole of Li_2S_4 requires a mixture of ¾ moles of sulfur and ¼ moles of lithium sulfide. This is why the concentration of the polysulfide solutions is referred to in terms of its total atomic sulfur concentration (i.e. $[S]_T^{Sol.}$ = 1 M is the same as $[S_5^{2-}]$ = 0.2 M since 0.2 M x 5 = 1 M) because of the sulfur atoms being present in lithium sulfide, polysulfides and sulfur. Know with the understanding of the molar equivalents of the two components used to prepare the polysulfide species relationship to the chain length, the masses of lithium sulfide and sulfur required were determined by;

$$m_{Li_2S} = \frac{[S]_T^{Sol.} \times V_{PS} \times M_{Li_2S}}{n} \qquad \text{Equation 6.2.2}$$

$$m_S = \frac{[S]_T^{Sol.} \times V_{PS} \times M_S \times (n-1)}{n} \qquad \text{Equation 6.2.3}$$

where m_{Li_2S} is the mass of lithium sulfide (g), $[S]_T^{Sol.}$ is the total atomic sulfur concentration (mol L^{-1}), V_{PS} is the polysulfide solution volume (L), M_{Li_2S} is the relative molar mass of lithium sulfide (g mol^{-1}), n is the chain length, m_S is the mass of sulfur (g) and M_S is the relative molar mass of sulfur (g mol^{-1}). Worked example, preparation of 10 ml solution of 1 M Li_2S_4 in 1 M LiTFSI in DOL.

$$m_{Li_2S} = \frac{1\ mol\ L^{-1} \times 0.01\ L \times 45.95\ g\ mol^{-1}}{4} = 0.1149\ g \qquad \text{Equation 6.2.4}$$

$$m_S = \frac{1\ mol\ L^{-1} \times 0.01\ L \times 32.07\ g\ mol^{-1} \times (4-1)}{4} = 0.2405\ g \qquad \text{Equation 6.2.5}$$

6.3 Density of the Polysulfide Solution

The reliability of the automatic pipette to transfer the volume of solution selected is low due to the viscosity of the polysulfide blend, which makes the solution stick to the inside of the pipette tip and for the large majority of cases the volume dispensed is less than the volume set. This error could also arise from the fact that the automatic pipette is set against water, which has a density of 1 g mL^{-1} whereas the polysulfide blends will at least have a density of 1.18 g mL^{-1} because the blends are prepared in a 1 M LiTFSI in DOL.

Both the $BaSO_4$ gravimetric analysis and the UV/vis titration experiments rely on knowing the volume of the polysulfide solution added. Therefore, to avoid the unknown associated error with using the automatic pipette and the inaccuracies of dispensing the set volume the density was determined. This meant the mass of the transferred polysulfide solution, determined by weighing the amount polysulfide solution added in a vial, can be translated into volume.

The polysulfide solution was added to a preweighed volumetric flask up to the graduated mark then the mass was recorded again. The density of the polysulfide solution was determined by;

$$\rho_{PS} = \frac{m_{After} - m_{Before}}{V_{Volumetric}} \qquad \text{Equation 6.3.1}$$

where ρ_{PS} is the density of the polysulfide solution (g mL^{-1}), m_{After} is the mass of the polysulfide solution inside the volumetric flask (g), m_{Before} is the mass of the volumetric flask (g) and $V_{Volumetric}$ is the volume of the volumetric flask (mL). Worked example, density of 2 M Li_2S_6 in 1 M LiTFSI in DOL measured in 5 mL volumetric flask.

$$\rho_{PS} = \frac{17.0574\ g - 10.9310\ g}{5\ mL} = 1.2\ g\ mL^{-1} \qquad \text{Equation 6.3.2}$$

6.4 Gravimetric Analysis

The stoichiometric ratio between the initial polysulfide species and the barium sulphate product is 1:1 as shown in the following equation.

$$S_n^{2-} \xrightarrow{[O]} n\ SO_4^{2-} \xrightarrow{n\ Ba(NO_3)_2} n\ BaSO_4 + 2n\ NO_3^-$$

Equation 6.4.1– Reaction scheme for the $BaSO_4$ gravimetric analysis experiment.

Therefore the total atomic sulfur concentration can be determined by;

$$[S]_T^{Sol.} = \frac{m_{BaSO_4}}{M_{BaSO_4} \times V_{PS}} \qquad \text{Equation 6.4.2}$$

where m_{BaSO_4} is the mass of barium sulphate from the gravimetric analysis experiment (g) and M_{BaSO_4} is the relative molar mass of barium sulphate (g mol^{-1}). Worked example, gravimetric analysis of 2 M Li_2S_6 in 1 M LiTFSI in DOL.

$$[S]_T^{Sol.} = \frac{1.4442\ g}{233.38\ g\ mol^{-1} \times 0.003\ L} = 2.1\ mol\ L^{-1} \qquad \text{Equation 6.4.3}$$

6.5 UV-visible Absorbance Spectroscopy Redox Titration

The redox reaction that occurs in the titration experiment between the polysulfide solution and the ferrocenium tetrafluoroborate ($FcBF_4$) solution is shown in the following equation.

$$2\ \mathrm{FcBF_4} + \mathrm{Li_2S_n} \rightarrow 2\ \mathrm{Fc} + 2\ \mathrm{LiBF_4} + \frac{\mathrm{n}}{8}\ \mathrm{S_8}$$

Equation 6.5.1 – Oxidation of the lithium polysulfide solution using ferrocenium tetrafluoroborate.

The equation used to determine the polysulfide concentration was initially derived from the Beer-Lambert law;

$$A_{FcBF_4} = \varepsilon_{FcBF_4} \times c_{FcBF_4} \times l \qquad \text{Equation 6.5.2}$$

where $A_{FcBF_4}$is the absorbance of the FcBF$_4$ solution, $\varepsilon_{FcBF_4}$is the molar extinction coefficient (L mol^{-1} cm^{-1}), c_{FcBF_4} is the concentration of the FcBF$_4$ solution and l is the path length of the cuvette (1 cm). Equation 6.5.2 was rearranged in terms of the concentration of the ferrocenium tetrafluoroborate solution;

$$c_{FcBF_4} = \frac{A_{FcBF_4}}{\varepsilon_{FcBF_4} \times l} = \frac{n_{FcBF_4}}{V_{FcBF_4}} \qquad \text{Equation 6.5.3}$$

where $n_{FcBF_4}$is the number of moles of FcBF$_4$ in the solution (mol) and V_{FcBF_4} is the volume of the FcBF$_4$ solution (L). The stoichiometric ratio between ferrocenium tetrafluoroborate and the polysulfide blend (Equation 6.5.1). Therefore, the number of moles of ferrocenium tetrafluoroborate consumed (negative sign) during the redox reaction is equal to the number of moles of polysulfide species in solution (described by its concentration and volume).

$$\Delta n_{FcBF_4} = -2\ n_{PS} = -2 \times [S_n^{2-}] \times V_{PS} \qquad \text{Equation 6.5.4}$$

where $\Delta n_{FcBF_4}$is the number of moles of FcBF$_4$ in the solution is consumed in the redox reaction (mol), n_{PS} is the number of moles of polysulfide species in the solution (mol) and $[S_n^{2-}]$ is the polysulfide concentration (mol L^{-1}). Equation 6.5.4 was substituted into equation 6.5.3;

$$\frac{-\Delta\ A_{FcBF_4}}{\varepsilon_{FcBF_4} \times l} = \frac{2 \times [S_n^{2-}] \times V_{PS}}{V_{FcBF_4}} \qquad \text{Equation 6.5.5}$$

where $-\Delta\ A_{FcBF_4}$ is the reduction in the absorbance of the FcBF$_4$ solution where FcBF$_4$ in the solution is consumed in the redox reaction. Equation 6.5.5 was rearranged in terms of the polysulfide concentration;

$$[S_n^{2-}] = \left(\frac{-\Delta\ A_{FcBF_4}}{V_{PS}}\right) \times \frac{V_{FcBF_4}}{2\ \times\ \varepsilon_{FcBF_4}\ \times\ l} \qquad \text{Equation 6.5.6}$$

where the variables inside the brackets are analogous to the gradient of the absorbance vs. volume of PS solution added plot.

$$[S_n^{2-}] = \frac{-Gradient \times V_{FcBF_4}}{2 \times \varepsilon_{FcBF_4} \times l} \qquad \text{Equation 6.5.7}$$

From the concentration of the polysulfide solution, the chain length of the polysulfide species (Equation 6.5.8) and the average sulfur oxidation state (Equation 6.5.9) can be calculated.

$$n = \frac{[S]_{sol.}^{T}}{[S_n^{2-}]} \qquad \text{Equation 6.5.8}$$

$$Average\ Sulfur\ Oxidation\ State = \frac{2}{n} \qquad \text{Equation 6.5.9}$$

Worked example, UV/vis redox titration of 2 M Li_2S_6 in 1 M LiTFSI in DOL.

$$[S]_{sol.}^{T} = \frac{-(-8.6\ cm^{-3}) \times 30\ cm^3}{2\ \times 1\ cm \times\ 390\ M^{-1}cm^{-1}} = 0.33\ M \qquad \text{Equation 6.5.10}$$

$$n = \frac{2.1\ M}{0.33\ M} = 6.4 \qquad \text{Equation 6.5.11}$$

$$Average\ Sulfur\ Oxidation\ State = \frac{2}{6.4} = 0.31 \qquad \text{Equation 6.5.12}$$

6.6 Molar Extinction Coefficient of Ferrocenium Tetrafluoroborate in DOL

The molar extinction coefficient is one of the two constants, along with path length of the sample cell that is included in the determination of the polysulfide concentration (Equation 6.5.7). Therefore, a reliable value of the molar extinction coefficient is required such that it will not affect the precision of further propagated results such as polysulfide chain length.

The solutions that were prepared for the serial dilution experiment were stirred for at least 1 day to fully dissolve the ferrocenium tetrafluoroborate and filtered to remove any solid particles in solution that would scatter the light in the UV/vis spectrometer. Then the solution was diluted five times and the absorbance was recorded (Figure 6.6.1 and Figure 6.6.2).

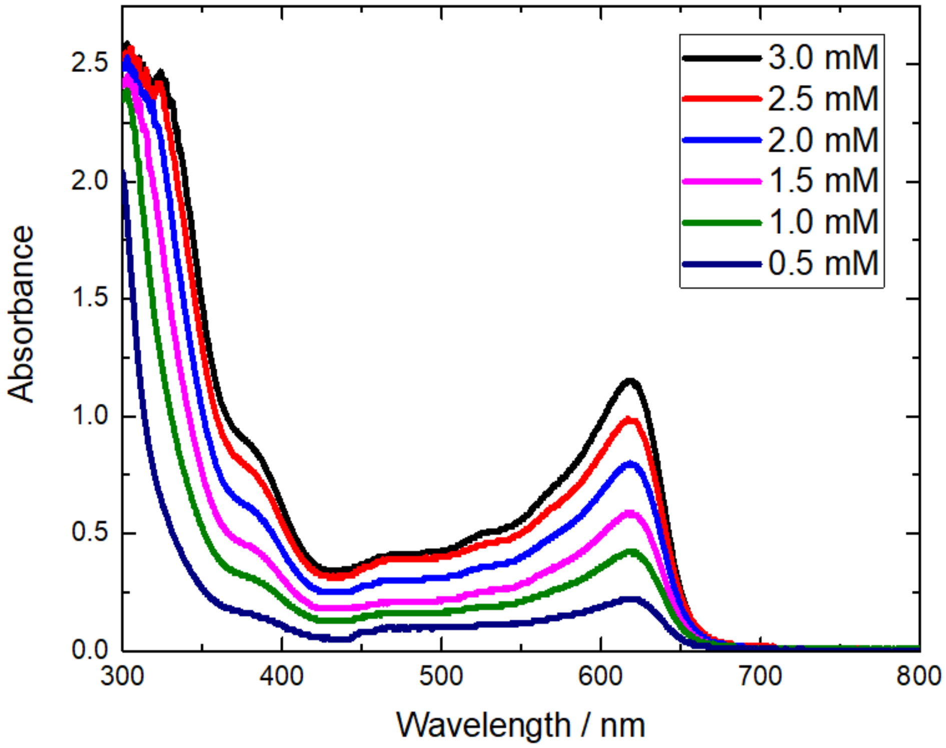

Figure 6.6.1 – UV-vis spectra with baseline correction obtained for the serial dilution of 3 mM ferrocenium tetrafluoroborate in DOL solution.

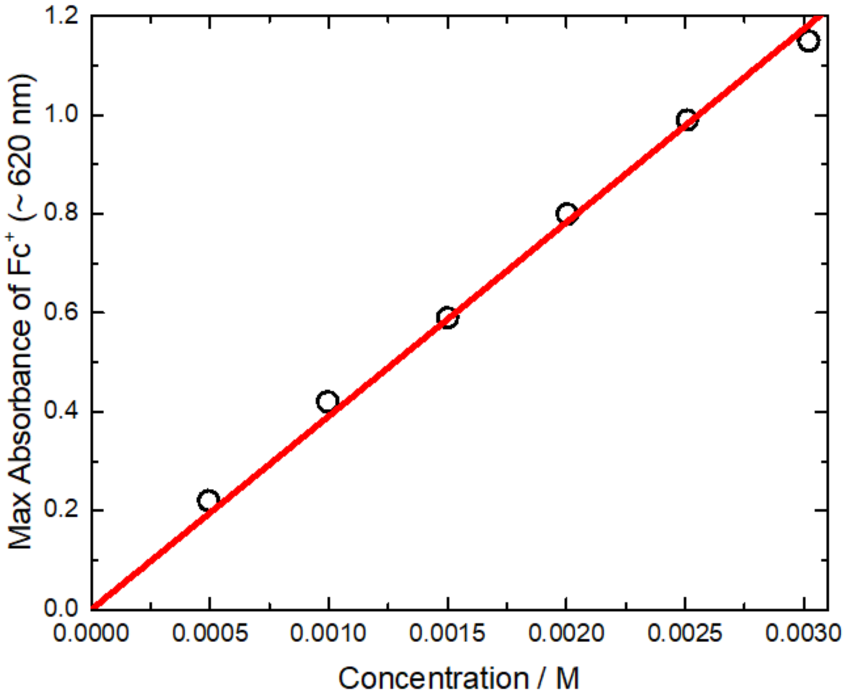

Figure 6.6.2 – Max absorbance of the ferrocenium tetrafluoroborate in DOL solution at 620 nm plotted against the ferrocenium tetrafluoroborate in DOL concentration to determine the molar extinction coefficient.

Beer-Lambert law states that the absorbance of a solution is directly proportional to the solutions concentration (Equation 6.5.2). Due to this relationship, the line of best-fit intercept was set to zero to obey Beer-Lambert law. The path length of the sample is 1 cm, which simplifies the equation such that the gradient is equal to molar extinction coefficient. This experiment was repeated five times to ascertain a reliable average value of the molar extinction coefficient (Table 6.6.1).

Serial Dilution Experiment No.	Molar Extinction Coefficient / M^{-1} cm^{-1}
1	392 ± 13
2	376.9 ± 6.6
3	398.2 ± 7.8
4	393.0 ± 3.1
5	381.5 ± 6.8
Average	388 ± 11

Table 6.6.1 – Averaged molar extinction coefficient determined from several serial dilution experiments. Error for individual experiments from regression analysis. Error for the average correspond to a confidence interval at a 95 % confidence level from repeat experiments.

Overall, a reliable value of the molar extinction coefficient of ferrocenium tetrafluoroborate in DOL solution has been determined to be 388 ± 11 M^{-1} cm^{-1} that can be used for the UV/vis titration experiment.

6.7 Molar Fraction Calculations

From the experimentally determined polysulfide solution density (ρ_{PS}), total atomic sulfur concentration ($[S]^{T}_{sol.}$), polysulfide concentration ($[S_n^{2-}]$) and polysulfide chain length (n) values the molar fractions of lithium sulphide, sulfur and electrolyte can be calculated to make the ternary phase diagram.

Any polysulfide solution or blend can be described as the mixture of three components (lithium sulfide, sulfur and electrolyte). For example, one mole of Li_2S_n would be described as one mole of Li_2S plus (n-1) moles of S (Equation 6.7.1).

$$(n-1)\ S + Li_2S \xrightarrow{1\ M\ LiTFSI\ in\ DOL} Li_2S_n$$

Equation 6.7.1 – Preparation of the lithium polysulfide solution where n is the chain length.

Thus, the total number of moles of the Li_2S component is equal to the number of moles of polysulfide species present. The polysulfide concentration was determined using the UV-visible absorbance spectroscopy redox titration (Equation 6.7.2);

$$moles_{Li_2S} = moles_{PS} = V_{PS} \times [S_n^{2-}] \qquad \text{Equation 6.7.2}$$

where $moles_{Li_2S}$ is the number of moles of lithium sulfide in the solution (mol) and $moles_{PS}$ is the number of moles of polysulfide species in solution (mol).

Since the total atomic sulfur concentration is known from the barium sulphate gravimetric analysis and the number of moles of lithium sulfide, the difference between these two values represents the number of moles of sulfur (Equation 6.7.3);

$$moles_S = (V_{PS} \times [S]^T_{sol.}) - moles_{Li_2S} \qquad \text{Equation 6.7.3}$$

where $moles_S$ is the number of moles of sulfur in the solution (mol).

To determine the number of moles of electrolyte present, the mass of the electrolyte present was calculated from the conservation of mass. Therefore, the mass of the electrolyte is equal to the total mass of the polysulfide solution minus the mass of the polysulfide species in solution (Equation 6.7.4 to Equation 6.7.6);

$$m_{Solution} = V_{PS} \times \rho_{PS} \qquad \text{Equation 6.7.4}$$

$$m_{PS} = moles_{PS} \times M_{PS} \qquad \text{Equation 6.7.5}$$

$$m_{Electrolyte} = m_{Solution} - m_{PS} \qquad \text{Equation 6.7.6}$$

where $m_{Solution}$ is the mass of the polysulfide solution (g), m_{PS} is the mass of the polysulfide species in the solution, M_{PS} is the relative molar mass of the polysulfide species in the solution (g);

$$M_{PS} = 2\, M_{Li} + n\, M_S \qquad \text{Equation 6.7.7}$$

that will be dependent on the polysulfide chain length where M_{Li} is the relative molar mass of lithium (g mol^{-1}) and $m_{Electrolyte}$ is the mass of the electrolyte solution (g).

The mass of the electrolyte was converted in volume via an experimentally determined density of the electrolyte ($\rho_{0.5\,M}$ = 1129.2 ± 9.3 g L^{-1}, $\rho_{1\,M}$ = 1192 ± 10 g L^{-1} and $\rho_{2\,M}$ = 1339 ± 12 g L^{-1}) (Equation 6.7.8);

$$V_{Electrolyte} = \frac{m_{Electrolyte}}{\rho_{Electrolyte}} \qquad \text{Equation 6.7.8}$$

where $\rho_{Electrolyte}$ is the electrolyte solution density (g L^{-1}).

Using the conservation of mass law again, the masses of LiTFSI and DOL used to prepare the electrolyte were determined (Equation 6.7.9 and Equation 6.7.10);

$$m_{LiTFSI} = c_{LiTFSI} \times V_{Electrolyte} \times M_{LiTFSI} \qquad \text{Equation 6.7.9}$$

$$m_{DOL} = m_{Electrolyte} - m_{LiTFSI} \qquad \text{Equation 6.7.10}$$

where m_{DOL} is the mass of DOL in the solution (g).

From these masses, the number of moles of both of the constituent parts that make up the electrolyte can be calculated (Equation 6.7.11 and Equation 6.7.12);

$$moles_{LiTFSI} = \frac{m_{LiTFSI}}{M_{LiTFSI}} \qquad \text{Equation 6.7.11}$$

$$moles_{DOL} = \frac{m_{DOL}}{M_{DOL}} \qquad \text{Equation 6.7.12}$$

where $moles_{LiTFSI}$ is the number of moles of LiTFSI in the electrolyte solution (mol), $moles_{DOL}$ is the number of moles of DOL in the electrolyte solution (mol) and M_{DOL} is the relative molar mass of DOL (g mol^{-1}).

The number of moles of electrolyte present is equal to the sum of the number of moles of LiTFSI and DOL present (Equation 6.7.13);

$$moles_{Electrolyte} = moles_{LiTFSI} + moles_{DOL} \qquad \text{Equation 6.7.13}$$

where $moles_{Electrolyte}$ is the number of moles of electrolyte (mol).

With the determined number of moles of the three components that make up the PS solution (lithium sulfide, sulfur and electrolyte), the molar fractions of these components were calculated;

$$MF_{Li_2S} = \frac{moles_{Li_2S}}{moles_{Li_2S} + moles_{Electrolyte} + moles_S} \qquad \text{Equation 6.7.14}$$

$$MF_{Electrolyte} = \frac{moles_{Electrolyte}}{moles_{Li_2S} + moles_{Electrolyte} + moles_S} \qquad \text{Equation 6.7.15}$$

$$MF_S = \frac{moles_S}{moles_{Li_2S} + moles_{Electrolyte} + moles_S} \qquad \text{Equation 6.7.16}$$

where MF_{Li_2S} is the molar fraction of lithium sulfide, $MF_{Electrolyte}$ is the molar fraction of the electrolyte and MF_S is the molar fraction of sulfur. The calculated molar fractions from experimental results were plotted into a ternary phase diagram where the x-axis is the MF_{Li_2S}, the y-axis is the $MF_{\mathrm{Electrolyte}}$ and the z-axis is the MF_{S}.

Worked Example, molar fractions of "10 M Li_2S_8 – 2" in 1 M LiTFSI in DOL blend that after filtration the polysulfide solution was 4.96 M $Li_2S_{5.63}$, where the volume of the polysulfide solution was set to an arbitrary value (1 mL).

$$\boldsymbol{moles_{Li_2S}} = moles_{PS} = 0.001\,L \times 0.88\,\mathrm{mol}\,L^{-1} = \mathbf{0.00088}\,\boldsymbol{mol} \qquad \text{Equation 6.7.17}$$

$$\boldsymbol{moles_S} = (0.001\,L \times 4.9\,mol\,L^{-1}) - 0.00088\,mol = \mathbf{0.0041}\;\boldsymbol{mol} \qquad \text{Equation 6.7.18}$$

$$m_{Solution} = 0.001\,L \times 1300\,g\,L^{-1} = 1.3\,g \qquad \text{Equation 6.7.19}$$

$$M_{PS} = (2 \times 6.941\,g\,mol^{-1}) + (5.63 \times 32.065\,g\,mol^{-1})$$
$$= 194.35\,g\,mol^{-1} \qquad \text{Equation 6.7.20}$$

$$m_{PS} = 0.00088\,mol \times 194.35\,g\,mol^{-1} = 0.17\,g \qquad \text{Equation 6.7.21}$$

$$m_{Electrolyte} = 1.3\,g - 0.17\,g = 1.13\,g \qquad \text{Equation 6.7.22}$$

$$V_{Electrolyte} = \frac{1.13\,g}{1192\,g\,L^{-1}} = 0.00095\,L \qquad \text{Equation 6.7.24}$$

$$m_{LiTFSI} = 1\,mol\,L^{-1} \times 0.00095\,L \times 287.09\,g\,mol^{-1} = 0.27\,g \qquad \text{Equation 6.7.25}$$

$$m_{DOL} = 1.13\,g - 0.27\,g = 0.86\,g \qquad \text{Equation 6.7.26}$$

$$moles_{LiTFSI} = \frac{0.27\,g}{287.09\;\;g\,mol^{-1}} = 0.00095\,mol \qquad \text{Equation 6.7.27}$$

$$moles_{DOL} = \frac{0.86\,g}{74.08\,g\,mol^{-1}} = 0.0116\,mol \qquad \text{Equation 6.7.28}$$

$$\boldsymbol{moles_{Electrolyte}} = 0.00095\,mol + 0.012\,mol = \mathbf{0.0125}\,\boldsymbol{mol} \quad \text{Equation 6.7.29}$$

$$MF_{Li_2S} = \frac{0.00088\,mol}{0.00088\,mol + 0.0125\,mol + 0.0041\;\,mol} = 0.05 \qquad \text{Equation 6.7.30}$$

$$MF_{Electrolyte} = \frac{0.0125\,mol}{0.00088\,mol + 0.0125\,mol + 0.0041\;\,mol} = 0.72 \qquad \text{Equation 6.7.31}$$

$$MF_S = \frac{0.0041\;\,mol}{0.00088\,mol + 0.0125\,mol + 0.0041\;\,mol} = 0.23 \qquad \text{Equation 6.7.32}$$

6.8 MEDAC Calculations

Calculations to convert the elemental analysis results as percentage found of each element in the polysulfide solution to the electrolyte concentration, the total atomic sulfur concentration and the polysulfide chain length.

The results from elemental analysis are mass percentage found values. The elements that were studied in the elemental analysis was lithium, sulfur, nitrogen and fluorine. There is an issue that lithium and sulfur atoms are present in both the LiTFSI molecule and polysulfide species dissolved in the polysulfide solution.

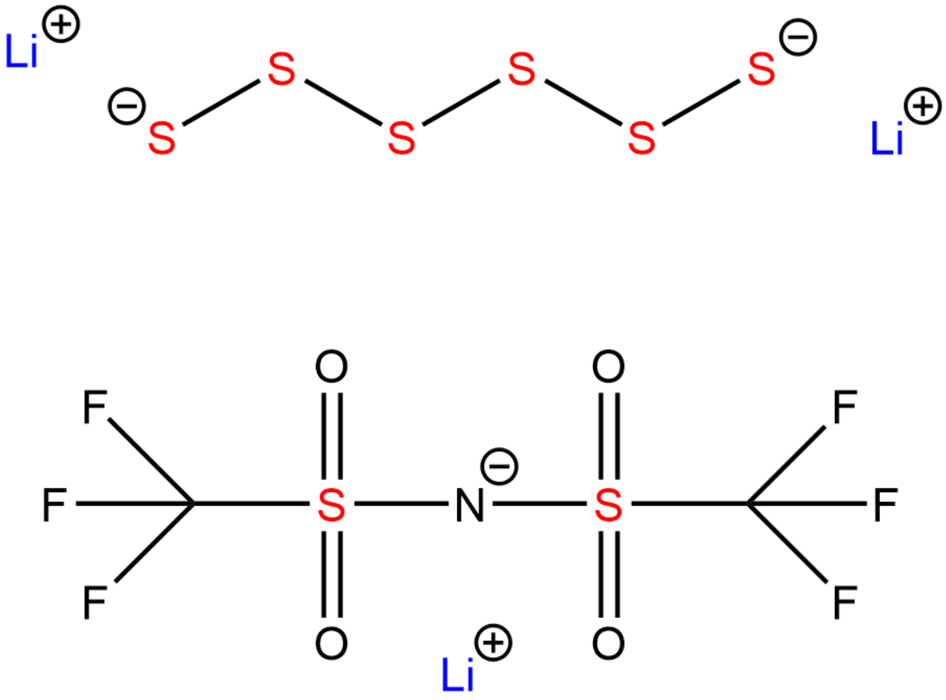

Figure 6.8.1 – Structure of the polysulfide species (top) and LiTFSI molecule (bottom).

Therefore the percentage found of the lithium and sulfur elements will be from both the LiTFSI molecule and polysulfide species. To determine the percentage found for each species separately, the atomic ratio of atoms in the LiTFSI molecule was used. For example, the atomic ratio between lithium and fluorine of 1/6 (1 lithium atom per 6 fluorine atoms in a LiTFSI molecule) can be used since fluorine is only present in the LiTFSI molecule. With this ratio the mass found of lithium in LiTFSI can be determined by;

$$F^{\%}_{Li-LiTFSI-F} = \frac{F^{\%}_{F} \times M_{Li}}{M_{F} \times AR_{Li:F}} \qquad \text{Equation 6.8.1}$$

where $F^{\%}_{Li-LiTFSI-F}$ is the mass percentage found of lithium in LiTFSI from fluorine (%), $F^{\%}_{F}$ is the mass percentage found of fluorine (%), M_F is the relative molar mass of fluorine (g mol^{-1}) and $AR_{Li:F}$ is the atomic ratio between lithium and fluorine. The mass found of lithium in LiTFSI can also be determined using the atomic ratio between lithium and nitrogen of 1:1;

$$F^{\%}_{Li-LiTFSI-N} = \frac{F^{\%}_{N} \times M_{Li}}{M_N \times AR_{Li:N}} \qquad \text{Equation 6.8.2}$$

where $F^{\%}_{Li-LiTFSI-N}$ is the mass percentage found of lithium in LiTFSI from nitrogen (%), $F^{\%}_{N}$ is the mass percentage found of nitrogen (%), M_N is the relative molar mass of nitrogen (g mol^{-1}) and $AR_{Li:N}$ is the atomic ratio between lithium and nitrogen. The mass percentage found of lithium in LiTFSI from fluorine and nitrogen should be the same, however there is small differences in the values from experimental uncertainties. Therefore, the mass percentage found of lithium in LiTFSI from fluorine and nitrogen were used to determine an average value of the mass percentage found of lithium in LiTFSI;

$$F^{\%}_{Li-LiTFSI-Average} = \frac{F^{\%}_{Li-LiTFSI-F} + F^{\%}_{Li-LiTFSI-N}}{2} \qquad \text{Equation 6.8.3}$$

where $F^{\%}_{Li-LiTFSI-Average}$ is the average value of the mass percentage found of lithium in LiTFSI (%).

From the average mass percentage found of lithium in LiTFSI, the concentration of lithium cations from LiTFSI (i.e. the electrolyte concentration) can be determined by;

$$[Li^{+}]_{LiTFSI} = c_{Electrolyte} = \frac{\left(\frac{F^{\%}_{Li-LiTFSI}}{M_{Li}} \times \frac{m_{Sample}}{100\ \%}\right)}{\left(\frac{m_{Sample}}{\rho_{PS}}\right)}$$

$$= \frac{F^{\%}_{Li-LiTFSI} \times \rho_{PS}}{M_{Li} \times 100\ \%} \qquad \text{Equation 6.8.4}$$

where $[Li^{+}]_{LiTFSI}$ is the concentration of lithium cations from LiTFSI (mol L^{-1}) and m_{Sample} is the mass of the sample taken for elemental analysis (g).

The mass percentage found of lithium in the polysulfide species can be determined by subtracting the mass percentage found of lithium in LiTFSI from the total mass percentage found of lithium;

$$F_{Li-PS}^{\%} = F_{Li}^{\%} - F_{Li-LiTFSI-Average}^{\%} \qquad \text{Equation 6.8.5}$$

where $F_{Li-PS}^{\%}$ is the mass percentage found of lithium in the polysulfide species (%) and $F_{Li}^{\%}$ is the mass percentage found of lithium (%). From the mass percentage found of lithium in polysulfide species, the concentration of lithium cations from the polysulfide species in the solution can be determined by;

$$[Li^{+}]_{PS} = \frac{F_{Li-PS}^{\%} \times \rho_{PS}}{M_{Li} \times 100\ \%} \qquad \text{Equation 6.8.6}$$

where $[Li^{+}]_{PS}$ is the concentration of lithium cations from the polysulfide species in the solution (mol L^{-1}). To determine the total atomic sulfur concentration the procedure is repeated with respect to the molar ratio between sulfur and fluorine, 1:3, or between sulfur and nitrogen, 2:1 (Equation 6.8.7 to Equation 6.8.11).

$$F_{S-LiTFSI-F}^{\%} = \frac{F_{F}^{\%} \times M_{S}}{M_{F} \times AR_{S:F}} \qquad \text{Equation 6.8.7}$$

$$F_{S-LiTFSI-N}^{\%} = \frac{F_{N}^{\%} \times M_{S}}{M_{N} \times AR_{S:N}} \qquad \text{Equation 6.8.8}$$

$$F_{S-LiTFSI-Average}^{\%} = \frac{F_{S-LiTFSI-F}^{\%} + F_{S-LiTFSI-N}^{\%}}{2} \qquad \text{Equation 6.8.9}$$

$$F_{S-PS}^{\%} = F_{S}^{\%} - F_{S-LiTFSI}^{\%} \qquad \text{Equation 6.8.10}$$

$$[S]_{PS} = [S]_{sol.}^{T} = \frac{F_{S-PS}^{\%} \times \rho_{PS}}{M_{S} \times 100\ \%} \qquad \text{Equation 6.8.11}$$

where $F_{S-LiTFSI-F}^{\%}$ is the mass percentage found of sulfur in LiTFSI from fluorine (%), M_S is the relative molar mass of sulfur (g mol^{-1}), $AR_{S:F}$ is the atomic ratio between sulfur and fluorine, $F_{S-LiTFSI-N}^{\%}$ is the mass percentage found of sulfur in LiTFSI from nitrogen (%), $AR_{S:N}$ is the atomic ratio between sulfur and nitrogen, $F_{S-LiTFSI-Average}^{\%}$ is the average value of the mass percentage found of sulfur in LiTFSI (%), $F_{S-PS}^{\%}$ is the mass percentage found of sulfur in the polysulfide species (%), $F_{S}^{\%}$ is the mass percentage found of sulfur (%) and $[S]_{PS}$ is the total atomic sulfur concentration (mol L^{-1}). With the lithium cation concentration and the total atomic sulfur concentration from the polysulfide species the chain length of the polysulfide species can be determined by;

$$n = \frac{[S]^{T}_{sol.}}{[S^{2-}_{n}]} \qquad \text{Equation 6.8.12}$$

where the concentration of the polysulfide species can be substituted by the lithium cation concentration because for each polysulfide anion there are two lithium cations. Therefore the concentration of lithium cations is double the polysulfide anions.

$$Li_2S_n \rightarrow [S^{2-}_{n}] = \frac{[Li^{+}]_{PS}}{2} \qquad \text{Equation 6.8.13}$$

Equation 6.8.12 was substituted into equation 6.8.13.

$$n = 2 \times \frac{[S]^{T}_{sol.}}{[Li^{+}]_{PS}} \qquad \text{Equation 6.8.14}$$

Worked example, elemental analysis results of “10 M Li_2S_6 – 3“ in 1 M LiTFSI in DOL.

Element	$F^{\%}$ / %
Lithium	1.68
Sulfur	19.535
Nitrogen	1.115
Fluorine	7.415

Table 6.8.1 – Elemental analysis results for the “10 M Li_2S_6“ in 1 M LiTFSI in DOL solution.

$$F^{\%}_{Li-LiTFSI} = \frac{7.415\ \% \times 6.941\ g\ mol^{-1}}{18.998\ g\ mol^{-1} \times 6} = 0.45\ \% \qquad \text{Equation 6.8.15}$$

$$F^{\%}_{Li-LiTFSI} = \frac{1.115\ \% \times 6.941\ g\ mol^{-1}}{14.0067\ g\ mol^{-1} \times 1} = 0.55\ \% \qquad \text{Equation 6.8.16}$$

$$F^{\%}_{Li-LiTFSI-Average} = \frac{0.45\ \% + 0.55\ \%}{2} = 0.5\ \% \qquad \text{Equation 6.8.17}$$

$$\boldsymbol{[Li^{+}]_{LiTFSI} = c_{Electrolyte}} = \frac{0.5\ \% \times 1300\ g\ L^{-1}}{6.941\ g\ mol^{-1} \times 100\ \%} = \boldsymbol{0.96\ M} \qquad \text{Equation 6.8.18}$$

$$F^{\%}_{Li-PS} = 1.68\ \% - 0.5\ \% = 1.18\ \% \qquad \text{Equation 6.8.19}$$

$$[Li^{+}]_{PS} = \frac{1.18\ \% \times 1300\ g\ L^{-1}}{6.941\ g\ mol^{-1} \times 100\ \%} = 2.2\ M \qquad \text{Equation 6.8.20}$$

$$F^{\%}_{S-LiTFSI} = \frac{7.415\ \% \times 32.065\ g\ mol^{-1}}{18.998\ g\ mol^{-1} \times 3} = 4.2\ \% \qquad \text{Equation 6.8.21}$$

$$F^{\%}_{S-LiTFSI} = \frac{1.115\ \% \times 32.065\ g\ mol^{-1}}{14.0067\ g\ mol^{-1} \times 0.5} = 5.1\ \% \qquad \text{Equation 6.8.22}$$

$$F^{\%}_{S-PS} = 19.535\ \% - 4.7\ \% = 14.835\ \% \qquad \text{Equation 6.8.23}$$

$$\boldsymbol{[S]_{PS}} = \boldsymbol{[S]^{T}_{sol.}} = \frac{14.835\ \% \times 1300\ g\ L^{-1}}{32.065\ g\ mol^{-1} \times 100\ \%} = \boldsymbol{6.2\ M} \qquad \text{Equation 6.8.24}$$

$$\boldsymbol{n} = 2 \times \frac{6.2\ M}{2.2\ M} = \boldsymbol{5.5} \qquad \text{Equation 6.8.25}$$

Results	$c_{Electrolyte}$ / M	$[S]^{T}_{sol.}$ / M	n
Experimental	1	5.81	5.26
MEDAC	0.96	6.2	5.5

Table 6.8.2 – Comparison between experimentally determined polysulfide species and the elemental analysis results.

6.9 Determination of SSA from Fitted Impedance Results

Two equivalent circuits were used to fit the raw impedance data, a resistor in series with a CPE (R-CPE) and a resistor in series with a CPE with a resistor in parallel (R-(CPE/R)).

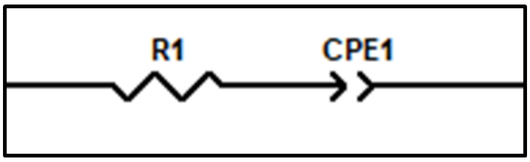

Figure 6.9.1 – Equivalent circuit of a resistor in series with a CPE (R-CPE).

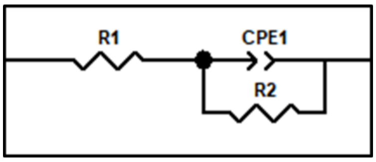

Figure 6.9.2 – Equivalent circuit of a resistor in series with a CPE with a resistor in parallel (R-(CPE/R)).

The impedance of a CPE can be described as;

$$Z_{CPE} = \frac{1}{T_{CPE}(i\omega)^{P_{CPE}}} \qquad \text{Equation 6.9.1}$$

where Z_{CPE} is the impedance of the CPE (Ω), T_{CPE} is related to the capacitance of the electrode ($F\ s^{1-P_{CPE}}$), ω is the angular frequency (rad s^{-1}) and P_{CPE} is the constant phase of the CPE. The CPE is defined by the T_{CPE} and P_{CPE} values. The first step to determining the SSA is to calculate the double layer capacitance (C_{dl}) of the electrode. If $P_{CPE} = 1$, then $T_{CPE} = C_{dl}$ because the T_{CPE} variable has units $F\ s^{1-P_{CPE}}$ which will simplify to F. This is identical to the behaviour of an ideal capacitor. However, from the impedance analysis of the different prepared electrodes the $P_{CPE} \neq 1$, meaning the double layer capacitance cannot be defined by T_{CPE} variable because the units will be $F\ s^{1-P_{CPE}}$. Equations derived by Lasia,[88] allow the estimation of the double layer capacitance of the CPE in a R-CPE (Equation 6.9.2) and R_1-(CPE/R_2) (Equation 6.9.3) equivalent circuits;

$$T_{CPE} = C_{dl}^{P_{CPE}} \times R_1^{-(1-P_{CPE})} \qquad \text{Equation 6.9.2}$$

$$T_{CPE} = C_{dl}^{P_{CPE}} \times (R_1^{-1} + R_2^{-1})^{(1-P_{CPE})} \qquad \text{Equation 6.9.3}$$

where C_{dl} is the double layer capacitance of the electrode (F), R_1 and R_2 are the resistances of their respective resistors (Ω). Equation 6.9.2 and equation 6.9.3 were rearranged in terms of the double layer capacitance.

$$C_{dl} = \left[T_{CPE} \times (R_1)^{(1-P_{CPE})}\right]^{1/P_{CPE}} \qquad \text{Equation 6.9.4}$$

$$C_{dl} = \left[T_{CPE} \times (R_1^{-1} + R_2^{-1})^{-(1-P_{CPE})}\right]^{1/P_{CPE}} \qquad \text{Equation 6.9.5}$$

Two different cell setups, conventional and symmetrical, were used for the impedance measurements. For the conventional cell setup, the double layer capacitance is equal to the capacitance of the electrode ($C_{dl} = C_{Electrode}$). For the symmetrical cell setup, the double layer capacitance is equal to half of the capacitance of the electrode because the two electrodes in the cell are like two capacitors in series;

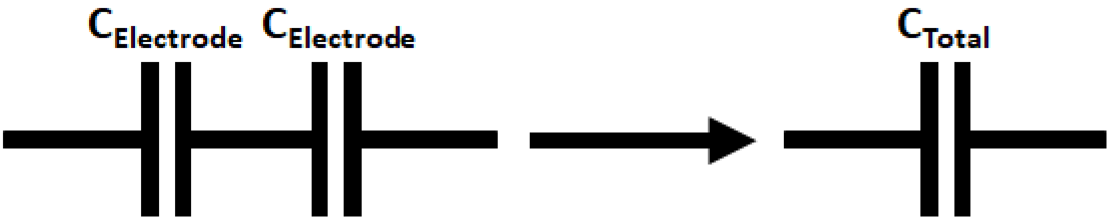

Figure 6.9.3 – Two capacitors in series equivalent to a single capacitor.

$$C_{Total} = \frac{1}{\left(\frac{1}{C_{Electrode}} + \frac{1}{C_{Electrode}}\right)} = \frac{1}{\left(\frac{2}{C_{Electrode}}\right)} = \frac{C_{Electrode}}{2} \qquad \text{Equation 6.9.6}$$

where C_{Total} is the total capacitance measured by impedance (F) and $C_{Electrode}$ is the double layer capacitance of one electrode (F). Therefore, the capacitance of each electrode is twice the total capacitance ($2\,C_{Total} = 2\,C_{dl} = C_{Electrode}$). With the capacitance of the electrode, the area of the can be determined by;

$$SA = \frac{C_{Electrode}}{C_A} \qquad \text{Equation 6.9.7}$$

where SA is the surface area of the electrode (m^2) and C_A is the areal capacitance of carbon (F m^{-2}). The areal capacitance of carbon was assumed to be 0.1 F m^{-2} based on an article that reports the carbon electrodes have a value of areal capacitance close to 0.1 F m^{-2} unless the pores are very small (i.e. < 2 nm).[89] This is not the case for the type of carbon (acetylene black) used in this work which has a mesoporous structure.

The assumed value suitability was proven experimentally from BET and impedance measurements by;

$$C_A = \frac{C_{Electrode\,(Impedance)}}{m_{Carbon} \times SSA_{(BET)}} \qquad \text{Equation 6.9.8}$$

where $C_{Electrode\,(Impedance)}$ is the capacitance of the electrode determined from impedance (F), m_{Carbon} is the mass of carbon in the electrode (g) and $SSA_{(BET)}$ is the specific surface area of the same electrode determined from BET (m^2 g^{-1}). For the carbon electrode an average areal capacity of 0.0997 ± 0.0057 F m^{-2} was obtained. With the specific area of the electrode, the SSA of the electrode can be determined by;

$$SSA = \frac{SA}{m_{Carbon}} \qquad \text{Equation 6.9.9}$$

where SSA is the specific surface area with respect to carbon (m^2 g^{-1}). Worked example for carbon vs carbon symmetrical cell with steel current collectors.

$$C_{dl} = \left[0.022\,F\,s^{0.05} \times (93\,\Omega)^{(1-0.95)}\right]^{1/0.95} = 0.023\,F \qquad \text{Equation 6.9.10}$$

$$C_{Electrode} = 2 \times 0.023\,F = 0.047\,F \qquad \text{Equation 6.9.11}$$

$$SA = \frac{0.047\ F}{0.1\ F\ m^{-2}} = 0.47\ m^2 \qquad \text{Equation 6.9.12}$$

$$SSA = \frac{0.47\ m^2}{0.0095\ g} = 49\ m^2 g^{-1} \qquad \text{Equation 6.9.13}$$

6.10 Determination of the Warburg Resistance

Fitting the symmetrical cell impedance data with an open Warburg element in series with a resistor.

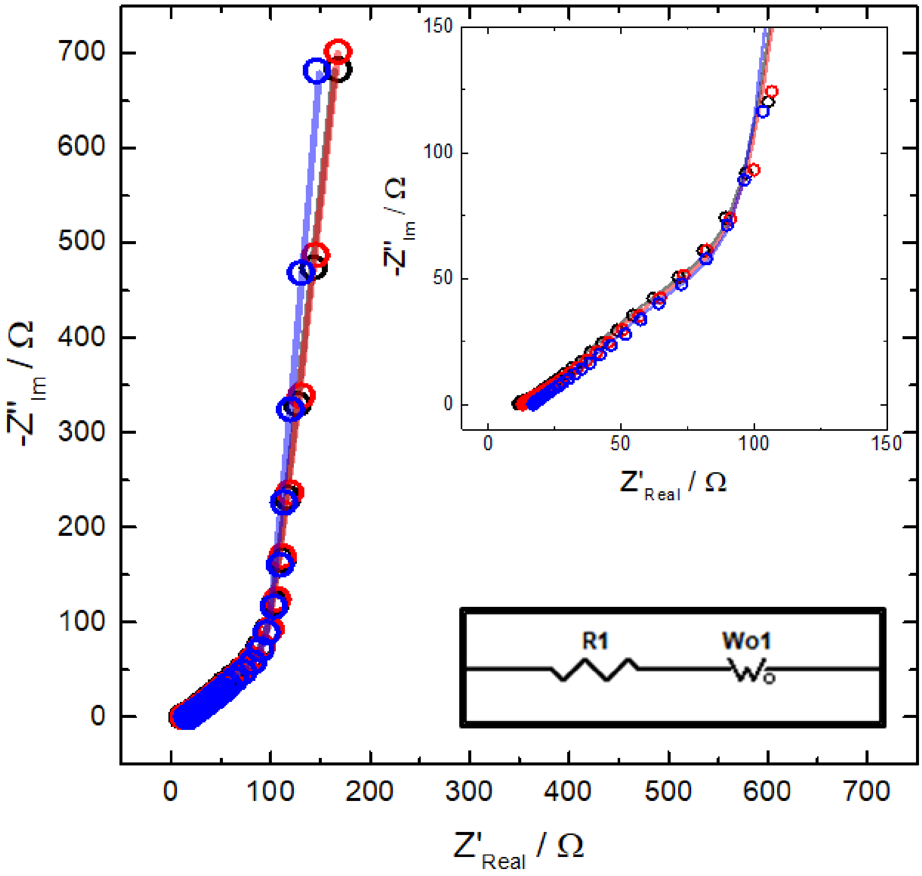

Figure 6.10.1 – Nyquist plot of carbon vs. carbon symmetrical cell with 1 M LiTFSI in DOL and polished copper current collectors in a ½ inch Swagelok cell repeated three times (data points – raw data, lines – fitted data). Equivalent circuit (black box) used to fit the raw impedance data. Frequency range – 200 kHz to 10 mHz. Voltage perturbation – 10 mV.

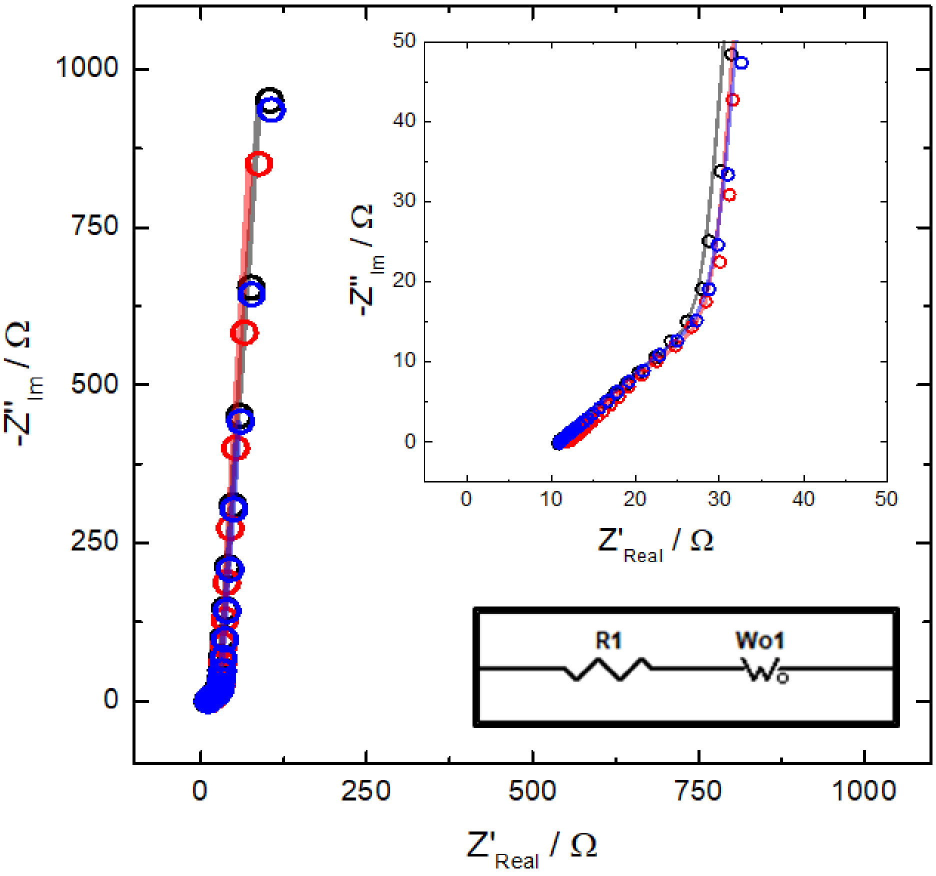

Figure 6.10.2 – Nyquist plot of C/S vs. C/S – 24 wt.% sulfur symmetrical cell with 1 M LiTFSI in DOL and polished copper current collectors in a ½ inch Swagelok cell repeated three times (data points – raw data, lines – fitted data). Equivalent circuit (black box) used to fit the raw impedance data. Frequency range – 200 kHz to 10 mHz. Voltage perturbation – 10 mV.

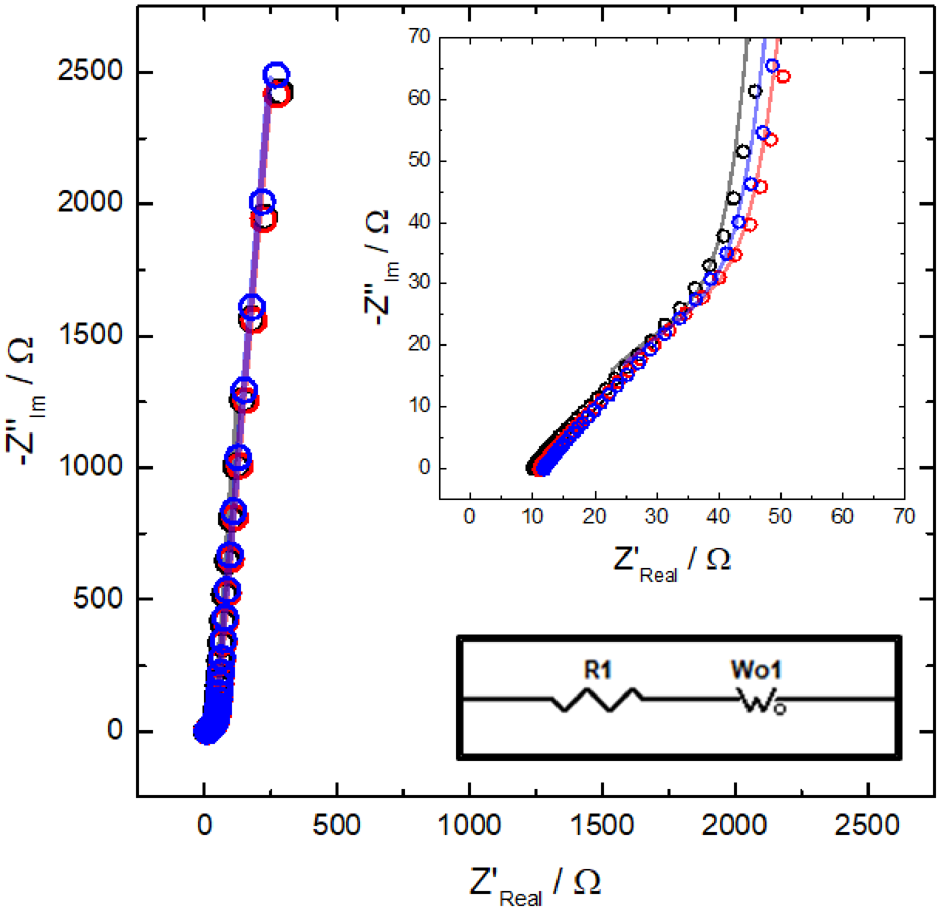

Figure 6.10.3 – Nyquist plot of C/S vs. C/S – 70 wt.% sulfur symmetrical cell with 1 M LiTFSI in DOL and polished copper current collectors in a ½ inch Swagelok cell repeated three times (data points – raw data, lines – fitted data). Equivalent circuit (black box) used to fit the raw impedance data. Frequency range – 200 kHz to 10 mHz. Voltage perturbation – 10 mV.

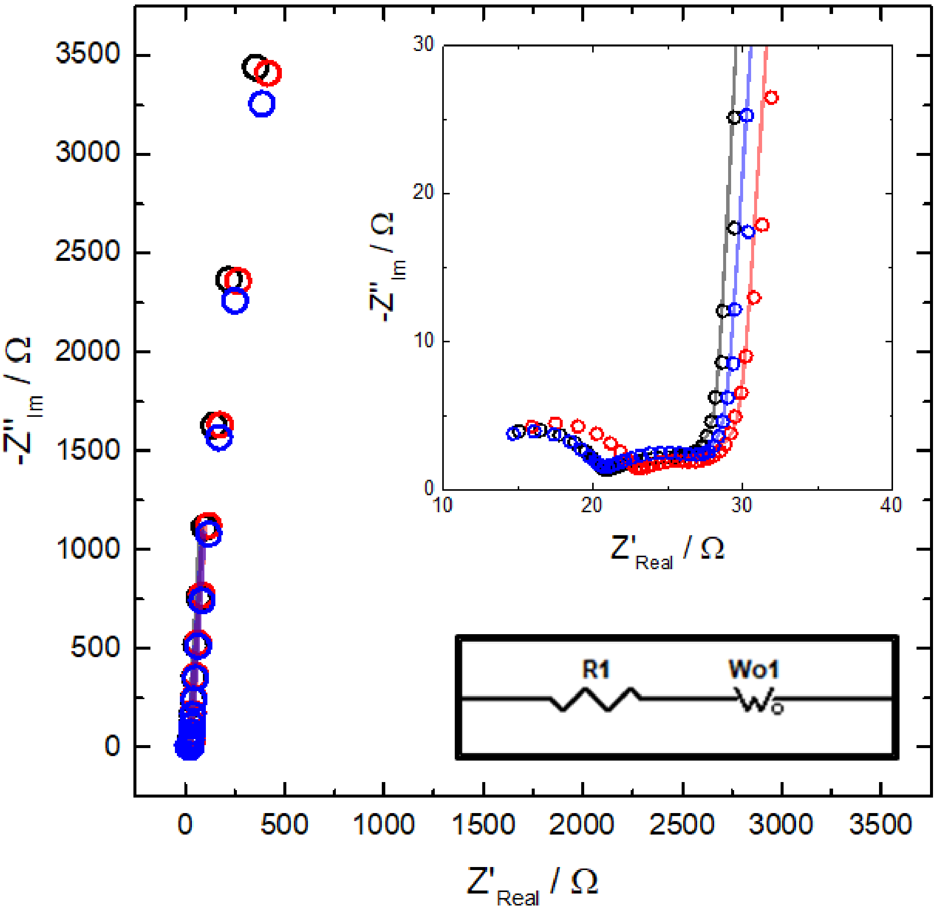

Figure 6.10.4 – Nyquist plot of OXIS cathode vs. OXIS cathode symmetrical cell with 1 M LiTFSI in DOL and polished copper current collectors in a ½ inch Swagelok cell repeated three times (data points – raw data, lines – fitted data). Equivalent circuit (black box) used to fit the raw impedance data. Frequency range – 200 kHz to 10 mHz. Voltage perturbation – 10 mV.

Cell Setup	Current Collector	R_1-W_{o1} Fit			
		R_1 / Ω	$\boldsymbol{R_{Wo1}}$**/ Ω**	T_{Wo1}/ s	P_{Wo1}
C vs. C	Copper	17.3 ± 6.3	**232 ± 15**	4.99 ± 0.31	0.469 ± 0.011
C/S vs. C/S – 24 wt.% S	Copper	11.4 ± 1.3	**51.9 ± 5.6**	0.81 ± 0.19	0.4804 ± 0.0057
C/S vs. C/S – 70 wt.% S	Copper	6.5 ± 1.2	**110 ± 14**	0.608 ± 0.074	0.4745 ± 0.0054
OXIS vs. OXIS	Copper	24.7 ± 1.8	**12.6 ± 1.6**	0.0473 ± 0.0049	0.4813 ± 0.0056

Table 6.10.1 – Summary of the averaged values obtained through fitting the raw impedance data from carbon, C/S – 24 wt.% sulfur, C/S – 70 wt.% sulfur and OXIS electrode symmetrical cell setups. Errors correspond to a confidence interval at a 95 % confidence level from repeat experiments

Chapter 7 References

1) M.-L. Tremblay, M. H. Martin, C. Lebouin, A. Lasia and D. Gauy, *Electrochim. Acta*, 2010, **55**, 6283–6291.

2) P. G. Bruce, S. A. Freunberger, L. J. Hardwick and J. -M. Tarascon, *Nat. Mater.*, 2012, **11**, 19–29.

3) A. S. Arico, P. Bruce, B. Scrosati, J. M. Tarascon and W Van Schalkwijk, *Nat. Mater.*, 2005, **4**, 366–377.

4) B. Dunn, H. Kamath and J. M. Tarascon, *Science*, 2011, **344**, 928-935.

5) House of Commons Business, Energy and Industrial Strategy Committee, Electric vehicles: driving the transition, *Fourteenth Report of Session 2017–19*, **HC 383.**

6) M. M. Thackeray, C. Wolverton and E. D. Isaacs, *Energy Environ. Sci.*, 2012, **5**, 7854–7863.

7) D. Eroglu, K. R. Zavadil and K. G. Gallagher, *J. Electrochem. Soc.*, 2015, **162**, 982–990.

8) M. Hagen, D. Hanselmann, K. Ahlbrecht, R. Maca, D. Gerber and J. Tubke, *Adv. Energy Mater.*, 2015, **5**, 14011986.

9) G. Li, Z. Chen and J. Lu, *Chem*, 2018, **4**, 3–7.

10) P. W. Gruber, P. A. Medina, G. A. Keoleian, S. E. Kesler, M. P. Everson and T. J. Wallington, *J. Ind. Ecol.*, 2011, **15**, 760–775.

11) U.S. Geological Survey, Mineral commodity summaries 2017, DOI: https://doi.org/10.3133/70180197.

12) G. Harper, R. Sommerville, E. Kendrick, L. Driscoll, P. Slater, R. Stolkin, A. Walton, P. Christensen, O. Heidrich, S. Lambert, A. Abbott, K. Ryder, L. Gaines and P. Anderson, *Nature*, 2019, **575**, 75–86.

13) P. Pangamol, C. Sirisinha, Y. Hu and S. G. Urquhart, *Ind. Eng. Chem. Res.*, 2013, **52**, 17179–17183.

14) M. Hagen, S. Dörfler, P. Fanz, T. Berger, R. Speck, J. Tübke, H. Althues, M. J. Hoffmann, C. Scherr and S. Kaskel, *J. Power Sources*, 2013, **224**, 260–268.

15) J. Zhu, J. Zou, H. Cheng, Y. Gu and Z. Lu, *Green Energy & Environment*, 2019, **4**, 345–359.

16) G. A. Elia, K. Marquardt, K. Hoeppner, S. Fantini, R. Lin, E. Knipping, W. Peters, J.-F. Drillet, S. Passerini and R. Hahn, *Adv. Mater.*, 2016, **28**, 7564–7579.

17) Y. Diao, K. Xie, S. Xiong and X. Hong, *J. Power Sources*, 2013, **235**, 181–186.

18) T. Zhang, M. Marinescu, S. Walus, P. Kovacik and G. J. Offer, *J. Electrochem. Soc.*, 2018, **165**, 6001–6004.

19) S. D. Talian, G. Kapun, J. Moškon, A. Vizintin, A. Randon-Vitanova, R. Dominko and M. Gaberšček, *Chem. Mater.*, 2019, **31**, 9012–9023.

20) Y.-C. Lu, Q. He and H. A. Gasteiger, *J. Phys. Chem. C*, 2014, **118**, 5733–5741.

21) X. Tang, Z. Xu, Z. Sun, J. Zhou, X. Wu, H. Lin, J. Rong, S. Zhuo and F. Li, *Energy Technol.*, 2019, **7**, 1900574

22) L. Wang, Y. Wang and Y. Xia, *Energy Environ. Sci.*, 2015, **8**, 1551–1558.

23) A. Berger, A. T. S. Freiberg, A. Siebel, R. Thomas, M. U. M. Patel, M. Tromp, H. A. Gasteiger and Y. Gorlin, *J. Electrochem. Soc.*, 2018, **165**, 1288–1296.

24) J. Xiao, Adv. *Energy Mater.*, 2015, **5**, 1501102.

25) H. Zhao, N. Deng, J. Yan, W. Kang, J. Ju, Y. Ruan, X. Wang, X. Zhuang, Q. Li and B. Cheng, *Chem. Eng. J.*, 2018, **347**, 343–365.

26) D. Aurbach, E. Zinigrad, Y. Cohen and H. Teller, *Solid State Ionics*, 2002, **148**, 405–416.

27) X. L. Xu, S. Wang, H. Wang, B. Xu, C. Hu, Y. Jin, J. B. Liu and H. Yan, *J. Energy Storage*, 2017, **13**, 387–400.

28) X.-B. Cheng, C. Yan, J.-Q. Huang, P. Li, L. Zhu, L. Zhao, Y. Zhang, W. Zhu, S.-T. Yang and Q. Zhang, *Energy Storage Mater.*, 2017, **6**, 18–25.

29) X. Chen, T.-Z. Hou, B. Li, C. Yan, L. Zhu, C. Guan, X.-B. Cheng, H.-J. Peng, J.-Q. Huang and Q. Zhang, *Energy Storage Mater.*, 2017, **8**, 194–201.

30) N. Ding, L. Zhou, C. Zhou, D. Geng, J. Yang, S. W. Chien, Z. Liu, M.-F. Ng, A. Yu, T. S. A. Hor, M. B. Sullivan and Y. Zong, *Sci. Rep.*, 2016, **6**, 33154.

31) X.-B. Cheng, C. Yan, X. Chen, C. Guan, J.-Q. Huang, H.-J. Peng, R. Zhang, S.-T. Yang and Q. Zhang, *Chem*, 2017, **2**, 258–270.

32) H. Kim, J. T. Lee, D.-C. Lee, M. Oschatz, W. I. Cho, S. Kaskel and G. Yushin, *Electrochem. Commun.*, 2013, **36**, 38–41.

33) J. Scheers, S. Fantini and P. Johansson, *J. Power Sources*, 2014, **255**, 204–218.

34) S. S. Zhang, *J. Power Sources*, 2013, **231**, 153–162.

35) D.-J. Lee, M. Agostini, J.-W. Park, Y.-K. Sun, J. Hassoun and B. Scrosati, *Chem. Sus. Chem.*, 2013, **6**, 2245–2248.

36) R. Younesi, G. M. Veith, P. Johansson, K. Edström and T. Vegge, *Energy Environ. Sci*., 2015, **8**, 1905–1922.

37) Y. Mikhaylik, I. Kovalev, R. Schock, K. Kumaresan, J. Xu and J. Affinito, *ECS Trans.*, 2010, **25**, 23–34.

38) N. Kang, Y. Lin, L. Yang, D. Lu, J. Xiao, Y. Qi and M. Cai, *Nat. Commun.*, 2019, **10**, 4597.

39) L. Sou, Y.-S. Hu, H. Li, M. Armand and L. Chen, *Nat. Commun*., 2013, **4**, 1481-1490.

40) M. Armand, F. Endres, D. R. MacFarlane, H. Ohno and B. Scrosati, *Nat. Mater.*, 2009, **8**, 621–629.

41) J.-W. Park, K. Yamauchi, E. Takashima, N. Tachikawa, K. Ueno, K. Dokko and M. Watanabe, *J. Phys. Chem. C.*, 2013, **117**, 4431–4440.

42) L. Wang and H. R. Byon, *J. Power Sources*, 2013, **236**, 207–214.

43) J. Hassoun and B. Scrosati, *Adv. Mater.*, 2010, **22**, 5198–5201.

44) J. H. Shin and E. J. Cairns, *J. Power Sources*, 2008, **177**, 537–545.

45) P. Arora and Z. Zhang, *Chem. Rev.*, 2004, 104, 4419–4462.

46) R. Raccichini, L. Furness, J. W. Dibden, J. R. Owen and N. Garcia-Araez, *J. Electrochem. Soc.*, 2018, **165**, 2741–2749.

47) M. S. Kiai and H. Kizil, *J. Electrochem. Soc.*, 2018, **165**, 3574–3581.

48) C. Dong, W. Gao, B. Jin and Q. Jiang, *iScience*, 2018, **6**, 151–198.

49) R. F. Bacon and R. Fanelli, *J. Am. Chem. Soc.*, 1943, **65**, 639–648.

50) S. Evers and L. F. Nazar, *Acc. Chem. Res.*, 2013, **46**, 1135–1143.

51) B. Zhang, X. Qin, G. R. Li and X. P. Gao, *Energy Environ. Sci.*, 2010, **3**, 1531–1537.

52) S. Zhang, M. Zheng, Z. Lin, N. Li, Y. Liu, B. Zhao, H. Pang, J. Cao, P. He and Y. Shi, J. *Mater. Chem. A*, 2014, **2**, 15889–15896.

53) C. Yan, X.-Q. Zhang, J.-Q. Haung, Q. Liu and Q. Zhang, *Trends Chem.*, 2019, **1**, 693–704.

54) X. Ji, K. T. Lee and L. F. Nazar, *Nature Mater.*, 2009, **8**, 500–506.

55) W. Ahn, K.-B. Kim, K.-N. Jung, K.-H. Shin and C.-S. Jin, *J. Power Sources*, 2012, **202**, 394–399.

56) S. Evers, T. Yim and L. F. Nazar, *J. Phys. Chem. C*, 2012, **116**, 19653–19658.

57) M. J. Lacey, F. Jeschull, K. Edstrom and D. Brandell, *J. Phys. Chem. C*, 2014, **118**, 25890–25898.

58) T. Cleaver, P. Kovacik, M. Marinescu, T. Zhang and G. Offer, *J. Electrochem. Soc.*, 2018, **165**, 6029–6033.

59) M. Wild, L. O'Neill, T. Zhang, R.Purkayastha, G. Minton, M. Marinescu and G. J. Offer, *Energy Environ. Sci.*, 2015, **8**, 3477 – 3494.

60) M. Marinescu, L. O’Neill, T. Zhang, S. Walus, T. E. Wilson and G. J. Offer, *J. Electrochem. Soc.*, 2018, **165**, 6107–6118.

61) X.Hua, T. Zhang, G. J. Offer and M. Marinescu, *J. Energy Storage*, 2019, **21**, 765–772.

62) C. Qu, Y. Chen, X. Yang, H. Zhang, X. Li and H. Zhang, *Nano Energy*, 2017, **39**, 262–272.

63) J. W. Dibden, J. W. Smith, N. Zhou, N. Garcia-Araez and J. R. Owen, *Chem. Commun.*, 2016, **52**, 12885–12888.

64) R. D. Rauh, F. S. Shuker, J. M. Marston and S. B. Brummer, *J. Inorg. Nucl. Chem.*, 1977, **39**, 1761–1766.

65) G. Schwarzenbach and A. Fischer, *Helv. Chim. Acta*, 1960, **43**, 1365–1390.

66) R.D. Rauh, K. M. Abraham, G. F. Pearson, J. K. Surprenant and S. B. Brummer, *J. Electrochem. Soc.*, 1979, **126**, 523–527.

67) K. Dokko, N. Tachikawa, K. Yamauchi, M. Tsuchiya, A. Yamazaki, E. Takashima, J.-W. Park, K. Ueno, S. Seki, N. Serizawa and M. Watanabe, *J. Electrochem. Soc.*, 2013, **160**, 1304–1310.

68) K. Ueno, J.-W. Park, A. Yamazaki, T. Mandai, N. Tachikawa, K. Dokko and M. Watanabe, *J. Phys. Chem. C*, 2013, **117**, 20509–20516.

69) J.-W. Park, K. Ueno, N. Tachikawa, K. Dokko and M. Watanabe, *J. Phys. Chem. C*, 2013, **117**, 20531–20541.

70) Z. Liu and P. P. Mukherjee, *ACS Appl. Mater. Interfaces*, 2017, **9**, 5263–5271.

71) T. Danner, G. Zhu, A. F. Hofmann and A. Latz, *Electrochim. Acta*, 2015, **184**, 124–133.

72) T. Zhang, M. Marinescu, S. Walus and G. J. Offer, *Electrochim. Acta*, 2016, **219**, 502–508.

73) S. Urbonaite, T. Poux and P. Novak, *Adv. Energy Mat.*, 2015, **5**, 1500118.

74) D. A. Dornbusch, R. Hilton, M. J. Gordon and G. J. Suppes, *J. Ind. Eng. Chem.*, 2013, **19**, 1968–1972.

75) C.-F. Chen, A. Mistry and P. P. Mukherjee, *J. Phys. Chem. C*, 2017, **121**, 21206–21216.

76) A. Ganesan, A. Varzi, S. Passerini and M. M. Shaijumon, *Electrochim. Acta*, 2016, **214**, 129–138.

77) D. N. Fronczek and W. G. Bessler, *J. Power Sources*, 2013, **244**, 183–188.

78) N. A. Canas, K. Hirose, B. Pascucci, N. Wagner, K. A. Freidrich and R. Hiesgen, *Electrochim. Acta*, 2013, **97**, 42–51.

79) Z. Deng, Z. Zhang, Y. Lai, J. Liu, J. Li and Y. Liu, *J. Electrochem. Soc.*, 2013, **160**, 553–558.

80) D. A. Dornbusch, R. Hilton, M. J. Gordon and G. J. Suppes, *J. Ind. Eng. Chem.*, 2013, **9**, 1968–1972.

81) A. A. Colville and K. Straudhammer, *Am. Mineral.*, 1967, **52**, 1877-1880.

82) H. Gamsjager, J. W. Lorimer, P. Scharlin and D. G. Shaw, *Pure Appl. Chem.*, 2008, **80**, 233–276.

83) Q. Cheng, W. Xu, S. Qin, S. Das, T. Jin, A. Li, A. C. Li, B. Qie, P. Yao, H. Zhai, C. Shi, X. Yong and Y. Yang, *Angew. Chem. Int. Ed.*, 2019, **58**, 5557–5561.

84) S. Dorfler, H. Althues, P. Hartel, T. Abendroth, B. Schumm and S. Kaskel, *Joule*, 2020, **4**, 539–554.

85) De Levie R. 1963 *Electrochim. Acta* **8** 751-780.

86) De Levie R. 1964 *Electrochim. Acta* **9** 1231-1245

87) J. Madjarov, S. C. Popat, J. Erben, A. Gotze, R. Zengerle and S. Kerzenmacher, *J. Power Sources*, 2017, **356**, 408–418.

88) A. Lasia, *Electrochemical Impedance Spectroscopy and its Applications*, Springer-Verlag New York, New York City, 1st edn, 2014, ch. 8, pp. 182–183.

89) J. Huang, B. G. Sumpter and V. Meunier, *Angew. Chem. Int. Ed.*, 2008, **47**, 520–524.

90) X. Qiu, Q. Hua, L. Zheng and Z. Dai, *RSC Adv.*, 2020, **10**, 5283–5293.

91) A. Lasia, *Electrochemical Impedance Spectroscopy and its Applications*, Springer-Verlag New York, New York City, 1st edn, 2014, ch. 4, pp. 94.

92) C. Zhao, H. Yang, X. Wang, H. Li, C. Qi, L. Wang and T. Liu, *Sustainable Energy Fuels*, 2019, **3**, 1966–1970.

93) C. Shen, J. Xie, M. Zhang, P. Andrei, M. Hendrickson, E. J. Plichta and J. P. Zheng, *J. Electrochem. Soc.*, 2019, **166**, A5287-A5294.

94) S. Dietrich and A. Haase, *Phys. Rep.*, 1995, **260**, 1–138.

95) G. S. Pawley and R. P. Rinaldi, *Acta Cryst.*, 1972, **28**, 3605–3609.

96) A. Claassen, *Recl. Trav. Chim. Pays-Bas*, 1925, **44**, 790–794.

97) A. S. Cooper, *Acta Cryst.*, 1962, **15**, 578–582.

98) C. Zu, Y.-S. Su, Y. Fu and A. Manthiram, *Phys. Chem. Chem. Phys.*, 2013, **15**, 2291–2297.